TESIS DE LA UNIVERSIDAD DE ZARAGOZA

2024 213

Nicolás Ignacio Villanueva Martínez

Electrodos avanzados para baterías recargables metal-aire

Director/es

Alegre Gresa, Cintia
Lázaro Elorri, María Jesús

ISSN 2254-7606

Prensas de la Universidad
Universidad Zaragoza

Universidad de Zaragoza
Servicio de Publicaciones

ISSN 2254-7606

Tesis Doctoral

ELECTRODOS AVANZADOS PARA BATERÍAS RECARGABLES METAL-AIRE

Autor

Nicolás Ignacio Villanueva Martínez

Director/es

Alegre Gresa, Cintia
Lázaro Elorri, María Jesús

UNIVERSIDAD DE ZARAGOZA
Escuela de Doctorado

Programa de Doctorado en Ingeniería Química y del Medio Ambiente

2024

Universidad Zaragoza
1542

Tesis Doctoral

Electrodos avanzados para baterías recargables metal-aire

Autor

Nicolás Villanueva Martínez

Director/es

María Jesús Lázaro Elorri
Cinthia Alegre Gresa

Escuela de Ingeniería
2023

UNIVERSIDAD DE ZARAGOZA

DEPARTMENTO DE INGENIERÍA QUÍMICA Y TECNOLOGÍAS

DEL MEDIO AMBIENTE

CONSEJO SUPERIOR DE INVESTIGACIONES CIENTÍFICAS (CSIC)

INSTITUTO DE CARBOQUÍMICA (ICB)

ELECTRODOS AVANZADOS PARA BATERÍAS RECARGABLES METAL-AIRE

Tesis para optar al grado de

Doctor en Ingeniería Química y del Medio Ambiente

Nicolás Villanueva Martínez

2023

Las doctoras **Dña. María Jesús Lázaro Elorri** y **Cinthia Alegre Gresa**, Investigadoras del Instituto de Carboquímica

CERTIFICAN

Que la presente memoria titulada "ELECTRODOS AVANZADOS PARA BATERÍAS RECARGABLES METAL-AIRE" corresponde al trabajo realizado por el Ingeniero Químico **D. Nicolás Ignacio Villanueva Martínez** en el Instituto de Carboquímica, de acuerdo al Proyecto de Tesis aprobado por el Departamento de Ingeniería Química y Tecnologías del Medio Ambiente de la Universidad de Zaragoza con fecha 15/06/2018, y autorizan su presentación para optar al Grado de Doctor en Ingeniería Química y del Medio Ambiente.

Y para que así conste, firman este certificado en Zaragoza, a 3 de octubre de 2023.

Fdo. Dra. Cinthia Alegre
Científica Titular CSIC

Fdo. Dra. María Jesús Lázaro
Profesora de Investigación CSIC

GOBIERNO DE ESPAÑA
MINISTERIO DE CIENCIA E INNOVACIÓN
AGENCIA ESTATAL DE INVESTIGACIÓN
CSIC
CONSEJO SUPERIOR DE INVESTIGACIONES CIENTÍFICAS

INSTITUTO DE CARBOQUÍMICA

Dr. **Tomás García Martínez**, director del Instituto de Carboquímica (ICB), perteneciente al Consejo Superior de Investigaciones Científicas (CSIC),

CERTIFICA

Que el trabajo que ha dado lugar a la presente tesis doctoral, titulada "ELECTRODOS AVANZADOS PARA BATERÍAS RECARGABLES METAL-AIRE", ha sido desarrollado por D. Nicolás Villanueva Martínez en el Instituto de Carboquímica (CSIC), bajo la supervisión de Dra. María Jesús Lázaro Elorri, Profesora de Investigación del Instituto, y Dra. Cinthia Alegre Gresa, Científico Titular dl Instituto.

Autorizo a la presentación de esta tesis al Programa de Doctorado en Ingeniería Química y del Medio Ambiente de la Universidad de Zaragoza.

Y para que así conste, firmo este certificado en Zaragoza, a 3 de octubre de 2023.

Firmado: Dr. Tomás García Martínez

INSTITUTO DE CARBOQUIMICA

CSIC
CONSEJO SUPERIOR DE INVESTIGACIONES CIENTÍFICAS

“Mira ese punto. Eso es aquí. Eso es nuestro hogar (...) no hay mejor demostración de la soberbia humana que esta imagen distante de nuestro minúsculo mundo. Para mí, subraya nuestra responsabilidad de tratarnos más amablemente los unos a los otros y de preservar y apreciar el pálido punto azul, el único hogar que hemos conocido.”

- Carl Sagan, observando la Tierra desde 6000 millones de kilómetros a través de la sonda Voyager 1

A Macarena y Martina, causas de mi felicidad (no incluyo en esta dedicatoria a Elur, ya que nunca sabrá leer)

Agradecimientos

Esta sección no puede empezar de otra manera que agradeciendo a dos mujeres que hicieron posible esta tesis. Me refiero, por supuesto, a las Doctoras María Jesús Lázaro Elorri y Cinthia Alegre Gresa, directoras de mi Tesis Doctoral. A Menchu, que confió en mí sin siquiera conocerme y me dio la oportunidad de unirme a su grupo de investigación, además de siempre haberse preocupado de que tuviésemos las condiciones necesarias para investigar. A Cinthia, por sus conocimientos y guía tanto en lo laboral y académico como en lo personal. Por ayudarme a organizar el trabajo de laboratorio y de oficina y por exigirme para obtener resultados, a pesar de que soy consciente de que no siempre es fácil trabajar conmigo. A ambas, estoy eternamente agradecido.

Agradezco también todo el personal del Instituto de Carboquímica, especialmente a Luis de Diego, Isabel Suelves y Tomás García, directores del instituto durante los años en que estuve. También a todo el personal científico, administrativo y del servicio de análisis. También al personal de la Universidad de Zaragoza, especialmente a Carlos Téllez, mi tutor, y a Pilar Sánchez y Begoña Esteban, secretarias del Departamento de Ingeniería Química, que tan buena disposición tuvieron siempre.

Quiero agradecer a la gente con la que compartí de forma más directa en el Instituto de Carboquímica, la gente del Grupo de Conversión de Combustibles. A David, por ayudarme tantas veces, a Giovanni, a Papu por tantas risas, a Laura y Antonio por su amistad, a Pedro y su voluntad de oro, a Manu, Sara, Abrham, Dani, Esther, Juan Carlos, Irene, Carlos, Cristina y varios más que me dejo en el tintero. Quiero agradecer también a los estudiantes a quienes debí guiar en prácticas, TFG o TFM: Nataly, Íñigo, África y Pablo. Espero que hayáis aprendido algo conmigo, yo ciertamente aprendí con vosotros.

Y fuera del GCC, a todos los estudiantes y otros investigadores con quienes compartí, especialmente a quienes fueron más cercanos: Óscar, Melanie, Miguel Ángel y su patinete asesino, “Clarardo” (os juro que un día de estos os devuelvo la Play), Charly, Víctor, José Miguel, Patri y muchas y muchos más, quienes podría estar nombrando por demasiadas líneas. Quiero hacer una mención especial a mis “roommates”, Alejandro y Javi, quienes me echaron varios cables, me vieron sufrir con las impedancias y me hicieron reír en innumerables ocasiones.

A los miembros del *Electrochemical Engineering Laboratory*, del *Energy Techonology Group*, de la Universidad de Southampton, quienes me recibieron en una estancia de 10 semanas de la que surgieron 3 publicaciones en colaboración. En especial, al Profesor Carlos Ponce de León, que me permitió trabajar en su grupo y usar sus instalaciones, y a Rachel y

Horacio, quienes guiaron mi trabajo durante la estancia. A la gente con la que compartí allí y que me acogió muy amablemente, como Sotiri o Recep.

Quiero también agradecer a mi familia, especialmente a mis padres, hermanos y suegra, quienes me apoyaron a la distancia y no dejaron de confiar en mí, aun cuando yo no lo hacía tanto. También a mis amigos, los del colegio, de la Universidad y de la vida. En especial a Pancho y Seli, padrinos de mi hija Martina, no saben chicos lo importante que ha sido contar con ustedes aquí cerca.

Y si hablamos de confiar, tengo que mencionar a un equipo que nunca deja de creer. Me refiero a la Primera Senior del Sala Arrabal-Intersala-El Burgo de Ebro FS, con quienes hemos pasado tremendos momentos tanto dentro como fuera del campo. Aunque las victorias hayan tardado dos años en llegar (al menos conmigo en la portería), han llegado, y se vienen muchas más, estoy seguro. Pero, más allá de cualquier resultado, vuestra amistad vale más que cualquier gol que haya marcado (que fue uno solo) o evitado (que tampoco fueron muchos).

Un pequeño apartado para Reyes y Fermín, regentes del Bar Nivola, cuyas tortillas, minis, cafés y menús hicieron estos años mucho más agradables de llevar.

Para el terminar, dejo los agradecimientos más importantes. Para Macarena, que ha estado conmigo durante todo este tiempo, alegrándome los buenos y aguantándome en los malos. Sin ti nada de esto sería posible, y nada de esto valdría la pena. Y a Martina, que, aunque haya llegado hace sólo unos meses le dio un nuevo sentido a mi vida y un nuevo significado a la palabra felicidad. Para ti, todo. Finalmente, a Elur, sin el que esta tesis probablemente habría estado lista bastante antes.

Tabla de contenido

Tesis por Compendio de Artículos

En concordancia con el Acuerdo de 25 de junio de 2020, del Consejo de Gobierno de la Universidad (BOUZ 7-20), modificado por Acuerdo de 29 de junio de 2022, del Consejo de Gobierno (BOUZ 08-22), en su Capítulo III, Artículo 20, se presenta esta Tesis Doctoral como Compendio de Publicaciones. La Tesis se titula "ELECTRODOS AVANZADOS PARA BATERÍAS RECARGABLES METAL-AIRE" y ha sido desarrollada por D. Nicolás Villanueva Martínez y supervisada por las Doctoras María Jesús Lázaro Elorri y Cinthia Alegre Gresa.

A continuación, se listan las publicaciones que conforman esta Tesis:

1. Villanueva, N., Alegre, C., Rubin, J., Figueredo-Rodriguez, H. A., McKerracher, R. D., de Leon, C. P., & Lázaro, M. J. (2022). Iron Electrodes Based on Sulfur-Modified Iron Oxides with Enhanced Stability for Iron–Air Batteries. *ACS Applied Energy Materials*, *5*(11), 13439-13451.
   DOI: 10.1021/acsaem.2c02123
   Área de conocimiento: MATERIALS SCIENCE, MULTIDISCIPLINARY
   Factor de impacto (2022): 6,4 (Q1)

2. Villanueva-Martínez, N. I., Alegre, C., Rubín, J., Mckerracher, R., de León, C. P., Rodríguez, H. A. F., & Lázaro, M. J. (2023). Investigation of the properties influencing the deactivation of iron electrodes in iron-air batteries. *Electrochimica Acta*, *465*, 142964.
   DOI: 10.1016/j.electacta.2023.142964
   Área de conocimiento: ELECTROCHEMISTRY
   Factor de impacto (2022): 6,6 (Q2)

3. Villanueva-Martínez, N. I., Alegre, C., Martínez-Visús, I., & Lázaro, M. J. (2023). Bifunctional oxygen electrocatalysts based on non-critical raw materials: Carbon nanostructures and iron-doped manganese oxide nanowires. *Catalysis Today*, *420*, 114083.
   DOI: 10.1016/j.cattod.2023.114083
   Área de conocimiento: CHEMISTRY, APPLIED y ENGINEERING, CHEMICAL
   Factor de impacto (2022): 5,3 (Q1)

4. Villanueva-Martínez, N. I., Alegre, C., Sebastián, D., Orozco, N., & Lázaro, M. J. (2023). On the Effect of the Nature of Carbon Nanostructures on the Activity of Bifunctional Catalysts Based on Manganese Oxide Nanowires. *Catalysts*, *13*(9), 1240.

DOI: 10.3390/catal13091240

Área de conocimiento: CHEMISTRY, PHYSICAL

Factor de impacto (2022): 3,9 (Q2)

Los cuatro artículos listados siguen una temática común, que es el desarrollo de materiales para electrodos de baterías hierro-aire, de acuerdo a lo propuesto y aceptado en el plan de investigación inicial de doctorado, del año 2018, y sus sucesivas actualizaciones anuales.

Resumen

Las necesidades de descarbonizar sectores claves de la economía, tales como el transporte y la generación eléctrica, han puesto el foco los últimos años en las tecnologías de almacenamiento energético, especialmente, en las tecnologías electroquímicas, de las cuales destacan las baterías. Dentro de las baterías, el sistema más usado en la actualidad son las baterías de ion-litio (LIB). A pesar de sus probadas ventajas, las LIB tienen algunos inconvenientes, como su costo relativamente elevado, problemas de seguridad asociados a sobrecalentamiento, incendios y explosiones, y el uso de materias primas críticas como el grafito, el cobalto y especialmente el litio, todos minerales críticos.

Un tipo de baterías que se ha planteado como alternativa a las LIB es el de las baterías metal-aire (MABs). Éstas están formadas por un electrodo negativo metálico y un electrodo positivo que funciona con oxígeno ambiental, lo que les permite tener mayores densidades energéticas. Dentro de las baterías MABs, las baterías hierro-aire (FABs) destacan por su relativamente alta densidad energética volumétrica (9.700 Wh l^{-1}), reversibilidad, electrolito acuoso y, sobre todo, la abundancia, bajo coste y reciclabilidad del hierro. Otra ventaja es la ausencia de formación de dendritas como las que aparecen en las baterías zinc-aire.

Pese a sus ventajas, las FABs presentan desafíos que limitan su aplicación a nivel tecnológico y económico. Durante la carga, ocurre en el electrodo negativo de hierro la parasitaria Reacción de Evolución de Hidrógeno (HER), la cual reduce la eficiencia faradaica del sistema. Otro de los desafíos que enfrentan los electrodos de hierro tiene que ver con la pérdida de capacidad durante la operación, lo que parece estar relacionado con la conductividad de las especies oxidadas. Una de las estrategias que se han aplicado en la literatura para contrarrestar estos desafíos es usar materiales de hierro ultrapuros, como el hierro carbonilo. Otra estrategia es el uso de aditivos tanto en el electrodo como en el electrolito, siendo los sulfuros metálicos los más estudiados, así como el óxido de bismuto o sulfuro de bismuto.

Por otra parte, el electrodo positivo debe efectuar las reacciones de evolución y reducción de oxígeno (OER y ORR, respectivamente), cuyas cinéticas son lentas, ya que involucran la transferencia de 4 electrones. Los catalizadores de referencia para la OER y ORR, Pt/C e IrO_2 o RuO_2, respectivamente, no son activos para la reacción inversa. Los catalizadores bifuncionales (que pueden realizar ambas reacciones) más investigados están basados en óxidos de cobalto. Sin embargo, el cobalto es un mineral con una cadena de suministro poco confiable y problemas éticos asociados a su extracción, por lo que se hace necesario buscar nuevos catalizadores bifuncionales de oxígeno para el electrodo positivo.

En esta tesis, se investigaron materiales tanto para el electrodo negativo como para el positivo de baterías hierro-aire. Para el electrodo negativo, se fabricaron electrodos de hierro basados en óxidos de hierro porosos modificados con azufre y en negro de carbono comercial. Los óxidos de hierro se obtuvieron en base a métodos de precipitación-calcinación con tres agentes precipitantes diferentes: ácido oxálico, hidróxido de sodio y ácido tartárico, y fueron tratados térmicamente en dos atmósferas distintas: en aire a 350 °C y en nitrógeno a 500 °C. Los óxidos de hierro fueron modificados con azufre añadiendo tiosulfato de sodio a su síntesis. Para el electrodo positivo, se obtuvieron catalizadores bifuncionales de oxígeno mediante un sencillo método de síntesis hidrotermal basados en nanofilamentos de óxido de manganeso dopados con hierro (Fe-MONW) y diferentes materiales carbonosos: nanofibras de carbono (CNF), nanotubos de carbono (CNT) y óxido de grafeno reducido (rGO).

Los materiales sintetizados para ambos electrodos fueron caracterizados físico-químicamente mediante técnicas de estado sólido: fisisorción de nitrógeno a 77 K, microscopía electrónica de transmisión (TEM), microscopía electrónica de barrido – espectroscopía de rayos X dispersiva de energía (SEM-EDX), difracción de rayos X (XRD), espectroscopía fotoelectrónica de rayos X (XPS), espectroscopía de emisión atómica por plasma acoplado inductivamente (ICP), espectroscopía Mössbauer (MS), espectroscopia Raman, espectroscopia de infrarrojo con transformada de Fourier (FT-IR) y análisis elemental (AE). Los materiales fueron caracterizados electroquímicamente mediante diversas técnicas: cronopotenciometría, voltametría lineal (LSV) y espectroscopía de impedancia electroquímica (EIS).

Los resultados de la caracterización físico-química para el electrodo negativo muestran que los óxidos de hierro obtenidos son mesoporosos, con áreas superficiales que van desde los 28 a los 141 $m^2\ g^{-1}$, siendo más alto este valor, así como también el volumen de poro, en los óxidos sintetizados con ácido tartárico y calcinados en aire. Las únicas fases cristalinas observadas fueron hematita y maghemita. En los óxidos modificados con azufre, éste se encontró en forma de sulfato, principalmente sobre la superficie de los materiales, y bien distribuido sobre ésta, como mostraron los análisis XPS y SEM-EDX.

Los resultados de las caracterizaciones electroquímicas mostraron que los óxidos modificados con azufre tienen una menor capacidad de descarga, pero una estabilidad considerablemente más alta que los óxidos no modificados. Esto se atribuye a que, como se mostró en caracterizaciones *post-mortem*, el sulfato se reduce a sulfuro durante la operación del electrodo, formándose sulfuro de hierro, que previene la pasivación. Se ajustó un modelo de disminución exponencial que permitió describir el comportamiento de los electrodos a lo largo

de los ciclos, algo que no se había visto reportado en la literatura hasta el momento. Dicho modelo incluye un factor de estabilidad, que toma valores entre 0 y 1, siendo 1 el valor correspondiente a un electrodo ideal, que mantiene su capacidad de descarga eternamente. Se correlacionó el factor de estabilidad contra las propiedades físico-químicas, obteniéndose correlaciones lineales fuertes (R^2 > 0,85) entre el factor de estabilidad y el área superficial (positiva) o el tamaño de poro (negativa). También se encontraron tendencias positivas entre el factor de estabilidad y el volumen de poro o el tamaño de cristal.

Para estudiar las causas de la desactivación de los electrodos de hierro, se realizaron estudios de EIS. Éstos revelaron que la resistencia a la transferencia de carga en la reducción de hidróxido de hierro (II) a hierro metálico aumenta hasta 15 después de 15 ciclos veces en los electrodos más inestables, mientras que prácticamente no cambia en los más estables. Con esta información y la obtenida mediante caracterizaciones *post-mortem*, concluimos que la desactivación de los electrodos de hierro se debe a la formación de una capa no reactiva y no conductiva de $Fe(OH)_2$. El electro más estable, sintetizado usando ácido tartárico, con adición de azufre y calcinado en aire, fue ciclado durante 500 horas, reteniendo casi el 75 % de su capacidad inicial.

Los catalizadores para el electrodo positivo consistieron en nanofilamentos de óxido de manganeso de ancho aproximado 75 nm y varias centenas de largo, áreas superficiales alrededor de los 25 m^2 g^{-1} y que tienen como única fase cristalina α-MnO_2. Los Fe-MONW contaron con un 2 – 7 % másico de hierro. El dopado con hierro no afectó la morfología ni propiedades texturales de los MONW. Sin embargo, introdujo defectos en la red cristalina debido a vacantes de oxígeno que se producen por el menor estado de oxidación del ion Fe^{3+} respecto al Mn^{4+}. Los materiales carbonosos mostraron diversas morfologías y propiedades texturales, teniendo las CNF una morfología *fishbone*, diámetro aproximado de 50 nm y áreas superficiales de 95 m^2 g^{-1}. Los CNT son de estructura multicapa, con 100 paredes aproximadamente, por lo que presentaron bajas áreas superficiales. El rGO está altamente reducido y cuenta con un promedio de 4,5 capas y 175 m^2 g^{-1} de área superficial.

Las LSV mostraron un claro efecto sinérgico para la ORR y OER entre las fases de carbonosas y de manganeso, al mostrar los composites menores sobrepotenciales para la ORR y OER que los materiales por separado, además de incrementarse el número de electrones transferidos en la ORR. En la ORR, el catalizador más activo fue el composite MONW/CNF, mientras que el composite MONW/rGO demostró una elevada actividad para la OER, superando incluso la del catalizador de referencia. Por estos motivos, se decidió sintetizar un material

híbrido haciendo crecer nanofibras de carbono sobre óxido de grafeno reducido (rGO-CNF). El composite MONW/rGO-CNF tuvo una actividad hacia la ORR incluso más elevada que MONW/CNF, y una actividad hacia la OER ligeramente inferior que MONW/rGO.

El dopado con hierro incrementó la actividad catalítica de los composites Fe-MONW/CNF tanto para la ORR como para la OER, reduciendo los sobrepotenciales. Esto se atribuyó a las vacantes de oxígeno inducidas por el ion Fe^{3+}, las que aumentan la capacidad de adsorción de oxígeno de los MONW. Los sobrepotenciales para la OER disminuyeron monótonamente con el porcentaje de hierro, mientras que, para la ORR, se alcanzó un óptimo a un 5 % de hierro.

Los materiales MONWrGO-CNF y Fe-MONW/CNF fueron probados en ensayos de larga duración a condiciones exigentes (±10 mA cm^{-2}), siendo capaces de operar en ciclos alternados de OER y ORR durante 20 horas a potenciales estables, con aumentos muy poco pronunciados de los sobrepotenciales.

Los resultados obtenidos en esta tesis doctoral entregan información novedosa y útil para el diseño y operación de electrodos para baterías hierro-aire, permitiendo avanzar en soluciones para la descarbonización de la economía.

Abstract

The need to decarbonize key sectors of the economy, such as transport and power generation, has focused attention in recent years on energy storage technologies, especially on electrochemical technologies, with batteries standing out. Within batteries, the most used system currently is lithium-ion batteries (LIB). Despite their proven advantages, LIBs have some issues, such as their relatively high cost, safety issues associated with overheating, fires and thermal runaway, and the use of critical raw materials like graphite, cobalt, and especially lithium.

An alternative to LIBs are metal-air batteries (MABs). They consist of a metallic negative electrode and a positive electrode that operates with ambient oxygen, allowing them to have higher energy densities. Among the MABs, iron-air batteries (FABs) stand out due to their relatively high volumetric energy density (9,700 Wh l^{-1}), reversibility, aqueous electrolyte and, especially, the abundance, low cost, and recyclability of iron. Another advantage is the absence of dendrite formation like the ones that show up in zinc-air batteries.

Despite their advantages, FABs hold challenges that limit their technological and economic application. During charging, the parasitic Hydrogen Evolution Reaction (HER) occurs at the iron negative electrode, which reduces the faradaic efficiency of the system. Another challenge faced by iron electrodes relates to the loss of capacity during operation, which seems to be related to the low conductivity of oxidized species. One of the strategies applied in literature to counter these challenges is the use of ultrapure iron materials, like carbonyl iron. Another strategy is the use of additives in both the electrode and the electrolyte, with metallic sulfides being the most studied, as well as bismuth oxide or bismuth sulfide.

On the other hand, the positive electrode must perform the oxygen evolution and reduction reactions (OER and ORR, respectively), whose kinetics are slow, as they involve the transfer of 4 electrons. The reference catalysts for OER and ORR, Pt/C, and IrO_2 or RuO_2, respectively, are not active for the reverse reaction. The most researched bifunctional catalysts (which can perform both reactions) are based on cobalt oxides. However, cobalt is a mineral with an unreliable supply chain and ethical issues related to its extraction, making it necessary to seek new bifunctional oxygen catalysts for the positive electrode.

In this thesis, materials for both the negative and positive electrodes of iron-air batteries were investigated. For the negative electrode, iron-based electrodes were manufactured based on porous sulphur-modified iron oxides and commercial carbon black. The iron oxides were obtained based on precipitation-calcination methods with three different precipitating agents:

oxalic acid, sodium hydroxide, and tartaric acid, and were thermally treated in two different atmospheres: in air at 350 °C and in nitrogen at 500 °C. The iron oxides were modified with sulfur by adding sodium thiosulfate to their synthesis. For the positive electrode, bifunctional oxygen catalysts based on iron-doped manganese oxide nanowires (Fe-MONW) and different carbonaceous materials: carbon nanofibers (CNF), carbon nanotubes (CNT), and reduced graphene oxide (rGO), were obtained through a simple hydrothermal synthesis method.

The synthesized materials for both electrodes were physically and chemically characterized through solid-state techniques: nitrogen physisorption at 77 K, transmission electron microscopy (TEM), scanning electron microscopy – energy-dispersive X-ray spectroscopy (SEM-EDX), X-ray diffraction (XRD), X-ray photoelectron spectroscopy (XPS), inductively coupled plasma atomic emission spectroscopy (ICP), Mössbauer spectroscopy (MS), Raman spectroscopy, Fourier transform infrared spectroscopy (FT-IR), and elemental analysis (EA). The materials were electrochemically characterized using different techniques: chronopotentiometry, linear sweep voltammetry (LSV), and electrochemical impedance spectroscopy (EIS).

The results of the physical-chemical characterization for the negative electrode show that the obtained iron oxides are mesoporous, with surface areas ranging from 28 to 141 $m^2 g^{-1}$, this value, as well as the pore volume, being higher in the oxides synthesized with tartaric acid and calcined in air. The only crystalline phases observed were hematite and maghemite. In the sulfur-modified oxides, it was found in the form of sulfate, mainly on the surface of the materials, and well distributed over it, as shown by the XPS and SEM-EDX analyses.

The results of the electrochemical characterizations showed that the sulfur-modified iron oxides have a lower discharge capacity, but considerably higher stability than the non-modified oxides. This is attributed to the fact that, as shown in post-mortem characterizations, the sulfate is reduced to sulfide during electrode operation, forming iron sulfide, which prevents passivation. An exponential decrease model was adjusted that allowed to describe the behavior of the electrodes throughout the cycles, something that had not been reported in the literature until now. This model includes a stability factor, which takes values between 0 and 1, 1 being the value corresponding to an ideal electrode, which maintains its discharge capacity forever. The stability factor was correlated against the physical-chemical properties, obtaining strong linear correlations (R2 > 0.85) between the stability factor and the surface area (positive) or the pore size (negative). Positive trends were also found between the stability factor and the pore volume or crystal size.

To study the causes of deactivation of the iron electrodes, EIS studies were performed. These revealed that the charge transfer resistance in the reduction of iron (II) hydroxide to metallic iron increases up to 15 times after 15 cycles in the least stable electrodes, while it almost did not change in the most stable ones. With this information, adding to what was found in post-mortem characterizations, we concluded that the deactivation of iron electrodes is caused by the formation of a non-conductive, non-reactive $Fe(OH)_2$ layer. The most stable electrode, the one obtained by precipitation with tartaric acid, sulphur-modified and calcined in air, was cycled during ca. 500 hours, retaining almost 75 % of its initial capacity.

Regarding the positive electrode, the results of the physical-chemical characterization showed that MONW had widths of ca. 75 nm and several nm of length. The only crystalline phase observed in these materials was α-MnO_2. Fe-MONW had 5 – 7 % wt. of iron. Iron-doping had no significant effect over the morphology or textural properties of the MONW. However, it introduced defects in the crystalline lattice, caused by vacancies, due to the lower oxidation state of Fe^{3+} ion compared to Mn^{4+}. Regarding the carbon materials, CNF had a fishbone morphology, 95 nm approximate diameter and a surface area of ca. 95 $m^2\ g^{-1}$. CNT have several layers, with ca. 100 walls, reason why they have low surface areas. rGO is highly reduced and has an average of 4.5 layers and a surface area of 175 $m^2\ g^{-1}$.

The LSVs showed a clear synergistic effect for the ORR and OER between the carbon and manganese phases, with the composites displaying lower overpotentials for the ORR and OER than the separate materials, in addition to an increase in the number of transferred electrons in the ORR. For the ORR, the most active catalyst was the MONW/CNF composite, while the MONW/rGO composite showed a high activity for OER, even surpassing that of the reference catalyst. Because of these reasons, it was decided to synthesize a hybrid material by growing carbon nanofibers on reduced graphene oxide (rGO-CNF). The MONW/rGO-CNF composite had an activity towards the ORR even higher than MONW/CNF, and an activity towards the OER slightly lower than MONW/rGO, but still higher than the reference catalyst.

Iron doping increased the catalytic activity of the Fe-MONW/CNF composites for both the ORR and OER, reducing overpotentials. This was attributed to the oxygen vacancies induced by the Fe^{3+} ion, which increase the oxygen adsorption capacity of the MONWs. The overpotentials for the OER decreased monotonously with the percentage of iron, while for the ORR, an optimum was reached at 5% iron.

The MONWrGO-CNF and Fe-MONW/CNF materials were tested in long-term trials under demanding conditions (±10 mA cm-2), being able to operate in alternating cycles of OER and ORR for 20 hours at stable potentials, with very slight increases in overpotentials.

The results obtained in this doctoral thesis provide novel and useful information for the design and operation of electrodes for iron-air batteries, allowing for advances in solutions for the decarbonization of the economy

CAPÍTULO I: INTRODUCCIÓN Y OBJETIVOS

En este capítulo se presentan los antecedentes que motivan el desarrollo de los estudios que componen esta tesis doctoral, así como también los fundamentos teóricos que rigen esta investigación. El capítulo incluye una descripción de las baterías metal-aire y específicamente las baterías hierro-aire, haciendo hincapié en los desafíos que enfrentan para poder convertirse en una tecnología madura y viable. Se revisa el estado del arte de los electrodos negativo y positivo de las baterías hierro-aire y, finalmente, se describen los objetivos generales y específicos que han guiado la tesis doctoral.

1. Antecedentes

1.1. Contexto global energético y ambiental

En su último informe, el Panel Intergubernamental para el Cambio Climático de las Naciones Unidas (IPCC) estima que, para limitar el aumento de la temperatura del planeta a 1,5 °C sobre los niveles preindustriales, las emisiones de gases de efecto invernadero deben ser reducidas a 25-30 Gton de CO_2eq al año [1]. De todas las emisiones de gases de efecto invernadero, el 24% provienen de la quema de combustibles fósiles para el transporte (72% de las cuales, provienen del transporte por carretera) [2,3] y el 34%, de la generación energética (electricidad y calor) [4]. Ambos sectores requieren ser descarbonizados urgentemente.

La estrategia principal para descarbonizar el sector de generación de energía radica en la adopción de fuentes de energía renovables, especialmente energía eólica y energía solar. Si bien la participación de estas tecnologías en la matriz eléctrica mundial ha crecido notablemente en los últimos años, aún están lejos de alcanzar o superar a los combustibles fósiles (**Figura 1**).

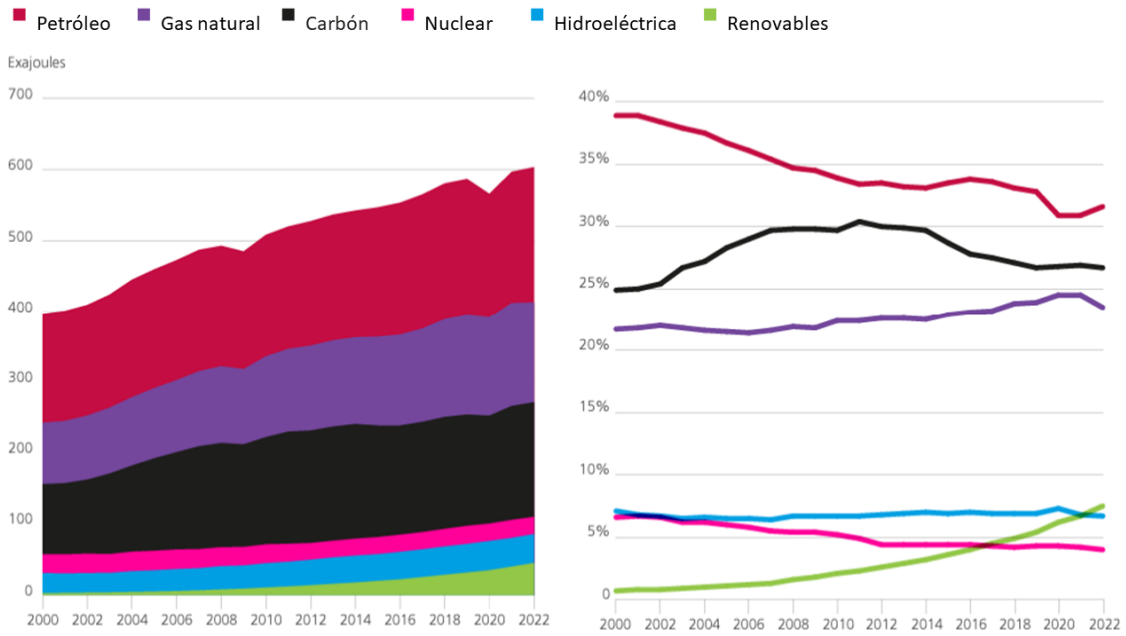

Figura 1. Cantidad de energía consumida mundialmente como consumo primario según fuente (izquierda) y porcentaje de participación en la matriz energética global de las distintas fuentes de energía primaria (derecha). Adaptado de [5].

Una de las grandes barreras que enfrentan las energías renovables en comparación con las fósiles es su intermitencia. Según la EIA (*U. S. Energy Information Administration*), el factor de planta promedio para las centrales de generación fotovoltaica de dicho país fue de 24.8% y para las centrales eólicas, de 36.1%, en 2022 [6]. Esto quiere decir que las centrales fotovoltaicas operaron al menos tres cuartos del tiempo a capacidad menor de la capacidad de diseño y las

eólicas, dos tercios del tiempo. La solución a estos problemas consiste en utilizar sistemas de almacenamiento energético, tales como el almacenamiento térmico, los sistemas de bombeo hidráulico o el almacenamiento electroquímico. Si bien hoy en día la capacidad instalada de almacenamiento energético en toda Europa apenas sobrepasa los 3 GWh, con una potencia instalada menor a 3 GW, se espera que a 2031 la capacidad llegue a 89 GWh y la potencia instalada a 45 GW [7].

La estrategia para la descarbonización del transporte de carretera consiste en la electrificación de los motores. Esto requiere sistemas de almacenamiento electroquímico (baterías) o de combustibles aptos para pilas de combustibles (como el hidrógeno). Los vehículos eléctricos representan hoy el 14 % de las ventas de vehículos en Europa, siendo casi el 80 % en Noruega y el 41 % en Suecia [8]. Para 2035, la Unión Europea planea vetar la venta de todo automóvil a combustión interna.

1.2. Sistemas electroquímicos de generación y almacenamiento de energía usados en la actualidad

Los sistemas de almacenamiento y generación electroquímicos son de vital importancia para todas las rutas hacia un futuro sostenible y con estabilidad climática, ya sea para estabilizar y asegurar la producción de electricidad de fuentes renovables o para descarbonizar el transporte de carretera. Estos sistemas se clasifican en tres grupos principales: baterías, pilas de combustible y supercondensadores.

Las baterías son sistemas de almacenamiento electroquímico que funcionan mediante reacciones redox. Están compuestas de dos electrodos, generalmente metálicos: un cátodo, en que ocurre la reducción durante la descarga, y un ánodo en que ocurre la oxidación. Entre los electrodos hay un electrolito, que conduce iones, pero no electrones. Estos electrolitos pueden ser ácidos, básicos, salinos, sólidos u orgánicos, lo que dependerá de las especies que reaccionen en los electrodos.

Las pilas de combustible, por otro lado, generan electricidad a partir de un gas que se oxida en un electrodo y oxígeno ambiental que se reduce en el otro. La reacción global es la combustión del gas (de ahí su nombre), siendo los más comunes el hidrógeno, el metano y el metanol. Las pilas de combustible tienen la ventaja de su ligereza al usar oxígeno ambiental y gases como combustible. Como contraparte, presentan bajas potencias específicas debido a la cinética lenta sobre todo de la reducción de oxígeno y el uso de materiales caros y escasos en sus electrodos (como el platino o el paladio).

Finalmente, los supercondensadores se basan en el almacenamiento de carga eléctrica en la doble capa eléctrica que se forma en la interfase entre superficies sólidas cargadas y electrolitos. Como la capacitancia de los condensadores es aproximadamente proporcional a su superficie, los supercondensadores requieren electrodos porosos de alta área superficial para maximizar la carga y energía específicas. Los condensadores presentan elevadas intensidades de corriente y potencias específicas, pero bajas energías específicas y densidades energéticas. El Diagrama de Ragone de la **Figura 2** muestra distintos sistemas de almacenamiento electroquímico y sus energías y potencias específicas (gravimétricas) típicas.

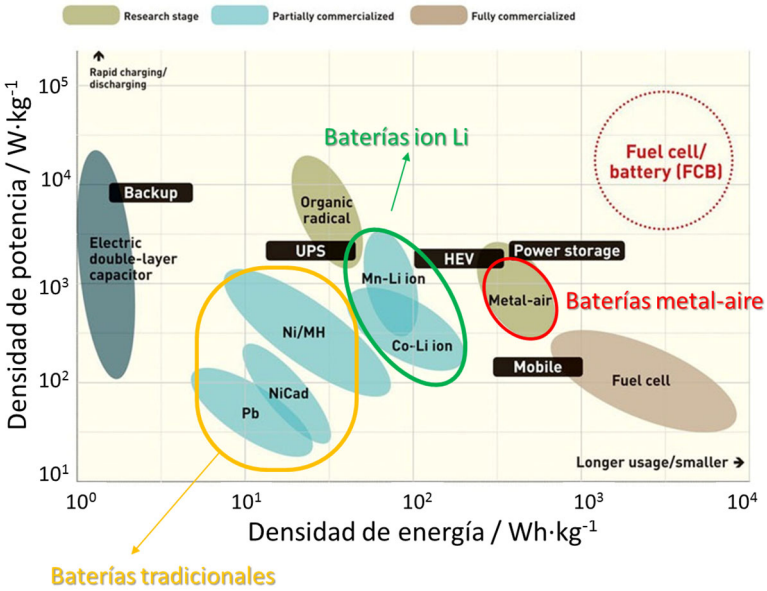

Figura 2. Diagrama de Ragone comparando distintos sistemas electroquímicos de almacenamiento de energía.

En la actualidad, los sistemas electroquímicos más usados de forma comercial son las baterías de ion-litio, seguidas por los sistemas de hidrógeno. Estas baterías presentan ventajas como su considerable energía específica (248 Wh kg^{-1} en el Tesla Model S, por ejemplo [9]), voltaje de celda elevado (3.7 V), estabilidad en la operación (más de 1000 ciclos de vida útil [10]) y elevada eficiencia energética, cerca de un 90%. Sin embargo, presentan desventajas como su costo relativamente elevado (alrededor de 125 € kWh^{-1} [11]), problemas de seguridad asociados a sobrecalentamiento, incendios y explosiones [9,12–14], y el uso de materias primas críticas como el grafito, el cobalto [15] y especialmente el litio, el 90 % de cuya producción está centrada únicamente en tres países: Australia, Chile y China [16]. Debido a estas cuestiones, nuevos sistemas de baterías avanzadas se encuentran en fase de investigación y desarrollo. Un grupo de sistemas que levanta un gran interés son las baterías metal-aire.

2. Baterías metal-aire

2.1. Descripción

Las baterías metal-aire son sistemas de almacenamiento de energía en las que, en el electrodo negativo, un metal se oxida durante la descarga y se reduce durante la carga de la batería. En el electrodo positivo, ocurre la reducción del oxígeno ambiental y la oxidación del agua, también conocida como evolución de oxígeno. El uso del oxígeno ambiental supone una ventaja sustancial en términos de peso y densidad de energía gravimétrica de estas baterías, al no estar uno de los reactivos almacenados en la batería, como en las convencionales. De esta forma, se posicionan como sistemas intermedios entre las baterías convencionales y las pilas de combustible, por lo que presentan un compromiso entre potencia y energía específicas interesante desde el punto de vista tecnológico, como se puede ver en el diagrama de Ragone (**Figura 2**).

Otra de las ventajas de las baterías metal-aire es que permiten el uso de metales abundantes, económicos y seguros, como son el aluminio, magnesio, zinc, sodio o hierro [17]. Tanto el potencial de celda como el electrolito que se use dependerán del metal del electrodo negativo, pudiendo ser acuoso (generalmente alcalino) u orgánico.

2.2. Tipos de baterías metal-aire

Como se ha mencionado anteriormente, en el electrodo negativo se pueden emplear distintos metales. Dentro de los que utilizan electrolito acuoso se encuentran el hierro y el zinc, mientras que los sistemas basados en aluminio, magnesio, sodio o litio, entre otros, requieren el uso de un electrolito orgánico, al encontrarse los potenciales de reducción de estos metales muy por debajo del potencial de evolución de hidrógeno (incluso, algunos metales como el sodio o litio reaccionan violentamente con el agua). La densidad y la cantidad de electrones de valencia del metal empleado, junto a su potencial de reducción, determinan la energía específica y densidad energética de las baterías. Así, los sistemas Li-aire y Al-aire rondan los 10.000 Wh kg^{-1} de energía específica (basado en la masa de metal), mientras que las baterías Fe-aire y Zn-aire sobrepasan ligeramente los 1.000 Wh kg^{-1}.

Otro aspecto importante en que influye el metal usado en el ánodo es la reversibilidad. Una batería secundaria puede ser recargada electroquímicamente, mientras que una primaria sólo puede ser descargada una vez (lo que comúnmente se conoce como pilas). En medio, se encuentran sistemas con reversibilidad limitada, que pueden ser recargados electroquímicamente unas cuantas veces hasta que pierden completamente su capacidad. Los nombrados sistemas Al-aire y Li-aire, por ejemplo, sólo muestran una reversibilidad limitada o

nula, dependiendo del electrolito utilizado (las baterías Al-aire pueden ser medianamente reversibles o primarias, si se usa un electrolito de líquido iónico o acuoso, respectivamente [18–20]). En la **Figura 3** se puede observar la comparación entre distintas baterías metal-aire.

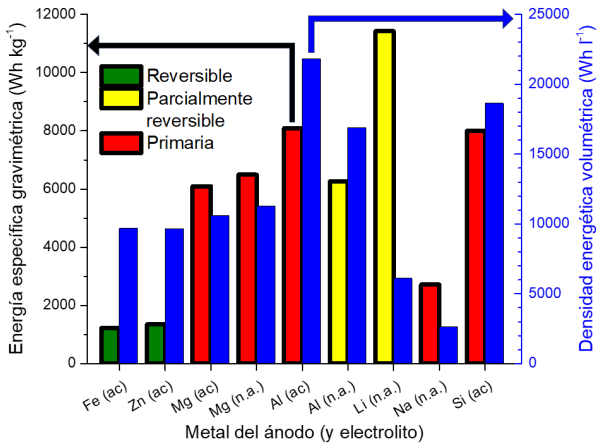

Figura 3. Energías específicas y densidades energéticas de distintos sistemas metal-aire. Se indica por colores la reversibilidad de los sistemas, mientras que ac significa batería de electrolito acuoso y n a. significa otro tipo de electrolito. Fuente: elaboración propia a partir de los datos de [17,21].

A día de hoy existen, ya ciertas aplicaciones que usan baterías metal-aire de forma comercial. Empresas como RiAlAir, Phinergy Marine y AlumaPower están desarrollando botes de pesca y de pasajeros de hasta 50 toneladas que baterías de aluminio-aire recargables mecánicamente (es decir, baterías primarias aluminio-aire que pueden ser "recargadas" cambiando el electrodo negativo). La empresa AlumaPower asegura que el uso de baterías primarias aluminio-aire puede reducir hasta en un 86 % las emisiones de gases de efecto invernadero en comparación con el uso de motores diésel en los barcos de pesca. Otras baterías metal-aire primarias que se han comercializado son las zinc-aire. Éstas se usan principalmente para sistemas de ayuda de ayuda a la audición (audífonos), debido a su seguridad, bajo coste relativo y energía específica relativamente alta. Según la empresa Duracell, las pilas de botón con química zinc-aire pueden alcanzar el doble de densidad energética y energía específica que una batería ion-litio de características equivalentes. No constan al momento de este estudio aplicaciones comerciales de baterías metal-aire secundarias, salvo un caso incipiente de baterías hierro-aire, que será discutido en la próxima sección.

3. Baterías hierro-aire

Dentro de las baterías metal-aire, las baterías hierro-aire cuentan con características interesantes desde un punto de vista tecnológico, como su relativamente alta densidad energética (9.700 Wh l^{-1}), reversibilidad, uso de electrolito acuoso y, sobre todo, la abundancia y bajo coste del hierro [22] (ver **Figura 4**). Pese a que cuentan con la energía específica teórica y

el potencial de circuito abierto de celda (1,28 V) más bajos de las baterías metal-aire, presenta también otras ventajas, como la ausencia de formación de dendritas que aparecen en las baterías zinc-aire [23], así como la facilidad de reciclado del hierro.

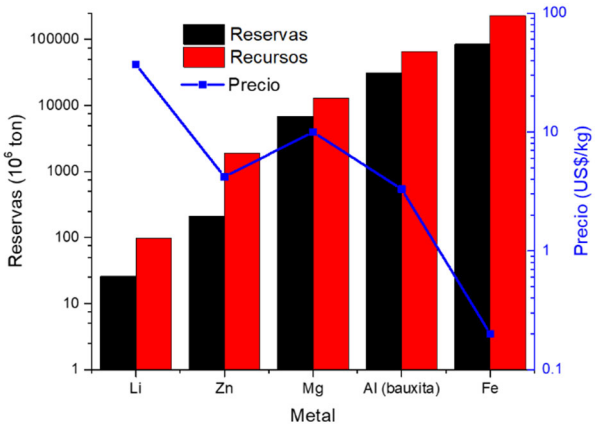

Figura 4. Reservas probadas, recursos y precio de distintos metales de electrodo negativo de baterías metal-aire. Fuente: elaboración propia a partir de los datos de [24].

Estas baterías comenzaron a ser investigadas a finales de la década de 1960, si bien los electrodos alcalinos de hierro ya habían sido descritos por primera vez a principios del siglo XX [25–27]. En el año 1968, aprovechando el impulso en las investigaciones sobre electrodos de hierro en la década de 1960 [28–31], la NASA desarrolló la primera batería hierro-aire, la cual contaba con una energía específica máxima de 154 Wh kg^{-1} y una capacidad de 20 Ah. Era capaz de operar hasta 200 ciclos. La crisis de los combustibles de la década de 1970 volvió a motivar la búsqueda de sistemas electroquímicos de almacenamiento de energía. De forma sucesiva, empresas como Siemens, Matsushita, Westinghouse y la Corporación Sueca de Desarrollo estudiaron e incluso llegaron a presentar prototipos. El de Westinghouse, por ejemplo, prometía una energía específica de 100 Wh kg^{-1} con una vida útil de 1000 ciclos y un coste de producción menor a 30 US$ kWh^{-1} [32].

En las décadas de 1990 y 2000, el moméntum acumulado se diluyó, principalmente debido a la caída en los precios del petróleo y al desarrollo exitoso de las baterías de ion-litio. Sin embargo, desde la década de 2010, y con el auge de las energías renovables y sus ya explicadas necesidades de almacenamiento energético, ha resurgido el intrés por el desarrollo de estos sistemas. Algunas muestras de ello son el proyecto ARPA-E de la Agencia Federal Estadounidense adjudicado a la Universidad del Sur de California para almacenamiento de electricidad de fuentes renovables o el proyecto NECOBAUT de la UE para estudiar baterías hierro-aire para automóviles. Otro ejemplo del interés suscitado por las baterías hierro aire es que, entre los años 2010 y 2023, se registran en la plataforma *Scopus* 80 artículos con las

palabras “iron air battery” en su título o palabras clave. Incluso, existen ya algunos productos comerciales incipientes, como los de la empresa Form Energy, quienes declaran que sus productos pueden almacenar el equivalente a 100 horas de producción de electricidad de fuentes renovables a un 1/10 del costo de las baterías de ion-litio [33]. La empresa Xcel Energy, con participación de los empresarios estadounidenses Bill Gates y Jeff Bezos, ha anunciado una recientemente una inversión de 20 millones de dólares en dos proyectos de almacenamiento de energía que utilizan la tecnología de Form Energy [34].

Durante la descarga de una batería hierro-aire, en el electrodo negativo, el hierro se oxida y en el electrodo positivo el oxígeno del aire se reduce (**Figura 5**). Las baterías hierro-aire operan con un electrolito básico, generalmente KOH concentrado, aunque también existen otras configuraciones, como baterías de estado sólido [35], o con líquidos iónicos [36] o sales fundidas [37] como electrolito. Los electrolitos sólidos y los líquidos iónicos tienen la ventaja de suprimir la reacción de evolución de hidrógeno (HER, que se detallará más adelante), pero presentan otras dificultades, como la elevada temperatura de operación que necesitan las baterías de estado sólido (necesaria para obtener una conductividad iónica aceptable) o la elevada viscosidad y corrosividad de los líquidos iónicos.

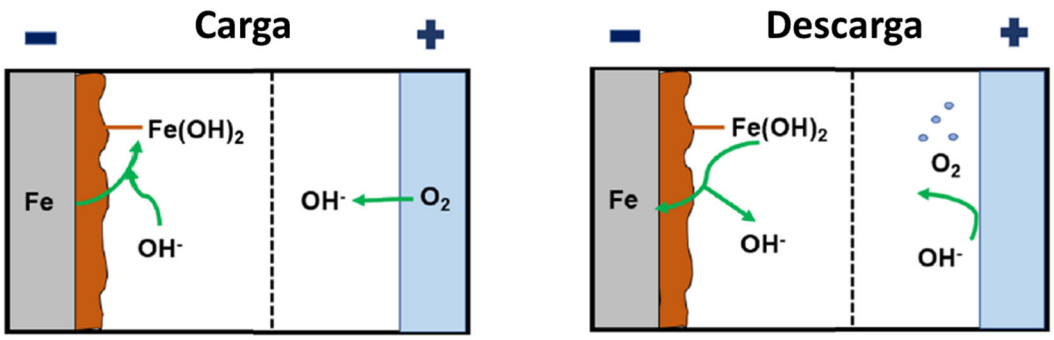

Figura 5. Esquema de la operación de una batería hierro-aire.

3.1. Electrodo de hierro

3.1.1. Las reacciones del electrodo de hierro

En los electrodos alcalinos de hierro, este metal se oxida en dos pasos, primero a hidróxido de hierro (II) (ecuación 1.1) y luego a magnetita (ecuación 1.2) o goetita (ecuación 1.3).

$$Fe + 2OH^- \rightleftharpoons Fe(OH)_2 + 2e^- \qquad E^0 = -0.88\ V\ vs\ SHE \quad (1.1)$$

$$3Fe(OH)_2 + 2OH^- \rightleftharpoons Fe_3O_4 + 4H_2O + 2e^- \qquad E^0 = -0.76\ V\ vs\ SHE \quad (1.2)$$

$$Fe(OH)_2 + OH^- \rightleftharpoons FeOOH + H_2O + e^- \qquad E^0 = -0.61\ V\ vs\ SHE \quad (1.3)$$

La primera etapa de descarga es preferida para aplicaciones tecnológicas debido a su potencial de equilibrio más negativo y mayor cantidad de electrones transferidos por átomo de hierro [21]. Las reacciones 1.2 y 1.3 implican una descarga más profunda del electrodo y proporcionan menos capacidad y voltaje. Especialmente, la ecuación 1.3 proporciona un voltaje de celda completa considerablemente más bajo y algunos autores han mencionado que estas descargas profundas pueden causar daños al electrodo [38]. En la práctica, las reacciones de la segunda etapa de descarga son complicadas y ocurren de forma paralela produciéndose, además de los mencionados FeOOH y Fe_3O_4, Fe_2O_3, ya sea como hematita (α-Fe_2O_3) o maghemita (γ- Fe_2O_3) [39–41].

Se ha mostrado que la reacción de hierro a hidróxido de hierro y viceversa (ecuación 1.1) ocurre mediante un intermediario disuelto, $HFeO_2^-$. El hierro sólido se oxida a $HFeO_2^-$ y este reprecipita a $Fe(OH)_2$, como se ve en las ecuaciones 1.1a y 1.1b:

$$Fe + 3OH^- \rightleftharpoons HFeO_2^- + H_2O + 2e^- \quad (1.1a)$$

$$HFeO_2^- + H_2O \rightleftharpoons +Fe(OH)_2 + OH^- \quad (1.1b)$$

La disolución y precipitación genera que, durante los primeros ciclos de operación de la batería, aumenta la rugosidad de la superficie a escala nanométrica, como Weinrich *et al.* comprobaron mediante estudios de microscopía de fuerza atómica [42]. Debido a esto, la capacidad de descarga del electrodo de hierro aumenta, debido a que se va exponiendo cada vez más material al electrolito, en un proceso conocido como formación del electrodo [43]. Este periodo de formación depende de las propiedades fisicoquímicas del electrodo y puede comprender desde unos pocos ciclos hasta centenas [44]. Se ha estudiado también que la corriente aplicada de carga durante el periodo de formación afecta fuertemente el comportamiento final de los electrodos de hierro [38]. Aumentar tanto la intensidad de corriente de carga como el tiempo de carga puede lograr que el electrodo tenga una mayor capacidad de descarga una vez completado el periodo de formación, pudiendo esta predecirse mediante una combinación lineal de la corriente y tiempo de descarga. También se ha demostrado que el uso de aditivos durante el periodo de formación afecta las propiedades finales del electrodo. Manohar *et al.* [44] mostraron que el uso de agentes que faciliten la mojabilidad del electrodo pueden acelerar la formación y el uso de agentes creadores de porosidad aumenta la capacidad del electrodo al final de la formación.

Como se ha mencionado previamente, el primer paso de descarga de la batería es capaz de entregar, teóricamente, 960 mAh g_{Fe}^{-1}, mientras que la reacción 1.2 entrega 320 mAh más por gramo de hierro. En la **Figura 6** se muestra un esquema de las reacciones de carga y descarga

de un electrodo de hierro contra un electrodo de mercurio-óxido de mercurio durante una cronopotenciometría.

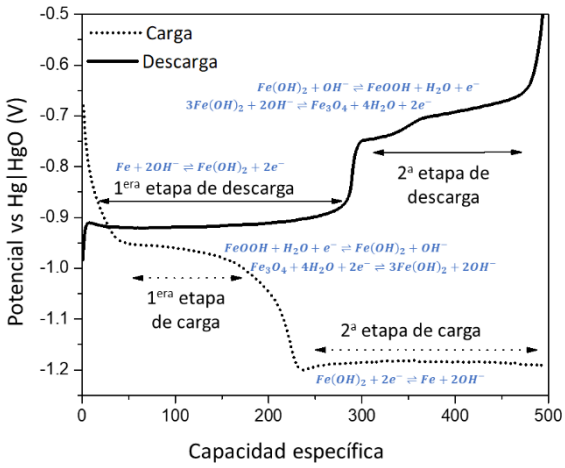

Figura 6. Esquema de las reacciones de carga y descarga de un electrodo alcalino de hierro. Adaptado de [45]

3.1.2. Desafíos del electrodo de hierro

3.1.2.1. Eficiencia coulómbica y Reacción de Evolución de Hidrógeno (HER)

Durante la carga del electrodo ocurre la parasitaria Reacción de Evolución de Hidrógeno (HER) (ecuación 1.4).

$$2H_2O + 2e^- \rightleftharpoons H_2 + 2OH^- \qquad E^0 = -0.83\ V\ vs\ SHE \quad (1.4)$$

La reacción 1.4 está favorecida termodinámicamente sobre la reacción 1.1 durante la carga del electrodo, como se observa en su potencial de equilibrio menos negativo. Esta reacción consume parte de la energía aportada al electrodo, reduciendo la eficiencia faradaica del sistema [46]. Además, las burbujas de hidrógeno producidas pueden generar estrés mecánico y dañar el electrodo. Una forma de evitar la HER es usar materiales de hierro ultrapuros, como el hierro carbonilo, debido a que se ha observado que impurezas de níquel, manganeso, calcio y fósforo promueven la HER [47,48]. El níquel y el manganeso son, de hecho, dos materiales muy estudiados como catalizadores para la HER.

Otra estrategia para evitar la evolución de hidrógeno y maximizar la eficiencia faradaica en la carga y descarga es el uso de aditivos tanto en el electrodo como en el electrolito. Dentro de los aditivos en el electrodo, destacan el sulfuro de bismuto [38,49,50], sulfuro de hierro [51–54] y óxido de bismuto [47]. Como aditivos en el electrolito, se han probado especies como sulfuro de sodio [52,55–58], alcanotioles [59] y estanato [60]. Las especies basadas en bismuto y estanato cumplen el rol de aumentar el sobrepotencial de la HER, reduciendo su velocidad

hasta ser prácticamente indetectable. Otras especies como los alcanotioles bloquean el paso de las moléculas de agua hasta el electrodo, lo que inhibe la reacción (ecuación 1.4). El uso de alcanotioles en el electrolito tiene la desventaja de que puede envenenar los catalizadores del electrodo positivo, disminuyendo su eficacia [61].

El óxido y el sulfuro de bismuto han sido probablemente los aditivos sólidos más estudiados para prevenir la evolución de hidrógeno, debido a que se conocía desde hace años que aumenta el sobrepotencial para esta reacción en electrodos de platino [62]. Manohar *et al.* comprobaron que la electrodeposición de una capa de bismuto permite reducir hasta 10 veces la velocidad de la evolución de hidrógeno, lo que lleva a un electrodo de carbonilo de hierro a alcanzar hasta un 96% de eficiencia faradaica con una capacidad de descarga de 300 mAh g_{fe}^{-1} [63]. Gil posada y Hall [52] probaron el efecto de sulfuro de bismuto contra el de otros aditivos como bismuto metálico, sulfuro de hierro y sulfuro de potasio. Descubrieron que el sulfuro de bismuto tiene una capacidad de reducir la tasa de evolución de hidrógeno superior al resto de los aditivos probados. Además, plantearon que la evolución de hidrógeno está directamente relacionada con la pasivación del electrodo (fenómeno que será discutido en la siguiente sección), lo que también indican otros autores [64].

3.1.2.2. Estabilidad en la operación

Otro de los desafíos que enfrentan los electrodos de hierro tiene que ver con la pérdida de capacidad durante la operación, lo que parece estar relacionado con la conductividad de las especies oxidadas. El hierro es un excelente conductor eléctrico, con una conductividad de 10^7 Ω^{-1} m^{-1}, pero los productos de descarga – salvo la magnetita – poseen una conductividad eléctrica 7 a 8 órdenes de magnitud menor [65]. Esto aumenta la resistencia del electrodo y reduce su reactividad, incrementando los sobrepotenciales (lo que disminuye la eficiencia energética de las baterías) y mermando las capacidades de descarga, en un fenómeno conocido como pasivación.

La mayor parte de los estudios señala al hidróxido de hierro, formado en la primera etapa de descarga, como el responsable de la pasivación del electrodo [50,56,57,66–74]. Sin embargo, no existe un consenso unánime con respecto a este tema. Otros autores han señalado que son los productos de la segunda etapa de descarga, especialmente maghemita (γ-Fe_2O_3), los que son incapaces de reaccionar una vez formados [39,51,52]. Incluso, se ha llegado a postular que la hematita, a pesar de su excelente conductividad eléctrica, forma en soluciones básicas un complejo hidratado estable y muy difícil de reducir [57,75].

Se ha planteado que el uso de sulfuros como aditivo, ya sea en el electrolito o en electrodo, permite evitar la pasivación del electrodo, debido a la formación de FeS, que tiene una mayor conductividad eléctrica que el $Fe(OH)_2$ [43]. Mitra *et al.* probaron distintos sulfuros metálicos como aditivo en el electrodo de hierro: Cu_2S, FeS, FeS_2 y ZnS, llegando a la conclusión de que el sulfuro de zinc es más efectivo en optimizar la eficiencia faradaica. Esto, argumentan, se debería a que su potencial de reducción más negativo impediría la disolución del ion sulfuro, manteniendo esta especie en contacto con el hierro del electrodo [72]. Una hipótesis diferente es la que presentan Wang y Wang [76]. Ellos plantean que la pasivación se debe a la pobre difusividad iónica del ion O_2^{2-} en el Fe_2O_3. Al usar Na_2S como co-electrolito, se forma una estructura *core-shell* en que la superficie del óxido de hierro (III) queda rodeada por una capa de FeS amorfo. Al reducirse el potencial en una siguiente etapa de carga, el sulfuro de hierro amorfo se transforma en pirrita, marcasita (FeS_2) y mackinawita ($FeS_{0.9}$). Estas especies promueven la difusión del ion O_2^{2-}, limitando la pasivación del hierro. En la misma línea, Shangguan *et al.* mostraron que azufre sublimado mezclado mecánicamente con magnetita tienen un efecto similar al uso de FeS como aditivo en el electrodo [77], lo que explican por la difusión del azufre al electrolito y su posterior reducción a sulfuro, para dar origen a FeS.

Otro aspecto a considerar es la diferencia de densidad entre el hierro y sus productos de descarga. El $Fe(OH)_2$ tiene un volumen molar 272 % mayor que el hierro, por lo que, al expandirse, el hidróxido de hierro puede provocar estrés mecánico sobre el electrodo y bloquear poros del mismo, evitando que el electrolito llegue a más átomos de hierro. Usando este dato de expansión molar, Bryant *et. al.* [78] y Yang *et. al.* [56] calcularon que un electrodo de hierro debe tener una porosidad, como mínimo, de un 73 % para poder lograr una reacción completa del material del electrodo.

3.1.3. Formulaciones para el electrodo de hierro

Varios compuestos de hierro han sido utilizados como material electroactivo para electrodos alcalinos de hierro. Uno de los más importantes es el hierro carbonilo. Este material es una forma de hierro metálico de alta pureza (<99.5%) y se obtiene mediante la descomposición de pentacarbonilo de hierro. Si bien el hierro carbonilo es un material con una alta pureza y de relativamente bajo coste, su obtención tiene la desventaja de que el pentacarbonilo de hierro tiene una elevada toxicidad, no recomendándose la exposición prolongada a una concentración en el aire de más de 0,1 ppm [79]. Además, los electrodos basados en hierro carbonilo necesitan, generalmente, periodos de formación que pueden sobrepasar los 100 ciclos, lo que tiene como efecto una mayor energía necesaria para la

producción de la batería y mayor coste [44,49]. Algunos electrodos de hierro carbonilo han reportado capacidades cercanas a los 300 mAh g_{Fe}^{-1} a velocidades de ciclado de C/5 [44,47,57]. Usando la técnica de sinterización, Yang, Manohar y Narayanan lograron mantener la eficiencia coulómbica aun aumentando la velocidad de carga y descarga hasta 1C, aunque con una capacidad de que no alcanzó los 200 mAhg $_{Fe}^{-1}$ [56].

Otros materiales de hierro probados como electrodos son óxido de hierro (III), magnetita o FeS. Figueredo-Rodríguez *et al.* estudiaron 5 compuestos de hierro como material electroactivo: los tres recién mencionados, hierro carbonilo y goetita [48]. Sin el uso de aditivos, el electrodo de hierro carbonilo destacó por su elevada capacidad de descarga, sobrepasando los 600 mAh g_{Fe}^{-1}. Los electrodos de hierro carbonilo, sulfuro de hierro y magnetita mostraron una estabilidad superior al resto, sin perder prácticamente capacidad de descarga en 50, 40 y 23 ciclos, respectivamente, a corrientes de carga y descarga de C/5. Sin embargo, se pudo apreciar que los dos primeros se encuentran después de dicha cantidad de ciclos aún en su periodo de formación. El electrodo de Fe_2O_3 comercial mostró un pobre rendimiento, perdiendo prácticamente toda su capacidad de descarga a los 15 ciclos. Por otro lado, el electrodo de goetita mostró una operación relativamente estable y una capacidad de alrededor de 300 mAh g_{Fe}^{-1}.

Los electrodos basados en óxidos u oxohidróxidos de hierro generalmente usan materiales carbonosos como aditivo conductor para superar las bajas conductividades de los óxidos, como los negros de carbono o nanoestructuras de carbono (nanotubos [80], nanofibras [81], óxido de grafeno reducido [82], entre otros.). El área superficial del carbono que se use como aditivo, así como su conductividad, juegan un papel fundamental en el desempeño de los electrodos, afectando a parámetros como la estabilidad, la capacidad de descarga y la eficiencia coulómbica [50,68,83]. En esta tesis, se propone, para el electrodo negativo, la síntesis mediante métodos simples y económicos de óxidos de hierro dopados químicamente con azufre. Estos óxidos de hierro se mezclarán con un negro de carbono comercial para obtener los electrodos mediante prensado en caliente. Los métodos de síntesis propuestos permiten modificar las propiedades físico-químicas de los óxidos de hierro, lo que permitirá establecer modelos que relacionen dichas propiedades con el rendimiento de los electrodos.

Como se ha explicado, son variadas las combinaciones de compuestos de hierro, aditivos conductores u otros aditivos con que se han construido electrodos de hierro, con distintas características y resultados. Para sintetizar la información encontrada en literatura, se ha elaborado la **Tabla 1**.

Tabla 1. Características y rendimiento de algunos electrodos de hierro en medio alcalino reportados en literatura

Grupo de investigación	Material electroactivo	Aditivos en el electrodo	Electrolito	Aditivos en el electrolito	Intensidad de corriente		Capacidad de descarga (mAh g_{Fe}^{-1})			Nro. de ciclos		Eficiencia coulómbica (%)	Ref.
					Carga	Descarga	Inicial	Máxima	Final	Formación	Totales		
Narayanan – USC	Hierro carbonilo y sulfuro de hierro prensado en caliente	10 % p/p Bi_2O_3 + K_2CO_3	KOH 30 % m/v	-	Hasta 3 C	Hasta 3 C		~200	~200	30-40	50-60	~90	[47]
	70 % Fe carbonilo, 10 % polietileno, prensado en caliente	5 % Bi_2O_3 5% K_2CO_3	KOH 30 % p/p	-	C/2	C/20	230	230	230	-	1200	92	[57]
	Fe carbonilo sinterizado a 850 ºC sobre malla Ni	$(NH_4)_2CO_3$	KOH 30 % m/v	Na_2S 6.4 x 10^{-2} M	1 C	1 C	~100	200	200	30	3000	96	[56]
	70 % Fe carbonilo, 5% polietileno	10 % Bi_2O_3 5 % ZnS 10 % K_2CO_3	KOH 30 % p/p	-	C/2	C/2	100	240	240	50	750	95	[72]
Weinrich – Forschungszentrum Jülich	Hierro carbonilo prensado en caliente	8.5 % p/p Bi_2S_3	KOH 6 M	-	C/6	C/60	0	225	225		329	80	[38]
	85 % hierro carbonilo, 6.5 % polietileno, prensado en caliente	8.5 % Bi_2S_3	KOH 6 M	-	C/6	C/60	0	200	200	400	450	96.7	[70]
	83 % polvo de hierro < 10 µm,	-	KOH 5.1 M	K_SS 0.4 M + LiOH 0.15 M	C/5	C/5	0	230	230		50	35	[46]

	11 % FeS, 6 % PTFE												
	85 % Fe carbonilo, 5% polietileno, prensado en caliente	5 % Bi_2S_3 5% K_2CO_3	KOH 28.5 % p/p	-	C/5	C/5	~100	240	240	25	35	30	[52]
Gil Posada – Universidad de Sheffield	80 % Fe carbonilo, 5% polietileno, prensado en caliente	5 % Bi_2S_3 5 % K_2S 5% K_2CO_3	KOH 28.5 % p/p	-	C/5	C/5	~100	200	200	25	35	25	[52]
	100 % FeS sobre espuma de níquel (impregnada en húmedo)	-	KOH 5.1 M	LiOH 0.3 M K_2S 0.44 M	C/5	C/5	~100	250	250	30	50	95	[54]
	75 % FeS, 10 % negro de carbono, prensado en caliente	5 % Bi_2S_3 K_2CO_3	KOH 6 M	-	C/5	C/5	30	300	300	35	50	-	[48]
Ponce de León – Universidad de Southampton	68 % hierro carbonilo, 14 % negro de carbono, prensado en caliente	7 % Bi_2S_3 K_2CO_3	KOH 6 M	-	C/5	C/5	150	650	600	28	40	-	[48]
	74 % Fe_3O_4 molida en molino de bolas, 12 % negro de carbono,	8 % Bi_2S_3 K_2CO_3	KOH 6 M	-	C/5	C/5	525	700	600	13	23	-	[48]

	prensado en caliente												
	Composite 50 % Fe, 46 % C, método de Adams	4 % Bi_2S_3	KOH 6 M	1-octanotiol 0.1 M	C/2	C/2	800	900	500	3	28	75	[59]
Hang – Agencia de Ciencia y Tecnología de Japón	Nanotubos de carbono rellenos de Fe_2O_3 (Fe/C =1/17 p/p)	-	KOH 8 M	-	0.5 mA cm^{-2}	0.2 mA cm^{-2}	350	350	150	0	30	-	[80]
	Nanopartículas de Fe_2O_3 soportadas en Acetylene Black (Fe/C = 1/8)	2 % Bi_2S_3	KOH 8 M	K_2S 0.1 M	0.5 mA cm^{-2}	0.2 mA cm^{-2}	100	400	300	20	50	-	[71]
Otros	75 % Fe_2O_3, 20 % nanotubos de carbono	5 % Bi_2S_3	KOH 6 M	-	10 mA cm^{-2}	10 mA cm^{-2}	-	350	-	-	-	82	[50]
	75 % Fe_2O_3, 20 % óxido de grafeno reducido	5 % Bi_2S_3	KOH 6 M	-	10 mA cm^{-2}	10 mA cm^{-2}	-	300	-	-	-	73	[50]
	Nanoreactores de FeS_2@carbono procedente de dopamina	-	KOH 3 M	-	0.65 C	0.65 C	250	273	220	-	1000	-	[51]
	80 % polvo Fe, 8 % grafito, 2 % negro de carbono, 5 % PTFE	5 % Bi_2S_3	KOH 6 M	LiOH 1 M + K_2SnO_3 0.1 M	C/5	C/5	150	475	400	30 (CV)	150	85	[60]

	80 % polvo de Fe dopado con Cu y Sn, 5 % Ketjenblack, 10 % PTFE	5 % Bi_2S_3	KOH 6 M	-	C/5	C/10	430	480	300	~10	400	93 (inicial)	[66]
	45 % nanpartículas de Fe_2O_3, 45 % Acetylene Black, 10 % PTFE	-	KOH 8 M	K_2S 0.01 M	CV	CV	450	575	350	3	27	-	[67]
	Composite: Fe de descomposición de oxalato sobre alcohol polivinílico calcinado (10 %)	1 % Bi_2S_3	KOH 6 M	LiOH 1% m/v	C/5	C/5	150	400	350	50	100	80	[69]
	Composite Fe_3O_4/C–Bi KS6 10% p/p	-	KOH 6M	LiOH 15 g/L + Na_2S 0.1%	C/4	C/4	550	700	600	20	100	94.5	[84]
	80 % hierro carbonilo, 20 % PureBLACK, prensado en húmedo	3 % p/p Bi_2S_3	KOH 8 M	LiOH 1 M	CV	CV	10	400	50		150	85 (máx.)	[39]
	Nanofilamentos de Fe_2O_3 crecidos sobre material híbrido de grafeno/CNT	-			~0.8 C	~0.8 C	275	275	250		1000	-	[40]

3.2. Electrodo de oxígeno

3.2.1. Las reacciones de reducción y evolución de oxígeno

Los electrodos positivos de baterías hierro-aire deben ser capaces de llevar a cabo el par reacción de evolución de oxígeno-reacción de reducción de oxígeno (OER-ORR). Estas reacciones se pueden apreciar en la ecuación 1.5, ORR en sentido de izquierda a derecha y OER en sentido opuesto:

$$O_2 + 2H_2O + 4e^- \rightleftharpoons 4OH^- \qquad E^0 = 0.401\ V\ vs\ SHE \quad (1.5)$$

Esta reacción involucra la transferencia de 4 electrones, lo que conlleva una cinética lenta. Además, tiene la desventaja de que los catalizadores que tienen una elevada actividad para la evolución de oxígeno no suelen ser activos para la ORR, y viceversa [85]. A esto se suman otras complicaciones, como el hecho de que los elevados potenciales a los que se debe llevar a cabo la OER (> 1,5 V *vs.* RHE) pueden corroer el electrodo [86,87].

La ORR es especialmente lenta debido a la elevada entalpía del enlace O=O, como se ve en la ecuación 1.6 [88]:

$$O = O_{(g)} \rightarrow 2O_{(g)} \qquad \Delta H^0 = 498\ kJ\ mol^{-1} \quad (1.6)$$

La reducción de oxígeno puede proceder mediante dos vías. La primera es la de 4 electrones, que involucra la reducción a ion hidróxido (o agua en medio ácido), tal como se muestra en la ecuación 1.21. Sin embargo, la reacción también puede proceder por una vía de 2 electrones, que implica la reducción a ion hidroperóxido (o peróxido de hidrógeno en medio ácido), como se ve en la ecuación 1.7:

$$O_2 + H_2O + 2e^- \rightleftharpoons HO_2^- + OH^- \qquad E^0 = -0.065\ V\ vs\ SHE \quad (1.7)$$

La reacción 1.23 tiene las desventajas de proveer la mitad de corriente y también un menor potencial, lo que se traduce en un menor voltaje de la batería. El ion hidroperóxido puede luego reducirse a hidróxido, completando lo que se conoce como mecanismo “2+2” electrones (ecuación 1.8), o descomponerse no electroquímicamente en agua y oxígeno (ecuación 1.9):

$$HO_2^- + H_2O + 2e^- \rightleftharpoons 3OH^- \qquad E^0 = 0.87\ V\ vs\ SHE \quad (1.8)$$

$$2HO_2^- \rightarrow H_2O + O_2 \quad (1.9)$$

El mecanismo generalmente aceptado para la reducción de oxígeno por la vía de 4 electrones sobre metales de transición se muestra en las ecuaciones 1.10 – 1.13 [89,90]. En óxidos metálicos sumergidos en medio básico fuerte, la superficie tiende a estar cubierta por grupos OH adsorbidos [91,92]. Debido a esto, el primer paso involucra la adsorción de una

molécula de oxígeno, desplazando el grupo hidroxilo, y la simultánea o posterior transferencia de un electrón, dependiendo de si es un mecanismo de transferencia interna o externa (ecuación 1.10). En seguida, el O_2 adsorbido es protonado por una molécula de agua y la transferencia de un electrón (ecuación 1.11), obteniéndose un grupo carboxilo adsorbido, del cual posteriormente se libera un ion hidróxido con la transferencia de otro electrón (ecuación 1.12). Finalmente, el átomo de oxígeno adsorbido restante es protonado por otra molécula de agua y electrón (ecuación 1.13), obteniéndose un grupo hidroxilo adsorbido y volviendo al inicio de la ecuación 1.10.

$$M(OH)_{ads} + O_{2(aq)} + e^- \rightarrow M(O_2)_{ads} + OH^- \quad (1.10)$$

$$M(O_2)_{ads} + H_2O + e^- \rightarrow M(OOH)_{ads} + OH^- \quad (1.11)$$

$$M(OOH)_{ads} + e^- \rightarrow M(O)_{ads} + OH^- \quad (1.12)$$

$$M(O)_{ads} + H_2O + e^- \rightarrow M(OH)_{ads} + OH^- \quad (1.13)$$

Donde M es un sitio de adsorción sobre la superficie metálica. En la vía de dos electrones, las dos primeras etapas son las mismas que en la de 4 electrones (ecuaciones 1.10 – 1.11). Sin embargo, la energía del sistema no es suficiente para romper el enlace O=O y el grupo peroxil adsorbido se desorbe como ion hidroperóxido y es reemplazado por un radical hidroxilo adsorbido (ecuación 1.14), cerrando el ciclo catalítico.

$$M(OOH)_{ads} + OH^- \rightleftharpoons M(OH)_{ads} + HO_2^- \quad (1.14)$$

En el mecanismo “2+2”, el ion hidroperóxido formado en la ecuación 1.14 puede reaccionar con un grupo hidroxilo adsorbido (recordar que la superficie metálica está cubierta principalmente por grupos hidroxilo) y la transferencia de un electrón para dar un átomo de oxígeno adsorbido (ecuación 1.15). Este átomo se reduce luego a hidróxido siguiendo la ecuación 1.13, completando el ciclo catalítico.

$$M(OH)_{ads} + HO_2^- + e^- \rightleftharpoons M(O)_{ads} + 2OH^- \quad (1.15)$$

En un mecanismo 2+2, la cantidad efectiva de electrones transferidos dependerá de la relación entre las velocidades de las reacciones 1.15 y 1.14. Mientras más rápida sea la readsorción del ion hidroperóxido en relación a su descomposición, el número de electrones se acercará más al valor ideal de 4. Una velocidad de descomposición mayor, hará que el número de electrones transferidos medido se acerque a 2.

El mecanismo que siga la ORR está fuertemente afectado por la adsorción de la especie reactiva sobre la superficie del catalizador. Ésta se ve a su vez determinada tanto por la energía de enlace entre los átomos del catalizador y del reactante como por la geometría de la superficie.

Debido a esto, la ORR es una reacción que depende directamente de la estructura, morfología y porosidad del catalizador, ya que todas esas propiedades afectan la configuración de la adsorción de la molécula de oxígeno [88,93–95]. La alta sensibilidad de la reacción a la estructura del catalizador permite que ocurran diferentes mecanismos incluso con catalizadores del mismo tipo pero con estructuras cristalinas diferentes, debido a diferencias en las configuraciones de la adsorción de O_2 y de las interacciones superficie-O_2 [96]. La adsorción de O_2 puede darse en configuración "bridge" o lineal [96–98]. En la primera de éstas, dos átomos de oxígeno se coordinan con la superficie del catalizador, lo que tiene como efecto que la reacción proceda por la vía directa de 4 electrones, como en el caso de los catalizadores de Pt [99]. En la segunda, un solo átomo de oxígeno se enlaza perpendicularmente a la superficie del catalizador, resultando en un mecanismo de 2 electrones.

El catalizador por excelencia para la reducción de oxígeno es el platino en forma de nanopartículas, generalmente soportado sobre negros de carbono. Debido a su elevada superficie específica y energía de enlace óptima, presenta la actividad más elevada de los metales para la ORR. Sin embargo, no está exento de desventajas, como su elevado costo y escasez, y tendencia a envenenarse [100]. Como se mencionó anteriormente, la actividad de un catalizador para la ORR está muy relacionada con la energía de adsorción del oxígeno. Esta relación da origen a lo que se conoce como "gráfica de volcán" (**Figura 7**), donde se puede apreciar que la actividad de los metales como catalizadores aumenta con la energía de adsorción del oxígeno hasta alcanzar un óptimo, para luego disminuir.

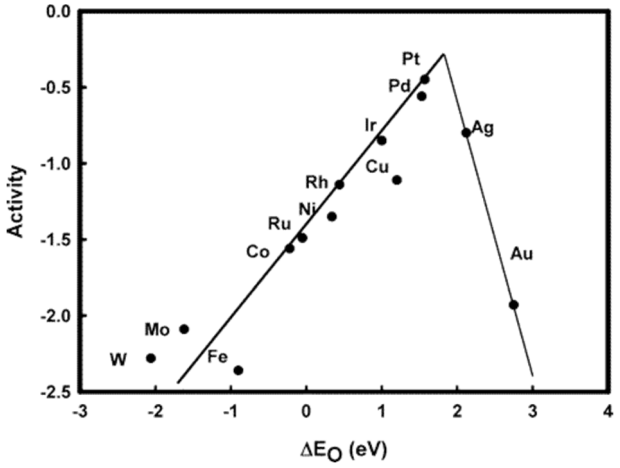

Figura 7. Relación entre la actividad para la ORR de distintos metales y la energía de adsorción de oxígeno sobre ellos [101].

La OER, por su parte, presenta la transferencia de 4 electrones que parte de un grupo hidroxilo adsorbido, como se ven en las ecuaciones 1.16-1.19 [102]:

$$M(OH)_{ads} + OH^- \rightarrow M(O)_{ads} + H_2O + e^- \quad (1.16)$$

$$M(O)_{ads} + OH^- \rightarrow M(OOH)_{ads} + e^- \quad (1.17)$$

$$M(OOH)_{ads} + OH^- \rightarrow M(O_2)_{ads} + H_2O + e^- \quad (1.18)$$

$$M(O_2)_{ads} + OH^- \rightarrow M(OH)_{ads} + O_{2(aq)} + e^- \quad (1.19)$$

Para la OER, los catalizadores que presentan una actividad más elevada son óxidos metálicos del grupo del platino. Por ejemplo, el dióxido de rutenio en fase rutilo muestra una excelente actividad catalítica tanto en medio ácido como básico [103–105]. Sin embargo, el RuO_2 es altamente inestable en ambos electrolitos a potenciales de oxidación elevados, pudiendo oxidarse a RuO_4 y disolverse en el electrolito [106]. Otro catalizador de referencia, del mismo grupo de la Tabla Periódica, es el dióxido de iridio. Si bien el IrO_2 presenta una elevada actividad y mayor estabilidad que el RuO_2, comparte con este material que ambos son escasos y caros: cada año se producen aproximadamente 35 toneladas de rutenio y 3 de iridio en todo el mundo.

Algunos parámetros importantes que describen el rendimiento de electrodos bifuncionales de oxígeno son: el potencial de semi-onda, ($E_{1/2}$), la corriente límite (j_d), el potencial de *onset* para la ORR ($E_{onset,ORR}$), los tres explicados en el Anexo I; el potencial al que la OER alcanza una densidad de corriente de 10 mA cm^{-2} (E_{10}) y el diferencial de reversibilidad (ΔE), calculado como la diferencia entre E_{10} y $E_{1/2}$ y que indica qué tan bifuncional es un catalizador (a menor ΔE, mayor actividad reversible o bifuncional tiene el electrodo). A partir de $E_{1/2}$ y E_{10} también se pueden obtener los sobrepotenciales de semi-onda y de 10 mA cm^{-2} ($\eta_{1/2}$ y η_{10}, respectivamente), pudiendo expresarse también el diferencial de reversibilidad como la suma de las magnitudes de ambos sobrepotenciales. Las pendientes de Tafel y densidad de corriente de intercambio también son parámetros importantes.

3.2.2. Catalizadores bifuncionales para ORR-OER en medio básico

Como se ha mencionado anteriormente, los catalizadores de referencia para la ORR y la OER son Pt/C y RuO_2 o IrO_2, respectivamente. Sin embargo, dichos catalizadores no son bifuncionales. En la última década, se han sintetizado diversos materiales que presentan elevadas actividades para ambas reacciones, conocidos como catalizadores reversibles o bifuncionales. El metal noble que presenta una mayor reversibilidad para ambas reacciones es el paladio. Este metal ha llegado a mostrar actividades superiores que los catalizadores de referencia [107,108], sin embargo, su baja abundancia y elevado precio hacen de su uso poco recomendable.

Una opción para aprovechar las propiedades catalíticas de los metales nobles es combinarlos con metales de transición o heteroátomos para incrementar su reversibilidad. Se

ha reportado que nanopartículas de Fe_3Pt, como catalizador de ORR, soportadas en nitruro de níquel-hierro (Ni_3FeN) poroso, como catalizador de OER, son un excelente catalizador bifuncional [109]. Su actividad superó a las de los catalizadores de referencia para y ORR OER. La voltametría lineal de ORR mostró que el potencial de *onset* de los catalizadores siguió la tendencia: Fe_3Pt/Ni_3FeN > Fe_3Pt/C > Pt/C > Ni_3FeN. En la región mixta de control cinética-difusivo, el potencial de semi-onda ($E_{1/2}$) de Fe_3Pt/Ni_3FeN exhibió el valor más positivo de los catalizadores estudiados (0,93 V), indicando una superior actividad para la ORR de Fe_3Pt/Ni_3FeN que los otros catalizadores. Fe_3Pt/Ni_3FeN también demostró una mejor actividad hacia la OER, con un potencial de *onset* más bajo y una mayor densidad de corriente que Ni_3FeN, Pt/C e IrO_2, obteniendo un ΔE de 0,65 V. Las pruebas de degradación acelerada demostraron una alta estabilidad de Fe_3Pt/Ni_3FeN, que tuvo una pérdida de masa de aproximadamente el 6.3% después de 5000 ciclos de ORR y del 5.2% después de 1000 ciclos de OER; para Pt/C e IrO_2, los valores fueron del 20,4 y 22,1%, respectivamente. Otra estrategia reportada fue soportar los átomos de Pt y Fe directamente en carbono dopado con nitrógeno (PtFeNC) para generar un nuevo catalizador para ORR [110]. Se observaron potenciales de *onset* y de semi-onda altos, de 1,05 y 0,895 V *vs.* RHE, respectivamente. Cálculos DFT mostraron que la ruptura del enlace de O_2 en los átomos individuales de Pt y Fe en el catalizador PtFeNC era el origen de su buen rendimiento para la ORR.

Para desarrollar catalizadores bifuncionales en base a rutenio, You y Hu prepararon soluciones sólidas de óxidos de rutenio y estaño mediante método hidrotermal, las que demostraron una excelente actividad tanto para la OER como para la ORR [111]. Entre los óxidos mixtos con proporciones variables de rutenio estaño, aquellos con 30 % y 70 % de Sn fueron más activos para ambas reacciones. El número de electrones transferidos en la ORR fue de 3,8 en ambos materiales, similar a los catalizadores de referencia. Los valores de E_{onset} y $E_{1/2}$ de los óxidos 70Ru–30Sn y 30Ru–70Sn fueron comparables a los de los catalizadores Pt/C y RuO_2. La adición de un 30% de SnO_2 al RuO_2 mejoró también su actividad para OER. Un sobrepotencial de 0,24 V fue suficiente para alcanzar una densidad de corriente de 10 mA cm^{-2} en la OER. El ΔE para estos catalizadores fue de 0,75 V.

Uno de los metales más investigados como catalizadores bifuncionales de oxígeno en medio básico son los óxidos de cobalto. Estructuras como las perovskitas o las espinelas han mostrado elevadas actividades para ambas reacciones [112–116]. Kim *et al*. sintetizaron un catalizador mixto perovskita/aleación de cobalto-hierro, de fórmula $Sr_{0.95}Nb_{0.1}Co_{0.7}Fe_{0.2}O_{3-\delta}/Co_3Fe$, que presentó un η_{10} de 246 mV *vs*. RHE y un $E_{1/2}$ de 0,690 V *vs.* RHE, para un ΔE de sólo 785 mV [117]. Este catalizador también presentó otras propiedades destacables, como una

pendiente de Tafel de sólo 45 mV dec^{-1} y una capacidad de operar por 500 horas. Otros catalizadores basados en espinelas de cobalto han mostrado valores de ΔE tan bajos como 0,73 V y pendientes de Tafel para OER con valores mínimos de 31 mV dec^{-1} [118]. Además de las perovskitas y espinelas, el Co_3O_4 también ha sido investigado como un potencial catalizador bifuncional [119–123]. Wang et al. reportaron las propiedades catalíticas de nanopartículas de óxido de cobalto dopado con nitrógeno ultrafinas (NP-Co_3O_4) con diámetros de 4-5 nm sobre tela de carbono (CC), obtenidas a partir de calcinación de estructuras de cobalto-zeolita-imidazolato (Co-ZIF) [124]. La calcinación de estas partículas a baja temperatura permitió que los nodos de Co de Co-ZIF se oxidaran en nanopartículas de Co_3O_4 ultrafinas y se comprobó, mediante análisis de XPS, la existencia de enlaces Co-N. Plantearon que el dopado con nitrógeno podría generar vacantes de oxígeno en la superficie de NP-Co_3O_4, mejorando su conductividad electrónica y propiedades catalíticas. La densidad de corriente en la ORR y OER del catalizador NP-Co_3O_4/CC fue superior en comparación con la obtenida por los catalizadores Pt/C e Ir/C. Este catalizador logró una elevada actividad y reversibilidad, con un ΔE de 0,66 V. Además, demostró una estabilidad notable, siendo capaz de operar por 400 horas en ciclos de OER y ORR a densidades de corriente de ±5 mA cm^{-2}.

La elevada actividad de los óxidos de cobalto para ambas reacciones también ha llevado a desarrollar catalizadores que combinen estos materiales con metales del grupo del platino para maximizar la actividad y la reversibilidad. Wang *et al.* desarrollaron un catalizador mixto que consiste en $Co(OH)_2$/CoPt/N–CN con una relación de peso de aproximadamente 45:45:0.77:9.23 de $Co(OH)_2$:N–CN:Co:Pt que mostró elevada actividad tanto para la ORR como para la OER [125]. Los resultados de SEM y TEM mostraron que las nanopartículas de CoPt y las láminas de $Co(OH)_2$ se adhirieron a la superficie de N–CN (láminas de carbono grafítico dopado con nitrógeno). Este catalizador mostró un E_{onset} para la ORR de 0.97 V y un $E_{1/2}$ de aproximadamente 0,83 V. El número de electrones transferidos fue de 3,81–3,95 en el rango de voltaje de 0,8–0,2 V, comparable con el catalizador Pt/C. En la OER, se necesitó un sobrepotencial de 0,32 V para obtener una densidad de corriente de 10 mA cm^{-2}. De esta forma, este catalizador logró un diferencial de reversibilidad de 0,72 V.

Uno de los principales desafíos que enfrentan los óxidos de metales de transición y sus estructuras derivadas es su baja conductividad [126]. La forma más común de enfrentar este problema es mezclar los óxidos metálicos con materiales de carbono. Se han estudiado negros de carbono comerciales, tales como Ketjenblack [127] o Vulcan [128], los cuales han mostrado mejorar las actividades catalíticas de los óxidos metálicos. A pesar de sus ventas, como bajo coste y alta área superficial, los negros de carbono presentan la desventaja de que pueden

oxidarse a dióxido de carbono durante la OER [112]. Debido a esto, son preferibles los carbonos grafíticos nanoestructurados, entre los que se encuentran el grafeno (u óxido de grafeno reducido), nanotubos de carbono, nanofibras, xerogeles, entre otros [129].

En el grupo de Conversión de Combustibles se han desarrollado electrocatalizadores basados en óxidos metálicos con altas actividades y reversibilidades para el par OER-ORR. Luque-Centeno *et al.* sintetizó composites de titanio y cobalto sobre óxido de grafeno reducido dopado con nitrógeno (Ti-NrGO y Co-NrGO, respectivamente) [130]. Sólo el catalizador Co-NrGO demostró una actividad para ORR comparable al catalizador Pt/C de referencia, con un E_{onset} sólo 50 mV más negativo y un $E_{1/2}$ 40 mV más negativo. Sin embargo, ambos catalizadores obtuvieron resultados de estabilidad muy superiores al catalizador de referencia, con desplazamientos de potencial de semi-onda inferiores a 15 mV después de 6.500 voltametrías lineales de ORR, mientras que, en el catalizador Pt/C, este parámetro se desplazó 120 mV. Para la OER, ambos catalizadores fueron superados por el catalizador de referencia IrO_2, que mostró un E_{10} 40 mV más negativo que el catalizador Co-NrGO, mientras que el catalizador Ti-NrGO no alcanzó los 10 mA cm^{-2} en el rango de potencial estudiado. En otro estudio, Luque-Centeno *et al.* sintetizó materiales basados en óxidos mixtos de cobalto y titanio que demostraron pendientes de Tafel para ORR de sólo 40 mV dec^{-1} y para OER de sólo 69 mV dec^{-1} [131]. También dentro del grupo, Ruiz-Cornejo *et al.* sintetizaron óxidos de tantalio soportados sobre nanofibras de carbono dopadas con azufre [132]. Encontraron que el dopado de las nanofibras con azufre mejora las interacciones entre las fases metálica y carbonosa, lo que aumenta la actividad catalítica para la ORR, pero la disminuye para la OER. De esta forma, lograron un catalizador TaO_x/CNF-S250 con el que se obtuvo un $E_{1/2}$ de 0,75 V *vs.* RHE y una pendiente de Tafel de 70 mV dec^{-1}. Por otro lado, el catalizador con soporte de nanofibras sin dopar obtuvo la mejor actividad para la OER, con un E_{10} de 1,63 V y una pendiente de Tafel de 72 mV dec^{-1}. Este material tuvo un interesante ΔE de 713 mV (corregido por IR).

Si bien los catalizadores basados en cobalto muestran actividades interesantes para las aplicaciones tecnológicas de la ORR y OER a un coste no excesivamente elevado, el uso del cobalto como componente fundamental de las baterías de ion-litio y los problemas éticos asociados a las condiciones de extracción, han significado que este metal sea catalogado como crítico, lo que ha motivado la búsqueda de catalizadores basados en otros metales de transición [15].

3.2.3. Catalizadores bifuncionales de oxígeno basados en óxido de manganeso y materiales carbonosos

Se han reportado en la literatura rendimientos interesantes tanto para la ORR como para la OER de materiales basados en manganeso [133]. Una ventaja de estos materiales es que existen en diferentes estados de oxidación (MnO, Mn_3O_4, Mn_2O_3, MnO_2, MnOOH) y en diferentes nanoestructuras, como cúbica [134], laminar [135] o espinelas [136], entre otros. Esto permite sintetizar materiales con características físico-químicas y propiedades electroquímicas ajustables.

Dentro de los óxidos de manganeso, el MnO_2 ha provocado interés en los últimos años debido a su reportada actividad para ambas reacciones. Este compuesto puede presentar una diversidad de fases cristalinas, morfologías, propiedades texturales, estructuras electrónicas y defectos, lo que dificulta comprender de forma precisa el origen de su actividad catalítica [89]. De estas propiedades, la fase cristalina parece tener un efecto especialmente importante. El MnO_2 puede adquirir distintas estructuras cristalinas, entre las que se encuentran: de túnel (α-MnO_2, β-MnO_2 y γ-MnO_2), laminar (δ-MnO_2) o red tridimensional (λ-MnO_2). Algunos estudios han reportado que la actividad catalítica de las distintas fases para la ORR sigue la tendencia: α-MnO_2 > δ-MnO_2 > γ-MnO_2 > λ-MnO_2 > β-MnO_2 [137], mientras que otros señalan que la tendencia es α-MnO_2 > β-MnO_2 > γ-MnO_2 [138]. A pesar de las discrepancias, los autores parecen estar de acuerdo que la fase α-MnO_2 es la más activa al menos para la ORR.

La estructura cristalina α-MnO_2 da también origen a distintas morfologías, como nanoesferas, nanoflores y nanofilamentos. Las nanoflores son una nueva clase de nanopartículas que muestra estructuras similares a las de una flor. Las nanoflores han llamado bastante la atención en los últimos años debido a su alta estabilidad y su alta relación área superficial/volumen [139]. Nanoflores obtenidas mediante método hidrotermal presentaron áreas BET de 40,1 $m^2\ g^{-1}$ [138] y de 65,7 $m^2\ g^{-1}$ [140]. En cuanto al rendimiento electrocatalítico para la ORR, las nanoflores sintetizadas por Cheng *et al*. [138] tienen un potencial de *onset* alrededor de 0,82 V *vs.* RHE y un $E_{1/2}$ de aproximadamente 072 V *vs.* RHE. Este catalizador demostró 3,7 electrones transferidos en la ORR (cerca del valor teórico de 4), lo que indica que la morfología de α-MnO_2 en forma de nanoflores promueve que la ORR ocurra a través de la vía directa de cuatro electrones. Para la OER, el catalizador de nanoflores con puntos cuánticos de carbono de Tian *et al.* [140] alcanzó un E_{10} de 1,55 V *vs.* RHE y una pendiente de Tafel de sólo 43,6 mV dec^{-1}.

Los nanofilamentos son la estructura más estudiada y presentan una conveniente bifuncionalidad y durabilidad debido a su estructura que favorece huecos dentro de ella, con octaedros de MnO_6 ligados a los bordes y esquinas [141,142]. Los nanofilamentos son nanoestructuras con una relación longitud-anchura superior a 1.000. Al igual que las nanoflores, los nanofilamentos también se pueden preparar mediante métodos hidrotermales [143–146]. El área superficial de los nanofilamentos suele ser ligeramente menor que la de las nanoflores, encontrándose alrededor de 25 $m^2\ g^{-1}$ [146], y un volumen de poros de 0,094 $cm^3\ g^{-1}$, menor que el de las nanoflores de α-MnO_2.

Meng *et al.* sintetizaron nanofilamentos de α-MnO_2 a partir de métodos hidrotermales (α-MnO_2-HT) y de estado sólido (α-MnO_2-SF) y los probaron como catalizadores bifuncionales de oxígeno [147]. Los valores de ΔE para estos materiales estuvieron alrededor de 0,85 V. El catalizador α-MnO_2-HT fue capaz de operar a una corriente de OER de 10 mA cm^{-2} por 6 horas antes de mostrar signos de desactivación, mientras que α-MnO_2-SF se desactivó luego de 3 horas.

Se ha propuesto el dopado de óxidos de manganeso con heteroátomos (principalmente Fe, Co o Ni) para aumentar su actividad y reversibilidad. Otra estrategia ha sido inducir térmicamente defectos en la superficie del MnO_2, lo que aumenta su actividad catalítica para la ORR [148]. Mathur y Halder desarrollaron un método para obtener, en un paso, nanofilamentos de MnO_2 dopados con hierro [149], obteniendo catalizadores bifuncionales con un potencial de *onset* para la ORR de 0,89 V *vs.* RHE en KOH 0.1 M, y un η_{10} de 660 mV, dando como resultado un ΔE de 1,17 V.

Independiente de cuál sea la estructura cristalina del catalizador, sufre las mismas dificultades asociadas a baja conductividad que el resto de los óxidos metálicos, por lo que se suelen usar carbones como aditivo conductor. De los catalizadores mencionados en esta sección, todos excepto los de Mathur y Halder [149] usan algún tipo de material de carbono como aditivo conductor. También se han sintetizado composites entre materiales de manganeso y estructuras de carbono. He *et al.* desarrollaron un composite de óxidos de manganeso y nanotubos de carbono (MnO_x/CNT) y encontraron que el composite MnO_2/CNT demostró una actividad y reversibilidad mayores que MnO_2 y que CNT por separado cuando la razón másica CNT:MnO_2 fue de 60:40 [150]. La reducción del composite MnO_2/CNT a 400 °C en presencia de azufre dio origen a un óxido de manganeso con iones Mn^{3+} que generaron vacancias de oxígeno (MnO_x/CNT). Los catalizadores MnO_2/CNT y MnO_x/CNT tuvieron ΔE de 0,92 V y 0,91 V, respectivamente. Con el catalizador MnO_x, además, se obtuvo una pendiente de Tafel en ORR

de 85,7 mV dec^{-1}, muy cercana a la obtenida con el catalizador de referencia Pt/C, 83,0 mV dec^{-1}.

Otro aspecto a considerar es que los materiales carbonosos también presentan actividad catalítica hacia la ORR y la OER. La ORR sobre el carbono se lleva a cabo a través de interacciones del O_2 con los grupos funcionales en la superficie [151]. Se ha observado la reducción de O_2 a H_2O_2 en el carbono vítreo y el grafito [152]. Se cree que los grupos de quinona en la superficie del carbono y el grafito participan en la reducción de O_2 a peróxido [153]. La modificación del carbono puede dar origen a sitios activos para la reacción electrocatalítica del oxígeno. La creación de defectos topológicos en los nanotubos de carbono de pared múltiple (MWCNTs) a través de la oxidación sucesiva en H_2SO_4 y HNO_3 concentrado, y el posterior tratamiento a alta temperatura en argón, puede mejorar significativamente la actividad de la ORR en comparación con los MWCNTs no modificados [154]. Lu et al. reportaron la formación de grupos funcionales cetónicos C=O en la pared externa de los MWCNTs después de oxidación superficial suave, el tratamiento hidrotérmico y la activación electroquímica; los MWCNTs mostraron una eficiente actividad para la OER con un η_{onset} de 0,3 V debido a que los grupos oxigenados modificaron la configuración electrónica de los átomos de carbono adyacentes [155].

Los resultados reportados en la literatura muestran que los materiales de carbono con defectos tienen mejores actividades que el carbono sin defectos [156]. Tao *et al.* confirmaron que los átomos de carbono en los bordes muestran una mayor actividad para la reducción de oxígeno que aquellos en el centro del plano debido a una mayor densidad de carga [157,158]. Incluso, Yao *et al.* demostraron que la actividad en la ORR de los materiales de grafénicos que poseen defectos atómicos (principalmente en los átomos de carbono en los bordes) es aún mayor que la de los grafenos dopados con nitrógeno y el grafeno puro [159]. Se ha demostrado también que los materiales carbonosos defectuosos tienen un rendimiento relativamente bueno en la oxidación y prometen ser utilizados en celdas de combustible de metal-aire. A pesar de estos resultados, el origen de la actividad de los carbones para la oxidación y la reducción del oxígeno sigue siendo motivo de debate. Yao *et al.* sintetizaron un catalizador de grafito pirolítico altamente orientado (HOPG) con patrones específicos de defectos de anillos pentagonales de carbono (D-HOPG). Los resultados experimentales y de cálculos teóricos de DFT revelaron que los defectos de pentagonales en los bordes son los centros activos principales para la ORR en medio ácido, siendo más activos que el nitrógeno piridínico en el HOPG dopado con nitrógeno [160].

En esta tesis doctoral, se plantean dos estrategias para estudiar los catalizadores bifuncionales de oxígeno en base a nanoestructuras de óxido de manganeso y de carbono: primero, se estudiará el dopado de nanofilamentos de dióxido de manganeso con heteroátomos de metales de transición (hierro) y cómo estos afectan la estructura y actividad catalítica de los nanofilamentos. La segunda estrategia será sintetizar distintos materiales nanoestructurados de carbono y estudiar cómo sus distintas propiedades afectan tanto el mecanismo como la actividad catalítica de composites MnO_2/C.

4. Objetivos generales y específicos de la tesis doctoral

4.1. Objetivo general

El objetivo general de la tesis doctoral es desarrollar electrodos avanzados para baterías de hierro-aire basados en materiales sostenibles y no críticos, poniendo énfasis en obtener electrodos eficientes y estables que permitan avanzar el conocimiento de las baterías hierro-aire y acercar su viabilidad técnica y económica.

4.2. Objetivos específicos

Los objetivos específicos de este trabajo son:

i) Sintetizar electrodos de hierro en base a métodos escalables, reproducibles y que permitan modificar las propiedades físico-químicas de los electrodos.

ii) Caracterizar físico-químicamente los óxidos de hierro y estudiar la relación entre sus propiedades físico-químicas y su rendimiento electroquímico, llegando a modelos que permitan correlacionar estas variables.

iii) Estudiar el efecto de las variables de operación del electrodo sobre su rendimiento.

iv) Estudiar las causas de la desactivación de los electrodos de hierro mediante caracterizaciones post-mortem y métodos electroquímicos

v) Sintetizar electrodos bifuncionales de oxígeno para medio alcalino en base a óxidos de manganeso dopados con heteroátomos y materiales nanoestructurados de carbono.

vi) Caracterizar físico-químicamente los óxidos manganeso y materiales de carbono y estudiar la relación entre sus propiedades físico-químicas y su rendimiento electroquímico.

vii) Estudiar los mecanismos de las reacciones de evolución y reducción de oxígeno y explicar la actividad catalítica de los materiales sintetizados en relación al mecanismo de reacción y las propiedades físico-químicas de los catalizadores.

5. Referencias

[1] IPCC, Global Warming of 1.5 ºC An IPCC special report on the impacts of global warming of 1.5 °C above pre-industrial levels and related global greenhouse gas emission pathways, in the context of strengthening the global response to the threat of climate change, 2018.

[2] D. Metzler, A. Humpe, S. Gössling, Is it time to abolish company car benefits? An analysis of transport behaviour in Germany and implications for climate change, Clim. Policy. 19 (2019) 542–555. https://doi.org/10.1080/14693062.2018.1533446.

[3] S. Solaymani, CO2 emissions patterns in 7 top carbon emitter economies: The case of transport sector, Energy. 168 (2019) 989–1001. https://doi.org/10.1016/j.energy.2018.11.145.

[4] W.F. Lamb, T. Wiedmann, J. Pongratz, R. Andrew, M. Crippa, J.G.J. Olivier, D. Wiedenhofer, G. Mattioli, A. Al Khourdajie, J. House, S. Pachauri, M. Figueroa, Y. Saheb, R. Slade, K. Hubacek, L. Sun, S.K. Ribeiro, S. Khennas, S. De La Rue Du Can, L. Chapungu, S.J. Davis, I. Bashmakov, H. Dai, S. Dhakal, X. Tan, Y. Geng, B. Gu, J. Minx, A review of trends and drivers of greenhouse gas emissions by sector from 1990 to 2018, Environ. Res. Lett. 16 (2021). https://doi.org/10.1088/1748-9326/abee4e.

[5] energy institute, Statistical Review of World Engergy, 2023. https://www.energyinst.org/__data/assets/pdf_file/0004/1055542/EI_Stat_Review_PDF_single_3.pdf.

[6] U.S. Energy Information Administration, Table 6.07.B. Capacity Factors for Utility Scale Generators Primarily Using Non-Fossil Fuels, Electr. Power Mon. (2023). https://www.eia.gov/electricity/monthly/epm_table_grapher.php?t=epmt_6_07_b (accessed July 31, 2023).

[7] J.A. Roca, La capacidad europea de almacenamiento a escala de red se multiplicará por 20 para 2031: España, entre los principales mercados, El Periódico La Energía. (2022). https://elperiodicodelaenergia.com/la-capacidad-europea-de-almacenamiento-a-escala-de-red-se-multiplicara-por-20-para-2031-espana-entre-los-principales-mercados/ (accessed August 1, 2023).

[8] Mobility Sweden, Ökning av nya personbilar i maj men årets nya ordrar har halverats, Press. Nyregistreringar. (2023).

https://mobilitysweden.se/statistik/Nyregistreringar_per_manad_1/nyregistreringar-2023_3/okning-av-nya-personbilar-i-maj-men-arets-nya-ordrar-har-halverats# (accessed September 20, 2023).

[9] M. Li, J. Lu, Z. Chen, K. Amine, 30 Years of Lithium-Ion Batteries, Adv. Mater. 30 (2018) 1–24. https://doi.org/10.1002/adma.201800561.

[10] A. Manthiram, An Outlook on Lithium Ion Battery Technology, ACS Cent. Sci. 3 (2017) 1063–1069. https://doi.org/10.1021/acscentsci.7b00288.

[11] Y. Ding, Z.P. Cano, A. Yu, J. Lu, Z. Chen, Automotive Li - Ion Batteries : Current Status and Future Perspectives, Electrochem. Energy Rev. 2 (2019) 1–28. https://doi.org/10.1007/s41918-018-0022-z.

[12] F.H. Gandoman, J. Jaguemont, S. Goutam, R. Gopalakrishnan, Y. Firouz, T. Kalogiannis, N. Omar, J. Van Mierlo, Concept of reliability and safety assessment of lithium-ion batteries in electric vehicles: Basics, progress, and challenges, Appl. Energy. 251 (2019) 113343. https://doi.org/10.1016/j.apenergy.2019.113343.

[13] P.G. Balakrishnan, R. Ramesh, T. Prem Kumar, Safety mechanisms in lithium-ion batteries, J. Power Sources. 155 (2006) 401–414. https://doi.org/10.1016/j.jpowsour.2005.12.002.

[14] X. Feng, S. Zheng, D. Ren, X. He, L. Wang, H. Cui, X. Liu, C. Jin, F. Zhang, C. Xu, H. Hsu, S. Gao, T. Chen, Y. Li, T. Wang, H. Wang, M. Li, M. Ouyang, Investigating the thermal runaway mechanisms of lithium-ion batteries based on thermal analysis database, Appl. Energy. 246 (2019) 53–64. https://doi.org/10.1016/j.apenergy.2019.04.009.

[15] M. Keersemaker, Critical Raw Materials, in: Suriname Revisit. Econ. Potential Its Miner. Resour., Springer, Cham, 2020: pp. 69–82. https://doi.org/10.1007/978-3-030-40268-6_9.

[16] Statista, Ranking de los principales países productores de litio a nivel mundial en 2022, (2023). https://es.statista.com/estadisticas/600308/paises-lideres-en-la-produccion-de-litio-a-nivel-mundial/#:~:text=Países líderes en la producción de litio a nivel mundial 2022&text=En 2022%2C Australia fue el,y 19.000 toneladas métricas%2C respectivamente. (accessed August 29, 2023).

[17] A.G. Olabi, E.T. Sayed, T. Wilberforce, A. Jamal, A.H. Alami, K. Elsaid, S.M.A. Rahman, S.K. Shah, M.A. Abdelkareem, Metal-air batteries—a review, Energies. 14 (2021) 1–46.

https://doi.org/10.3390/en14217373.

[18] R. Buckingham, T. Asset, P. Atanassov, Aluminum-air batteries : A review of alloys , electrolytes and design, J. Power Sources. 498 (2021) 229762. https://doi.org/10.1016/j.jpowsour.2021.229762.

[19] J. Ryu, M. Park, J. Cho, Advanced Technologies for High-Energy Aluminum – Air Batteries, 1804784 (2019) 1–8. https://doi.org/10.1002/adma.201804784.

[20] X. Liu, H. Jiao, M. Wang, W. Song, J. Xue, S. Jiao, Current progresses and future prospects on aluminium–air batteries, Int. Mater. Rev. 67 (2022) 734–764. https://doi.org/10.1080/09506608.2021.2006968.

[21] H. Weinrich, Y.E. Durmus, H. Tempel, H. Kungl, R.A. Eichel, Silicon and iron as resource-efficient anode materials for ambient-temperature metal-air batteries: A review, Materials (Basel). 12 (2019) 2134. https://doi.org/10.3390/ma121321341-55.

[22] R.D. McKerracher, C. Ponce de Leon, R.G.A. Wills, A.A. Shah, F.C. Walsh, A Review of the Iron-Air Secondary Battery for Energy Storage, Chempluschem. 80 (2015) 323–335. https://doi.org/10.1002/cplu.201402238.

[23] C. Wang, Y. Yu, J. Niu, Y. Liu, D. Bridges, X. Liu, J. Pooran, Y. Zhang, A. Hu, Recent progress of metal-air batteries-A mini review, Appl. Sci. 9 (2019) 1–22. https://doi.org/10.3390/app9142787.

[24] U.S. Geological Survey, Mineral commodity summaries 2023, Reston, Virginia, 2023. https://doi.org/10.3133/mcs2023.

[25] F. Krull, Der Edison-Akkumulator, Zeitschrift Für Angew. Chemie. 18 (1905) 216–217.

[26] A.B. Lamb, The potential of iron calculated from equilibria measurements, J. Am. Chem. Soc. 32 (1910) 1214–1220.

[27] F. Foerster, Die Vorgänge im Eisennickel-Superoxydsammler. II. Das Verhalten des Elektrolyten, Zeitschrift Für Angew. Chemie. 14 (1908) 285–300.

[28] A.J. Salkind, C.J. Venuto, S.U. Falk, The Reaction at the Iron Alkaline Electrode, J. Electrochem. Soc. 111 (1964) 493. https://doi.org/10.1149/1.2426166.

[29] A.M. Sukhotin, K.M. Kartashova, The passivity of iron in acid and alkaline solutions, Corros. Sci. 5 (1965) 393–407. https://doi.org/10.1016/S0010-938X(65)90560-3.

[30] T. Hurlen, Anodic behaviour of iron in alkaline solutions, Eelctrochimica Acta. 8 (1963) 609–619.

[31] K.M. Gorbunova, L.I. Liamina, On the mechanism of iron reduction from alkaline solutions, Electrochim. Acta. 11 (1966) 457–467. https://doi.org/10.1016/0013-4686(66)80023-3.

[32] E.S. Buzzelli, C.T. Liu, W.A. Bryant, Iron-air batteries for electric vehicles, in: Intersoc. Energy Convers. Eng. Conf. 13th, San Diego, Calif., August 20-25, 1978, Proceedings. Vol. 1., 1978: pp. 745–749.

[33] Form Energy, Multi-day storage, the pathway to a clean, reliable and secure grid, Batter. Technol. (n.d.). https://formenergy.com/technology/battery-technology/ (accessed September 3, 2023).

[34] E. Jiménez, La innovadora batería hierro-aire por la que han apostado Bill Gates y Jeff Bezos con capacidad para almacenar energía durante 100 horas, D. Mot. (2023). https://www.diariomotor.com/energia-sostenibilidad/innovadora-bateria-hierro-aire-tiene-100-horas-de-duracion/ (accessed September 3, 2023).

[35] X. Zhao, Y. Gong, X. Li, N. Xu, K. Huang, Performance of Solid Oxide Iron-Air Battery Operated at 550°C, J. Electrochem. Soc. 160 (2013) A1241–A1247. https://doi.org/10.1149/2.085308jes.

[36] M.A. Deyab, Q. Mohsen, Improved battery capacity and cycle life in iron-air batteries with ionic liquid, Renew. Sustain. Energy Rev. 139 (2021) 110729. https://doi.org/10.1016/j.rser.2021.110729.

[37] S. Zhang, Y. Yang, L. Cheng, J. Sun, X. Wang, P. Nan, C. Xie, H. Yu, Y. Xia, B. Ge, J. Lin, L. Zhang, C. Guan, G. Xiao, C. Peng, G.Z. Chen, J.Q. Wang, Quasi-solid-state electrolyte for rechargeable high-temperature molten salt iron-air battery, Energy Storage Mater. 35 (2021) 142–147. https://doi.org/10.1016/j.ensm.2020.11.014.

[38] H. Weinrich, M. Gehring, H. Tempel, H. Kungl, R.A. Eichel, Impact of the charging conditions on the discharge performance of rechargeable iron-anodes for alkaline iron–air batteries, J. Appl. Electrochem. 48 (2018) 451–462. https://doi.org/10.1007/s10800-018-1176-4.

[39] D.C. Lee, D. Lei, G. Yushin, Morphology and Phase Changes in Iron Anodes Affecting their Capacity and Stability in Rechargeable Alkaline Batteries, ACS Energy Lett. 3 (2018) 794–

801. https://doi.org/10.1021/acsenergylett.8b00063.

[40] J. Liu, M. Chen, L. Zhang, J. Jiang, J. Yan, Y. Huang, J. Lin, H.J. Fan, Z.X. Shen, A flexible alkaline rechargeable Ni/Fe battery based on graphene foam/carbon nanotubes hybrid film, Nano Lett. 14 (2014) 7180–7187. https://doi.org/10.1021/nl503852m.

[41] D. Sarkar, A. Shukla, D.D. Sarma, Substrate Integrated Nickel-Iron Ultrabattery with Extraordinarily Enhanced Performances, ACS Energy Lett. 1 (2016) 82–88. https://doi.org/10.1021/acsenergylett.6b00067.

[42] H. Weinrich, J. Come, H. Tempel, H. Kungl, R.A. Eichel, N. Balke, Understanding the nanoscale redox-behavior of iron-anodes for rechargeable iron-air batteries, Nano Energy. 41 (2017) 706–716. https://doi.org/10.1016/j.nanoen.2017.10.023.

[43] K. Vijayamohanan, A.K. Shukla, S. Sathyanarayana, Formation mechanism of porous iron electrodes, J. Power Sources. 32 (1990) 329–339.

[44] A.K. Manohar, C. Yang, S. Malkhandi, B. Yang, G.K. Surya Prakash, S.R. Narayanan, Understanding the Factors Affecting the Formation of Carbonyl Iron Electrodes in Rechargeable Alkaline Iron Batteries, J. Electrochem. Soc. 159 (2012) A2148–A2155. https://doi.org/10.1149/2.021301jes.

[45] I. Villanueva-martínez, C. Alegre, J. Rubín, R. Mckerracher, H. Antonio, F. Rodríguez, M.J. L, Investigation of the properties influencing the deactivation of iron electrodes in iron-air batteries, Electrochim. Acta. 465 (2023). https://doi.org/10.1016/j.electacta.2023.142964.

[46] J.O. Gil Posada, P.J. Hall, Controlling hydrogen evolution on iron electrodes, Int. J. Hydrogen Energy. 41 (2016) 20807–20817. https://doi.org/10.1016/j.ijhydene.2016.04.123.

[47] A.K. Manohar, C. Yang, S. Malkhandi, G.K.S. Prakash, S.R. Narayanan, Enhancing the Performance of the Rechargeable Iron Electrode in Alkaline Batteries with Bismuth Oxide and Iron Sulfide Additives, J. Electrochem. Soc. 160 (2013) A2078–A2084. https://doi.org/10.1149/2.066311jes.

[48] H.A. Figueredo-Rodríguez, R.D. McKerracher, C. Ponce de León, F.C. Walsh, Improvement of Negative Electrodes for Iron-Air Batteries: Comparison of Different Iron Compounds as Active Materials H., J. Electrochem. Soc. 166 (2019) A107–A117. https://doi.org/10.1149/2.1071816jes.

[49] H. Weinrich, M. Gehring, H. Tempel, H. Kungl, R.A. Eichel, Electrode thickness-dependent formation of porous iron electrodes for secondary alkaline iron-air batteries, Electrochim. Acta. 314 (2019) 61–71. https://doi.org/10.1016/j.electacta.2019.05.025.

[50] P.S. Arunkumar, T. Maiyalagan, S. Kheawhom, S. Mao, Z. Jiang, Effect of carbon material additives on hydrogen evolution at rechargeable alkaline iron battery electrodes, Mater. Sci. Energy Technol. 4 (2021) 236–241. https://doi.org/10.1016/j.mset.2021.06.007.

[51] J. Yao, Y. Liu, H. Zhang, L. Ma, T. Meng, N. Li, J. Jiang, J. Zhu, C.M. Li, Configuring Optimal FeS2@Carbon Nanoreactor Anodes: Toward Insights into Pyrite Phase Change/Failure Mechanism in Rechargeable Ni-Fe Cells, ACS Appl. Mater. Interfaces. 11 (2019) 42032–42041. https://doi.org/10.1021/acsami.9b12153.

[52] J.O. Gil Posada, P.J. Hall, Post-hoc comparisons among iron electrode formulations based on bismuth, bismuth sulphide, iron sulphide, and potassium sulphide under strong alkaline conditions, J. Power Sources. 268 (2014) 810–815. https://doi.org/10.1016/j.jpowsour.2014.06.126.

[53] T.S. Balasubramanian, A.K. Shukla, Effect of metal-sulfide additives on charge/discharge reactions of the alkaline iron electrode, J. Power Sources. 41 (1993) 99–105. https://doi.org/10.1016/0378-7753(93)85008-C.

[54] J.O.G. Posada, P.J. Hall, Towards the development of safe and commercially viable nickel–iron batteries: improvements to Coulombic efficiency at high iron sulphide electrode formulations, J. Appl. Electrochem. 46 (2016) 451–458. https://doi.org/10.1007/s10800-015-0911-3.

[55] B. Tian, J. Światowska, V. Maurice, S. Zanna, A. Seyeux, P. Marcus, The effect of Na2S additive in alkaline electrolyte on improved performances of Fe-based air batteries, Electrochim. Acta. 259 (2018) 196–203. https://doi.org/10.1016/j.electacta.2017.10.136.

[56] C. Yang, A.K. Manohar, S.R. Narayanan, A High-Performance Sintered Iron Electrode for Rechargeable Alkaline Batteries to Enable Large-Scale Energy Storage, J. Electrochem. Soc. 164 (2017) A418–A429. https://doi.org/10.1149/2.1161702jes.

[57] A.K. Manohar, C. Yang, S.R. Narayanan, The Role of Sulfide Additives in Achieving Long Cycle Life Rechargeable Iron Electrodes in Alkaline Batteries, J. Electrochem. Soc. 162 (2015) A1864–A1872. https://doi.org/10.1149/2.0741509jes.

[58] P. Periasamy, B. Ramesh Babu, S. Venkatakrishna Iyer, Cyclic voltammetric studies of porous iron electrodes in alkaline solutions used for alkaline batteries, J. Power Sources. 58 (1996) 35–40. https://doi.org/10.1016/0378-7753(95)02274-0.

[59] R.D. McKerracher, H.A. Figueredo-Rodriguez, C. Alegre, A.S. Aricò, V. Baglio, C. Ponce de León, Improving the stability and discharge capacity of nanostructured Fe2O3/C anodes for iron-air batteries and investigation of 1-octhanethiol as an electrolyte additive, Electrochim. Acta. 318 (2019) 625–634. https://doi.org/10.1016/j.electacta.2019.06.043.

[60] M. Chamoun, B. Skårman, H. Vidarsson, R.I. Smith, S. Hull, M. Lelis, D. Milcius, D. Noréus, Stannate Increases Hydrogen Evolution Overpotential on Rechargeable Alkaline Iron Electrodes, J. Electrochem. Soc. 164 (2017) A1251–A1257. https://doi.org/10.1149/2.1401706jes.

[61] R.D. McKerracher, H.A. Figueredo-Rodriguez, K. Dimogiannis, C. Alegre, N.I. Villanueva-Martinez, M.J. Lázaro, V. Baglio, A.S. Aricò, C. Ponce de León, Effect of 1-octanethiol as an electrolyte additive on the performance of the iron-air battery electrodes, J. Solid State Electrochem. 25 (2021) 225–230. https://doi.org/10.1007/s10008-020-04738-4.

[62] R. Gomez, a Fernandezvega, J.M. Feliu, a Aldaz, Hydrogen Evolution on Pt Single-Crystal Surfaces - Effects of Irreversibly Adsorbed Bismuth and Antimony on Hydrogen Adsorption and Evolution on Pt(100), J. Phys. Chem. 97 (1993) 4769–4776. https://doi.org/Doi 10.1021/J100120a032.

[63] A.K. Manohar, S. Malkhandi, B. Yang, C. Yang, G.K. Surya Prakash, S.R. Narayanan, A High-Performance Rechargeable Iron Electrode for Large-Scale Battery-Based Energy Storage, J. Electrochem. Soc. 159 (2012) A1209–A1214. https://doi.org/10.1149/2.034208jes.

[64] I. Flis-kabulska, Transient hydrogen permeation through iron after potential jumps from cathodic to anodic polarisation in NaOH solution, Electrochem. Commun. 11 (2009) 54–56. https://doi.org/10.1016/j.elecom.2008.10.022.

[65] B.E. Poling, G.H. Thomson, D.G. Friend, R.L. Rowley, W.V. Wilding, Physical and Chemical Data, in: D.W. Green (Ed.), Perry's Chem. Eng. Handb., 8th editio, McGraw-Hill, 2008. https://doi.org/10.1036/0071511253.

[66] A.R. Paulraj, Y. Kiros, M. Chamoun, H. Svengren, D. Noréus, M. Göthelid, B. Skårman, H. Vidarsson, M.B. Johansson, Electrochemical performance and in operando charge

efficiency measurements of Cu/Sn-doped nano iron electrodes, Batteries. 5 (2019) 1–15. https://doi.org/10.3390/batteries5010001.

[67] H.T. Bui, T.M. Vu, Hydrothermal Preparation of Fe2O3 Nanoparticles for Fe-Air Battery Anodes, J. Electron. Mater. 48 (2019) 7123–7130. https://doi.org/10.1007/s11664-019-07522-x.

[68] B.T. Hang, M. Eashira, I. Watanabe, S. Okada, J.I. Yamaki, S.H. Yoon, I. Mochida, The effect of carbon species on the properties of Fe/C composite for metal-air battery anode, J. Power Sources. 143 (2005) 256–264. https://doi.org/10.1016/j.jpowsour.2004.11.044.

[69] A.S. Rajan, S. Sampath, A.K. Shukla, An in situ carbon-grafted alkaline iron electrode for iron-based accumulators, Energy Environ. Sci. 7 (2014) 1110–1116. https://doi.org/10.1039/c3ee42783h.

[70] H. Weinrich, J. Pleie, B. Schmid, H. Tempel, H. Kungl, R.A. Eichel, In Situ Hydrogen Evolution Monitoring During the Electrochemical Formation and Cycling of Pressed-Plate Carbonyl Iron Electrodes in Alkaline Electrolyte, Batter. Supercaps. 5 (2022) 3–10. https://doi.org/10.1002/batt.202100415.

[71] B.T. Hang, S.H. Yoon, S. Okada, J. ichi Yamaki, Effect of metal-sulfide additives on electrochemical properties of nano-sized Fe2O3-loaded carbon for Fe/air battery anodes, J. Power Sources. 168 (2007) 522–532. https://doi.org/10.1016/j.jpowsour.2007.02.067.

[72] D. Mitra, A.S. Rajan, A. Irshad, S.R. Narayanan, High Performance Iron Electrodes with Metal Sulfide Additives, J. Electrochem. Soc. 168 (2021) 030518. https://doi.org/10.1149/1945-7111/abe9c7.

[73] A.S. Rajan, M.K. Ravikumar, K.R. Priolkar, S. Sampath, A.K. Shukla, Carbonyl-Iron Electrodes for Rechargeable-Iron Batteries, Electrochem. Energy Technol. 1 (2014) 2–9. https://doi.org/10.1515/eetech-2014-0002.

[74] B.T. Hang, T. Watanabe, M. Egashira, I. Watanabe, S. Okada, J. ichi Yamaki, The effect of additives on the electrochemical properties of Fe/C composite for Fe/air battery anode, J. Power Sources. 155 (2006) 461–469. https://doi.org/10.1016/j.jpowsour.2005.04.010.

[75] D. Lei, D.C. Lee, A. Magasinski, E. Zhao, D. Steingart, G. Yushin, Performance Enhancement and Side Reactions in Rechargeable Nickel-Iron Batteries with Nanostructured Electrodes, ACS Appl. Mater. Interfaces. 8 (2016) 2088–2096.

https://doi.org/10.1021/acsami.5b10547.

[76] Q. Wang, Y. Wang, Overcoming the Limiting Step of Fe2O3 Reduction via in Situ Sulfide Modification, ACS Appl. Mater. Interfaces. 8 (2016) 10334–10342. https://doi.org/10.1021/acsami.6b01737.

[77] E. Shangguan, S. Fu, C. Wu, X. Cai, J. Li, Z. Chang, Z. Wang, Q. Li, Sublimed sulfur powders as novel effective anode additives to enhance the high-rate capabilities of iron anodes for advanced iron-based secondary batteries, Electrochim. Acta. 301 (2019) 162–173. https://doi.org/10.1016/j.electacta.2019.01.139.

[78] W.A. Bryant, The Importance of Physical Structure to the Capacity of Porous Iron Electrodes, J. Electrochem. Soc. 126 (1979) 1899–1901. https://doi.org/10.1149/1.2128822.

[79] The National Institute for Occupational Safety and Health (NIOSH), Iron pentacarbonyl (as Fe), NIOSH Pocket Guid. to Chem. Hazards. (2019). https://www.cdc.gov/niosh/npg/npgd0345.html (accessed August 8, 2023).

[80] B.T. Hang, H. Hayashi, S.H. Yoon, S. Okada, J. ichi Yamaki, Fe2O3-filled carbon nanotubes as a negative electrode for an Fe-air battery, J. Power Sources. 178 (2008) 393–401. https://doi.org/10.1016/j.jpowsour.2007.12.012.

[81] B.T. Hang, D.H. Thang, N.T. Nga, P.T. Le Minh, E. Kobayashi, Nanoparticle Fe2O3-Loaded Carbon Nanofibers as Iron-Air Battery Anodes, J. Electrochem. Soc. 160 (2013) A1442–A1445. https://doi.org/10.1149/2.066309jes.

[82] E. Shangguan, L. Guo, F. Li, Q. Wang, J. Li, Q. Li, Z. Chang, X.Z. Yuan, FeS anchored reduced graphene oxide nanosheets as advanced anode material with superior high-rate performance for alkaline secondary batteries, J. Power Sources. 327 (2016) 187–195. https://doi.org/10.1016/J.JPOWSOUR.2016.07.031.

[83] M. Egashira, J. ya Kushizaki, N. Yoshimoto, M. Morita, The effect of dispersion of nano-carbon on electrochemical behavior of Fe/nano-carbon composite electrode, J. Power Sources. 183 (2008) 399–402. https://doi.org/10.1016/j.jpowsour.2008.05.009.

[84] Z. Sun, L. Kong, X. Wang, Y. Lei, X. Li, H. Tang, Y. Hou, K. Chang, Z. Chang, Study of the electrochemical properties of Fe3O4/C–Bi composites prepared by spray drying and their use in cylindrical sealed nickel iron batteries, Int. J. Hydrogen Energy. 48 (2023) 9785–9796. https://doi.org/10.1016/j.ijhydene.2022.11.241.

[85] H. Osgood, S. V Devaguptapu, H. Xu, J. Cho, G. Wu, Transition metal (Fe, Co, Ni, and Mn) oxides for oxygen reduction and evolution bifunctional catalysts in alkaline media, Nano Today. 11 (2016) 601–625. https://doi.org/10.1016/j.nantod.2016.09.001.

[86] N.-T. Suen, S.-F. Hung, Q. Quan, N. Zhang, Y.-J. Xu, H.M. Chen, Electrocatalysis for the oxygen evolution reaction: recent development and future perspectives, Chem. Soc. Rev. 46 (2017) 337–365. https://doi.org/10.1039/C6CS00328A.

[87] M. Shao, Q. Chang, J.-P. Dodelet, R. Chenitz, Recent Advances in Electrocatalysts for Oxygen Reduction Reaction, Chem. Rev. 116 (2016) 3594–3657. https://doi.org/10.1021/acs.chemrev.5b00462.

[88] J.H. Siow, M.R. Bilad, W. Caesarendra, J.J. Leam, M.A. Bustam, Progress in Development of Nanostructured Manganese Oxide as Catalyst for Oxygen Reduction and Evolution Reaction, Energies. 14 (2021) 6385.

[89] K.A. Stoerzinger, M. Risch, B. Han, Y. Shao-Horn, Recent Insights into Manganese Oxides in Catalyzing Oxygen Reduction Kinetics, ACS Catal. 5 (2015) 6021–6031. https://doi.org/10.1021/acscatal.5b01444.

[90] Y. Wang, J. Li, Z. Wei, Transition-metal-oxide-based catalysts for the oxygen reduction reaction, J. Mater. Chem. A. 6 (2018) 8194–8209. https://doi.org/10.1039/c8ta01321g.

[91] N. Ramaswamy, S. Mukerjee, Influence of inner- and outer-sphere electron transfer mechanisms during electrocatalysis of oxygen reduction in alkaline media, J. Phys. Chem. C. 115 (2011) 18015–18026. https://doi.org/10.1021/jp204680p.

[92] T. Poux, A. Bonnefont, A. Ryabova, G. Kéranguéven, G.A. Tsirlina, E.R. Savinova, Electrocatalysis of hydrogen peroxide reactions on perovskite oxides: Experiment versus kinetic modeling, Phys. Chem. Chem. Phys. 16 (2014) 13595–13600. https://doi.org/10.1039/c4cp00341a.

[93] H. Jo, H.-J. Ahn, Accelerating the Oxygen Reduction Reaction and Oxygen Evolution Reaction Activities of N and P Co-Doped Porous Activated Carbon for Li-O2 Batteries, Catalysts. 10 (2020) 1316.

[94] F.D. Speck, P.G. Santori, F. Jaouen, S. Cherevko, Mechanisms of Manganese Oxide Electrocatalysts Degradation during Oxygen Reduction and Oxygen Evolution Reactions, J. Phys. Chem. C. 123 (2019) 25267−25277. https://doi.org/10.1021/acs.jpcc.9b07751.

[95] T.J. Bandosz, Revealing the impact of small pores on oxygen reduction on carbon

electrocatalysts : A journey through recent findings, Carbon N. Y. 188 (2022) 289–304. https://doi.org/10.1016/j.carbon.2021.11.071.

[96] F. Cheng, J. Chen, Metal–air batteries: From oxygen reduction electrochemistry to cathode catalysts, Chem. Soc. Rev. 41 (2012) 2172–2192. https://doi.org/10.1039/c1cs15228a.

[97] D. Yang, L. Zhang, X. Yan, X. Yao, Recent Progress in Oxygen Electrocatalysts for Zinc–Air Batteries, Small Methods. 1 (2017) 1–16. https://doi.org/10.1002/smtd.201700209.

[98] J.S. Spendelow, A. Wieckowski, Electrocatalysis of oxygen reduction and small alcohol oxidation in alkaline media, Phys. Chem. Chem. Phys. 9 (2007) 2654–2675. https://doi.org/10.1039/b703315j.

[99] J. Wu, H. Yang, Platinum-based oxygen reduction electrocatalysts, Acc. Chem. Res. 46 (2013) 1848–1857. https://doi.org/10.1021/ar300359w.

[100] T.R. Ralph, M.P. Hogarth, Catalysis for Low Temperature Fuel Cells PART II: THE ANODE CHALLENGES, Platin. Mater. Rev. 46 (2002) 117–135.

[101] J.K. Nørskov, J. Rossmeisl, A. Logadottir, L. Lindqvist, J.R. Kitchin, T. Bligaard, H. Jónsson, Origin of the overpotential for oxygen reduction at a fuel-cell cathode, J. Phys. Chem. B. 108 (2004) 17886–17892. https://doi.org/10.1021/jp047349j.

[102] N.T. Suen, S.F. Hung, Q. Quan, N. Zhang, Y.J. Xu, H.M. Chen, Electrocatalysis for the oxygen evolution reaction: Recent development and future perspectives, Chem. Soc. Rev. 46 (2017) 337–365. https://doi.org/10.1039/c6cs00328a.

[103] R. Frydendal, E.A. Paoli, B.P. Knudsen, B. Wickman, P. Malacrida, I.E.L. Stephens, I. Chorkendorff, Benchmarking the Stability of Oxygen Evolution Reaction Catalysts: The Importance of Monitoring Mass Losses, ChemElectroChem. 1 (2014) 2075–2081. https://doi.org/10.1002/celc.201402262.

[104] Y. Lee, J. Suntivich, K.J. May, E.E. Perry, Y. Shao-Horn, Synthesis and activities of rutile IrO2 and RuO2 nanoparticles for oxygen evolution in acid and alkaline solutions, J. Phys. Chem. Lett. 3 (2012) 399–404. https://doi.org/10.1021/jz2016507.

[105] T. Reier, M. Oezaslan, P. Strasser, Electrocatalytic oxygen evolution reaction (OER) on Ru, Ir, and Pt catalysts: A comparative study of nanoparticles and bulk materials, ACS Catal. 2 (2012) 1765–1772. https://doi.org/10.1021/cs3003098.

[106] R. Kötz, H.J. Lewerenz, S. Stucki, XPS Studies of Oxygen Evolution on Ru and RuO2 Anodes, J. Electrochem. Soc. 130 (1983) 825. https://doi.org/10.1149/1.2119829.

[107] Y. Wang, W. Huang, C. Si, J. Zhang, X. Yan, C. Jin, Y. Ding, Z. Zhang, Self-supporting nanoporous gold-palladium overlayer bifunctional catalysts toward oxygen reduction and evolution reactions, Nano Res. 9 (2016) 3781–3794. https://doi.org/10.1007/s12274-016-1248-x.

[108] C. Alegre, A. Stassi, E. Modica, C. Lo Vecchio, A.S. Aricò, V. Baglio, Investigation of the activity and stability of Pd-based catalysts towards the oxygen reduction (ORR) and evolution reactions (OER) in iron-air batteries, RSC Adv. 5 (2015) 25424–25427. https://doi.org/10.1039/c4ra15578e.

[109] Z. Cui, G. Fu, Y. Li, J.B. Goodenough, Ni3FeN-Supported Fe3Pt Intermetallic Nanoalloy as a High-Performance Bifunctional Catalyst for Metal–Air Batteries, Angew. Chemie - Int. Ed. 56 (2017) 9901–9905. https://doi.org/10.1002/anie.201705778.

[110] X. Zhong, S. Ye, J. Tang, Y. Zhu, D. Wu, M. Gu, H. Pan, B. Xu, Engineering Pt and Fe dual-metal single atoms anchored on nitrogen-doped carbon with high activity and durability towards oxygen reduction reaction for zinc-air battery, Appl. Catal. B Environ. 286 (2021) 119891. https://doi.org/10.1016/j.apcatb.2021.119891.

[111] T.H. You, C.C. Hu, Designing Binary Ru-Sn Oxides with Optimized Performances for the Air Electrode of Rechargeable Zinc-Air Batteries, ACS Appl. Mater. Interfaces. 10 (2018) 10064–10075. https://doi.org/10.1021/acsami.7b18948.

[112] X. Cai, L. Lai, J. Lin, Z. Shen, Recent advances in air electrodes for Zn-air batteries: Electrocatalysis and structural design, Mater. Horizons. 4 (2017) 945–976. https://doi.org/10.1039/c7mh00358g.

[113] X. Ge, A. Sumboja, D. Wuu, T. An, B. Li, F.W.T. Goh, T.S.A. Hor, Y. Zong, Z. Liu, Oxygen Reduction in Alkaline Media: From Mechanisms to Recent Advances of Catalysts, ACS Catal. 5 (2015) 4643–4667. https://doi.org/10.1021/acscatal.5b00524.

[114] C. Alegre, E. Modica, M. Rodlert-Bacilieri, F.C. Mornaghini, A.S. Aricò, V. Baglio, Enhanced durability of a cost-effective perovskite-carbon catalyst for the oxygen evolution and reduction reactions in alkaline environment, Int. J. Hydrogen Energy. (2017). https://doi.org/10.1016/j.ijhydene.2017.03.216.

[115] C. Alegre, C. Busacca, A. Di Blasi, O. Di Blasi, A.S.S. Aricò, V. Antonucci, E. Modica, V.

Baglio, Electrospun carbon nanofibers loaded with spinel-type cobalt oxide as bifunctional catalysts for enhanced oxygen electrocatalysis, J. Energy Storage. 23 (2019) 269–277. https://doi.org/10.1016/J.EST.2019.04.001.

[116] J.M. Luque-Centeno, M.V. Martínez-Huerta, D. Sebastián, G. Lemes, E. Pastor, M.J. Lázaro, Bifunctional N-doped graphene Ti and Co nanocomposites for the oxygen reduction and evolution reactions, Renew. Energy. 125 (2018) 182–192. https://doi.org/10.1016/J.RENENE.2018.02.073.

[117] S. Kim, J.W. Jung, D.H. Song, S.H. Cho, J. Kim, J.K. Kim, D.H. Oh, H. Sun, E.A. Cho, I.D. Kim, W.C. Jung, Exceptionally durable CoFe-exsolved Sr0.95Nb0.1Co0.7Fe0.2O3–δ catalyst for rechargeable Zn–air batteries, Appl. Catal. B Environ. 315 (2022) 121553. https://doi.org/10.1016/j.apcatb.2022.121553.

[118] Q. Zhao, Z. Yan, C. Chen, J. Chen, Spinels: Controlled Preparation, Oxygen Reduction/Evolution Reaction Application, and beyond, Chem. Rev. 117 (2017) 10121–10211. https://doi.org/10.1021/acs.chemrev.7b00051.

[119] J.T. Ren, G.G. Yuan, C.C. Weng, Z.Y. Yuan, Rationally Designed Co3O4-C Nanowire Arrays on Ni Foam Derived from Metal Organic Framework as Reversible Oxygen Evolution Electrodes with Enhanced Performance for Zn-Air Batteries, ACS Sustain. Chem. Eng. 6 (2018) 707–718. https://doi.org/10.1021/acssuschemeng.7b03034.

[120] C. Guan, A. Sumboja, H. Wu, W. Ren, X. Liu, H. Zhang, Z. Liu, C. Cheng, S.J. Pennycook, J. Wang, Hollow Co3O4 Nanosphere Embedded in Carbon Arrays for Stable and Flexible Solid-State Zinc–Air Batteries, Adv. Mater. 29 (2017) 1–9. https://doi.org/10.1002/adma.201704117.

[121] S.K. Singh, V.M. Dhavale, S. Kurungot, Surface-Tuned Co3O4 Nanoparticles Dispersed on Nitrogen-Doped Graphene as an Efficient Cathode Electrocatalyst for Mechanical Rechargeable Zinc-Air Battery Application, ACS Appl. Mater. Interfaces. 7 (2015) 21138–21149. https://doi.org/10.1021/acsami.5b04865.

[122] Z. Wang, W. Xu, X. Chen, Y. Peng, Y. Song, C. Lv, H. Liu, J. Sun, D. Yuan, X. Li, X. Guo, D. Yang, L. Zhang, Defect-Rich Nitrogen Doped Co3O4/C Porous Nanocubes Enable High-Efficiency Bifunctional Oxygen Electrocatalysis, Adv. Funct. Mater. 29 (2019). https://doi.org/10.1002/adfm.201902875.

[123] V. Duraisamy, N. Arumugam, A.I. Almansour, Y. Wang, T.X. Liu, S.M.S. Kumar, In situ

decoration of Co3O4 on N-doped hollow carbon sphere as an effective bifunctional oxygen electrocatalyst for oxygen evolution and oxygen reduction reactions, Colloids Surfaces A Physicochem. Eng. Asp. 656 (2023) 130347. https://doi.org/10.1016/j.colsurfa.2022.130347.

[124] X. Wang, Z. Liao, Y. Fu, C. Neumann, A. Turchanin, G. Nam, E. Zschech, J. Cho, J. Zhang, X. Feng, Confined growth of porous nitrogen-doped cobalt oxide nanoarrays as bifunctional oxygen electrocatalysts for rechargeable zinc–air batteries, Energy Storage Mater. 26 (2020) 157–164. https://doi.org/10.1016/j.ensm.2019.12.043.

[125] K. Wang, W. Wu, Z. Tang, L. Li, S. Chen, N.M. Bedford, Hierarchically Structured Co(OH)2/CoPt/N-CN Air Cathodes for Rechargeable Zinc-Air Batteries, ACS Appl. Mater. Interfaces. 11 (2019) 4983–4994. https://doi.org/10.1021/acsami.8b18424.

[126] J. Jiang, Y. Li, J. Liu, X. Huang, C. Yuan, X.W. Lou, Recent advances in metal oxide-based electrode architecture design for electrochemical energy storage, Adv. Mater. 24 (2012) 5166–5180. https://doi.org/10.1002/adma.201202146.

[127] C. Alegre, E. Modica, A.S. Aricò, V. Baglio, Bifunctional oxygen electrode based on a perovskite/carbon composite for electrochemical devices, J. Electroanal. Chem. 808 (2018) 412–419. https://doi.org/10.1016/j.jelechem.2017.06.023.

[128] T. An, X. Ge, T.S.A. Hor, F.W.T. Goh, D. Geng, G. Du, Y. Zhan, Z. Liu, Y. Zong, Co3O4 nanoparticles grown on N-doped Vulcan carbon as a scalable bifunctional electrocatalyst for rechargeable zinc-air batteries, RSC Adv. 5 (2015) 75773–75780. https://doi.org/10.1039/c5ra11047e.

[129] M.S. Burke, L.J. Enman, A.S. Batchellor, S. Zou, S.W. Boettcher, Oxygen Evolution Reaction Electrocatalysis on Transition Metal Oxides and (Oxy)hydroxides: Activity Trends and Design Principles, Chem. Mater. 27 (2015) 7549–7558. https://doi.org/10.1021/acs.chemmater.5b03148.

[130] J.M. Luque-Centeno, M. V. Martínez-Huerta, D. Sebastián, G. Lemes, E. Pastor, M.J. Lázaro, Bifunctional N-doped graphene Ti and Co nanocomposites for the oxygen reduction and evolution reactions, Renew. Energy. 125 (2018) 182–192. https://doi.org/10.1016/j.renene.2018.02.073.

[131] J.M. Luque-Centeno, M. V. Martínez-Huerta, D. Sebastián, J.I. Pardo, M.J. Lázaro, CoTiO3/NrGO nanocomposites for oxygen evolution and oxygen reduction reactions:

Synthesis and electrocatalytic performance, Electrochim. Acta. 331 (2020). https://doi.org/10.1016/j.electacta.2019.135396.

[132] J.C. Ruiz-Cornejo, D. Sebastián, J.I. Pardo, M.V. Martínez-Huerta, M.J. Lázaro, Sulfur-doped carbon nanofibers as support for tantalum oxides bifunctional catalysts for the oxygen reduction and evolution reactions, J. Power Sources. 546 (2022). https://doi.org/10.1016/j.jpowsour.2022.231988.

[133] A.B. Haruna, K.I. Ozoemena, Manganese-based bifunctional electrocatalysts for zinc-air batteries, Curr. Opin. Electrochem. 21 (2020) 219–224. https://doi.org/10.1016/j.coelec.2020.02.021.

[134] K.K. Hazarika, C. Goswami, H. Saikia, B.J. Borah, P. Bharali, Cubic Mn2O3 nanoparticles on carbon as bifunctional electrocatalyst for oxygen reduction and oxygen evolution reactions, Mol. Catal. 451 (2018) 153–160. https://doi.org/10.1016/j.mcat.2017.12.012.

[135] Y. Wang, D. Yang, S. Li, L. Zhang, G. Zheng, L. Guo, Layered copper manganese oxide for the efficient catalytic CO and VOCs oxidation, Chem. Eng. J. 357 (2019) 258–268. https://doi.org/10.1016/j.cej.2018.09.156.

[136] S. Yang, Z. Wang, Z. Cao, X. Mao, M. Shi, Y. Li, R. Zhang, Y. Yin, Facile synthesis of well dispersed spinel cobalt manganese oxides microsphere as efficient bi-functional electrocatalysts for oxygen reduction reaction and oxygen evolution reaction, J. Alloys Compd. 721 (2017) 482–491. https://doi.org/10.1016/j.jallcom.2017.05.221.

[137] Y.L. Cao, H.X. Yang, X.P. Ai, L.F. Xiao, The mechanism of oxygen reduction on MnO2-catalyzed air cathode in alkaline solution, J. Electroanal. Chem. 557 (2003) 127–134. https://doi.org/10.1016/S0022-0728(03)00355-3.

[138] F. Cheng, Y. Su, J. Liang, Z. Tao, J. Chen, MnO2-based nanostructures as catalysts for electrochemical oxygen reduction in alkaline media, Chem. Mater. 22 (2010) 898–905. https://doi.org/10.1021/cm901698s.

[139] P. Shende, P. Kasture, R.S. Gaud, Nanoflowers: the future trend of nanotechnology for multi-applications, Artif. Cells, Nanomedicine Biotechnol. 46 (2018) 413–422. https://doi.org/10.1080/21691401.2018.1428812.

[140] L. Tian, J. Wang, K. Wang, H. Wo, X. Wang, W. Zhuang, T. Li, X. Du, Carbon-quantum-dots-embedded MnO2 nanoflower as an efficient electrocatalyst for oxygen evolution in alkaline media, Carbon N. Y. 143 (2019) 457–466.

https://doi.org/10.1016/j.carbon.2018.11.041.

[141] Y. Gu, G. Yan, Y. Lian, P. Qi, Q. Mu, C. Zhang, Z. Deng, Y. Peng, MnIII-enriched α-MnO2 nanowires as efficient bifunctional oxygen catalysts for rechargeable Zn-air batteries, Energy Storage Mater. 23 (2019) 252–260. https://doi.org/10.1016/j.ensm.2019.05.006.

[142] M. Chatenet, B.G. Pollet, D.R. Dekel, F. Dionigi, J. Deseure, P. Millet, R.D. Braatz, M.Z. Bazant, M. Eikerling, I. Staffell, P. Balcombe, Y. Shao-Horn, H. Schäfer, Water electrolysis: from textbook knowledge to the latest scientific strategies and industrial developments, Chem. Soc. Rev. 51 (2022) 4583–4762. https://doi.org/10.1039/d0cs01079k.

[143] C.M. Julien, A. Mauger, Nanostructured MnO2 as electrode materials for energy storage, Nanomaterials. 7 (2017). https://doi.org/10.3390/nano7110396.

[144] Y. Haoran, D. Lifang, L. Tao, C. Yong, Hydrothermal synthesis of nanostructured manganese oxide as cathodic catalyst in a microbial fuel cell fed with leachate, Sci. World J. 2014 (2014). https://doi.org/10.1155/2014/791672.

[145] L. Wang, G. Duan, S.M. Chen, X. Liu, Hydrothermally controlled synthesis of α-MnO2, γ-MnOOH, and Mn3O4 nanomaterials with enhanced electrochemical properties, J. Alloys Compd. 752 (2018) 123–132. https://doi.org/10.1016/j.jallcom.2018.03.244.

[146] K. Selvakumar, S.M. Senthil Kumar, R. Thangamuthu, K. Ganesan, P. Murugan, P. Rajput, S.N. Jha, D. Bhattacharyya, Physiochemical investigation of shape-designed MnO2 nanostructures and their influence on oxygen reduction reaction activity in alkaline solution, J. Phys. Chem. C. 119 (2015) 6604–6618. https://doi.org/10.1021/jp5127915.

[147] Y. Meng, W. Song, H. Huang, Z. Ren, S.Y. Chen, S.L. Suib, Structure-property relationship of bifunctional MnO2 nanostructures: Highly efficient, ultra-stable electrochemical water oxidation and oxygen reduction reaction catalysts identified in alkaline media, J. Am. Chem. Soc. 136 (2014) 11452–11464. https://doi.org/10.1021/ja505186m.

[148] B. Lan, X. Zheng, G. Cheng, J. Han, W. Li, M. Sun, L. Yu, The art of balance: Engineering of structure defects and electrical conductivity of α-MnO2 for oxygen reduction reaction, Electrochim. Acta. 283 (2018) 459–466. https://doi.org/10.1016/j.electacta.2018.06.195.

[149] A. Mathur, A. Halder, One-step synthesis of bifunctional iron-doped manganese oxide nanorods for rechargeable zinc-air batteries, Catal. Sci. Technol. 9 (2019) 1245–1254. https://doi.org/10.1039/c8cy02498g.

[150] M. He, X. Jin, F. Chen, J. Chen, J. Min, H. Duan, X. Kuang, J. Li, Z. Wu, J. Li, Synergistic effect of Mn3+ and oxygen vacancy on the bifunctional oxygen electrocatalytic performance of MnOX/CNTs composites, J. Alloys Compd. 933 (2023). https://doi.org/10.1016/j.jallcom.2022.167728.

[151] X. Wu, C. Tang, Y. Cheng, X. Min, S.P. Jiang, S. Wang, Bifunctional Catalysts for Reversible Oxygen Evolution Reaction and Oxygen Reduction Reaction, Chem. - A Eur. J. 26 (2020) 3906–3929. https://doi.org/10.1002/chem.201905346.

[152] E. Yeager, Dioxygen electrocatalysis: mechanisms in relation to catalyst structure, J. Mol. Catal. 38 (1986) 5–25. https://doi.org/10.1016/0304-5102(86)87045-6.

[153] T.J. Bandosz, C.O. Ania, Chapter 4 Surface chemistry of activated carbons and its characterization, in: T.J.B.T.-I.S. and T. Bandosz (Ed.), Act. Carbon Surfaces Environ. Remediat., Elsevier, 2006: pp. 159–229. https://doi.org/https://doi.org/10.1016/S1573-4285(06)80013-X.

[154] K. Waki, R.A. Wong, H.S. Oktaviano, T. Fujio, T. Nagai, K. Kimoto, K. Yamada, Non-nitrogen doped and non-metal oxygen reduction electrocatalysts based on carbon nanotubes: Mechanism and origin of ORR activity, Energy Environ. Sci. 7 (2014) 1950–1958. https://doi.org/10.1039/c3ee43743d.

[155] X. Lu, W.L. Yim, B.H.R. Suryanto, C. Zhao, Electrocatalytic oxygen evolution at surface-oxidized multiwall carbon nanotubes, J. Am. Chem. Soc. 137 (2015) 2901–2907. https://doi.org/10.1021/ja509879r.

[156] D. Yan, Y. Li, J. Huo, R. Chen, L. Dai, S. Wang, Defect Chemistry of Nonprecious-Metal Electrocatalysts for Oxygen Reactions, Adv. Mater. 29 (2017) 1–20. https://doi.org/10.1002/adma.201606459.

[157] L. Tao, Q. Wang, S. Dou, Z. Ma, J. Huo, S. Wang, L. Dai, Edge-rich and dopant-free graphene as a highly efficient metal-free electrocatalyst for the oxygen reduction reaction, Chem. Commun. 52 (2016) 2764–2767. https://doi.org/10.1039/c5cc09173j.

[158] A. Shen, Y. Zou, Q. Wang, R.A.W. Dryfe, X. Huang, S. Dou, L. Dai, S. Wang, Oxygen reduction reaction in a droplet on graphite: Direct evidence that the edge is more active than the basal plane, Angew. Chemie - Int. Ed. 53 (2014) 10804–10808. https://doi.org/10.1002/anie.201406695.

[159] Y. Jia, L. Zhang, A. Du, G. Gao, J. Chen, X. Yan, C.L. Brown, X. Yao, Defect Graphene as a

Trifunctional Catalyst for Electrochemical Reactions, Adv. Mater. 28 (2016) 9532–9538. https://doi.org/10.1002/adma.201602912.

[160] Y. Jia, L. Zhang, L. Zhuang, H. Liu, X. Yan, X. Wang, J. Liu, J. Wang, Y. Zheng, Z. Xiao, E. Taran, J. Chen, D. Yang, Z. Zhu, S. Wang, L. Dai, X. Yao, Identification of active sites for acidic oxygen reduction on carbon catalysts with and without nitrogen doping, Nat. Catal. 2 (2019) 688–695. https://doi.org/10.1038/s41929-019-0297-4.

CAPÍTULO II: COPIA DE LAS PUBLICACIONES QUE CONFORMAN LA TESIS

En este capítulo, se muestran las 4 publicaciones a las que ha dado origen el trabajo experimental desarrollado durante el doctorado. Las publicaciones 1 y 2 tratan sobre el electrodo negativo de baterías hierro-aire, mientras que las publicaciones 3 y 4 tratan sobre el electrodo positivo.

Artículo 1

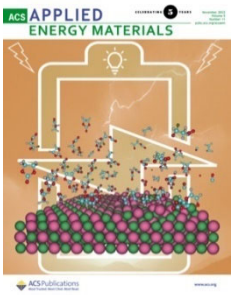

Villanueva, N., Alegre, C., Rubin, J., Figueredo-Rodriguez, H. A., McKerracher, R. D., de Leon, C. P., & Lázaro, M. J. (2022). Iron Electrodes Based on Sulfur-Modified Iron Oxides with Enhanced Stability for Iron–Air Batteries. *ACS Applied Energy Materials*, *5*(11), 13439-13451.

DOI: 10.1021/acsaem.2c02123

ACS APPLIED ENERGY MATERIALS

www.acsaem.org

Article

Iron Electrodes Based on Sulfur-Modified Iron Oxides with Enhanced Stability for Iron−Air Batteries

Nicolás Villanueva, Cinthia Alegre,* Javier Rubin, Horacio A. Figueredo-Rodríguez, Rachel D. McKerracher, Carlos Ponce de León, and María Jesús Lázaro*

Cite This: *ACS Appl. Energy Mater.* 2022, 5, 13439−13451

Read Online

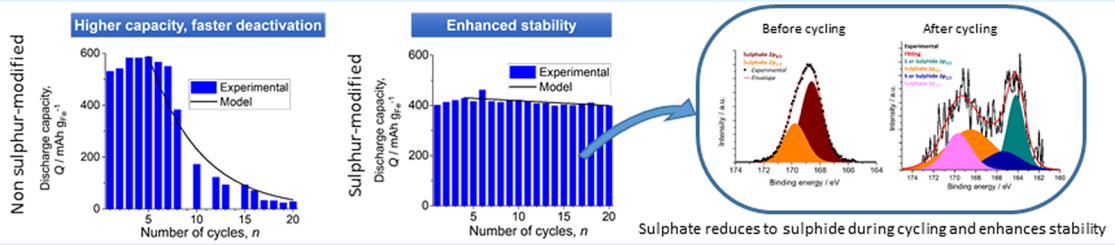

ABSTRACT: Iron−air systems are a very promising technology with the potential to become one of the cheapest and safest energy storage solutions of the future. However, iron anodes still face some challenges like passivation, resulting in loss of capacity, due to the formation of nonconductive species during cycling as well as the hydrogen evolution reaction, a parasitic reaction interfering with the charging of the electrode. In the present work these two issues are addressed: Sulfur-modified mesoporous iron oxides are obtained and used as hot-pressed negative electrodes for alkaline iron−air batteries. Iron electrodes present average capacity values between 400 and 500 mA h g $_{Fe}^{-1}$ for ∼100 h of operation, the S-modified iron oxides being the most stable ones. An exponential deactivation model fitting the discharge capacity of the different electrodes compared to the number of cycles was proposed. According to the model, the best of the electrodes loses less than 0.5% of its capacity per cycle. Furthermore, doubling the charge and discharge rates allows increasing both the discharge capacity and the Coulumbic efficiency, though at the expense of stability. This manuscript proves that the proper distribution of sulfur on the surface of the iron oxide is fundamental to suppress the HER and passivation, enhancing the stability of the electrode. These properties were further corroborated in long test-runs which comprised more than 400 h of charging and discharging.

KEYWORDS: *electrodes, hydrogen evolution, iron−air batteries, passivation, stability, sulfur-modified*

1. BACKGROUND

In order to limit the rise of the global temperature below 1.5 °C, the Intergovernmental Panel on Climate Change (IPCC) estimates that greenhouse gas (GHG) emissions must be cut down to 25−30 Gton of CO_2e per year by 2030.[1] As the transport sector accounts for 29% of the total world energy consumption[2] and 72% of this sector's emissions are related to road transport,[3] the transition from oil-based mobility to electromobility will have a high importance and impact in the following years. Lithium-ion batteries are the most used power storage devices for electric vehicles, but there are still concerns related to their specific energy (commercial Li-ion batteries reach up to 248 Wh kg^{-1}), cost (>$150 USD (kW h)$^{-1}$), and safety issues such as thermal runaway,[4] causing fires and explosions.[5,6] Besides, given that lithium ion batteries need some scarce elements and the global supply chains are put under a lot of pressure, batteries made with iron are becoming more attractive.

Metal−air batteries (MABs) are an alternative promising system due to their high theoretical energy densities (from 1000 to 11 000 W h kg^{-1}). MABs consist of a negative electrode, a metal that oxidizes during discharge, an electrolyte, and a positive electrode, in which ambient oxygen is reduced. Since air/oxygen is not stored within the cell, MABs present a high theoretical gravimetric energy density and a light weight.[7] Several metals can be used as anodes, such as lithium, sodium, magnesium, potassium, aluminum, zinc, and iron. This will determine the type of electrolyte to be used: nonaqueous for Li, Na, Mg, and Al and aqueous for Zn and Fe. Among all MABs, iron−air batteries (IABs) have several advantages. The Fe−air battery is a space-saving technology due to the high theoretical volumetric energy density of iron of 9700 kW h m^{-3} (versus 270−670 kW h m^{-3} of Li-ion batteries) and iron

Received: July 6, 2022
Accepted: October 8, 2022
Published: October 19, 2022

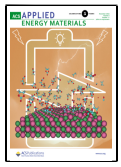

reacting directly with an aqueous electrolyte, not intercalating in a material like lithium cations. Although IABs have the lowest open circuit voltage and theoretical gravimetric specific energy of all the aforementioned systems of 1.28 V and 1080 W h kg_{Fe}^{-1}, respectively,[7] IABs have the potential to become one of the cheapest and safest energy storage solutions of the future. Iron is one of the most abundant elements in the Earth's crust (4th position),[8] is economic, is safe to handle, and is easy to refine. Besides, IABs can be electrically recharged (unlike Al−air), do not form dendrites during operation (as Zn−air), and operate with an aqueous electrolyte, usually KOH, which is cheaper than organic electrolytes and more environmentally friendly.[9,10] However, IABs still face some challenges that need to be tackled before IABs are technically and commercially viable. Challenges on the air electrode are widely known and common to other metal−air systems. On the other hand, the negative electrode of IAB presents the following problems: (a) the parasitic hydrogen evolution reaction (HER) during the charge, which reduces the Coulombic efficiency of the system, (b) the electrode passivation due to the formation of electrically nonconductive compounds (such as iron(II) hydroxide and goethite) during discharge, and (c) the molar volume change of iron discharge products related to metallic iron.

Most approaches aimed at inhibiting or reducing the rate of the HER are based on certain additives in the electrolyte like alkanethiols[11,12] or sulfide salts such as K_2S or Na_2S [13] that have been proved to effectively suppress HER. Other approaches including sulfides (FeS, Bi_2S_3, Na_2S, or K_2S)[14−18] in the iron electrode composition have shown good performances at relatively low additive concentrations (<10% wt), and it has also been established that sulfide species can also prevent passivation. However, these approaches incorporate the sulfide additives either by ball-milling (in which additives and active electrode species are merely physically mixed) or in the electrolyte (adding complexity to the design of the cell and contaminating the air electrode, as recently established[12]). In addition certain additives like those based on bismuth are not desirable since bismuth is a critical raw material.[19] New methods of incorporating H_2-inhibiting elements are then necessary. During the charging cycle of iron−air batteries (or in general in aqueous electrochemical devices dealing with HER), hydrogen is formed on the surface of the iron particles; therefore it is highly desirable to obtain an iron electroactive material with a proper distribution of the H_2-inhibiting elements.

Recently, Shangguan et al.[20] showed that adding sublimated sulfur to an Fe_3O_4 oxide in a ball mill also helps to prevent passivation by giving a supply of sulfide ions to the electrolyte and by forming pores in the electrode when dissolving. In line with this work, we propose the use of sulfur-modified iron oxides as electroactive material for iron−air batteries. Sulfur-doped or S-modified iron oxides based on hematite have been widely used as Fenton catalysts, since hematite is easily doped with heteroatoms. In the present work, we show a facile method to obtain highly pure sulfur-modified iron oxides as electroactive material for the negative electrode of an iron−air battery. The synthesis method employed herein ensures that sulfur gets introduced in the iron oxide structure, reaching an intimate and optimized distribution of sulfur on the electroactive materials,[21] with the aim of increasing the HER-suppressing effect and inhibiting passivation. Besides, the synthesis is optimized to obtain mesoporous iron oxides able to cope with the change of volume of the electrodes during cycling, 272% molar volume increase from Fe to $Fe(OH)_2$.[22] The novelty of the present research lies in the combination of properties within one material able to tackle the three main drawbacks of iron electrodes: HER, passivation, and volume changes. These features are correlated to the discharge capacity of the iron anodes, and in fact, a model relating the discharge capacity and the number of cycles for each electrode is also presented. Operation variables such as charge and discharge rate are also investigated to elucidate the conditions that could maximize the performance of the system.

2. MATERIALS AND METHODS

2.1. Materials Synthesis. Porous sulfur-modified iron oxides were synthesized following the method presented by Du et al.[23] Oxalic acid dihydrate ($C_2H_2O_4{\cdot}2H_2O$, 0.04 mol) was dissolved in 100 mL of deionized (DI) water and heated up to 50 °C under vigorous stirring. Another solution containing 0.04 mol of iron(II) sulfate heptahydrate ($FeSO_4{\cdot}7H_2O$) and 0.02 mol of sodium thiosulfate ($Na_2S_2O_3$) in 100 mL of DI water at room temperature was prepared and added drop by drop to the first solution, maintaining the temperature at 50 °C. A yellow precipitate formed that after cooling down was filtered, washed with abundant DI water, and dried overnight at 75 °C. Iron oxides obtained from oxalic acid were named as S-Fe_2O_3-OXL. Iron oxides without sulfur (named as Fe_2O_3-OXL) were also synthesized for the sake of comparison, following the same procedure previously described without the addition of sodium thiosulfate. Another iron oxide using sodium hydroxide (NaOH) instead of oxalate as precipitating agent (named as S-Fe_2O_3-SHX) was also prepared. In this case, 0.04 mol of iron(II) sulfate heptahydrate ($FeSO_4{\cdot}7H_2O$) and 0.02 mol of sodium thiosulfate ($Na_2S_2O_3$) were dissolved in 100 mL of DI water at room temperature. Subsequently, 80 mL of NaOH 1.0 mol/L was added under vigorous stirring, drop-by-drop. The black precipitate that formed was filtered and washed with DI water and dried overnight at 75 °C. All the samples were calcined in air at 350 °C for 1 h. Subsequently, the so obtained iron oxides were mixed with Vulcan XC-72R carbon black (1:1 mass ratio) in a planetary ball mill at 100 rpm for 2 h, using ethanol 96% vol as dispersing agent. Afterward, samples were dried in an oven at 75 °C. Carbon is needed in iron electrodes to provide electrical conductivity and to maximize the utilization of the iron material. A commercial iron oxide (III) nanopowder (<50 nm, Sigma-Aldrich, named as Fe_2O_3-COM) was also studied and mixed with Vulcan for the sake of comparison.

2.2. Materials Characterization. The textural properties of the iron oxides were investigated through nitrogen physisorption at 76 K in a Micromeritics ASAP 2020. The specific surface area was determined by the Brunauer−Emmet−Teller (BET) equation, whereas the single-point and the Barrett−Joyner−Halenda (BJH) methods were used to calculate the pore volume and the average pore size, respectively. An ESCA Plus Omicron spectrometer (Scienta Omicron) with a Mg (1253.6 eV) anode setup was employed to perform X-ray photoelectron spectroscopy (XPS) studies. C 1s, O 1s, S 2p, and Fe 2p orbital signals were obtained with a step of 0.1 eV step, a dwell time of 0.5 s, and 20 eV pass energy. The quantification of orbital signals and data analysis were curated using CasaXPS software (Casa Software Ltd., CasaXPS version 2.3.18). The baseline for the different peaks was estimated through a Shirley background subtraction, and the signals were fitted with 70% Gaussian/30% Lorentzian peaks. The carbon and sulfur content of the samples was determined by elemental analysis (EA) in a Thermo Flash 1112 analyzer (Thermoscientific Waltham). A Bruker AXS D8 Advance diffractometer (Bruker) with a θ−θ configuration and a Ru2500 diffractometer (RIGAKU) with rotating anode and θ−2θ configuration, both using Cu Kα radiation, were employed to investigate the crystalline structure of the iron oxides using X-ray diffraction (XRD). The crystallite size of the different phases was calculated applying Scherrer's equation to the iron oxide peaks. The iron amount was

https://doi.org/10.1021/acsaem.2c02123
ACS Appl. Energy Mater. 2022, 5, 13439−13451

Table 1. Chemical Composition of the Sulfur-Modified Iron Oxides Determined by Elemental Analyses (EA), ICP, and XPS

material	elemental analysis, sulfur		ICP, iron		S/Fe atomic ratio (calculated from EA and ICP measurements)	XPS, atom %	
	wt %	atom %	wt %	atom %		iron	sulfur
S-Fe_2O_3-OXL	4.6	4.0	56	27.8	0.14	21.9	6.9
S-Fe_2O_3-SHX	6.6	5.5	51	24.2	0.23	18.0	4.8

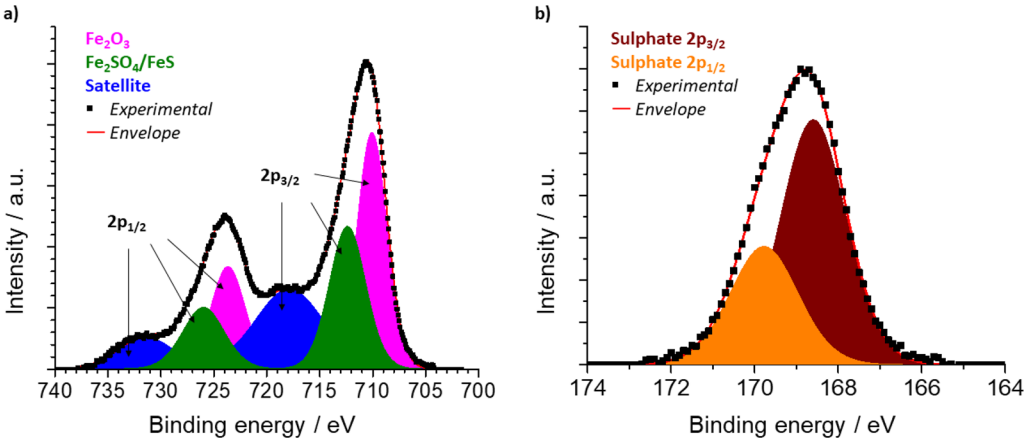

Figure 1. High-resolution XPS spectra of (a) Fe 2p orbital and (b) S 2p orbital in S-Fe_2O_3-OXL.

determined by inductively coupled plasma atomic emission spectroscopy (ICP-AES) using a Jobin Ybon 2000 spectrometer. The sample was previously fused using sodium peroxide. Each sample was measured twice, the average value being presented. The morphology of the iron oxides was investigated with a scanning electron microscope (SEM), model Hitachi S-3400N. Combining SEM with energy dispersive X-ray spectroscopy (SEM-EDX) allowed us to determine the dispersion of iron and sulfur in the composites. The equipment used was an EDX Röntec XFlash analyzer of Si(Li). FTIR analysis were performed in a Vertex 70 spectrophotometer (Bruker). The analyses were performed in the middle infrared region (from 4000 to 400 cm^{-1}) recording 32 scans at 4 cm^{-1} spectral resolution. KBr-matrix pellets were made to carry out transmittance analysis. To prepare the pellets, 2 mg of sample was mixed with 200 mg of dry KBr (>99% FTIR grade, Sigma-Aldrich), milled in an agate mortar, and pressed. Mössbauer spectroscopy (MS) data were acquired at room temperature using a constant acceleration spectrometer with symmetrical waveform and a 25 mCi ^{57}Co/Rh source. The spectrometer was calibrated at room temperature with α-Fe foil, and isomer shift values are given with respect to α-Fe.

2.3. Electrode Preparation. Iron electrodes were prepared by hot-pressing the obtained Fe_2O_3/C composites. A paste, prepared with 100 mg of the Fe_2O_3/C composite, 14 mg of PTFE (60% wt PTFE dispersion in water), and some drops of DI water, was placed within two stainless-steel meshes (2.5 cm × 7.5 cm) and hot-pressed at 25 kN and 140 °C for 90 s. The iron percentage in the electrodes ranged between 28 and 35% wt, depending on the composition of each oxide.

2.4. Electrochemical Setup and Cycling Procedures. The electrodes were tested in a conventional three-electrode cell, using a 6.0 M KOH solution as electrolyte (prepared from highly pure KOH, Alfa-Aesar-99.98% (metals basis), 85% min), a Ni sheet as counter electrode, and a Hg|HgO reference electrode, as in previous works.[15,24] To minimize the electrolyte overpotential, the working electrode and the counter electrode were placed in a holder where they faced each other separated by 0.5 cm (Figure S1). The electrodes were submitted to repeated galvanostatic charge and discharge cycles at a charge rate of 0.4 C and a discharge rate of 0.2 C, according to the theoretical capacity of the electrodes. The current (I) for each electrode and C-rate was calculated from eq 1, assuming 1273 mA h g_{Fe}^{-1} as the theoretical capacity of iron (two discharge steps considered):

$$I = m_{Fe}[g]\cdot 1273\left[\frac{\text{mAh}}{\text{g}}\right]\cdot(C - \text{rate})[\text{h}^{-1}] \quad (1)$$

3. RESULTS AND DISCUSSION

3.1. Physical−Chemical Characterization. *3.1.1. Chemical Composition.* The elemental analysis (EA) of the iron oxides (prior to the ball-milling mixing with Vulcan) (Table 1) shows that the sulfur content is 4.6 wt % for the S-Fe_2O_3-OXL and 6.6 wt % for the S-Fe_2O_3-SHX according to the EA analysis, and 6.9 atom % for S-Fe_2O_3-OXL and 4.8 atom % S-Fe_2O_3-SHX according to the XPS, meaning that S-Fe_2O_3-OXL has a S-enriched surface. The amount of sulfur in the composite is around 2.3 and 3.3 wt % in S-Fe_2O_3-OXL/C and S-Fe_2O_3-SHX/C, respectively. In the literature, the amount of sulfur used as an additive in the negative electrode ranges between 0.2 wt % as bismuth sulfide[15,25,26] and 2 wt % as iron sulfide.[14,27] Deng et al.[21] determined by DFT calculations that hematite iron oxides synthesized from ferrous sulfate and sodium thiosulfate mixtures (as in the present work) can be doped with sulfur, as is the case of our iron oxides, by two mechanisms: either interstitial or with sulfur replacing O atom in the crystalline structure of hematite. The amount of iron was also calculated by both XPS and ICP to estimate the ratio of S/Fe (also shown in Table 1). The weight % of iron is similar for both materials, around 50 wt %, equivalent to around 25 atom %. This means that S-Fe_2O_3-OXL presents a S/Fe ratio of 0.14 with respect to the S-Fe_2O_3-SHX with a S/Fe ratio of 0.23.

High-resolution XPS spectra of the Fe 2p orbital reveals that iron is mostly present as iron(III) oxide (Figure 1a), even though other forms of iron oxides or hydroxides might be present. The deconvolution of the iron spectrum curve of S-Fe_2O_3-OXL shows three Fe $2p_{3/2}$ peaks, at 710.9, 712.6, and 718.9 eV, which are ascribed to iron sulfate or sulfide, iron(III) oxide, and the classic satellite peak of Fe_2O_3 $2p_{3/2}$, respectively;[23,28] in samples without sulfur, only peaks related

https://doi.org/10.1021/acsaem.2c02123
ACS Appl. Energy Mater. 2022, 5, 13439−13451

to Fe_2O_3 can be seen (Figure S2). Due to the proximity of the characteristic binding energies of iron sulfate and iron sulfide (FeS) in the high-resolution iron XPS spectrum,[29] it is hard to distinguish among these two species. The observation and analysis of the sulfur orbital help to elucidate this ambiguity (Figure 1b). The main $2p_{3/2}$ peak is observed at 168.7 eV, which should correspond to sulfate.[28,30,31] The absence of peaks at lower binding energies (see Figure S2e) (mackinawite and pyrite show sulfur peaks at around 162 eV [32]) allows us to dismiss the presence of sulfides. Using oxalate as precipitating agent during the synthesis entails a more acidic pH (approximately 4−5) that eventually favors the adsorption of sulfate groups on the surface.[33]

3.1.2. Crystallographic Structure: Mössbauer Spectroscopy and X-ray Diffraction. The phases present in the samples were determined by XRD (Figure S3), FTIR (Figure S4), and Mossbauer spectroscopy (Figure 2). The room temperature

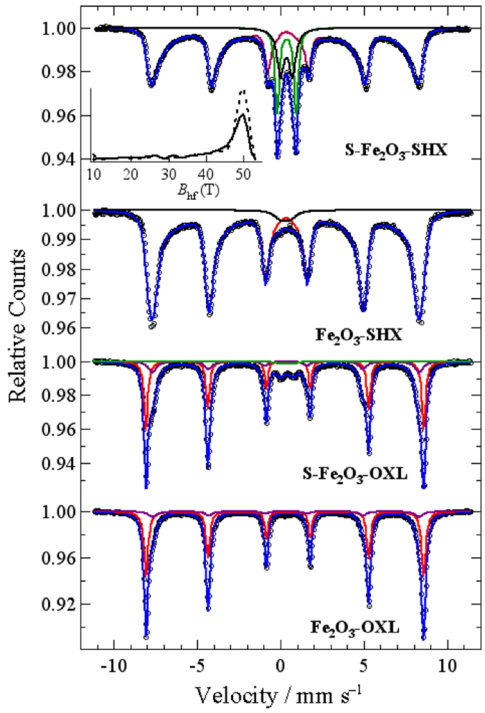

Figure 2. Mössbauer spectra of samples Fe_2O_3-OXL, S-Fe_2O_3-OXL, Fe_2O_3-SHX, and S-Fe_2O_3-SHX. For the SHX samples, the distribution of hyperfine field values is shown in the inset (dotted line, Fe_2O_3-SHX; full line, S-Fe_2O_3-SHX).

Mössbauer spectra of the oxides obtained by precipitation with oxalic acid (named as OXL) or sodium hydroxide (named as SHX) are shown in Figure 2 along with the spectra of the corresponding sulfur modified samples. The spectrum of Fe_2O_3-OXL was fitted with two sextets, while for the sulfur modified sample S-Fe_2O_3-SHX a doublet was added (Table S1). The sextets are straightforwardly (columns marked with S1 and S2 in Table S1 in Supporting Information) assigned to hematite and maghemite, respectively, according to their hyperfine parameters, while the intensity at the center of the S-Fe_2O_3-OXL spectrum, modeled as small doublet of very broad peaks, can be assigned to a paramagnetic Fe^{3+} compound because of its isomer shift value. In contrast, the samples prepared with NaOH do not display neat sextets but broad peaks which are asymmetric toward the center of the spectrum. This is an indication of a distribution of particle size including very small particles with superparamagnetic behavior at room temperature, which can also be observed in the XRD patterns (Figure S3). In this case, the spectra were fitted with a distribution of sextets and a broad central doublet to account for the iron oxides and their superparamagnetic behavior of very small particles, while the distribution of sextets and two doublets was used in the spectrum of the sulfur modified sample. In S-Fe_2O_3-OXL the isomer shift and quadrupole splitting values of the doublets are consistent with $Fe_2(SO_4)_3 \cdot 5H_2O$;[34] however, the relative areas of the doublets do not match those of pure $Fe_2(SO_4)_3 \cdot 5H_2O$,[34] with an extra intensity in the inner (lowest quadrupole splitting) doublet, which may be assigned to the superparamagnetic contribution of iron oxides. Using the spectral area of the outer (largest quadrupole splitting) doublet as pure $Fe_2(SO_4)_3 \cdot 5H_2O$, we can estimate a sulfur to iron atomic ratio of $\frac{3}{2}15.5 \approx 23\%$, in good agreement with the results of AE and ICP of 22.7% (Table 1).

The relative areas of the hematite and maghemite sextets in the samples prepared with oxalic acid show that maghemite formation is promoted when sodium thiosulfate is used to introduce sulfur, and Fe^{3+} sulfates still unidentified are formed at the expense of the hematite yield. The process is similar in the samples prepared with NaOH, as it can be observed by the decrease in the contribution of the largest hyperfine field values (Figure 2, inset) associated with hematite, but in this case the production of a Fe^{3+} sulfate, identified as $Fe_2(SO_4)_3 \cdot 5H_2O$, is much higher.

The synthesis method has a clear effect on the crystal structure: the oxides obtained by precipitation with oxalic acid (OXL) consist of mixtures of well crystallized hematite and maghemite, whereas the one obtained by precipitation with sodium hydroxide (SHX) shows broad reflections, especially those that can be assigned to hematite; e.g., note reflection (1 0 4) at $2\theta \approx 33°$ (Figure S3 in Supporting Information). Table 2 shows the approximate proportion of each phase in our iron oxides determined by MS and Rietveld profile fits using the FullProf code,[35] and average crystal size was obtained by Scherrer's equation. The fits included the refinement of the occupancy of one of the octahedral sites in maghemite;[36] in both cases the refined occupancy indicated close to stoichiometric maghemite. The profile of the diffractogram of

Table 2. Crystalline Phases and Average Crystal Size of the Different Iron Oxides

	crystal phase, %		average crystallite size, nm		from sextet areas in MS, %	
material	hematite	maghemite	hematite	maghemite	hematite	maghemite
Fe_2O_3-COM		100		20		
Fe_2O_3-OXL	79	21	17	17	76.1	23.9
S-Fe_2O_3-OXL	65	35	14	19	56.4	43.6
S-Fe_2O_3-SHX			8	4		

https://doi.org/10.1021/acsaem.2c02123
ACS Appl. Energy Mater. 2022, 5, 13439−13451

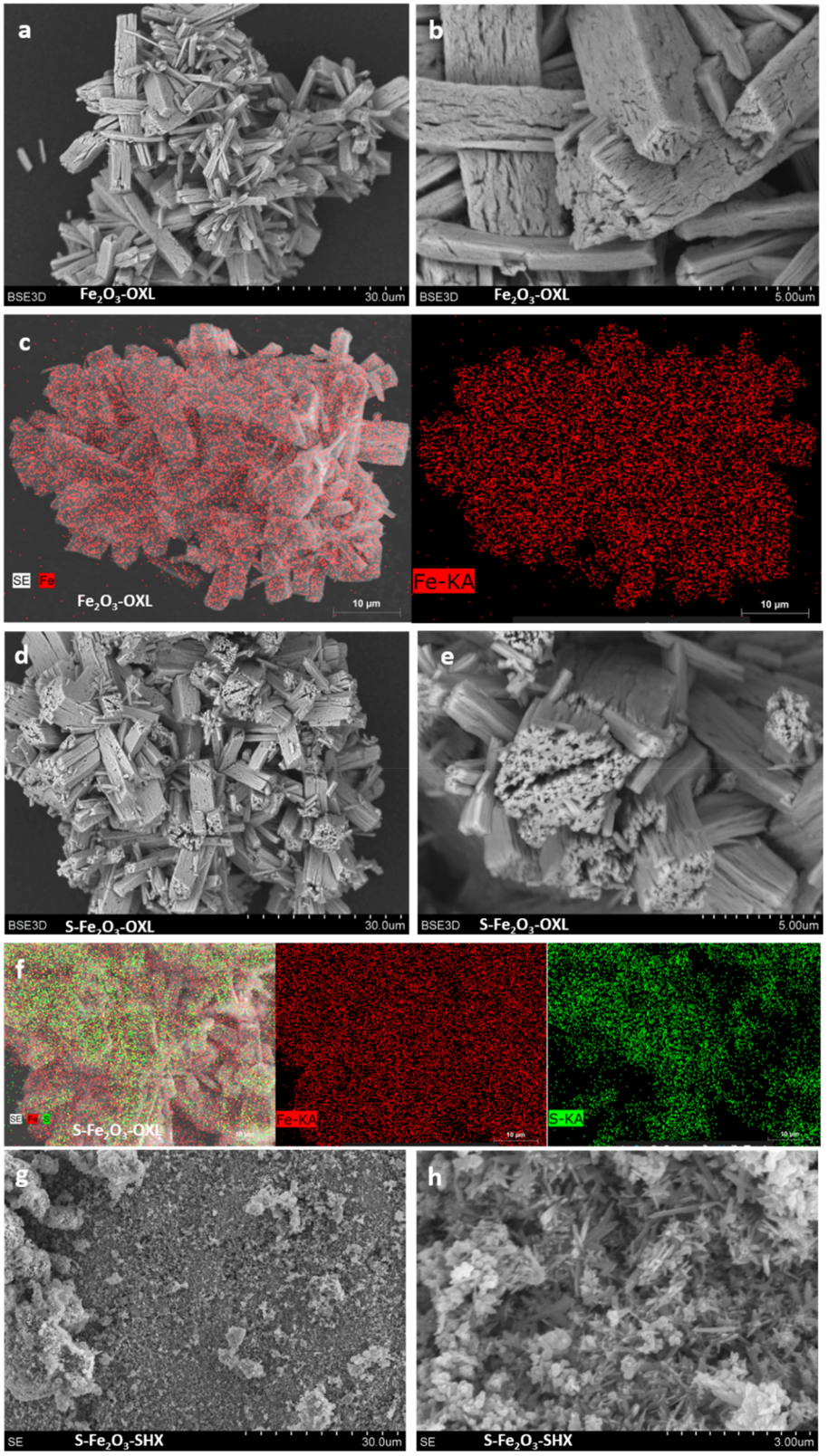

Figure 3. continued

https://doi.org/10.1021/acsaem.2c02123
ACS Appl. Energy Mater. 2022, 5, 13439−13451

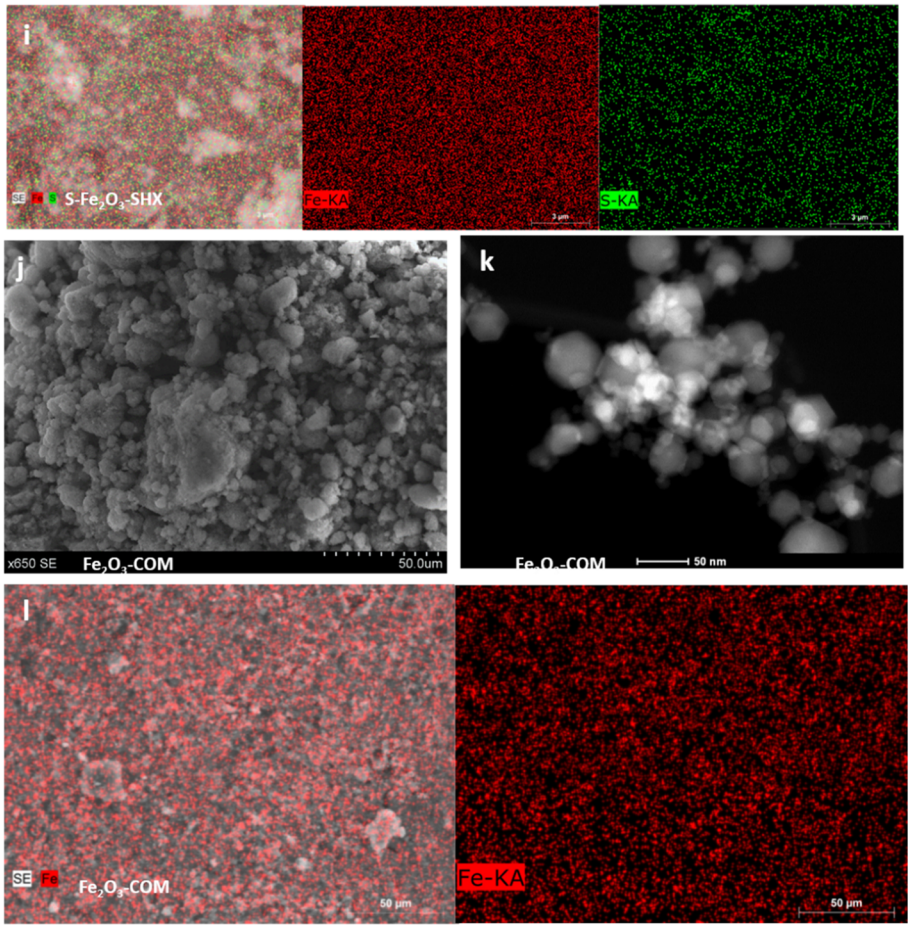

Figure 3. Micrographs at low (left) and high (right) magnification and EDX mapping for (a–c) Fe_2O_3-OXL, (d–f) S-Fe_2O_3-OXL, (g–i) S-Fe_2O_3-SHX, (j–l) Fe_2O_3-COM.

S-Fe_2O_3-SHX could not be fitted properly; hence no phase proportion is provided from these data and the crystallite size can only be estimated as 4–8 nm from the average width of some reflections.

According to previous studies, maghemite transition to hematite starts at around 320 °C for pure iron oxides and around 450 °C and at low rates for iron oxides with impurities,[37] which is a sign that impurities (such as sulfur, in this case) stabilize maghemite and, hence, promote its formation. Also, previous works show that hematite is obtained when calcining hydrated iron oxalates in air at around 400 °C.[38] In the present study, sulfur seems to promote the formation of maghemite upon iron oxalate calcination, as can be inferred from the fact that S-Fe_2O_3-OXL has a lower fraction of hematite than Fe_2O_3-OXL, as was also observed by MS. In addition, it has been reported that hematite is obtained from hydrothermal treatment of $FeSO_4$ with bases.[39]

The average crystal sizes (calculated from Scherrer's formula) are between 4 and 20 nm (Table 2). Fe_2O_3-COM, Fe_2O_3-OXL, and S-Fe_2O_3-OXL, have similar average crystal size, whereas for S-Fe_2O_3-SHX crystal size is considerably lower. The small size of particles and large area are also important to provide good contact between the carbon and the metal oxide phase, which is crucial to reduce the ohmic overpotential. Like what is observed in XPS, no sulfide crystal phases are observed in XRD. However, some peaks are appreciated which could correspond to sulfate phases (green marks in Figure S3). This is another evidence suggesting that there is no sulfide in the samples and that all the sulfur is in the form of sulfate groups.

Figure S4a,b in the Supporting Information shows the FTIR spectra for the different iron oxides, evidencing notorious differences between samples. FTIR results confirm XRD identification of phases (Figure S4). Besides, for the sulfur modified sample obtained from oxalic acid, the FTIR analysis reveals the presence of adsorbed sulfate groups, which is in concordance with the greater amount of sulfur observed in the surface of this sample by XPS. Gotic et al.[33] also described the presence of adsorbed sulfates on iron oxides obtained at acidic pH values, as is the case for S-Fe_2O_3-OXL.

3.1.3. Textural Properties. All the iron oxides show a type-IV adsorption–desorption isotherm (see Figure S5 in the Supporting Information), characteristic of mesoporous materials, and surface areas between 30 and 55 m^2/g (see Table S2), with porosity values around 50% and large mesopores (~15 nm) that may help accommodate the volume changes of the electrodes upon cycling.

3.1.4. Morphology. Figure 3 shows the SEM micrographs at different magnifications. Both Fe_2O_3-OXL (Figure 3a and Figure 3b) and S-Fe_2O_3-OXL (Figure 3d and Figure 3e) consist of agglomerates of parallelepipeds of around 5 μm of average transversal length made of iron oxide crystallites. These structures show irregularities (Figure 3a–f), cracks, and fissures, which are formed during the thermal decomposition of oxalate ions.[23] Iron oxide S-Fe_2O_3-SHX has a completely different morphology. At low magnifications (Figure 3g) it

https://doi.org/10.1021/acsaem.2c02123
ACS Appl. Energy Mater. 2022, 5, 13439–13451

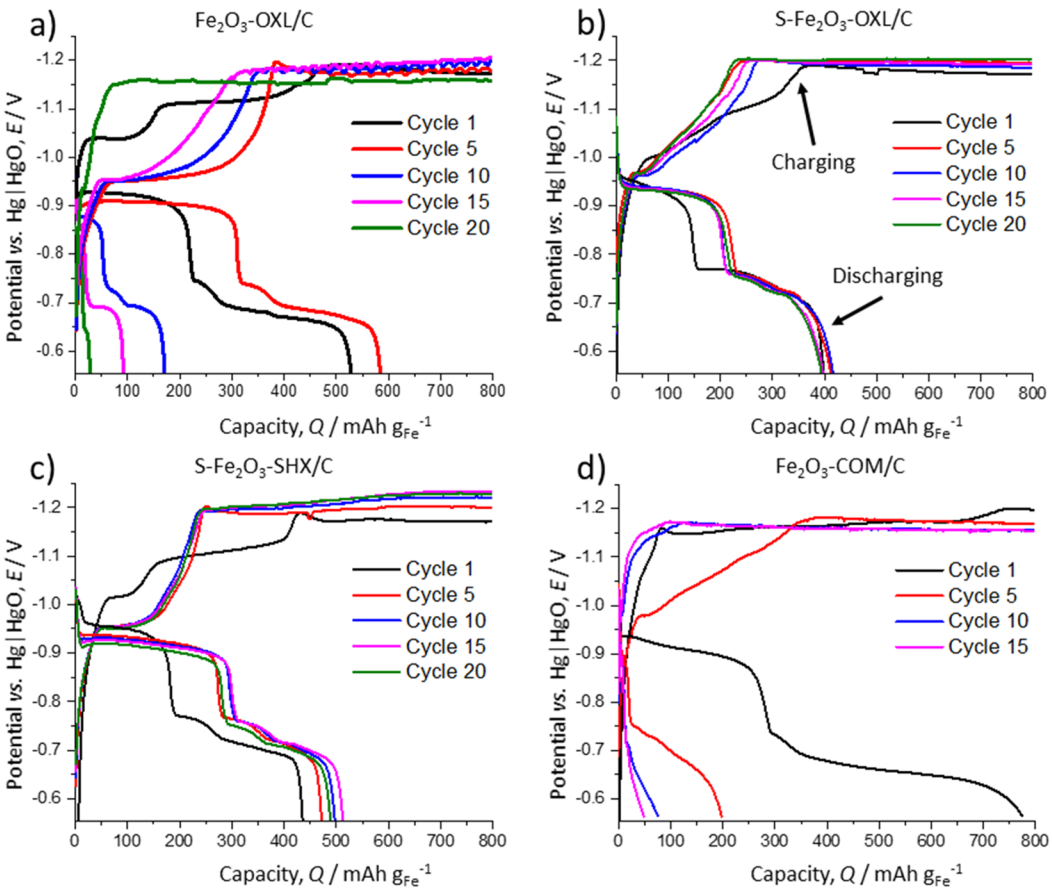

Figure 4. Charge−discharge cycles of the electrodes manufactured with (a) Fe_2O_3-OXL/C, (b) S- Fe_2O_3-OXL/C, (c) S- Fe_2O_3-SHX/C, and (d) Fe_2O_3-COM/C. Charge rate, 0.4 C; discharge rate, 0.2 C.

looks like a compact irregular material, while zooming in Figure 3h lets us appreciate a mixture of ball-like and needle-like shape of the particles. The mesoporosity observed for this material is a consequence of the spaces between these small structures. The SEM image of Fe_2O_3-COM, Figure 3j, shows it has a blackberry-like morphology, consisting of aggregates of thousands of smaller particles. The STEM image (Figure 3k) shows that this material is composed of nanometric regular polyhedron particles. According to the manufacturer, the maximum diameter of these particles is 50 nm. Indeed, it can be observed that the size of the Fe_2O_3 particles ranges from approximately 10 to 50 nm.

EDX mapping was performed to evaluate the distribution of both iron and sulfur on the obtained materials. Fe_2O_3-OXL (Figure 3c) and Fe_2O_3-COM (Figure 3l) present a homogeneous distribution of iron, without any trace of sulfur, whereas S-Fe_2O_3-OXL (Figure 3f) and S-Fe_2O_3-SHX (Figure 3i) present a proper distribution of both iron and sulfur. This means that the sulfur present in the sulfur-modified materials comes from the thiosulfate added in the synthesis and not from the iron(II) sulfate employed as iron precursor. As can be seen in Figure 3f and Figure 3i, sulfur is well dispersed over the iron particles, suggesting a homogeneous mixture between iron oxide and sulfate phases or sulfur species adsorbed over the entire iron oxide surface. Additionally, STEM-EDS analyses were carried out to corroborate that sulfur was present along all of the iron particles. Indeed, as seen in Figure S6, there is presence of sulfur in every iron crystallite, in both S-Fe_2O_3-OXL and S-Fe_2O_3-SHX.

3.2. Electrochemical Characterization. *3.2.1. Discharge Capacities.* The four materials were characterized in a three-electrode cell to determine their discharge capacities and test their stability. The charge−discharge potentiometric curves are shown in Figure 4. A total of 20 cycles (between 70 and 100 h) were performed. Figure 4 indicates the differences in stability for the assessed electrodes, the sulfur-modified iron oxides (S-Fe_2O_3-OXL/C and S-Fe_2O_3-SHX/C) being the most stable ones, which will be deeply discussed in the following section.

During the discharge, a first plateau can be observed at −0.94 V vs Hg|HgO, corresponding to the oxidation of metallic iron to iron(II) hydroxide. As metallic iron, an excellent electrical conductor is oxidized to $Fe(OH)_2$, which is an insulator, the resistance of the system increases, and so the potential reaches more negative values. Studies have shown that the oxidation of metallic iron to iron(II) hydroxide occurs through a dissolved intermediate, $HFeO_2^-$, which then precipitates as crystallite particles, increasing the surface roughness.[40−43] When all the crystallization sites are covered (at low overpotential), an insulating layer is formed. When all the remaining iron atoms are covered by the insulating layer, the overpotential increases and the inner atoms oxidize at potentials where the second discharge step also occurs. The second discharge plateau can be divided into two smaller plateaus, suggesting the second discharge step is composed by two reactions: the oxidation of iron(II) hydroxide to magnetite, and then the oxidation of magnetite to iron(III) oxyhydroxide, as can be inferred from the post-mortem XRD analysis (Figure S7).

https://doi.org/10.1021/acsaem.2c02123
ACS Appl. Energy Mater. 2022, 5, 13439−13451

Figure 5 shows the maximum discharge capacity (black bar) reached by the different iron anodes tested during 20 cycles,

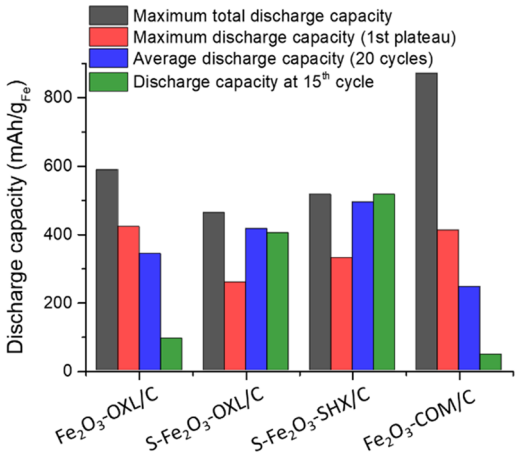

Figure 5. Discharge capacity values for each material: max = best discharge capacity of all cycles, 15th cycle = discharge capacity at 15th cycle; max first step = maximum discharge capacity at −0.75 V vs Hg|HgO. Charge rate: 0.4 C. Discharge rate: 0.2 C.

along with the maximum discharge capacity obtained at the first plateau (after the first oxidation reaction, from Fe to $Fe(OH)_2$,) at approximately −0.75 V vs Hg|HgO (blue bar). This value is of interest for the practical application of these electrodes, as the first discharge plateau provides more energy due to its higher electrochemical potential. Figure 5 also presents the average discharge capacity (medium value considering the 20 charge−discharge cycles) and the discharge capacity at the 15th cycle (red bar); these data will be important in the next section. The electrode with the highest capacity, the one prepared with commercial iron(III) oxide nanoparticles, reaches a maximum discharge capacity of 881 mA h g_{Fe}^{-1}, which is almost 70% of the theoretical capacity (considering both discharge steps), that however is not sustained with time (capacity decays to 40 mA h g_{Fe}^{-1} in the 15th cycle). On the other hand, the two composites based on sulfur-modified iron oxides show a maximum capacity ranging from 450 to 500 mA h g_{Fe}^{-1} (superior to current lithium ion-batteries) and a higher stability, retaining most of their maximum capacity. Iron oxides obtained with either oxalic acid (OXL) or sodium hydroxide (SHX) present capacity values at the first plateau from 250 to 420 mA h g_{Fe}^{-1}, in comparison to the commercial composite reaching as high as 400 mA h g_{Fe}^{-1}, but it is not sustained during cycling. In terms of Coulombic efficiencies, the best value is achieved by Fe_2O_3-COM/C, with almost 70% as a maximum, whereas Fe_2O_3-OXL/C shows a sustained 50%.

It is interesting to note that the maximum capacity of the electrodes is not correlated to the surface area or the crystal size of the iron oxides, which is a consequence of the described dissolution−precipitation reaction mechanism; the dissolution of $HFeO_2^-$ exposes new iron atoms that are then oxidized, as was explained above. In fact, Fe_2O_3-COM/C has the highest maximum discharge capacity and the second-to-lowest surface

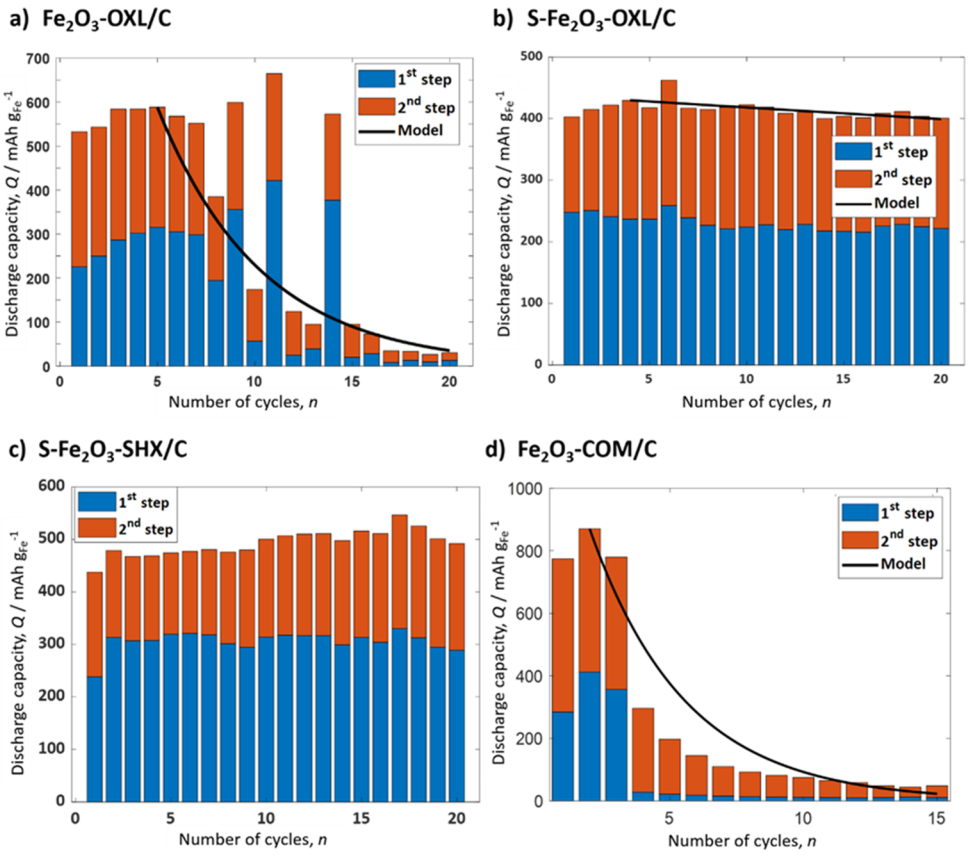

Figure 6. Discharge capacity values for each cycle for the electrodes manufactured with composites (a) Fe_2O_3-OXL/C, (b) S-Fe_2O_3-OXL/C, (c) S-Fe_2O_3-SHX/C, and (d) Fe_2O_3-COM/C. Charge rate: 0.4 C. Discharge rate: 0.2 C. Black line corresponds to the model adjusting the capacity fading with the cycles.

https://doi.org/10.1021/acsaem.2c02123
ACS Appl. Energy Mater. 2022, 5, 13439−13451

area of all the samples (Table S2), showing similar crystal sizes when compared to iron oxides obtained from oxalate precipitation (Table 2). The crystalline phases also do not behave as reported by Lee et al.,[44] with S-Fe_2O_3-OXL/C showing a much more stable performance than Fe_2O_3-OXL/C, even though they are composed of 44% and 24% maghemite, respectively (Table 2). In fact, in the cited article, maghemite electrodes do not reach capacities higher than 80 mA h g_{Fe}^{-1}, while in the present work the 100% maghemite electrode achieves more than 10 times that amount, although for only three cycles.

3.2.2. Stability of the Electrodes. Another information obtained from the charge−discharge cycles was the mid-term stability in operation, i.e., how fast the discharge capacity was lost during repeated cycling. Figure 6 shows that as the electrode charges and discharges, the discharge capacity increases for the first cycles, which is known as the formation period. In carbonyl−iron electrodes, the formation period can last from 20 up to 200 cycles,[22,24,26,45] while in nanometric iron oxide electrodes it can take only a few cycles or even none,[24,46] as is the case of our electrodes. The authors attribute this to the combination of sufficient surface area and small particle size of our iron oxides. After the formation period, the discharge capacity slowly decreases but not at the same rate for all materials. Both Fe_2O_3-OXL/C (Figure 6a) and Fe_2O_3-COM/C (Figure 6d), the latter with the highest maximum discharge capacity, quickly deactivate and lose capacity upon cycling. On the other hand, sulfur-modified iron oxides, namely, S-Fe_2O_3-OXL/C (Figure 6b) and S-Fe_2O_3-SHX/C (Figure 6c), present a very stable behavior upon cycling, barely losing discharge capacity with time. To elucidate the mechanism of deactivation and compare the different iron−carbon composites, a mathematical model was developed and adjusted to the capacity of the composites over the cycles. A full description can be found in the Supporting Information. The black line corresponds to the model adjusting the capacity fading with the cycles, which will be discussed ahead.

The mechanism by which the iron electrodes deactivate is still under discussion. Most authors propose that deactivation is due to the passivation of the electrode, i.e., the repetitive formation and dissolution of an insulating layer of $Fe(OH)_2$ over the iron atoms.[47−49] When this layer reaches certain thickness, due to the inefficiency of the dissolution (charge process), the resistance increases and subsequently so does the overpotential, up to the limit where it is practically impossible to reduce the iron(II) hydroxide to iron at reasonable working potentials. Another hypothesis for the loss of capacity of iron electrodes regards the plugging of the pores[47] (which also causes an ohmic loss of potential) and the loss of electroactive material. The plugging effect is significant mainly because of the increase in molar volume during the discharge, as the oxidation products of iron are much less dense than metallic iron. The volume change of iron after discharging can be clearly observed by SEM in Figure S8, showing an increase of the size of the iron oxide particles upon cycling. The hypothesis of material loss during the cycling was studied by Kitamura et al.[50] and by Figueredo-Rodríguez et al.,[16] who observed a structural change in the iron particles after 20 cycles and also some damage due to gas evolution. During our experiments, we were able to see that material dropped from the electrode into the electrolyte and settled at the bottom of the cell. This effect was stronger in the electrodes manufactured with nonmodified iron oxide and could be caused by mechanical stress applied by hydrogen bubbles formed within the electrode, which indicates the importance of a proper distribution of the inhibiting HER elements within the structure of the electrode

To elucidate the mechanism of deactivation and compare the different iron−carbon composites, a mathematical model was developed and adjusted to the capacity of the composites over the cycles. A full description can be found in the Supporting Information. The assumptions made for this model, described in eq 2, were the following: (i) the electrodes take a few cycles to activate, in which their capacity increases, and after that, (ii) the capacity decreases exponentially down to zero after infinite cycles.

$$Q = Q_i \cdot f^{n-i} \tag{2}$$

where Q is the discharge capacity of the electrode at a cycle n, i is the number of the first cycle after activation, Q_i is the discharge capacity of the electrode in that cycle, and f is a factor that indicates how ideally the electrode works or how fast it deactivates. In an electrode that does not lose capacity at all, f would be equal to 1 ($f = 1$). The electrode manufactured with Fe_2O_3-OXL/C (Figure 6a) needs four cycles to activate, while S- Fe_2O_3-OXL/C (Figure 6b) needs three. After that, the discharge capacity of Fe_2O_3-OXL/C (Figure 6a) rapidly decreases, almost monotonically, except for the 9, 11, and 14 cycles, where a sharp but not sustained increase in the capacity is observed. The most plausible explanation for this phenomenon is that hydrogen bubbles delaminate the electrode and break the material, creating new pores and exposing new active surface. Nevertheless, those pores are quickly plugged again by inactive material. In this case, we believe that both passivation and plugging of the pores take place at the same time, which would sustain the previous explanation. The f factor calculated for this electrode is 0.829.

The electrode manufactured with the S-Fe_2O_3-OXL/C composite shows a very steady behavior (Figure 6b). From cycle 4 and on, the discharge capacity slowly decreases at a pace less than 0.5%/cycle (f = 0.995). Comparing the properties of Fe_2O_3-OXL/C and S-Fe_2O_3-OXL/C, the two oxides used for these composites present close values of surface area, porosity, pore size, and crystal size. The only differences are the absence or presence of sulfur and the ratio of maghemite to hematite. Nevertheless, the Fe_2O_3-COM/C composite is exclusively formed by maghemite and has a very poor performance in terms of stability (Figure 6d), so the most plausible explanation is that sulfur is indeed preventing passivation in S-Fe_2O_3-OXL/C.

For the two other composites (S-Fe_2O_3-SHX/C, Figure 6c and Fe_2O_3-COM/C, Figure 6d), the proposed model does not fit the data as well as it does with the oxalate-based iron oxide composites. S-Fe_2O_3-SHX/C (Figure 6c) shows a different behavior. During the first 20 cycles, the tendency is that its capacity increases, indicating that the material is still not fully activated. This behavior will be deeply discussed in the next section. However, both S-Fe_2O_3-SHX/C and S-Fe_2O_3-OXL/C, present a more stable performance than the electrodes that did not contain sulfur.

For the Fe_2O_3-COM/C electrode (Figure 6d), the first three cycles have an exceptionally high discharge capacity, which immediately decays to less than half in the following cycles. As seen in Table S2, the oxide in which this composite is based has the lowest surface area and porosity of all, which makes it prone to pore plugging. As the cycling advances, the electrode

https://doi.org/10.1021/acsaem.2c02123
ACS Appl. Energy Mater. 2022, 5, 13439−13451

loses capacity especially in the first discharge plateau. This is a signal that iron hydroxide is not reducing to metallic iron, which supports the hypothesis of passivation by insulating layer.

According to several studies,[14,51,52] sulfur prevents passivation of iron electrodes when present as iron sulfide or bismuth sulfide. Some new studies have shown that adding elemental sulfur to the electrodes can have a strong impact in preventing passivation. As Shangguan et al. showed by XRD analysis,[20] sublimated sulfur can reduce to S^{2-}, which dissolves into the electrolyte and then is adsorbed by iron particles, forming FeS and other nonstoichiometric iron sulfides. In this case, the post-mortem XRD analysis was inconclusive (see Figure S7 in the Supporting Information), but XPS shows that, indeed, sulfate present in the fresh sulfur-modified iron oxides reduces to species that, according to the binding energies, could be S or

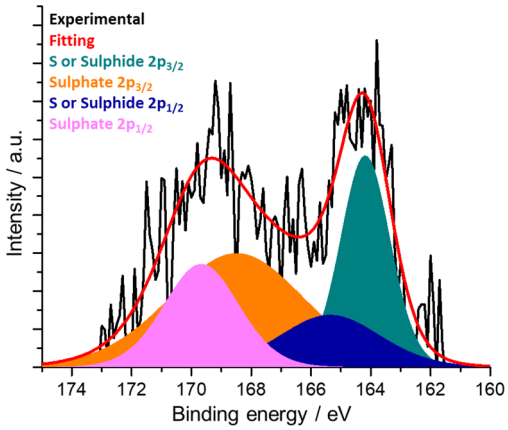

Figure 7. XPS post-mortem spectrum of the composite S-Fe_2O_3-OXL/C in the sulfur 2p orbital region.

S^{2-} (Figure 7). Equations 3−5 show the path that sulfur can follow in alkaline media to reduce from sulfate to sulfide:

$$SO_4^{2-} + H_2O + 2e^- \rightarrow SO_3^{2-} + 2OH^-; \quad E^0 = -0.93\ \text{V vs SHE} \tag{3}$$

$$SO_3^{2-} + 3H_2O + 4e^- \rightarrow S^0 + 6OH^-; \quad E^0 = -0.66\ \text{V vs SHE} \tag{4}$$

$$S^0 + 2e^- \rightarrow S^{2-}; \quad E^0 = -0.48\ \text{V vs SHE} \tag{5}$$

The reduction from sulfate to sulfite (eq 3) takes place at a more negative potential than the reduction of iron(II) hydroxide. Nevertheless, −0.93 V vs SHE is equivalent to −1.03 V vs Hg|HgO, so the standard potential for this reaction is less negative than the potentials at which the system is working. Once the sulfate is reduced to sulfite, it should rapidly reduce to sulfur and then sulfide, as the standard equilibrium potentials for these reactions (eqs 4 and 5) are much less negative than those at the working electrode. This explains why no sulfite peaks are observed in Figure 7 being highly probable that the peak at 163.9 eV corresponds to sulfide. As has been demonstrated in previous literature,[53,54] sulfide ions react with iron(II) hydroxide to form the much more conductive iron(II) sulfide and other conductive iron sulfide species.

More evidence for the passivation preventing effect of sulfur can be found in the fresh and post-mortem electrode SEM images and EDX analyses (Figure S9). It can be seen that the iron crystal agglomerates grow after 20 cycles, and this effect is more evident in electrode Fe_2O_3-COM/C than in S-Fe_2O_3-OXL/C, consistent with the higher maximum discharge capacity of the first electrode over the latter. Especially interesting are the EDX analyses of the electrodes before and after cycling. Before cycling, it can be seen that the electrode Fe_2O_3-COM/C has a high amount of oxygen in the iron particle, which means the iron is oxidized. After 20 cycles, the amount of oxygen detected by EDX is considerably lower, which is a signal that only a small amount of the iron was able to oxidize. This is consistent with the electrode being passivated by a layer of iron(II) hydroxide over the metallic particles which does not allow the bulk of them to react. In electrode S-Fe_2O_3-OXL/C, the height of the oxygen peak in the EDX scan relative to the iron peak is almost the same in the fresh electrode and in the electrode cycled 20 times, showing that the passivation of iron in this electrode is much slower.

Electrodes based on sulfur-modified iron oxides were subjected to extended cycling (60 cycles, approximately 200−280 h). Further details on these experiments can be found in the Supporting Information.

Operation variables were also investigated to elucidate the conditions that could maximize the performance of the system. Electrodes manufactured with S-Fe_2O_3-OXL/C were cycled at higher C-rates (i.e., higher charging and discharging currents). The detailed information can be found in the Supporting Information.

4. CONCLUSIONS

We prepared mesoporous sulfur-modified iron oxides, which were mixed with commercial carbon (Vulcan XC-72R) to form Fe/C composites and tested as negative electrodes for iron−air batteries. Unlike most previous negative iron electrodes, the sulfur was directly produced as a composite material with the iron rather than being added by simple physical mixing. The synthesis of the iron oxide was facile, and it could be prepared in a scalable manner at low cost. The following paragraphs will summarize the significant findings that were observed.

The discharge capacities of the iron electrodes ranged from 400 to 850 mA h g_{Fe}^{-1}; although the iron electrodes with sulfur modification had lower capacities than those without, the cycle stability was vastly improved by the addition of sulfur. The positive effect of sulfur outstrips any the effect of any other feature such as phase composition or particle size.

The oxalate-precipitated sulfur-modified iron oxide (S-Fe_2O_3-OXL) proved to be a superior material for long-term cycling. The exponential decay in the discharge capacity was much lower such that it was able to maintain 95% of its initial capacity after 20 cycles (∼100 h) at 0.4 C (charge) to 0.2 C (discharge) rates. It even maintained 65% discharge capacity after 500 h of operation. In comparison, the same material prepared without sulfur almost completely deactivated after 20 cycles and commercial iron(III) oxide nanopowder deactivated after 15 cycles.

The synthesis method allowed uniform distribution of sulfur on the surface of the iron oxide. The high degree of physical contact between the iron and sulfur phases improves the electrochemical stability of the electrode by enhancing the suppression of hydrogen evolution and passivation (as demonstrated by the improved Coulombic efficiency).

https://doi.org/10.1021/acsaem.2c02123
ACS Appl. Energy Mater. 2022, 5, 13439−13451

The mechanism by which prevention of passivation occurs is reduction of sulfate species into sulfide under the operating conditions, which then decreases the potential for hydrogen evolution at the electrode surface area.

Finally, we demonstrated control of the charge and discharge rates to enhance different properties. Lower charge and discharge rates resulted in the operation of the electrodes being more stable (less than 0.5% capacity loss per cycle), and by increasing the rates, we could increase the Coulombic efficiency of the process from 35% up to 65%.

The results obtained from this research present a useful tool for manufacture and operation of iron electrodes in an iron−air battery. In order to achieve the highest Coulombic efficiency, a charging rate of 0.8 C and a charge time of 50 min are recommended. A lower charge rate, 0.4 C, is recommended to extend the useful life of the electrode.

■ ASSOCIATED CONTENT

Supporting Information

The Supporting Information is available free of charge at https://pubs.acs.org/doi/10.1021/acsaem.2c02123.

Complementary physical−chemical and electrochemical characterizations; scheme and photograph of the electrochemical cell (PDF)

■ AUTHOR INFORMATION

Corresponding Authors

Cinthia Alegre − *Instituto de Carboquímica, Consejo Superior de Investigaciones Científicas, 50018 Zaragoza, Spain;* orcid.org/0000-0003-1221-6311; Email: cinthia@icb.csic.es

María Jesús Lázaro − *Instituto de Carboquímica, Consejo Superior de Investigaciones Científicas, 50018 Zaragoza, Spain*; Email: mlazaro@icb.csic.es

Authors

Nicolás Villanueva − *Instituto de Carboquímica, Consejo Superior de Investigaciones Científicas, 50018 Zaragoza, Spain*

Javier Rubin − *Instituto de Nanociencia y Materiales de Aragón (INMA), CSIC-Universidad de Zaragoza, 50009 Zaragoza, Spain; Departamento de Ciencia y Tecnología de Materiales y Fluidos, Universidad de Zaragoza, 50018 Zaragoza, Spain;* orcid.org/0000-0003-1029-3751

Horacio A. Figueredo-Rodríguez − *Electrochemical Engineering Laboratory, Energy Technology Research Group, Faculty of Engineering and Physical Sciences, Southampton University, Southampton SO17 1BJ, U.K.;* Present Address: Escuela de Ingeniería y Ciencias, Tecnológico de Monterrey, CCM, 14380, CDMX, México; orcid.org/0000-0003-2892-6780

Rachel D. McKerracher − *Electrochemical Engineering Laboratory, Energy Technology Research Group, Faculty of Engineering and Physical Sciences, Southampton University, Southampton SO17 1BJ, U.K.*

Carlos Ponce de León − *Electrochemical Engineering Laboratory, Energy Technology Research Group, Faculty of Engineering and Physical Sciences, Southampton University, Southampton SO17 1BJ, U.K.*

Complete contact information is available at: https://pubs.acs.org/10.1021/acsaem.2c02123

Author Contributions

The manuscript was written through contributions of all authors. All authors have given approval to the final version of the manuscript.

Notes

The authors declare no competing financial interest.

■ ACKNOWLEDGMENTS

The authors acknowledge the financial support from the Aragón Government to the Fuel Conversion Group (Grant T06-20R). C.A. also acknowledges MICINN for her Juan de la Cierva Contract IJCI-2017-32354. N.V. acknowledges the Aragón Government for his predoctoral contract and Ibercaja and Erasmus programs for the funding of his research stay in the University of Southampton in July 2018. The microscopy works have been conducted in the Laboratorio de Microscopias Avanzadas at Instituto de Nanociencia de Aragón—Universidad de Zaragoza. The authors acknowledge the LMA-INA for offering access to their instruments and expertise. The authors also acknowledge the use of Servicio General de Apoyo a la Investigación—SAI, Universidad de Zaragoza.

■ REFERENCES

(1) Masson-Delmotte, V. P.; Zhai, H.-O.; Pörtner, D.; Roberts, J.; Skea, P. R.; Shukla, A. P. W.; Moufouma-Okia, C.; Péan, R.; Pidcock, S.; Connors, J.B. R.; Matthews, Y.; Chen, X.; Zhou, M. I.; Gomis, E.; Lonnoy, T.; Maycock, M.; Tignor, T. W.Global Warming of 1.5°C. An IPCC Special Report on the Impacts of Global Warming of 1.5°C above Pre-Industrial Levels and Related Global Greenhouse Gas Emission Pathways, in the Context of Strengthening the Global Response to the Threat of Climate Change. Cambridge University Press: Cambridge, U.K., 2018; 616 pp, 2 (October); pp 17−20.

(2) Solaymani, S. CO2 Emissions Patterns in 7 Top Carbon Emitter Economies: The Case of Transport Sector. *Energy* **2019**, *168*, 989−1001.

(3) Metzler, D.; Humpe, A.; Gössling, S. Is It Time to Abolish Company Car Benefits? An Analysis of Transport Behaviour in Germany and Implications for Climate Change. *Clim. Policy* **2019**, *19* (5), 542−555.

(4) Gandoman, F. H.; Jaguemont, J.; Goutam, S.; Gopalakrishnan, R.; Firouz, Y.; Kalogiannis, T.; Omar, N.; Van Mierlo, J. Concept of Reliability and Safety Assessment of Lithium-Ion Batteries in Electric Vehicles: Basics, Progress, and Challenges. *Appl. Energy* **2019**, *251*, 113343.

(5) Li, M.; Lu, J.; Chen, Z.; Amine, K. 30 Years of Lithium-Ion Batteries. *Adv. Mater.* **2018**, *30* (33), 1800561.

(6) Balakrishnan, P. G.; Ramesh, R.; Prem Kumar, T. Safety Mechanisms in Lithium-Ion Batteries. *J. Power Sources* **2006**, *155* (2), 401−414.

(7) Wang, C.; Yu, Y.; Niu, J.; Liu, Y.; Bridges, D.; Liu, X.; Pooran, J.; Zhang, Y.; Hu, A. Recent Progress of Metal-Air Batteries-A Mini Review. *Appl. Sci.* **2019**, *9* (14), 2787.

(8) Yaroshevsky, A. A. Abundances of Chemical Elements in the Earth's Crust. *Geochemistry Int.* **2006**, *44* (1), 48−55.

(9) Weinrich, H.; Durmus, Y. E.; Tempel, H.; Kungl, H.; Eichel, R.-A. A. Silicon and Iron as Resource-Efficient Anode Materials for Ambient-Temperature Metal-Air Batteries: A Review. *Materials* **2019**, *12* (13), 2134.

(10) McKerracher, R. D.; Ponce de Leon, C.; Wills, R. G. A.; Shah, A. A.; Walsh, F. C. A Review of the Iron-Air Secondary Battery for Energy Storage. *ChemPlusChem* **2015**, *80* (2), 323−335.

(11) Malkhandi, S.; Yang, B.; Manohar, A. K.; Prakash, G. K. S.; Narayanan, S. R. Self-Assembled Monolayers of n-Alkanethiols Suppress Hydrogen Evolution and Increase the Efficiency of Rechargeable Iron Battery Electrodes. *J. Am. Chem. Soc.* **2013**, *135* (1), 347−353.

(12) McKerracher, R. D.; Figueredo-Rodriguez, H. A.; Alegre, C.; Aricò, A. S.; Baglio, V.; Ponce de León, C. Improving the Stability and Discharge Capacity of Nanostructured Fe2O3/C Anodes for Iron-Air Batteries and Investigation of 1-Octhanethiol as an Electrolyte Additive. *Electrochim. Acta* **2019**, *318*, 625−634.
(13) Posada, J. O. G.; Hall, P. J. Controlling Hydrogen Evolution on Iron Electrodes. *Int. J. Hydrogen Energy* **2016**, *41* (45), 20807−20817.
(14) Manohar, A. K.; Yang, C.; Malkhandi, S.; Prakash, G. K. S.; Narayanan, S. R. Enhancing the Performance of the Rechargeable Iron Electrode in Alkaline Batteries with Bismuth Oxide and Iron Sulfide Additives. *J. Electrochem. Soc.* **2013**, *160* (11), A2078−A2084.
(15) Manohar, A. K.; Malkhandi, S.; Yang, B.; Yang, C.; Surya Prakash, G. K.; Narayanan, S. R. A High-Performance Rechargeable Iron Electrode for Large-Scale Battery-Based Energy Storage. *J. Electrochem. Soc.* **2012**, *159*, A1209−A1214.
(16) Figueredo-Rodríguez, H. A.; McKerracher, R. D.; Insausti, M.; Luis, A. G.; de León, C. P.; Alegre, C.; Baglio, V.; Aricò, A. S.; Walsh, F. C. A Rechargeable, Aqueous Iron Air Battery with Nanostructured Electrodes Capable of High Energy Density Operation. *J. Electrochem. Soc.* **2017**, *164* (6), A1148−A1157.
(17) Vijayamohanan, K.; Balasubramanian, T. S.; Shukla, A. K. Rechargeable Alkaline Iron Electrodes. *J. Power Sources* **1991**, *34* (3), 269−285.
(18) Posada, J. O. G.; Hall, P. J. The Effect of Electrolyte Additives on the Performance of Iron Based Anodes for NiFe Cells. *J. Electrochem. Soc.* **2015**, *162* (10), A2036−A2043.
(19) Keersemaker, M.Critical Raw Materials. In *Suriname Revisited: Economic Potential of Its Mineral Resources*; Springer, Cham, Switzerland, 2020; pp 69−82, DOI: 10.1007/978-3-030-40268-6_9.
(20) Shangguan, E.; Fu, S.; Wu, C.; Cai, X.; Li, J.; Chang, Z.; Wang, Z.; Li, Q. Sublimed Sulfur Powders as Novel Effective Anode Additives to Enhance the High-Rate Capabilities of Iron Anodes for Advanced Iron-Based Secondary Batteries. *Electrochim. Acta* **2019**, *301*, 162−173.
(21) Deng, J.; Ye, C.; Cai, A.; Huai, L.; Zhou, S.; Dong, F.; Li, X.; Ma, X. S-Doping α-Fe2O3 Induced Efficient Electron-Hole Separation for Enhanced Persulfate Activation toward Carbamazepine Oxidation: Experimental and DFT Study. *Chem. Eng. J.* **2021**, *420* (P1), 129863.
(22) Yang, C.; Manohar, A. K.; Narayanan, S. R. A High-Performance Sintered Iron Electrode for Rechargeable Alkaline Batteries to Enable Large-Scale Energy Storage. *J. Electrochem. Soc.* **2017**, *164* (2), A418−A429.
(23) Du, J.; Bao, J.; Fu, X.; Lu, C.; Kim, S. H. Mesoporous Sulfur-Modified Iron Oxide as an Effective Fenton-like Catalyst for Degradation of Bisphenol A. *Appl. Catal. B Environ.* **2016**, *184*, 132−141.
(24) Rodríguez, H. A. F.; McKerracher, R. D.; de León, C. P.; Walsh, F. C. Improvement of Negative Electrodes for Iron-Air Batteries: Comparison of Different Iron Compounds as Active Materials. *J. Electrochem. Soc.* **2019**, *166* (2), A107−A117.
(25) Balasubramanian, T. S.; Shukla, A. K. Effect of Metal-Sulfide Additives on Charge/Discharge Reactions of the Alkaline Iron Electrode. *J. Power Sources* **1993**, *41* (1−2), 99−105.
(26) Rajan, A. S.; Ravikumar, M. K.; Priolkar, K. R.; Sampath, S.; Shukla, A. K. Carbonyl-Iron Electrodes for Rechargeable-Iron Batteries. *Electrochem. Energy Technol.* **2014**, *1*, 2−9.
(27) Gil Posada, J. O.; Hall, P. J. Post-Hoc Comparisons among Iron Electrode Formulations Based on Bismuth, Bismuth Sulphide, Iron Sulphide, and Potassium Sulphide under Strong Alkaline Conditions. *J. Power Sources* **2014**, *268*, 810−815.
(28) Siriwardane, R. V.; Poston, J. A.; Fisher, E. P.; Shen, M. S.; Miltz, A. L. Decomposition of the Sulfates of Copper, Iron (II), Iron (III), Nickel, and Zinc: XPS, SEM, DRIFTS, XRD, and TGA Study. *Appl. Surf. Sci.* **1999**, *152* (3), 219−236.
(29) Briggs, D. Handbook of X-Ray Photoelectron Spectroscopy C. D. Wanger, W. M., Riggs; L. E., Davis; J., F.; Moulder and G. E. Muilenberg Perkin-Elmer Corp., Physical Electronics Division, Eden Prairie, Minnesota, USA, 1979. 190 Pp. *Surf. Interface Anal.* **1981**, *3* (4), v−v.
(30) Brion, D. Etude Par Spectroscopie de Photoelectrons de La Degradation Superficielle de FeS2, CuFeS2, ZnS et PbS a l'air et Dans l'eau. *Appl. Surf. Sci.* **1980**, *5* (2), 133−152.
(31) Descostes, M.; Mercier, F.; Thromat, N.; Beaucaire, C.; Gautier-Soyer, M. Use of XPS in the Determination of Chemical Environment and Oxidation State of Iron and Sulfur Samples: Constitution of a Data Basis in Binding Energies for Fe and S Reference Compounds and Applications to the Evidence of Surface Species of an Oxidized Py. *Appl. Surf. Sci.* **2000**, *165* (4), 288−302.
(32) Laajalehto, K.; Kartio, I.; Suoninen, E. XPS and SR-XPS Techniques Applied to Sulphide Mineral Surfaces. *Int. J. Miner. Process.* **1997**, *51* (1−4), 163−170.
(33) Gotić, M.; Musić, S. Mössbauer, FT-IR and FE SEM Investigation of Iron Oxides Precipitated from FeSO4 Solutions. *J. Mol. Struct.* **2007**, *834−836*, 445−453.
(34) de Oñate Martínez, J.; Aguila, C. D.; Bertrán, J. F.; Ruíz, E. R.; Vergara, C. P.; Malherbe, R. R. Tribochemical Reactions of Erionite and Na-LTA Zeolites with Fe2 (SO4) 3.5 H2O: A Mössbauer Study. *Hyperfine Interact.* **1992**, *73* (3), 371−375.
(35) Rodriguez-Carvajal, J.FULLPROF: A Program for Rietveld Refinement and Pattern Matching Analysis. In *Satellite Meeting on Powder Diffraction of the XV Congress of the IUCr (Vol. 127)*; IUCr, 1990.
(36) Vandenberghe, R. E.; Barrero, C. A.; Da Costa, G. M.; Van San, E.; De Grave, E. Mössbauer Characterization of Iron Oxides and (Oxy)Hydroxides: The Present State of the Art. *Hyperfine Interact.* **2000**, *126* (1−4), 247−259.
(37) Sidhu, P. S. Transformation of Trace Element-Substituted Maghemite To Hematite. *Clays Clay Miner.* **1988**, *36* (1), 31−38.
(38) Zhou, W.; Tang, K.; Zeng, S.; Qi, Y. Room Temperature Synthesis of Rod-like FeC2O4· 2H2O and Its Transition to Maghemite, Magnetite and Hematite Nanorods through Controlled Thermal Decomposition. *Nanotechnology* **2008**, *19* (6), 065602.
(39) Lian, S.; Wang, E.; Kang, Z.; Bai, Y.; Gao, L.; Jiang, M.; Hu, C.; Xu, L. Synthesis of Magnetite Nanorods and Porous Hematite Nanorods. *Solid State Commun.* **2004**, *129* (8), 485−490.
(40) Weinrich, H.; Come, J.; Tempel, H.; Kungl, H.; Eichel, R. A.; Balke, N. Understanding the Nanoscale Redox-Behavior of Iron-Anodes for Rechargeable Iron-Air Batteries. *Nano Energy* **2017**, *41*, 706−716.
(41) Muller-Zulow, B.; Kipp, S.; Lacmann, R.; Schneeweiss, M.A. Topological Aspects of Iron Corrosion in Alkaline Solution by Means of Scanning Force Microscopy (SFM). *Surf. Sci.* **1994**, *311*, 153−158.
(42) Dražić, D. M.; Hao, C. S. The Anodic Dissolution Process on Active Iron in Alkaline Solutions. *Electrochim. Acta* **1982**, *27* (10), 1409−1415.
(43) Dıez-Pérez, I.; Gorostiza, P.; Sanz, F.; Müller, C. First Stages of Electrochemical Growth of the Passive Film on Iron. *J. Electrochem. Soc.* **2001**, *148* (8), B307.
(44) Lee, D. C.; Lei, D.; Yushin, G. Morphology and Phase Changes in Iron Anodes Affecting Their Capacity and Stability in Rechargeable Alkaline Batteries. *ACS Energy Lett.* **2018**, *3* (4), 794−801.
(45) Weinrich, H.; Gehring, M.; Tempel, H.; Kungl, H.; Eichel, R. A. Impact of the Charging Conditions on the Discharge Performance of Rechargeable Iron-Anodes for Alkaline Iron-Air Batteries. *J. Appl. Electrochem.* **2018**, *48* (4), 451−462.
(46) Kitamura, H.; Zhao, L.; Hang, B. T.; Okada, S.; Yamaki, J. Effect of Binder Materials on Cycling Performance of Fe2O3 Electrodes in Alkaline Solution. *J. Power Sources* **2012**, *208*, 391−396.
(47) Vijayamohanan, K.; Shukla, A. K.; Sathyanarayana, S. Kinetics of Electrode Reactions Occurring on Porous Iron Electrodes in Alkaline Media. *J. Electroanal. Chem.* **1990**, *295* (1−2), 59−70.
(48) Shangguan, E.; Guo, L.; Li, F.; Wang, Q.; Li, J.; Li, Q.; Chang, Z.; Yuan, X. Z. FeS Anchored Reduced Graphene Oxide Nanosheets as Advanced Anode Material with Superior High-Rate Performance for Alkaline Secondary Batteries. *J. Power Sources* **2016**, *327*, 187−195.

(49) Narayanan, S. R. R.; Prakash, G. K. K. S. S.; Manohar, A.; Yang, B.; Malkhandi, S.; Kindler, A. Materials Challenges and Technical Approaches for Realizing Inexpensive and Robust Iron-Air Batteries for Large-Scale Energy Storage. *Solid State Ionics* **2012**, *216*, 105−109.
(50) Kitamura, H.; Zhao, L.; Hang, B. T.; Okada, S.; Yamaki, J. I. Effect of Binder Materials on Cycling Performance of Fe2O3 Electrodes in Alkaline Solution. *J. Power Sources* **2012**, *208*, 391−396.
(51) Yang, J.; Chen, J.; Wang, Z.; Wang, Z.; Zhang, Q.; He, B.; Zhang, T.; Gong, W.; Chen, M.; Qi, M.; Coquet, P.; Shum, P.; Wei, L. High-Capacity Iron-Based Anodes for Aqueous Secondary Nickel-Iron Batteries: Recent Progress and Prospects. *ChemElectroChem* **2021**, *8* (2), 274−290.
(52) Manohar, A. K.; Yang, C.; Narayanan, S. R. The Role of Sulfide Additives in Achieving Long Cycle Life Rechargeable Iron Electrodes in Alkaline Batteries. *J. Electrochem. Soc.* **2015**, *162* (9), A1864−A1872.
(53) Wang, Q.; Wang, Y. Overcoming the Limiting Step of Fe2O3 Reduction via in Situ Sulfide Modification. *ACS Appl. Mater. Interfaces* **2016**, *8* (16), 10334−10342.
(54) Manohar, A. K.; Yang, C.; Narayanan, S. R. The Role of Sulfide Additives in Achieving Long Cycle Life Rechargeable Iron Electrodes in Alkaline Batteries. *J. Electrochem. Soc.* **2015**, *162* (9), A1864−A1872.

https://doi.org/10.1021/acsaem.2c02123
ACS Appl. Energy Mater. 2022, 5, 13439−13451

Supporting information

Iron electrodes based on sulfur-modified iron oxides with enhanced stability for iron-air batteries

Nicolás Villanueva[1], Cinthia Alegre[1,], Javier Rubin[2,3], Horacio A. Figueredo-Rodríguez[4,†], Rachel D. McKerracher[4], Carlos Ponce de León[4], María Jesús Lázaro[1,*]*

[1]Instituto de Carboquímica, Consejo Superior de Investigaciones Científicas. C/. Miguel Luesma Castán, 4, 50018, Zaragoza (Spain)

[2] Instituto de Nanociencia y Materiales de Aragón (INMA), CSIC-Universidad de Zaragoza, 50009, Zaragoza (Spain)

[3] Departamento de Ciencia y Tecnología de Materiales y Fluidos, Universidad de Zaragoza, 50018 Zaragoza (Spain)

[4]Electrochemical Engineering Laboratory, Energy Technology Research Group, Faculty of Engineering and Physical Sciences, Southampton University, Southampton, SO17 1BJ (UK)

[†] Escuela de Ingeniería y Ciencias, Tecnológico de Monterrey, CCM, 14380, CDMX, (México)

***Corresponding authors:** cinthia@icb.csic.es; mlazaro@icb.csic.es

S.1. Experimental details

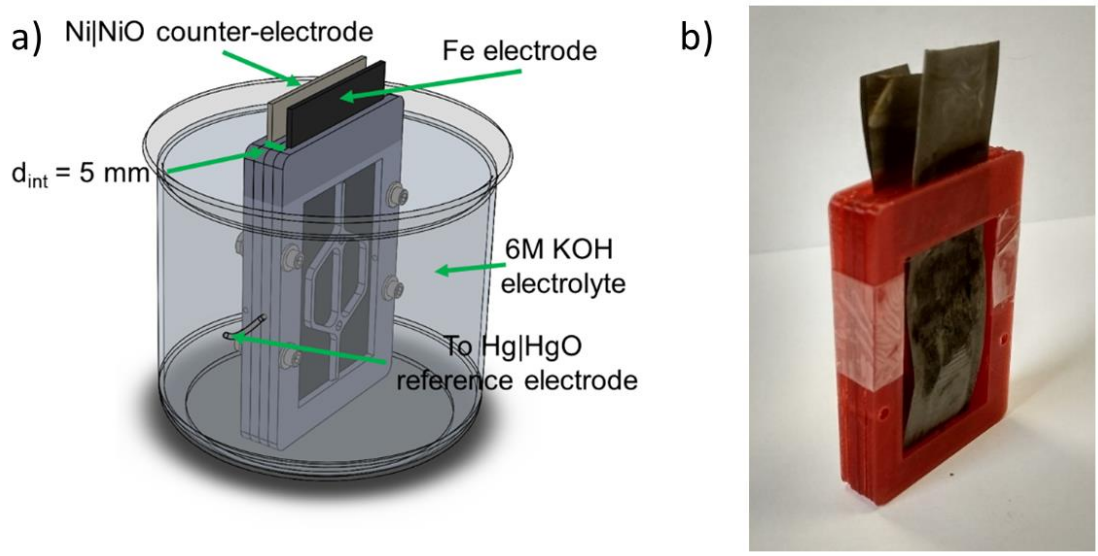

Figure S1. a) Schematic view of the holder employed for the electrochemical tests, b) Image of the holder containing the working electrode and counter electrode.

A scheme and an actual photograph of the electrodes system and cell is shown in **Figure S1**. The reference and counter electrodes are held only 5 mm apart to reduce the electrical resistance in the electrolyte and the overpotential related to it. The reference electrode is connected through a capillary, contacting close to the working electrode.

S.2. Additional physical-chemical characterization

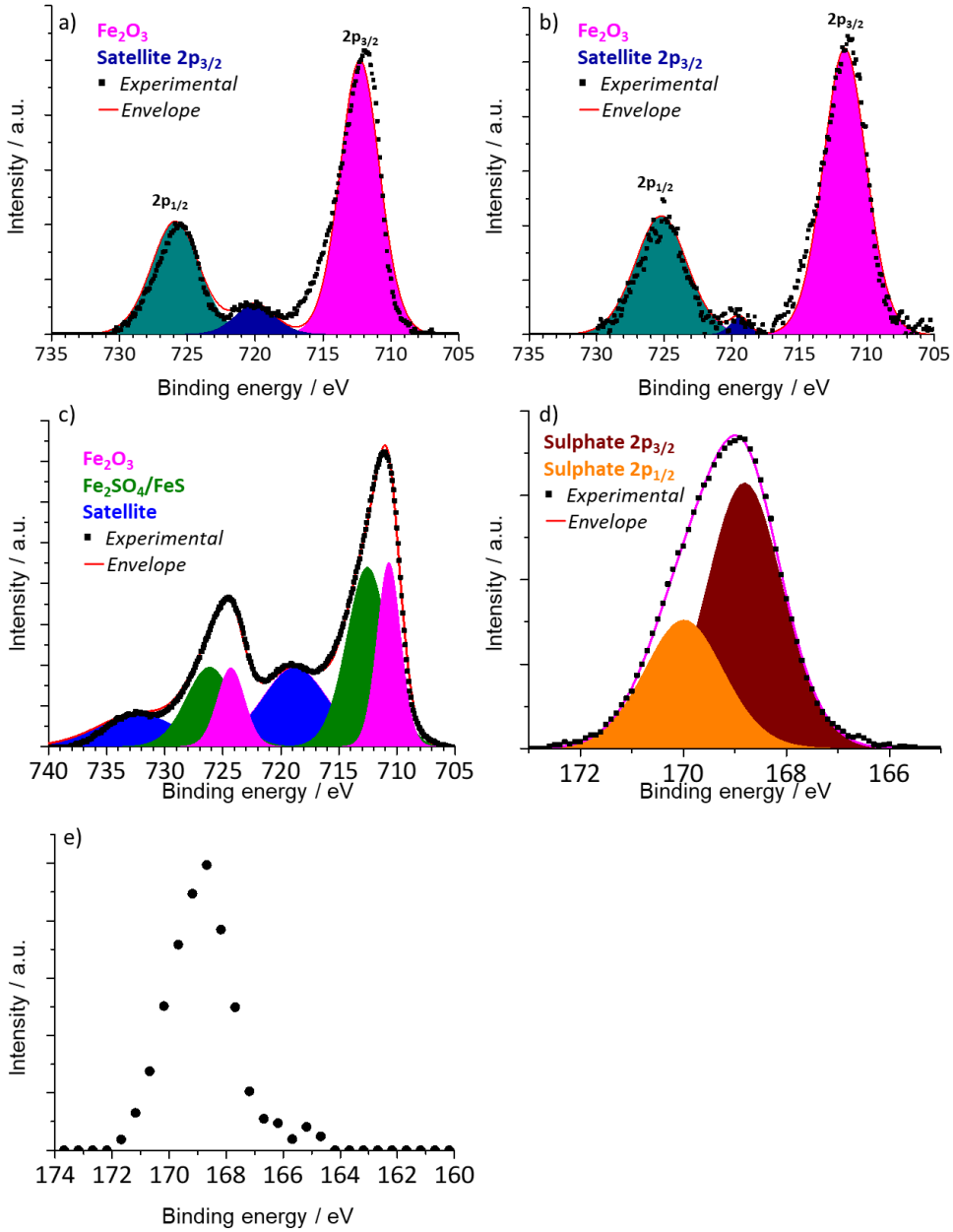

Figure S2. High-resolution XPS spectra of Fe2p in a) Fe_2O_3-COM and b) Fe_2O_3-OXL. High-resolution XPS spectra of (c) Fe2p and (d) S2p in S-Fe_2O_3-SHX. e) High-resolution XPS spectra of S2p in S-Fe_2O_3-OXL with a wider B.E. range.

Table S1. Mössbauer hyperfine parameters for samples Fe_2O_3-OXL, S-Fe_2O_3-OXL, Fe_2O_3-SHX and S-Fe_2O_3-SHX.

	Fe_2O_3-OXL		**S-Fe_2O_3-OXL**			**Fe_2O_3-SHX**		**S-Fe_2O_3-SHX**		
	S1	S2	S1	S2	D	S1	D	S	D1	D2
B_{hf} (T)	51.62(1)	49.54(2)	51.66(1)	49.60(2)	–	45.1[(b)]	–	43.3[(b)]	–	–
δ (mm/s)	0.374(1)	0.325(2)	0.372(1)	0.318(1)	0.382(5)	0.33[(b)]	0.29(2)	0.346[(b)]	0.377(5)	0.369(1)
2ε/QS (mm/s)[(a)]	–0.208(1)	0[(c)]	–0.208(1)	0[(c)]	0.760(8)		0.60(3)	–0.204(2)	1.144(3)	0.72(2)
FWHM (mm/s)	0.250(2)	0.474(7)	0.231(2)	0.504(5)	0.71(1)		0.83(8)		0.311(5)	0.50(1)
Area (%)	76.1(1)	23.9(1)	52.6(1)	40.7(1)	6.7(1)	96.9(3)	3.1(5)	71.2(1)	15.5(1)	13.3(1)

Isomer shifts δ relative to α-Fe.

(a) 2ε for sextets, QS for doublets.

(b) Weighted average values. Median values of B_{hf}: 49.1 T for Fe_2O_3-SHX, 46.9 T for S-Fe_2O_3-SHX.

(c) Fixed values.

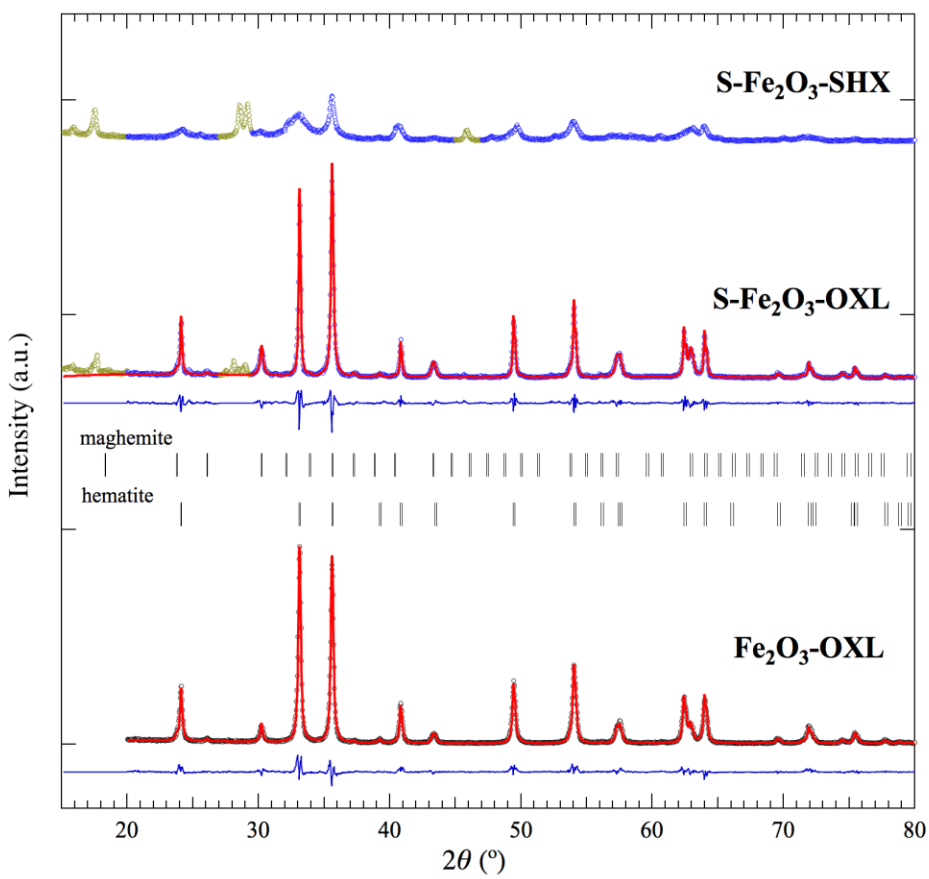

Figure S3. Experimental diffraction patterns (dots), fitted patterns (thick lines) and difference patterns (thin lines). Vertical lines show calculated reflection positions for maghemite (upper) and hematite (lower). Regions excluded from the fits carried out to determine the relative maghemite and hematite mass fractions are shown in green.

Figure S4a and **S4**b shows FTIR spectra for the different iron oxides, evidencing clear differences between samples. All the iron oxides, present absorption peaks observed at 3429 and 1630 cm^{-1} that are assigned to the stretching mode of hydroxyl group of water molecules. **Figures S4**c to **S4**f show the region from 1600 to 400 cm^{-1} for all the individual samples. Typical modes of maghemite are present in the FTIR spectra for the commercial sample, Fe_2O_3-COM (**Figure S4**c), composed of pure maghemite (γ-Fe_2O_3), as also determined by XRD. Klotz et al. mentioned well defined spectrum with peaks at 560, 587, 636, 690, 724 cm^{-1}, because of the vacancies in octahedral sides of γ-Fe_2O_3, also visible in our Fe_2O_3-COM sample, what corroborates its crystallographic structure [1]. On the other hand, S-Fe_2O_3-SHX shows two characteristic bands at 889 cm^{-1} and 796 cm^{-1} assigned to Fe-O-H bending vibrations as well as typical bands associated to hematite, in the range within 662-526 cm^{-1} and 494-437 cm^{-1} as referred by [2]. On the other hand, Fe_2O_3-OXL and S-Fe_2O_3-OXL show a mixed FTIR spectra with bands typical from both hematite (bands at 637, 538 and 462 cm^{-1}) and maghemite (bands at 694 and 480 cm^{-1}) (in accordance to XRD). Besides S-Fe_2O_3-OXL shows four bands at 1227, 1139, 1074 and 1000 cm^{-1} that could be assigned to adsorbed sulfates groups. Gotic et al. also described the presence of adsorbed sulphates on iron oxides obtained at acidic pH values, as is the case for S-Fe_2O_3-OXL [3,4].

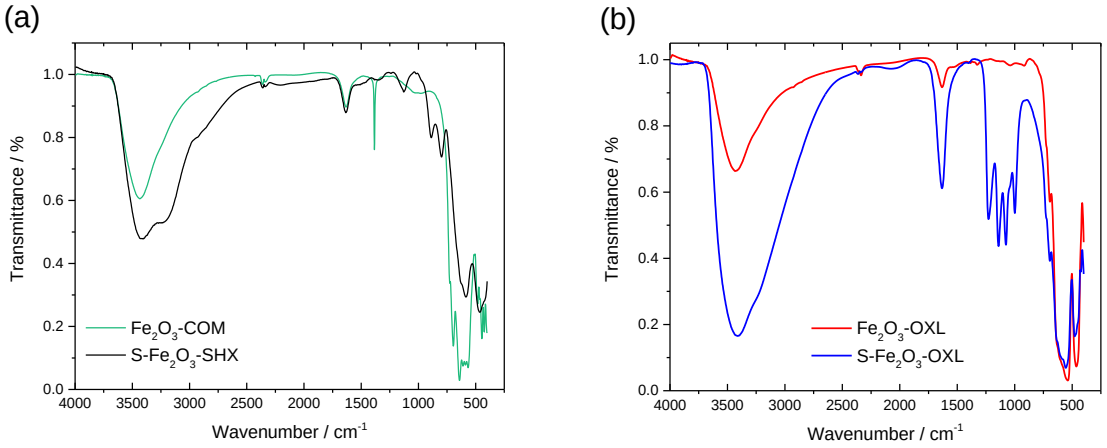

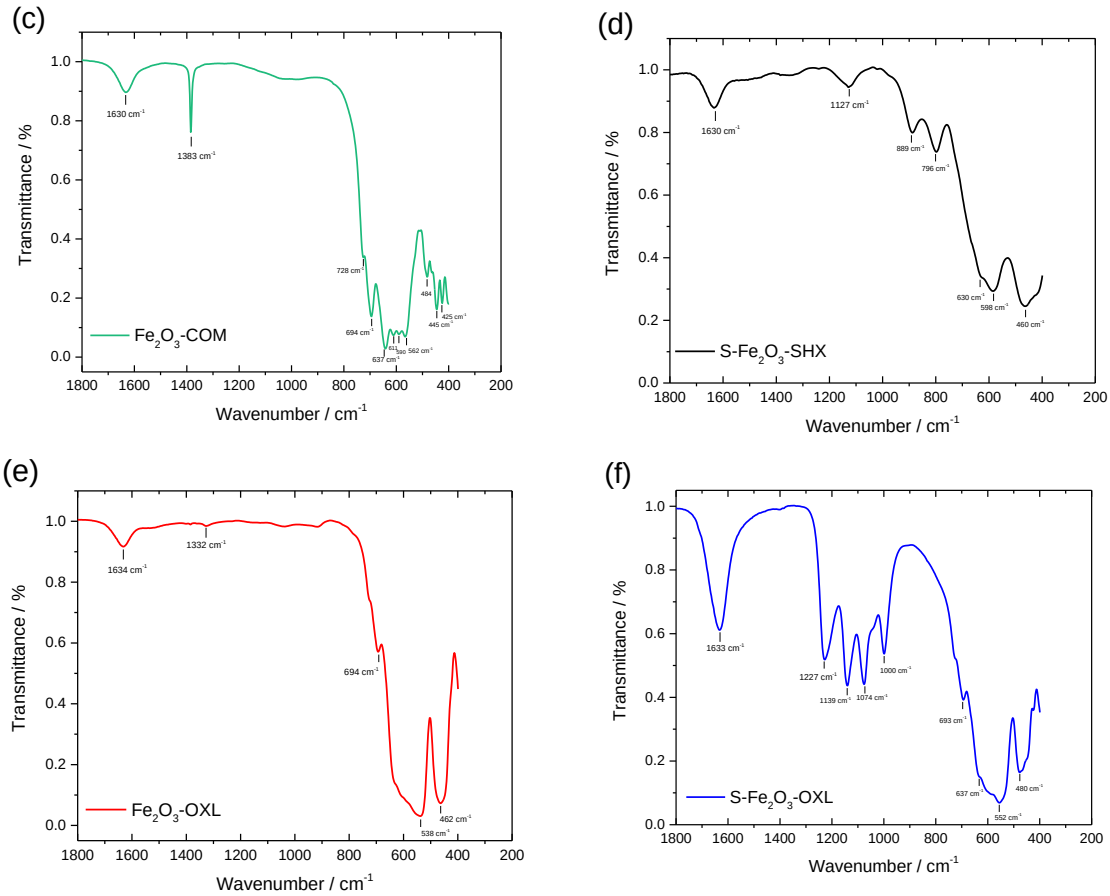

Figure S4. FTIR spectra for the different iron oxides synthesized: (a) Comparison between Fe_2O_3-COM vs. S-Fe_2O_3-SHX; (b) Comparison between Fe_2O_3-OXL vs. S-Fe_2O_3-OXL; (c) Fe_2O_3-COM (d) S-Fe_2O_3-SHX (e) Fe_2O_3-OXL (f) S-Fe_2O_3-OXL

Table S2 shows the quantitative results obtained from the fitting of N_2-adsorption/desorption isotherms (**Figure S5**a), along with the average porosity of the obtained samples, calculated from the ratio between the pore volume and the density (being the density considered for iron oxide: 5.26 g cm^{-3})[5]. Iron oxides obtained present a porosity around 50 %, which will be useful to hold the change of volume of the iron products during discharge. Commercial iron oxide presents the lowest pore volume and porosity of all the oxides. In Fe_2O_3-COM, the pores exist due to the small particle size, which creates small voids between the particles, as can be ascribed from the TEM image shown in **Figure 3**k (in the main manuscript). The regular shape of its particles allows the particles to stack better, and fewer voids are left in between, as can be seen in the mentioned image (**Figure 3**k).

In the case of Fe_2O_3-OXL and S-Fe_2O_3-OXL, the mesoporosity is consequence of the pores open in the bulk of the material by the decomposition of the organic salt. As a result, Fe_2O_3-OXL and S-Fe_2O_3-OXL have an almost identical surface area, around 55 m^2 g^{-1} which is the double of S-Fe_2O_3–SHX and around 33% larger than the surface area of the commercial sample, Fe_2O_3-COM (Table S2). Iron oxides obtained from oxalic acid present an average pore size around 14 nm, a similar value to the one of the commercial iron oxide. Whereas S-Fe_2O_3-SHX (obtained by precipitation with NaOH) presents the largest average pore size, ca. 24 nm. The use of NaOH in the synthesis might act as pore generator, favoring a larger pore size [6]. In any case, large mesopores may help accommodating the volume changes of the electrodes upon cycling. **Figure S5**b shows the pore size distribution of the iron oxides.

Table S2. Textural properties of the iron oxides

Sample	BET surface area / m^2 g^{-1}	Pore volume / cm^3 g^{-1}	BJH pore size / nm	Porosity
Fe_2O_3-COM	38.9	0.13	13.3	40 %
Fe_2O_3-OXL	55.5	0.24	14.6	55 %
S-Fe_2O_3-OXL	55.8	0.20	14.9	51 %
S-Fe_2O_3-SHX	28.3	0.19	23.8	50 %

Figure S5a shows the nitrogen physisorption isotherms for the four different iron oxides. The two oxides synthesized *via* precipitation with oxalic acid have a larger total pore volume (as can be ascribed from the maximum adsorbed quantity) and a larger surface area (seen from the slope at relative pressure 0.05 – 0.3) than the two other oxides. In addition, Fe_2O_3-OXL and S-Fe_2O_3-OXL (**Figure S5**b) have pores around 10 nm and 40-45 nm wide (Fe_2O_3-OXL has three times more 10 nm pore volume than S- Fe_2O_3-OXL), while S-Fe_2O_3-SHX and Fe_2O_3-COM only have 35 – 40 nm pores.

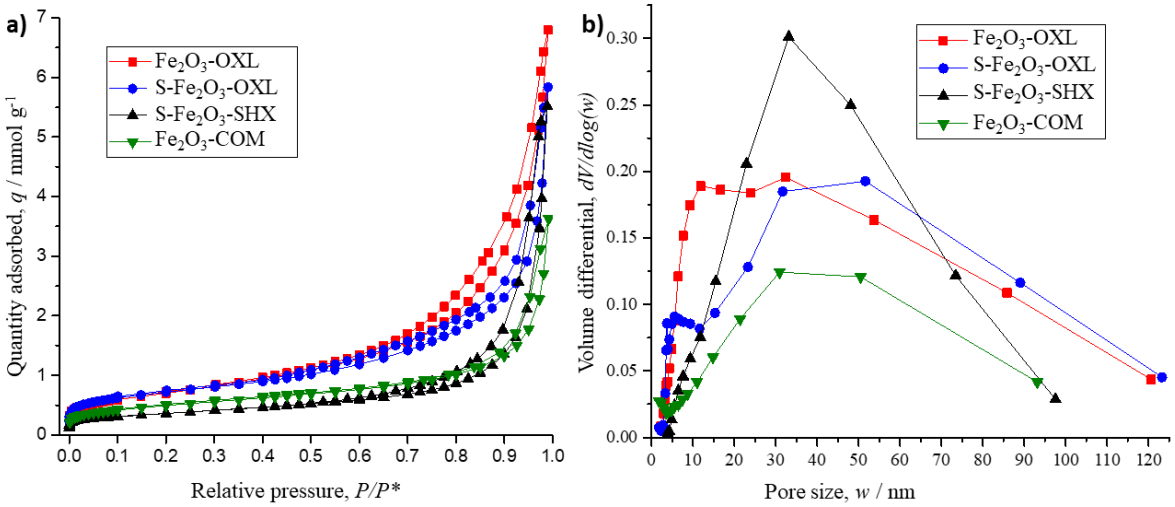

Figure S5. a) Nitrogen adsorption-desorption isotherms at 77K over the four synthesized iron oxides. b) Pore size distribution of the iron oxides

STEM-EDS analyses confirmed that sulfur is present along all of the iron particles (Figure S6).

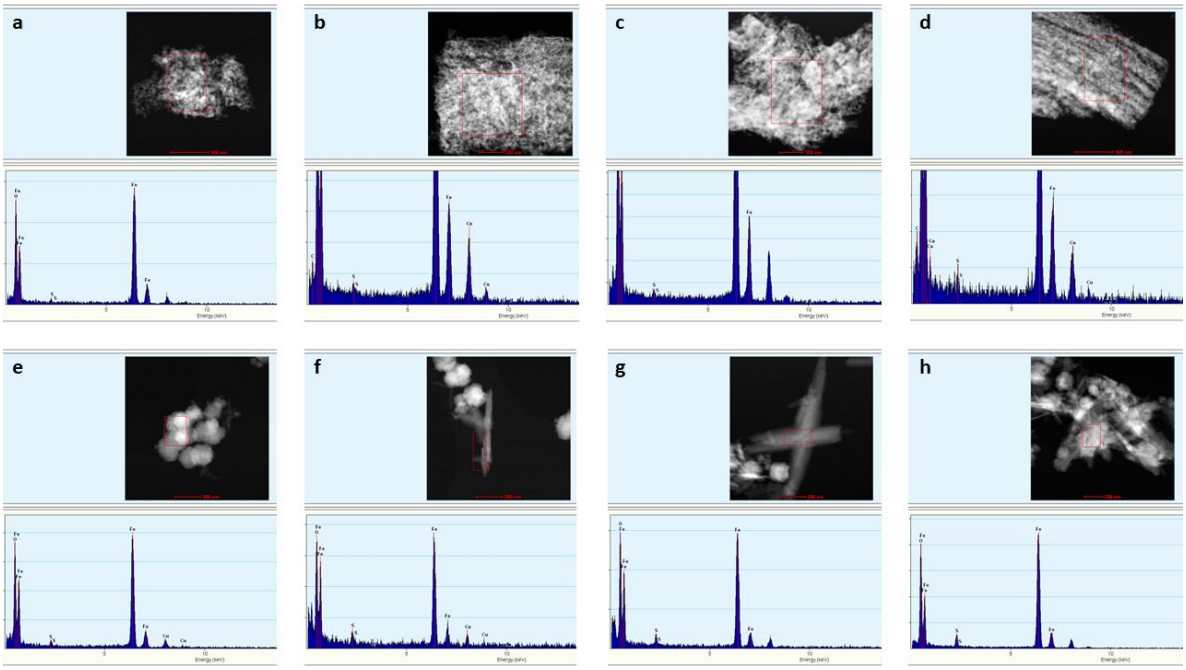

Figure S6. STEM images and EDS analysis of different iron crystallites in composites S-Fe_2O_3-OXL/C (a, b, c, and d) and S-Fe_2O_3-SHX/C (e, f, g and h)

Post-mortem XRD of the S-Fe_2O_3-OXL/C electrode after the first charge step, first discharge step and second discharge step are shown in **Figure S7**. It was not possible to see any sulfur phases. Only the sample examined after the second discharge step shows clear presence of goethite, but it was not possible to quantify the phases, as most of the peaks of Fe_3O_4 and $Fe(OH)_2$ overlap or are very close.

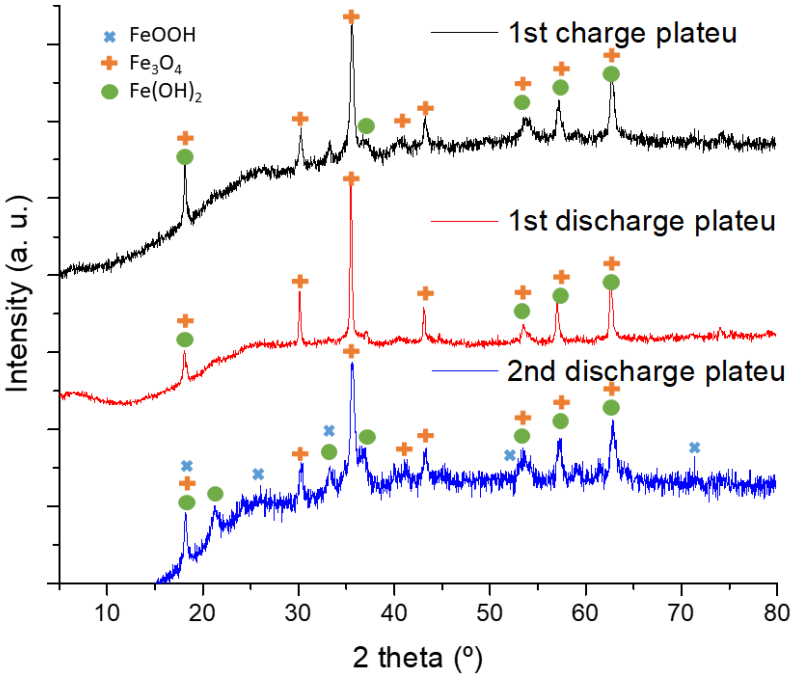

Figure S7. X-ray diffraction spectra of S-Fe_2O_3-OXL/C electrodes after the first charge plateau (top), first discharge plateau (middle) and second discharge plateau (bottom)

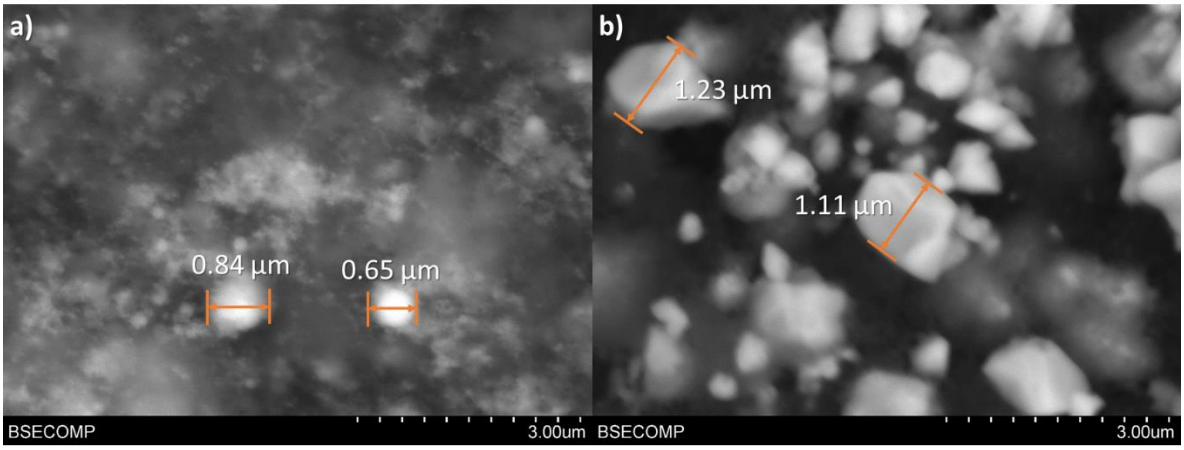

Figure S8. SEM images (16000x magnification back-scattered electrons) of electrode Fe_2O_3-COM/C before (a) and after (b) discharging.

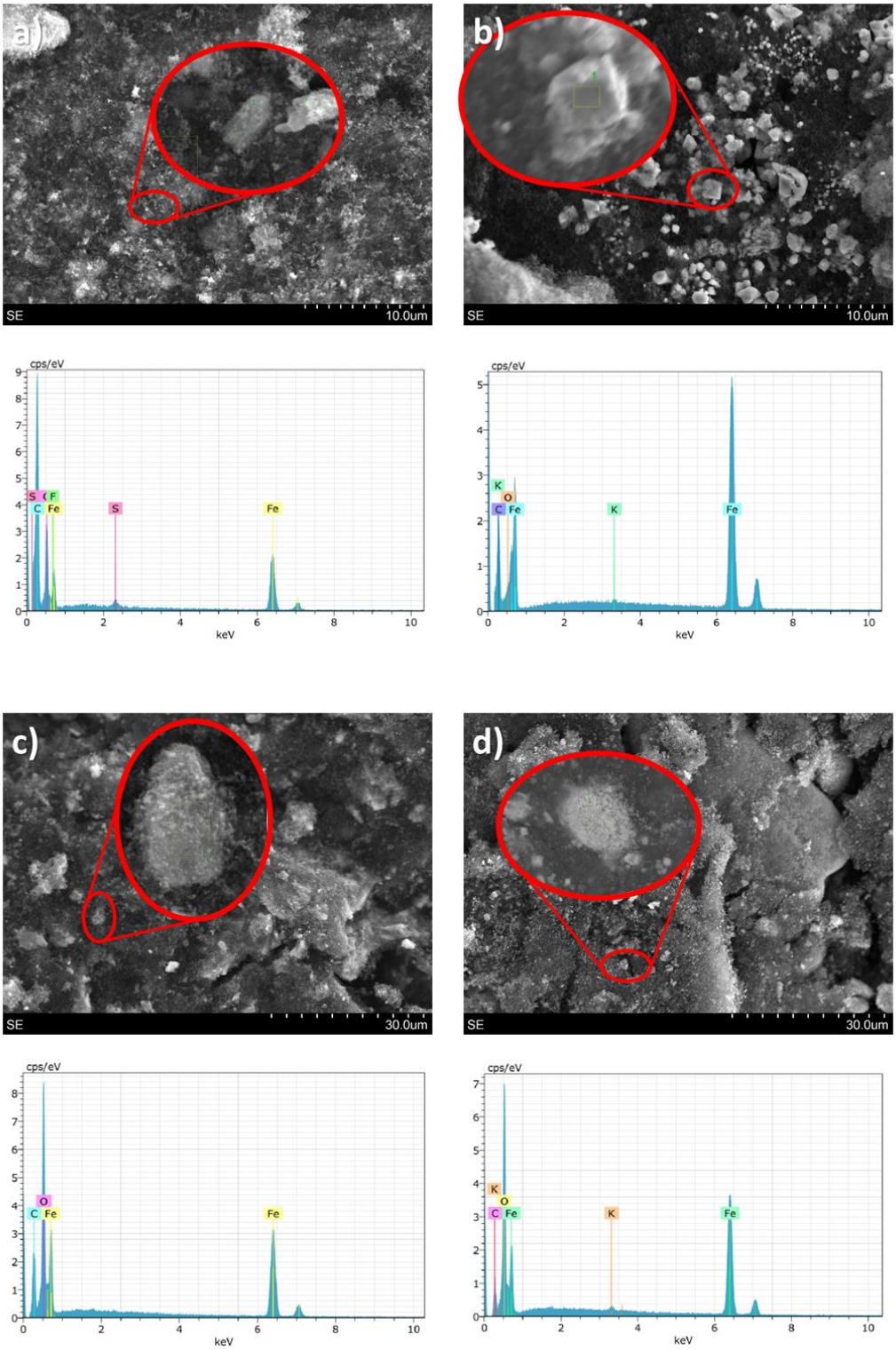

Figure S9. SEM images and EDX analyses for the electrode Fe_2O_3-COM/C: a) fresh electrode and b) after 20 cycles; SEM images and EDX analyses for the electrode S-Fe_2O_3-OXL/C: c) fresh electrode and d) after 20 cycles. Insets are the areas where EDX was measured

S.3. Extended cycling

As stated in the main text, S-Fe_2O_3-SHX/C (**Figure S10**b) increases its capacity during the first 20 cycles, indicating that the material is still not fully activated. According to nitrogen physisorption (Table S2), this oxide has the lowest surface area of all the materials, which means it needs more cycles to increase its area by successive expansions and contractions in order to expose more iron atoms to the electrolyte. After the first 20 cycles, the capacity of the electrode becomes erratic There is a clear tendency to deactivation, but some spikes with high discharge capacity values can be seen (cycles 24, 30, 36, 40, 43). The model estimates a 7 % loss of capacity per cycle, which means a faster deactivation for S-Fe_2O_3-SHX/C than for S-Fe_2O_3-OXL/C (**Figure S10**a). Even though S-Fe_2O_3-SHX has a higher percentage of Sulfur in the bulk (as obtained by elemental analysis), it has less surface Sulfur than S-Fe_2O_3-OXL (Table 1), meaning less sulfate that can reduce to sulfide and help to prevent passivation. Shangguan et al. [7] reached a similar conclusion. Their materials had 5-10 % wt. Sulfur and, and they also reported that the stability and the performance of the electrodes increased with the amount of Sulfur. Another factor for the worse stability of S-Fe_2O_3-SHX when compared to S-Fe_2O_3-OXL is the different crystal size. Being much smaller in the former, this means also a higher tendency to passivation, since small particles are more prone to passivation phenomena than large ones. This manuscript adds another conclusion: it is the amount of Sulfur on the surface, and not necessary in the bulk of the iron oxide the most important property that enhances the stability of the electrode, along with a proper crystal size.

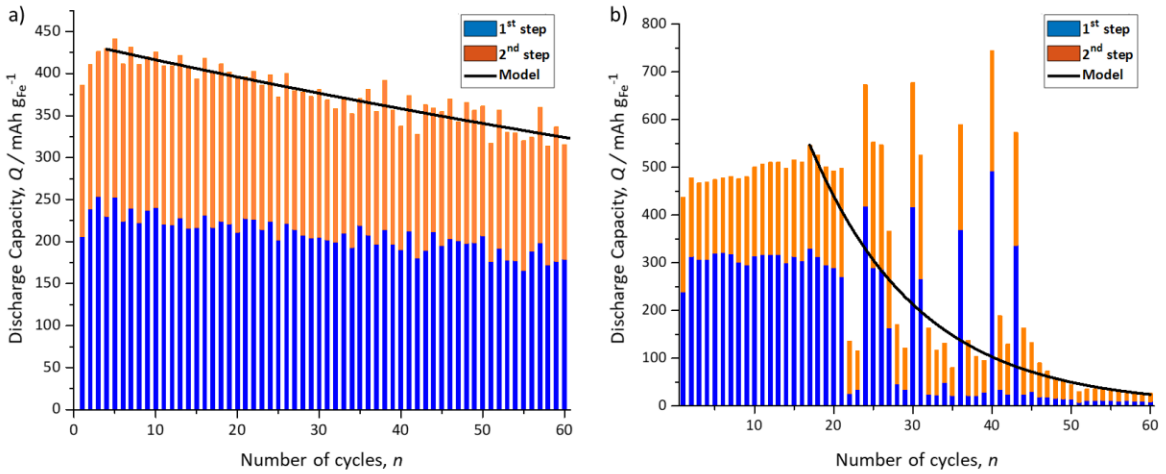

Figure S10. Extended cycling of a) S-Fe_2O_3-OXL; b) S-Fe_2O_3-SHX

To prove the deactivation model adjusted to the first 20 cycles and test the long-term performance of the synthesized materials, a 100-charge-discharge cycles (400 hours) was performed using the most stable material, S-Fe_2O_3-OXL/C. As **Figure S11** shows, the model predicts accurately the behavior of the electrode for *ca.* 70 cycles. From cycle 73 to cycle 74 (green rectangle in **Figure S11**), the capacity decreases circa 14% and never recovers, so the model overestimates the discharge capacity from that moment on. The capacity loss after 100 cycles (350 hours) predicted by the model for this electrode was 39%, while the loss experimentally determined was 49%, still, the model gives an excellent estimation of the behavior of the electrode for 70 cycles. The difference in the expected and experimental values can be attributed to the slight loss of Sulfur along cycling. The amount of Sulfur in the fresh electrode measured by Elemental Analysis was 1.37 wt. %, and upon cycling it slightly decreased to 1.29 wt. %.

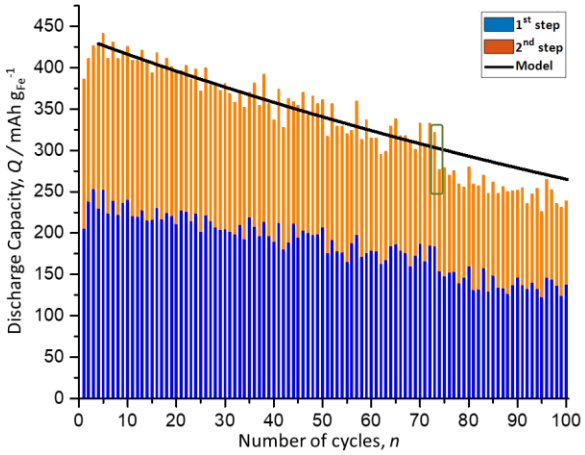

Figure S11. Discharge capacity of the electrode manufactured with Fe_2O_3-OXL-S/C along 100 cycles. Charge rate: 0.4C, discharge rate: 0.2C.

Similar trends can be observed in literature. Tan *et al.*[8] synthesized iron particles embedded in graphitic networks and found out that, after a 30-cycle formation period, the capacity decreases. In that study, the authors attribute the capacity loss to the consumption of sulfide ions, as they use Na_2S 0.01 M as additive in the electrolyte. In fact, they show that the electrodes can recover their capacity by adding again Na_2S to the electrolyte, but other studies have shown that electrolyte additives can poison the positive electrode of iron-air batteries [9]. Other studies show even more look-alike trends. In the paper by Ito *et al.*[10], carbon nanofibers loaded with Fe_3O_4 nanoparticles achieved a maximum of *ca.* 800 mAh g_{Fe}^{-1} at fifth cycle, decreasing their capacity slowly to approx. 650 mAh g_{Fe}^{-1} at 30th cycle, which is roughly a

0.75% capacity loss per cycle. A different but still related deactivation behavior is presented by Manohar *et al.*[11], whose carbonyl iron and bismuth sulfide electrodes showed a remarkable almost 100% charging efficiency for the first 14 cycles, but dropped to 95% in the 15th cycle and did not recover its previous value later on. It must be mentioned that this last study used a discharge rate of 0.05 C, while in the present study it is four times higher.

An electrode manufactured with S-Fe_2O_3-OXL/C was charged at 0.8 C rate and discharged at 0.4 C rate for 34 cycles (**Figure S12**a); and another identical electrode was charged at 1.6 C rate and discharged at 0.8 C rate for 20 cycles (**Figure S12**b). The increase in the charge and discharge C-rates resulted in a high increase in the discharge capacity, especially when charging at 0.8C and discharging at 0.4C (**Figure S12**a). In these conditions, the electrode manufactured with S-Fe_2O_3-OXL/C reached a total of almost 800 mAh g_{Fe}^{-1} of discharge capacity. The highest discharge capacity value we have found in literature is 900 mAh g_{Fe}^{-1} [12], but the performance of the electrodes manufactured in this study is more stable than in the cited article. Especially promising is the maximum of almost 500 mA h g_{Fe}^{-1} in the first discharge plateau. In the case of the electrode cycled at a charge rate of 0.8C and discharge rate of 0.4C (**Figure S12**a), after 17 cycles, a cut-off was applied at 50 minutes of charge for the subsequent cycles. This turned into a slight decrease in discharge capacity, but an important increase in coulombic efficiency (green circle), from 49 % to 62 %, which is a 27 % increase with respect to the efficiency obtained before the charging-time shortening. However, this increase in efficiency comes with a 15 % decrease in the maximum capacity (green circle in **Figure S12**a).

A higher C-rate (**Figure S12**b), namely 1.6 C rate for charging and 0.8 C for discharging, does not increase the capacity of the electrode as much as the intermediate C-rate. Another effect of the increase in the charge and discharge rate is a reduction in the stability factor f for the electrode and a bell-shape curve for maximum discharge capacities (**Figure S12**c). The loss of stability with higher charge and discharge rates was expected and may be due to the formation of goethite with rapid oxidation of iron (II) hydroxide, according to literature [13]. The increase in discharge capacity can seem surprising, but it is a phenomenon that has been previously studied. According to Kitamura et al. [14], this effect in Fe_2O_3/carbon electrodes is explained by the difference of the potentials at which the HER and $Fe(OH)_2$

reduction reach their diffusional limit, being that potential less negative for hydrogen evolution that for iron (II) hydroxide reduction. Additionally, as Weinrich et al. showed with carbonyl iron electrodes [15], a higher charge current can have a positive impact in the formation of the electrodes, as it promotes a higher surface area. However, when the discharge rate is too high, the capacity starts going down. Manohar et al. [11] observed this effect in bismuth-sulfide-doped carbonyl iron electrodes and also found a linear negative correlation between the discharge rate and the discharge capacity.

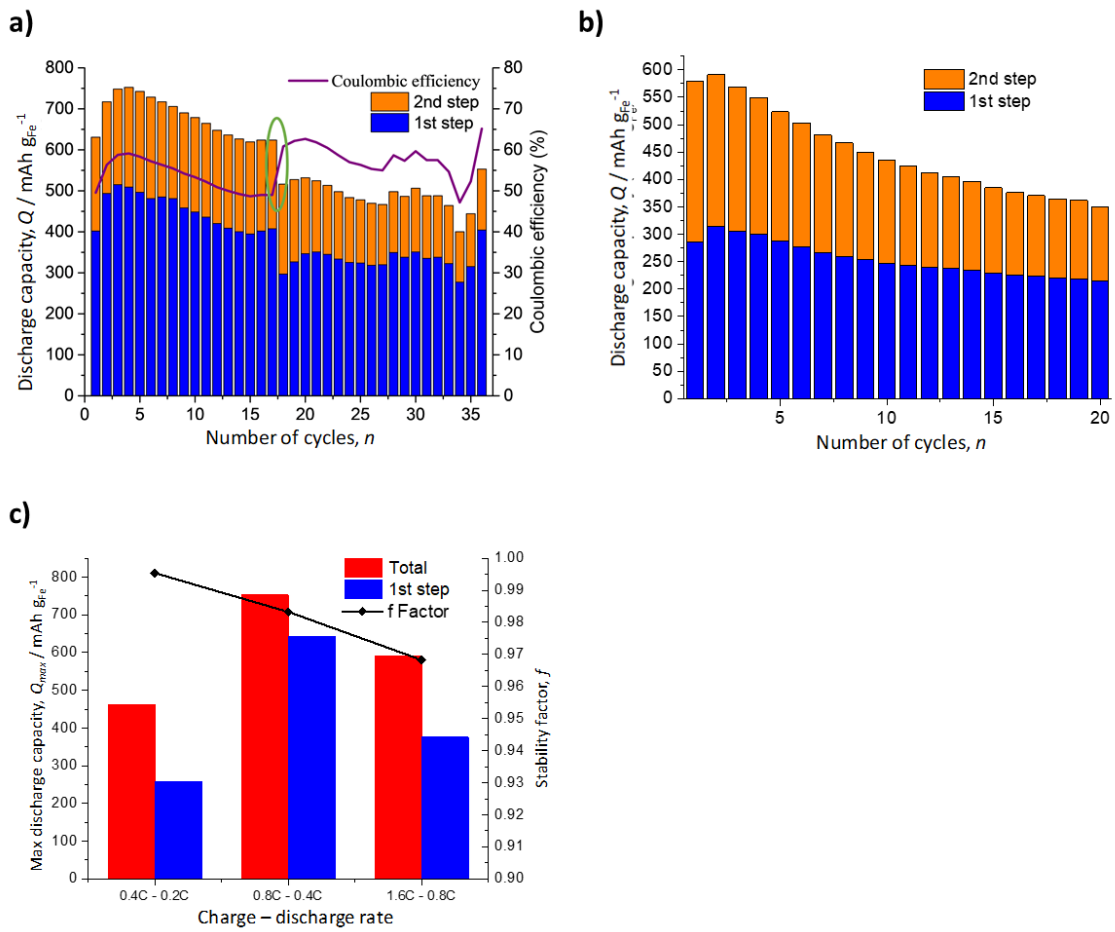

Figure S12. Effect of the charge and discharge C-rate on the electrochemical behavior of electrodes manufactured wit S-Fe_2O_3-OXL/C. a) Charge-discharge cycles of S-Fe_2O_3-OXL at 0.8C rate for charging and 0.4C rate for discharging; b) Charge-discharge cycles of S-Fe_2O_3-OXL at 1.6C rate for charging and 0.8C rate for discharging; c) dependance of maximum capacity and f factor with charge and discharge rates.

The increase in the C-rate also turned into an increase in the charge-discharge potential gap (ΔE) between the charge and discharge plateaus. In **Figure S13**c, ΔE_1 *(black bar)* is the

potential difference between the 1st charge plateau and the 2nd discharge plateau, *i.e.* the potential difference between the oxidation of iron (II) hydroxide to goethite or magnetite and the reduction of these species to iron (II) hydroxide. ΔE_2 (*r*ed bar in **Figure S13**c) is the potential difference between the 2nd charge plateau (reduction of iron (II) hydroxide to metallic iron) and the 1st discharge plateau, which corresponds to the oxidation of metallic iron. From this information, we can deduct that, at low discharge rates (0.2 C - 0.8 C), charge transfer controls the system.

The Butler-Volmer equation (1) indicates that the current increases exponentially with the overpotential, i.e. the overpotential increases logarithmically with the current, and this would explain why increasing the charge-discharge rates from 0.4 C (charge) – 0.2 C (discharge) to 0.8 C (charge) – 0.4 C (discharge) turns into a small increase in the charge-discharge potential gap.

$$i = i_0\left[\exp\left(-\frac{\alpha zF\eta}{RT}\right) - \exp\left(\frac{(1-\alpha)zF\eta}{RT}\right)\right] \quad (1)$$

On the other hand, when electrochemical reactions are controlled by mass transport or mixed regime, it is necessary a high increase in overpotential to obtain an increase in current, which is what happens when the rates are increased from 0.8 C (charge) – 0.4 C (discharge) to 1.6 C (charge) – 0.8 C (discharge).

In addition, the potential difference between the second charge plateau and the HER was calculated (ΔE_{HER}, **Figure S13**d). The reduction of iron hydroxide and the hydrogen evolution occur simultaneously when the charge and discharge rate are 0.4 C and 0.2 C, respectively. When the C-rate is increased twice fold, the second charge plateau separates some millivolts (around 20) from the HER plateau. By increasing furthermore, the charge rate, this effect magnifies. This could allow us to control HER by varying the charge rate (it would not even be necessary to modify the discharge rate, just the charge rate).

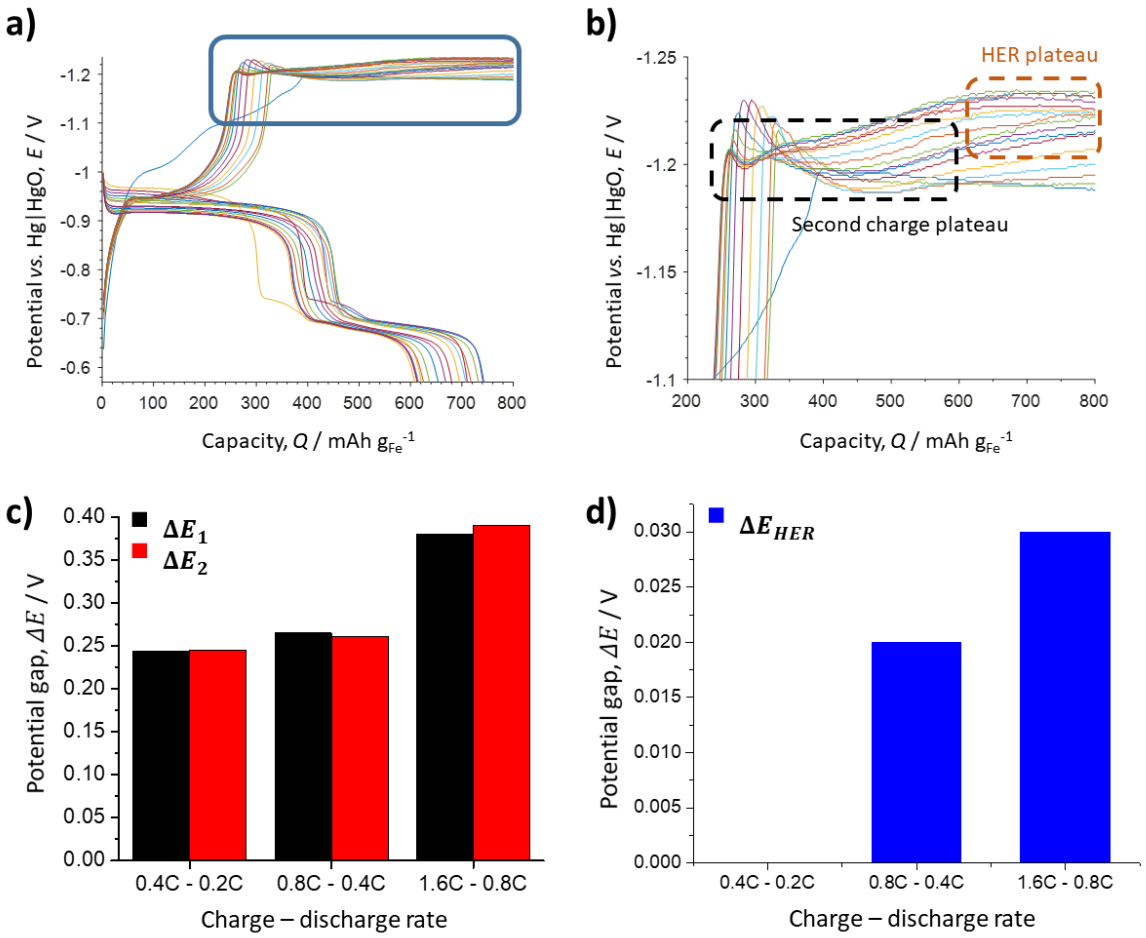

Figure S13. a) 17 first charge and discharge cycles for the S-Fe_2O_3-OXL/C electrode at 0.8C rate for charging and 0.4C rate for discharging. b) Zoom view of the area marked with the rectangle in (a); (c) Average potential gaps for the first and second charge-discharge steps (d) Average potential gap between the second charge plateau and the HER plateau

The increase in coulombic efficiency is a signal that, indeed, most of the HER occurs after the second charge plateau, as seen in the zoomed part of the graph in **Figure S13**b, while almost none of it occurs in the first charge plateau. However, part of the HER takes place together with the charge, and not after it, as can be deducted from the fact that the discharge capacity falls when the charge time is reduced (if the HER took place *after* the charge, reducing the charge time would not affect the charge and, by consequence, the discharge). As expected, the reduction in discharge capacity affects principally the first discharge step (which is related to the second charge step) in the 18th cycle, while the second step retains its capacity. Nonetheless, in the next cycles, the capacity of the first step increases and the one

of the second step slightly decreases, so the ratio of charge between the first and the second discharge steps goes back to 2:1, just like in the beginning of the experiment. The reason for this to happen is that, when the cut-off is applied, the less exposed iron (II) hydroxide molecules cannot be reduced to iron, so less iron atoms can oxidize to iron (II) hydroxide in the next discharge.

(1) Can, M. M.; Ozcan, S.; Ceylan, A.; Firat, T. Effect of Milling Time on the Synthesis of Magnetite Nanoparticles by Wet Milling. *Mater. Sci. Eng. B Solid-State Mater. Adv. Technol.* **2010**, *172* (1), 72–75. https://doi.org/10.1016/j.mseb.2010.04.019.

(2) Chernyshova, I. V.; Hochella, M. F.; Madden, A. S. Size-Dependent Structural Transformations of Hematite Nanoparticles. 1. Phase Transition. *Phys. Chem. Chem. Phys.* **2007**, *9* (14), 1736–1750. https://doi.org/10.1039/b618790k.

(3) Gotić, M.; Musić, S.; Popović, S.; Sekovanić, L. Investigation of Factors Influencing the Precipitation of Iron Oxides from Fe(II) Containing Solutions. *Croat. Chem. Acta* **2008**, *81* (4), 569–578.

(4) Gotić, M.; Musić, S. Mössbauer, FT-IR and FE SEM Investigation of Iron Oxides Precipitated from FeSO4 Solutions. *J. Mol. Struct.* **2007**, *834–836* (SPEC. ISS.), 445–453. https://doi.org/10.1016/j.molstruc.2006.10.059.

(5) Dana, J. D. *System of Mineralogy: V. 1*, 7th ed.; Dana, E. S., Palache, C., Berman, H., Frondel, C., Eds.; Wiley–Blackwell, 1944.

(6) Cazetta, A. L.; Vargas, A. M. M.; Nogami, E. M.; Kunita, M. H.; Guilherme, M. R.; Martins, A. C.; Silva, T. L.; Moraes, J. C. G.; Almeida, V. C. NaOH-Activated Carbon of High Surface Area Produced from Coconut Shell: Kinetics and Equilibrium Studies from the Methylene Blue Adsorption. *Chem. Eng. J.* **2011**, *174* (1), 117–125. https://doi.org/10.1016/j.cej.2011.08.058.

(7) Shangguan, E.; Fu, S.; Wu, C.; Cai, X.; Li, J.; Chang, Z.; Wang, Z.; Li, Q. Sublimed Sulfur Powders as Novel Effective Anode Additives to Enhance the High-Rate Capabilities of Iron

Anodes for Advanced Iron-Based Secondary Batteries. *Electrochim. Acta* **2019**, *301*, 162–173. https://doi.org/10.1016/j.electacta.2019.01.139.

(8) Tan, W. K.; Asami, K.; Maegawa, K.; Kawamura, G.; Muto, H.; Matsuda, A. Formation of Fe-embedded Graphitic Carbon Network Composites as Anode Materials for Rechargeable Fe-air Batteries. *Energy Storage* **2020**, *2* (6). https://doi.org/10.1002/est2.196.

(9) McKerracher, R. D.; Figueredo-Rodriguez, H. A.; Dimogiannis, K.; Alegre, C.; Villanueva-Martinez, N. I.; Lázaro, M. J.; Baglio, V.; Aricò, A. S.; Ponce de León, C. Effect of 1-Octanethiol as an Electrolyte Additive on the Performance of the Iron-Air Battery Electrodes. *J. Solid State Electrochem.* **2021**, *25* (1), 225–230. https://doi.org/10.1007/s10008-020-04738-4.

(10) Ito, A.; Zhao, L.; Okada, S.; Yamaki, J. I. Synthesis of Nano-Fe3O4-Loaded Tubular Carbon Nanofibers and Their Application as Negative Electrodes for Fe/Air Batteries. *J. Power Sources* **2011**, *196* (19), 8154–8159. https://doi.org/10.1016/j.jpowsour.2011.05.043.

(11) Manohar, A. K.; Malkhandi, S.; Yang, B.; Yang, C.; Surya Prakash, G. K.; Narayanan, S. R. A High-Performance Rechargeable Iron Electrode for Large-Scale Battery-Based Energy Storage. *J. Electrochem. Soc.* **2012**, *159* (8), A1209–A1214. https://doi.org/10.1149/2.034208jes.

(12) McKerracher, R. D.; Figueredo-Rodriguez, H. A.; Alegre, C.; Aricò, A. S.; Baglio, V.; Ponce de León, C. Improving the Stability and Discharge Capacity of Nanostructured Fe2O3/C Anodes for Iron-Air Batteries and Investigation of 1-Octhanethiol as an Electrolyte Additive. *Electrochim. Acta* **2019**, *318*, 625–634. https://doi.org/10.1016/j.electacta.2019.06.043.

(13) Balasubramanian, T. S.; Vijayamohanan, K.; Shukla, A. K. Mechanisms of the Discharge of Porous-Iron Electrodes in Alkaline Medium. *J. Appl. Electrochem.* **1993**, *23* (9), 947–950. https://doi.org/10.1007/BF00251032.

(14) Kitamura, H.; Zhao, L.; Hang, B. T.; Okada, S.; Yamaki, J. Effect of Charge Current

Density on Electrochemical Performance of Fe/C Electrodes in Alkaline Solutions. *J. Electrochem. Soc.* **2012**, *159* (6), A720–A724. https://doi.org/10.1149/2.049206jes.

(15) Weinrich, H.; Gehring, M.; Tempel, H.; Kungl, H.; Eichel, R. A. Impact of the Charging Conditions on the Discharge Performance of Rechargeable Iron-Anodes for Alkaline Iron–Air Batteries. *J. Appl. Electrochem.* **2018**, *48* (4), 451–462. https://doi.org/10.1007/s10800-018-1176-4.

Artículo 2

Villanueva-Martínez, N. I., Alegre, C., Rubín, J., Mckerracher, R., de León, C. P., Rodríguez, H. A. F., & Lázaro, M. J. (2023). Investigation of the properties influencing the deactivation of iron electrodes in iron-air batteries. *Electrochimica Acta*, *465*, 142964.

DOI: 10.1016/j.electacta.2023.142964

Electrochimica Acta 465 (2023) 142964

Contents lists available at ScienceDirect

Electrochimica Acta

journal homepage: www.journals.elsevier.com/electrochimica-acta

Investigation of the properties influencing the deactivation of iron electrodes in iron-air batteries

Nicolás I. Villanueva-Martínez [a], Cinthia Alegre [a,*], Javier Rubín [b,c], Rachel Mckerracher [d], Carlos Ponce de León [d], Horacio Antonio Figueredo Rodríguez [e], María Jesús Lázaro [a,*]

[a] Instituto de Carboquímica, Consejo Superior de Investigaciones Científicas. C/. Miguel Luesma Castán, 4, Zaragoza 50018, Spain
[b] Instituto de Nanociencia y Materiales de Aragón (INMA), CSIC-Universidad de Zaragoza, Zaragoza 50009, Spain
[c] Departamento de Ciencia y Tecnología de Materiales y Fluidos, Universidad de Zaragoza, Zaragoza 50018, Spain
[d] Electrochemical Engineering Laboratory, Energy Technology Research Group, Faculty of Engineering and Physical Sciences, University of Southampton, Highfield Campus, University Road, Southampton SO17 1BJ, United Kingdom
[e] Escuela de Ingeniería y Ciencias, Tecnológico de Monterrey, Campus Ciudad de México, Tlalpan, Ciudad de México 14380, Mexico

ARTICLE INFO

Keywords:
Deactivation
Electrochemical impedance spectroscopy
Iron-air batteries
Porous electrodes

ABSTRACT

Iron-air batteries hold the potential to be a key technology for energy storage, thanks to their energy density, low cost, safety and abundance of their materials. In order to scale the technology up and optimize the cell formulations, it is key to obtain a clear understanding of how the physical-chemical properties of the electrode influence their electrochemical behaviour, in particular, the capacity loss. In this work, we propose for the first time mathematical correlations between textural and crystallographic properties of iron electrodes and their electrochemical stability. By adjusting synthesis parameters, we were able to tune pore size and volume, surface area and crystal size of iron oxides, and found that stability is highly correlated to both surface area and pore size. Large surface area and small average pore size provide electrodes with enhanced stability. We hypothesize that the cause for deactivation is the passivation of the electrodes ascribed to the formation of a non-conductive, non-reactive iron (II) hydroxide layer during discharge, which then cannot be reduced to iron again. We validate this hypothesis with electrochemical impedance spectroscopy studies, which show that, in the more stable electrodes, the charge transfer resistance in the $Fe(OH)_2$ to Fe reduction does not significantly change after cycling, contrary to the behaviour of the less stable electrodes, corroborating our hypothesis. Furthermore, the electrode with the best properties was cycled 100 times, retaining almost 75% of its initial capacity at the end of the 100 cycles. These results are highly relevant for the future design and operation of iron-air batteries.

1. Introduction

Metal-air batteries (MABs) have gained traction in recent years due to their advantages like high theoretical energy density and specific energy, which make them suitable candidates for applications such as renewable electricity storage and electro-mobility. MABs are systems that comprise a negative electrode, where a metal (Li, Al, Zn, Fe, etc.) oxidizes, and a positive air electrode, where ambient oxygen reduces [1–3].

One type of MABs is the iron-air battery (FAB, from Fe-air battery). Its properties include 1229 Wh kg_{Fe}^{-1} of theoretical specific energy and 1273 Ah kg_{Fe}^{-1} of theoretical discharge capacity, low cost (less than 100 € kWh^{-1}), open circuit potential of 1.28 V and a high volumetric energy density of 2500 Wh L^{-1} [4]. Other interesting properties of FABs are the use of aqueous low-cost electrolyte – generally concentrated KOH – and the safety, abundance and recyclability of iron [5]. Eqs. (1)–(3) show the half-reactions occurring during the discharge of the negative iron electrode:

$$Fe + 2OH^- \rightleftharpoons Fe(OH)_2 + 2e^- E^0 = -0.88\ V\ vs\ SHE \quad (1)$$

$$3Fe(OH)_2 + 2OH^- \rightleftharpoons Fe_3O_4 + 4H_2O + 2e^- E^0 = -0.76\ V\ vs\ SHE \quad (2)$$

$$Fe(OH)_2 + OH^- \rightleftharpoons FeOOH + H_2O + e^- E^0 = -0.61\ V\ vs\ SHE \quad (3)$$

Reaction 1 is the first discharge step, which is usually preferred for technological applications due to its lower equilibrium potential and

* Corresponding authors.
E-mail addresses: cinthia@icb.csic.es (C. Alegre), mlazaro@icb.csic.es (M.J. Lázaro).

https://doi.org/10.1016/j.electacta.2023.142964
Received 15 April 2023; Received in revised form 28 July 2023; Accepted 29 July 2023
Available online 30 July 2023

higher number of electrodes per atom of iron involved [4]. Reactions 2–3 involve a deeper discharge of the electrode and provide less capacity and voltage. Especially, Eq. (3) provides a much lower full-cell voltage and some authors have mentioned that these deep discharges can cause damage to the electrode [6]. Even though major advances and breakthroughs have taken place in the research of FABs, two fundamental issues of the alkaline iron electrode have not been fully overcome: the low efficiency and the loss of capacity of the electrode upon cycling, also referred as deactivation, term that will be used in this work.

It has been well established that the parasitic hydrogen evolution reaction (HER) is the major cause of coulombic efficiency loss [7,8]. Together with reaction 1, HER can occur, since its standard reduction potential is less negative than the one of iron (II) hydroxide reduction, as shown in Eq. (4).

$$2H_2O + 2e^- \rightleftharpoons H_2 + 2OH^- E^0 = -0.83\ V\ vs\ SHE \quad (4)$$

On the other hand, there is no consensus concerning the causes for deactivation and the physical-chemical properties of the electrode affecting it. Two main hypotheses have been presented to explain the loss of capacity of the iron electrode upon cycling, both of them related to the discharge products of the reactions Eqs. (1)–((3)). The first one is called passivation, which is the formation of a non-conductive, non-reactive layer. The electrical conductivities of metallic iron and magnetite are around $10^7\ \Omega^{-1}\ m^{-1}$ and $10^6\ \Omega^{-1}\ m^{-1}$, respectively [9], however, iron (III) oxide and iron (II) hydroxide, have a much lower electrical conductivity, 7 to 8 orders of magnitude lower [10]. Passivation ascribed to a $Fe(OH)_2$ layer is the most cited explanation for the phenomenon of the deactivation of iron alkaline electrodes [11–22]. Some authors have pointed out that iron (III) oxides or hydroxides formed in the second discharge step – especially maghemite, γ-Fe_2O_3 –form a non-reactive layer [8,23,24].

The second hypothesis to explain deactivation is the molar volume increase that takes place upon oxidation of iron. When iron oxidizes to iron (II) hydroxide, it increases its molar volume up to a 272% [25]. In order to achieve a high utilization of the surface of the electrode, the former must present a large porosity, since the expansion of the iron can block those pores and prevent the electrolyte from reaching active sites [26]. Bryant et al. [27] and Yang et al. [18] calculated, based on the expansion datum, that an iron electrode should have a porosity of no less than 73% in order to be able to achieve the maximum theoretical capacity. The possibility must also not be disregarded that both molar expansion and passivation are responsible for iron electrode deactivation. Yang et al. for instance, mention an insulating layer of iron (II) hydroxide, formed after the first discharge step, that cannot be oxidized to Fe(III) and support their theory with SEM images, but they do not dismiss the effect of the porosity and the blocking effect of the molar expansion [18]. Moreover, they explain the limit of their electrodes' capacity with their lack of porosity.

Despite the major advances on electrode formulations (such as the use of additives like iron sulphide [23,24,28,29], bismuth sulphide [30,31], bismuth oxide [32] or potassium carbonate [24,33]), to the best of our knowledge, there are no mathematical correlations able to predict the stability or capacity of iron electrodes based on their physical-chemical properties. Correlating physical-chemical properties of the electrodes to their electrochemical performance is fundamental for the rational understanding and design of efficient, cost-effective batteries. Moreover, despite several studies rely on physical-chemical characterizations of the electrodes to assert one cause or another for the electrode deactivation, no electrochemical impedance spectroscopy (EIS) studies have been carried out to investigate how the charge transfer resistance or pore diffusion resistance change over time on a single porous iron electrode. We have found in the literature one study applying EIS to assess the charge transfer resistance in porous iron electrodes. Lei et al. [34] performed EIS studies over a Ni-Fe battery after more than 100 cycles and found that the charge transfer resistance in the iron electrode could increase up to tenfold, due to the morphological changes in the electrode.

In a previous work [35], we demonstrated that sulphur-modified iron oxides present an enhanced stability, mainly because of sulphate reduction forming sulphide, increasing conductivity. Here we evaluate the mechanisms behind the deactivation of sulphur-modified iron oxides by EIS studies. Besides, to tackle the deactivation due to the molar expansion, porous iron oxides were obtained. Mathematical correlations between their textural and crystallographic properties and their discharge capacity and stability are proposed. This work also evaluates how the charge transfer resistance changes upon cycling, indicating the causes for the electrode deactivation.

2. Experimental

2.1. Materials and methods

Porous iron oxides were synthesized according to a method established by Li et al. [36]. Since in a previous work the modification with sulphur of iron oxides proved to be effective to enhance the stability of iron electrodes, porous iron oxides were modified with sulphur by adding sodium thiosulphate in the initial mixture. 0.02 mol of tartaric acid (99.5% Labkem) plus 0.02 mol of iron (II) sulphate heptahydrate (Labkem) and 0.01 mol of sodium thiosulphate (99% Thermo Scientific Chemicals) were dissolved in 120 mL of deionized water (DI). Subsequently, 40 mL of a 1 M sodium hydroxide solution (99.99% Alfa-Aesar) was added drop by drop to the former solution under stirring for 15 min. The mixture was transferred to a Teflon-lined autoclave that was placed in a stove at 150 °C for 6 h. After the reaction time, a grey precipitate was obtained, subsequently vacuum-filtered and washed with 2 L of DI water to eliminate impurities. The obtained powder was dried overnight at 70 °C. Then, two different thermal treatments were carried out in order to assess its influence on the physical-chemical features of the sulphur-modified porous iron oxides. Half of the obtained powder was heat-treated in air atmosphere at 350 °C, and the other half was heat-treated in nitrogen atmosphere at 500 °C for 1 h. In both cases, a heating ramp of 4 °C min^{-1} was employed. Non sulphur-modified iron oxides were also synthesized for the sake of comparison employing the same method, except for the addition of sodium thiosulphate to the initial mixture. Iron oxides so obtained (Fe_2O_3-TAR and S-Fe_2O_3-TAR) were also compared with an iron oxide obtained precipitating the iron precursor with sodium hydroxide (Fe_2O_3-SHX). Table 1 summarizes the relation of samples investigated.

2.2. Physical-chemical characterization

Nitrogen physisorption was employed to investigate the textural properties of the porous iron oxides. Isotherms at 76 K were acquired with a Micromeritics ASAP 2020 gas sorption system. Different models were applied to the N_2-isotherms to determine the surface area, pore volume, and pore size, respectively (Brunauer-Emmet-Teller, single

Table 1
Synthesis conditions of the different iron oxides.

Sample	Addition of tartaric acid	Addition of sodium thiosulphate	Annealing conditions
Fe_2O_3-TAR-air	Yes	No	Air @ 350 °C
S-Fe_2O_3-TAR-air	Yes	Yes	Air @ 350 °C
Fe_2O_3-TAR-N_2	Yes	No	N_2 @ 500 °C
S-Fe_2O_3-TAR-N_2	Yes	Yes	N_2 @ 500 °C
Fe_2O_3-SHX-air	No	No	Air @ 350 °C

point and Barret-Joyner-Halenda). X-ray photoelectron spectroscopy (XPS) studies were performed to evaluate the chemical composition of the samples, with an ESCA Plus Omicron spectrometer (Scienta Omicron) operated with a Mg (1253.6 eV) anode, a pass energy of 20 eV, dwell time of 0.5 s and 0.1 eV step. Orbitals C1s, O1s, S2p and Fe2p were scanned and deconvolution was carried out with the software CasaXPS (Casa Software Ltd, CasaXPS Version 2.3.18). All the peaks were fitted with a 70% Gauss / 30% Lorentz curve applying a Shirley-type baseline. Field-Emission Scanning Electron Microscopy (FESEM) was carried out with a Carl Zeiss MERLIN microscope to investigate the morphology of the samples. Transmission and Scanning Transmission Electron Microscopy (TEM/STEM) was carried out in a Tecnai F30 microscope operated at 300 kV belonging to the LMA Service of the University of Zaragoza. The samples were ultrasonically dispersed in ethanol for 15 min and then placed in a Cu carbon grid. The amounts of sulphur and oxygen in the samples were determined by Elemental Analysis (EA) in a Thermo Flash 1112 analyser (Thermoscientific Waltham), whereas the iron content was obtained using inductively coupled plasma atomic emission spectroscopy (ICP-AES) with a Jobin Ybon 2000 spectrometer. Powder X-ray diffraction (PXRD) patterns were collected with a Ru2500 Rigaku diffractometer with rotating anode and theta-2theta configuration and Cu-Kα radiation, in order to calculate phase fractions and crystallite sizes. Information on the software used to fit the diffractograms and the procedure to determine crystallite size is included in the Supporting Information (Section S3). Mössbauer spectroscopy (MS) data were acquired using a constant acceleration spectrometer with symmetrical waveform at room temperature. The source was 25 mCi 57Co/Rh. The spectra were analysed with WinNormos software and all isomer shift values are reported with respect to α-Fe.

2.3. Preparation of electrode samples

Iron oxides were mixed in a planetary ball mill with a commercial carbon black (Vulcan XC-72R) in a 1:1 mass ratio at 100 rpm for 1 h, using ethanol to favour the mixture of the solid phases. The Fe_2O_3/C composite so obtained was finally dried overnight at 70 °C. Subsequently, a mixture of polytetrafluoroethylene (PTFE) solution (60 wt% in H_2O) and water was added to the dry powder mixture in order to form a paste, that was sandwiched between two sheets of stainless-steel mesh (Alfa-Aesar, dimensions 2.5 cm x 7.5 cm) and hot-pressed at 140 °C for 90 s to obtain the working iron electrode. See Fig. S1 in Section S1 in the Supporting Information file for a scheme of the manufacturing of the electrode.

2.4. Electrochemical measurements

The electrochemical measurements were carried out with an Autolab potentiostat and Nova software in a conventional three electrode set-up consisting of a 150 cm^3 glass cell, at a temperature of 25 °C, flowing nitrogen to the electrolyte to avoid carbonation. The working electrode (WE) was placed in a PTFE holder facing the counter-electrode (CE), a nickel sheet, separated by 5 mm, as in previous works [35]. The reference electrode, an Hg|HgO in 1 M KOH solution, was placed between the WE and the CE. The electrolyte was a 6 M KOH solution (99.99% KOH, Alfa-Aesar). To determine the discharge capacity of our iron electrodes, chrono-potentiometries were carried out at a C-rate of 0.4 C (equivalent to *ca.* 16 mA) during charging and 0.2 C (equivalent to *ca.* 8 mA) during discharging (calculated according to the theoretical capacity of the electrode) [35]. Electrochemical impedance spectroscopies were carried out at −1.16 V *vs.* Hg|HgO, applying a sine wave of 10 mV, with frequencies from 1 kHz to 1 Hz and 10 points per decade.

3. Results and discussion

3.1. Iron oxides characterization

X-ray diffractograms reported in Fig. 1, confirmed that iron is present as iron (III) oxide, either as haematite or maghemite phase, in different proportions as presented in Table 2. Sulphur-modified oxides present some other minor contributions at 25° and 34° (see the fit differences, thin lines under each diffractogram, at the cited angles). In general, the fit of the experimental data to the proposed crystalline phases is good. No other crystalline phases could be clearly identified, which suggests that sulphur is present as an amorphous phase or adsorbed over the surface.

Treatment temperature and the presence of sulphur had a strong influence on both crystal phase distributions and average crystal sizes. Samples calcined in air, Fe_2O_3-TAR-air and S-Fe_2O_3-TAR-air, are composed by 80% and 65% of haematite, respectively, which is expected, since haematite is the most stable iron (III) oxide phase at room temperature. The higher amount of maghemite in S-Fe_2O_3-TAR-air is due to the presence of sulphur, that promotes a higher yield of maghemite at the expense of haematite, as reported in previous works [35]. Besides, it has been reported that impurities in iron oxides, such as sulphur, promote defects, and in fact, maghemite can be modelled as a defective iron oxide. Nitrogen-annealed samples show the opposite trend, with Fe_2O_3-TAR-N_2 and S-Fe_2O_3-TAR-N_2 having a majority of maghemite, 86% and 80%, respectively. The reducing conditions (higher temperature and nitrogen atmosphere) promote the formation of maghemite, as this phase can be obtained by the reduction of haematite [37]. In the case of Fe_2O_3-SHX-air, the high proportion of maghemite can be explained because the precipitation of iron with sodium hydroxide produces iron (II) and (III) hydroxides (green rust), which are a precursor of maghemite [38].

In all of the iron oxides, except Fe_2O_3-SHX-air, maghemite phase has an average crystal size between 9 and 10 nm, while the crystal size of haematite ranges between 12 and 24 nm (Table 2). It must be noted that crystallites of the haematite phase in Fe_2O_3-SHX-air were found to be very small, and the fit can only estimate a size below 5 nm. However, as this is the minority phase in this iron oxide, the uncertainty in the estimate does not greatly affect the average size of the said sample. S-Fe_2O_3-TAR-air has a lower crystal size than Fe_2O_3-TAR-air, explained by the defects caused by the presence of sulphur atoms, which indicates that impurities hinder the growth of Fe crystals. Li et al., found that the presence of sodium sulphate hinders the growth of haematite crystals, and seeds of Fe_2O_3 crystals were required to ensure the formation of haematite [39]. The samples annealed in nitrogen show an average crystal size around 10–11 nm, mainly due to their high maghemite content.

In an attempt to corroborate the results of X-Ray diffraction, Mössbauer spectroscopy (MS) analyses were performed (Fig. S2). Except in the sample S-Fe_2O_3-TAR-N_2, sextets corresponding to haematite and maghemite could be included in the fits and the central intensity was taken into account with a distribution of doublets. The maxima of these distributions are compatible with wüstite $Fe_{1-x}O$, oxyhydroxides [40] and hydrated iron (III) sulphates [41,42]. The higher contribution of the paramagnetic doublets in the sulphur-modified samples could indicate the presence of both oxyhydroxides and sulphates. The samples heat-treated in nitrogen atmosphere required a distribution of sextets. In the case of Fe_2O_3-TAR-N_2 this is the only component that could be included to fit the spectrum, although when a fine histogram of sextets is used a contribution of haematite is revealed, whose relative contribution has been derived by fitting the distribution above 47 T with two gaussian functions. In contrast, the spectrum of sample S-Fe_2O_3-TAR-N_2 allowed sextets for haematite and maghemite as in the samples heated in air. The need of sextets distributions in the sulphur-modified samples can be assigned to broader distributions of crystallite size including very small values, although the average sizes determined by XRD are similar to

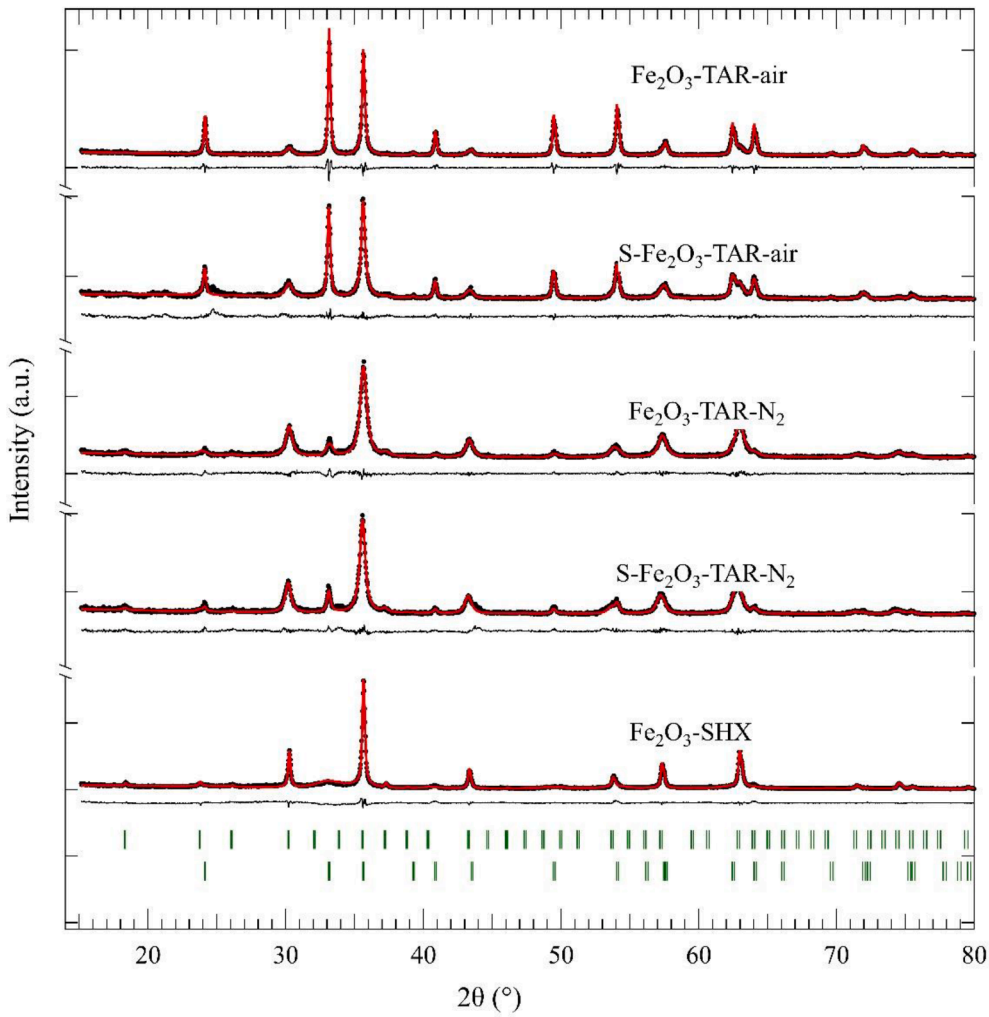

Fig. 1. Experimental X-ray diffractograms (dots), fitted profiles (thick red lines) and fit differences (thin lines). Upper row of vertical lines: maghemite reflections, lower row: haematite reflections.

Table 2
Crystal phases composition and average crystal size for the iron oxides.

Sample	Crystalline phases (%)		Crystal size (nm)		Average crystal size (nm)
	haematite	maghemite	haematite	Maghemite	
Fe_2O_3-TAR-air	80	20	24	10	21.2
S-Fe_2O_3-TAR-air	65	35	16	9	13.6
Fe_2O_3-TAR-N_2	14	86	12	10	10.3
S-Fe_2O_3-TAR-N_2	20	80	22	9	11.6
Fe_2O_3-SHX-air	15	85	4	17	15.1

Table 3
Textural properties obtained by nitrogen physisorption of the synthesized iron oxides.

Sample	Surface area (m^2g^{-1})	Pore volume (cm^3g^{-1})	Pore size (nm)	Porosity (%)
Fe_2O_3-TAR-air	141	0.30	4.8	61
S-Fe_2O_3-TAR-air	117	0.21	5.0	52
Fe_2O_3-TAR-N_2	28	0.10	15.9	34
S-Fe_2O_3-TAR-N_2	40	0.14	17.0	42
Fe_2O_3-SHX-air	77	0.17	10.3	47

those of the samples heated in air. In general, there is good agreement between XRD and MS results.

Nitrogen physisorption isotherms (Fig. S3) were carried out to investigate the textural properties of the iron oxides, reported in Table 3. Iron oxides synthesized with tartaric acid and calcined in air show type-IV isotherms, ascribed to mesoporous materials, with an hysteresis loop that could be identified as type H4, typical of mesoporous materials with pore size greater than 4 nm [43,44]. Iron oxides annealed in nitrogen exhibit a type II isotherm, which is found in solids with little porosity [45]. A slight type H3 hysteresis loop is visible, suggesting non-rigid aggregates of plate-like particles or non-filled voids between particles (which is more plausible according to SEM images, as will be discussed later).

Surface areas range between 28 and 141 m^2g^{-1} and pore volumes range between 0.10 and 0.30 cm^3 g^{-1}. Both iron oxides synthesized upon tartaric acid precipitation and calcination in air at low temperature

(Fe_2O_3-TAR-air and S-Fe_2O_3-TAR-air) present the highest surface area and pore volume values. As has been described elsewhere [36,46], tartaric acid reacts in hot basic conditions with iron salts to form iron (II) tartrate. This organic salt burns or decomposes – depending on the heat-treatment conditions – and forms CO_2 bubbles, water and iron (III) oxides. The CO_2 bubbles generate voids in the iron oxides, which leads to pores in the structure. A large porosity of iron oxides is of interest, since it would entail a larger metal-electrolyte interface, and eventually, a larger specific capacity of the iron electrode. Previous reports in the literature using precipitation with tartaric acid have a significantly lower surface area (half) and larger pore size (threefold) using the same calcination conditions (air, 350 °C, 1 h), with the difference that, in the referenced work, the salt used for synthesis was iron (II) chloride [31].

Iron oxides annealed in nitrogen at higher temperatures (Fe_2O_3-TAR-N_2 and S-Fe_2O_3-TAR-N_2) present reduced values of surface area and pore volume. This could be due to a combination of the faster decomposition (due to the higher temperature) of the tartrate ion, collapsing the pore structure, along with the sintering of the iron particles, decreasing the surface area and pore volume of these iron oxides. Iron oxide obtained by precipitation with sodium hydroxide (Fe_2O_3-SHX-air) shows intermediate values of surface area and pore volume (77 m^2g^{-1} and 0.17 cm^3g^{-1} respectively) to the other set of samples, and a pore size around 10 nm (equivalent to a porosity percentage of 52%).

Porosity values (determined from the ratio between the pore volume and the density of the iron oxide, 5.26 g cm^{-3} [35]) range from 47 to 61% for the iron oxides calcined in air, and around 34 and 42% for those calcined in nitrogen. Iron oxides calcined in air are close to the 73% porosity calculated by Bryant et al., necessary to achieve an optimal utilization of the electrode surface and avoid pore plugging [27].

Bulk and surface chemical analyses, reported in Table 4, were conducted on the iron oxides by elemental analysis, ICP and XPS. Iron oxides present Fe contents ranging from 57 to 65 wt% (bulk), corresponding to around 20 at% in the surface. Sulphur-modified samples (S-Fe_2O_3-TAR-air, S-Fe_2O_3-TAR-N_2) present 3.5 and 2.1 wt% of S (bulk), respectively. S-Fe_2O_3-TAR-N_2 obtained after annealing in nitrogen at 500 °C has the lowest sulphur content, since sulphur decomposes (vaporizes) at 440 °C [47,48]. XPS results show that sulphur-modified iron oxides present high S-contents on the surface, in accordance to Li et al. work, reporting that sulphate ions remained adsorbed on the surface [36]. Table 4 also reveals that iron oxides obtained with tartaric acid present a negligible amount of carbon (*ca.* 0.2 wt%, except for S-Fe_2O_3-TAR-N_2 with 2.5 wt% C), meaning that tartrate ions are almost fully calcined during the thermal treatments, particularly using air. The large amount of surface oxygen in all the samples can be ascribed to residual water and to the presence of hydroxides, sulphate groups and hydrated sulphates, as described by Li et al. [36].

Figs. S4 and S5 show the results from the XPS characterization, the survey scan and the high resolution spectra for Fe2p and S2p orbitals, respectively. Fe_2O_3-TAR-air, Fe_2O_3-TAR-N_2 and Fe_2O_3-SHX-air only showed peaks at binding energies corresponding to Fe, O, and C. S2p region of S-Fe_2O_3-TAR-air and S-Fe_2O_3-TAR-N_2 shows one peak around 168.5 eV ($2p_{3/2}$) which was ascribed to sulphate ions, probably coming from the decomposition of the thiosulphate precursor upon oxidation in air at 350 °C. Fe2p spectrum, on its hand, shows three $2p_{3/2}$ peaks at 710.7, 712.4 and 718.0 eV, which were assigned to Fe_2O_3, hydrated iron sulphates (either $FeSO_4$ or $Fe_2(SO_4)_3$) and the satellite of Fe_2O_3, respectively. The peak at 712 eV, according to [33], could be due to the presence of iron sulphate or iron sulphide (FeS), but the absence of peaks related to sulphide in the S2p spectrum allowed us to rule out the sulphide and conclude it is sulphate. The XPS spectra of O1s orbital (Fig. S6) shows two peaks, one around 530 eV ascribed to Fe_2O_3 and another peak around 531.5 eV, that could be ascribed to adsorbed oxygen or sulphate. Fig. S6 reveals there is a greater amount of adsorbed oxygen (or sulphate) in sulphur-modified iron oxides than in the non-modified oxides.

Table 4
Elemental composition of the different iron oxides determined by ICP, EA and XPS.

Sample	Weight% (ICP)	Weight% (EA)			Atomic% (XPS)		
	Fe	S	O	C	Fe	S	O
Fe_2O_3-TAR-air	63	–	35	0.18	22.2	–	67.1
S-Fe_2O_3-TAR-air	57	3.5	38	0.27	20.4	4.3	65.3
Fe_2O_3-TAR-N_2	65	–	32	0.09	19.2	–	54.4
S-Fe_2O_3-TAR-N_2	64	2.1	32	2.59	15.7	2.8	53.9
Fe_2O_3-SHX-air	57	–	37	–	21.8	–	66.7

FESEM micrographs (Fig. S7 in the Supporting Information), alongside TEM/STEM images (Fig. S8) revealed the morphology of the iron oxides. Iron oxides based on tartaric acid and calcined in air (TAR-air, Figs. S7a and S7b, S8a–S8d) show a straw-like morphology, with pores and irregularities (formed during the calcination of the organic salt) that enhance their surface area, as mentioned before. This internal porosity can be also appreciated in the TEM images in Fig. S8. Iron oxides calcined in nitrogen (TAR-N_2, Fig. S7c and S7d) show signs of sintering due to the higher annealing temperature, with smaller particles, but more compact and close to each other. As a result, there are fewer voids and less space in between particles, which explains the lower pore volume and surface area of these materials. Fe_2O_3-SHX-air (Fig. S7e) presents a totally different morphology, consisting in more regular, smaller and platelet-like particles. These particles are close to each other, but the material appears to be less compact than the samples annealed in nitrogen.

3.2. Electrochemical characterization

The specific discharge capacity of the iron electrodes obtained from the previously described iron oxides was evaluated by means of charge-discharge cycles. Specifically, twenty charge-discharge galvanostatic cycles were performed at 0.4 C and 0.2 C rate respectively. Fig. 2a shows the charge and discharge curves for the fifth cycle of every Fe_2O_3/C composite. For a more detailed description of the oxidation/reduction processes, see Fig. S9.

Iron electrodes based on non-modified iron oxides, Fe_2O_3-TAR-air and Fe_2O_3-SHX-air, present the largest discharge capacities, *ca.* 300 mAh·g_{Fe}^{-1} and 260 mAh· g_{Fe}^{-1} for Fe_2O_3-TAR-N_2 at the 1st plateau (around 450–530 mAh·g_{Fe}^{-1} total discharge capacity). On the other hand, electrodes based on sulphur-modified iron oxides, present lower values of discharge capacity, around 200 mAh·g^{-1} Fe (350–450 mAh·g_{Fe}^{-1} total discharge capacity).

Fig. 2b–2d plot the maximum discharge capacity at the 1st plateau of each electrode against the different textural and crystallographic properties of the iron oxides. As previous studies have shown [49–51], the oxidation/reduction of iron to/from iron(II) hydroxide occurs through a dissolved intermediate, namely $HFeO_2^-$, which then precipitates. This means that the surface atoms dissolve and expose new atoms, so a lower surface area or pore volume does not necessarily mean that fewer atoms are able to react. However, there are trends between the physical-chemical properties and the discharge capacities, when considering sulphur-modified and non-sulphur modified iron oxides as different sets of data. The discharge capacity increases with surface area (Fig. 2b) and crystal size (Fig. 2d), and decreases with pore size (Fig. 2c). Due to the small amount of data points for each subset, nevertheless, it is not possible to establish correlations. The presence of sulphur diminishes the maximum discharge capacity by *ca.* 20–25%, what could be due to sulphur preventing the reduction of iron. As previously shown by XPS, sulphur is present mainly on the surface. In our previous article [35], we showed that sulphate requires several charge/discharge cycles before fully reducing to sulphide (iron sulphide can reduce to metallic iron and act as electroactive material). Besides this, the effect of the different sample morphology cannot be discarded. Samples obtained from sodium hydroxide (SHX) present a platelet-like shape whereas iron

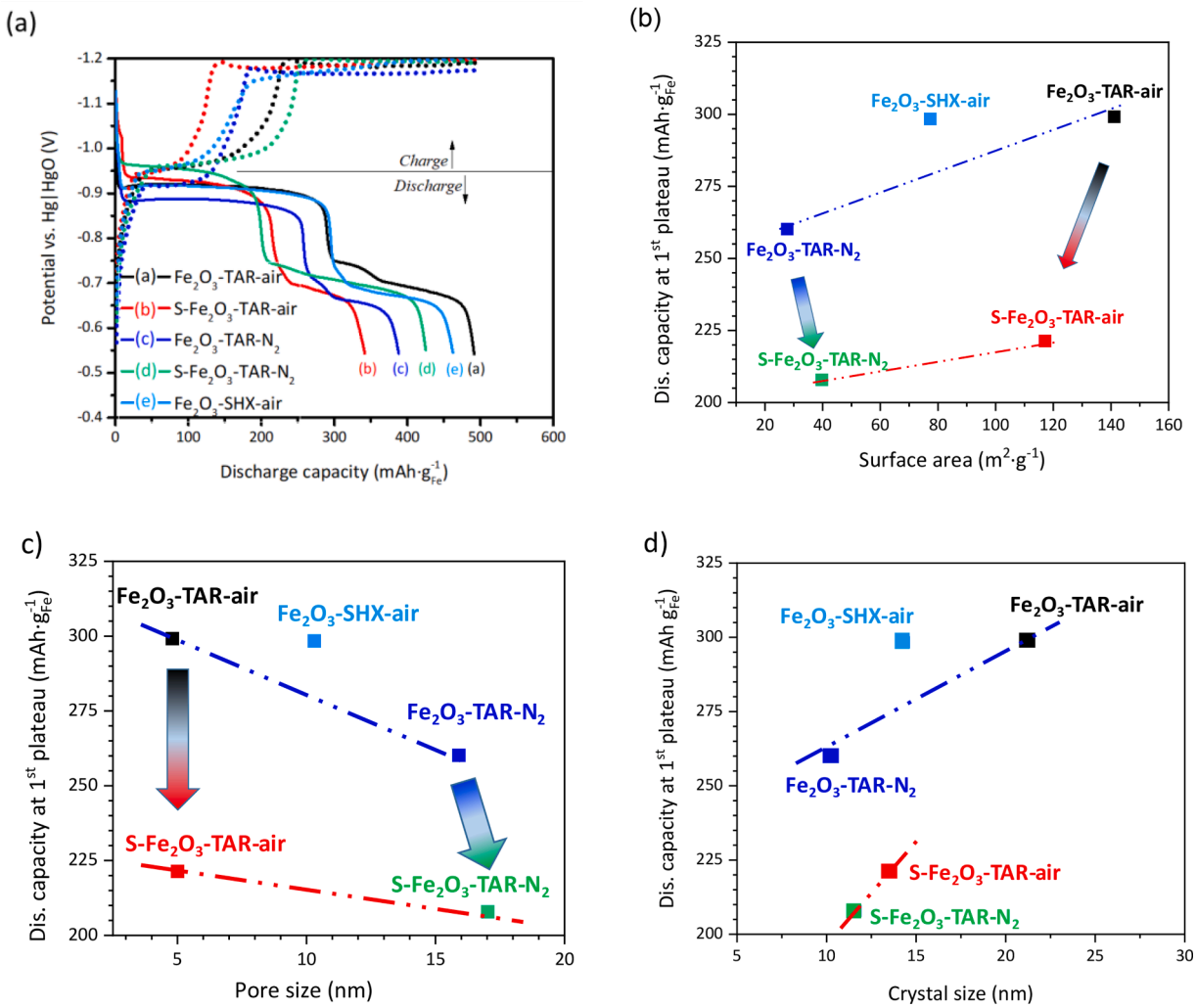

Fig. 2. (a) Chronopotentiometries of the fifth cycle of each electrode and discharge capacity at the first discharge step of the different electrodes *vs.* (b) BET surface area; (c) Average pore size; and (d) average crystal size.

oxides from tartaric acid are constituted either by porous parallelepipeds (TAR-air) or spherical-agglomerates (TAR-N_2) (Fig. S7).

Fig. 3 shows a bar diagram of the maximum, average and discharge capacity at the end of the 20 charge-discharge cycles. As previously established, electrodes manufactured with Fe_2O_3-TAR-air and Fe_2O_3-SHX-air show the greatest maximum discharge capacity (more than 500 mAh·g_{Fe}^{-1} total discharge capacity) but the discharge capacity decrease by 12% and 22% after 20 cycles, respectively. On the contrary, S-Fe_2O_3-TAR-air has the lowest discharge capacity but exhibits a remarkable stability. Both samples obtained from tartaric acid calcined in air (TAR-air), show a higher stability that those calcined in nitrogen (TAR-N_2). In the case of Fe_2O_3-TAR-air, the capacity of the first discharge plateau decreases more than the one of the second (13% and 9%, respectively), which is a sign of passivation due to the formation of an insulating Fe$(OH)_2$ layer. On the other hand, Fe_2O_3-TAR-N_2 loses capacity mainly in the second discharge step (37% in the first plateau and 65%, in the second one), which means that, after Fe^0 is oxidized to $Fe(OH)_2$, it cannot be further oxidized to Fe_3O_4, FeOOH or Fe_2O_3. More evidence of this effect is found in the post-mortem XPS analysis of this electrode (Fig. S11). After full discharge, when the surface of the electrode should be completely oxidized, XPS of Fe2p region reveals that *ca.* 40% of the surface iron has 2+ oxidation state. The O1s region shows approximately that half of the surface oxygen is present as hydroxide, confirming an important coverage of iron (II) hydroxide. This could be evidence for a passivation layer formed by iron (III) oxides, but also the

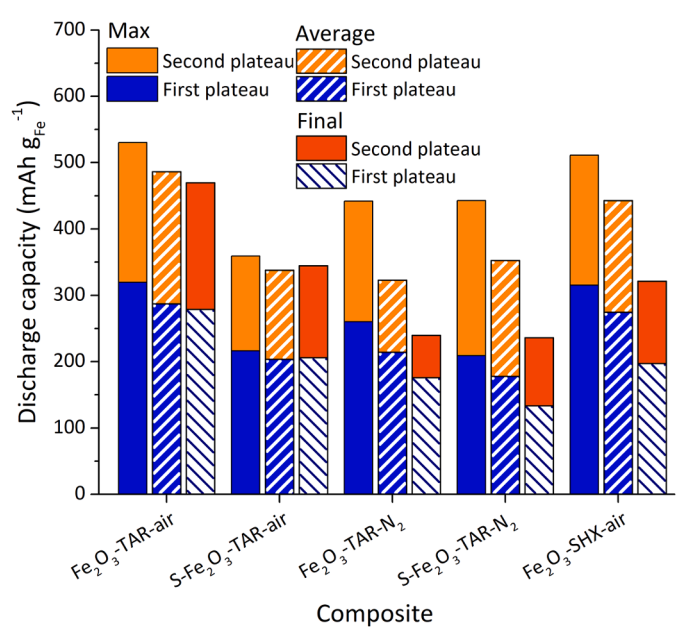

Fig. 3. Maximum, average and final discharge capacity at the 20th cycle of the iron electrodes.

explanation for this phenomenon could be found in the difference in molar volume between metallic iron and iron oxides. The expansion that comes with the oxidation, blocks the pores and prevents the electrolyte from reaching the inner iron (II) hydroxide molecules and, therefore, they cannot react and be oxidized to iron (III).

In a previous work, we established that the capacity of the electrodes slowly declines after a brief period of activation, and that the capacity of the electrodes through cycling can be described by an exponential relation [35]. Fig. 4a shows the evolution of the discharge capacity of the different electrodes during cycling. The number of activation cycles is different for each electrode, ranging from just one cycle for S-Fe_2O_3-TAR-N_2 to 10 for Fe_2O_3-TAR-air. In contrast, the formation of porous iron electrodes studied by Vijayamohanan et al., found that the capacity of the electrodes increases during the first cycles because the iron exposed area increases (due to dissolution and precipitation) and the electrolyte penetrates slowly in the electrode matrix [52]. Weinrich et al., also proposed that formation is partly driven by micro-structural changes in the electrode, caused by hydrogen evolution [30]. Eq. (5) models the behaviour of the electrodes upon cycling after the formation (or activation) period:

$$Q_{dis}(n) = Q_0 * f^{n-i} \tag{5}$$

where Q_{dis} (n) is the discharge capacity of a cycle n, Q_0 is the discharge capacity at the end of activation and i is the number of activation cycles. The f factor, presented for the first time in our previous work, measures the stability of each electrode [34]. An ideal electrode would have an f factor of one, meaning its capacity remains constant over time; whereas an electrode with an f factor near zero would deactivate extremely fast. Fig. 4b shows the model fitted to the data from iron oxide S-Fe_2O_3--TAR-N_2. Fig. S10 shows the fitting of the model to the data from the other electrodes.

Table 5 reports the f factor for each electrode, obtained by applying the model from Eq. (5) to the experimental data obtained.

Iron electrodes present stability factors above 0.95, meaning that, even the less stable material, Fe_2O_3-TAR-N_2, retains more than 95% of its capacity in each cycle, while S-Fe_2O_3-TAR-air, the best electrode in terms of stability, loses less than 0.2% of its discharge capacity with each cycle. The modification of the iron oxides with sulphur results in an increased stability, compensating for the loss in capacity.

The stability factor was plotted against the textural and crystallographic properties of the iron oxides, to investigate the reasons behind the enhanced stability of some electrodes *versus* others (Fig. 5). Considering the R^2 values, the stability factor correlates well with surface area (Fig. 5a) and pore size (Fig. 5c), as demonstrated by the correlation coefficients of 0.87 and 0.90, respectively. It was also

Table 5
Stability factors of the manufactured electrodes.

Electrode	f factor
Fe_2O_3-TAR-air	0.989
S-Fe_2O_3-TAR-air	0.998
Fe_2O_3-TAR-N_2	0.953
S-Fe_2O_3-TAR-N_2	0.962
Fe_2O_3-SHX-air	0.975

investigated whether the textural and crystallographic properties influence the rate capability of the electrodes. For further information, see Fig. S12 in Supporting Information. Pore volume (Fig. 5b) and crystal size (Fig. 5d) do not show a high linear correlation coefficient, however, it is possible to see that there is a general trend that higher pore volume and crystal size result in a better stability. In both of them, it is the superior stability of the electrode S-Fe_2O_3-TAR-air that steers away from the lineal trend. There are three plausible hypotheses that could explain this phenomenon.

The first hypothesis is related to the molar volume change of iron species upon oxidation. A larger surface area and smaller pore size would be related to a better chance to accommodate the molecular expansion of $Fe(OH)_2$ related to metallic iron. However, if molecular expansion was the main cause for deactivation, it would be expected that the main parameter that would improve stability would be pore volume, which is not the case, as R^2 value is lower in Fig. 5b than in Fig. 5a and 5c.

The second hypothesis bases the cause of deactivation on the plugging of the pores in iron oxides, thus decreasing the active area [26]. Our evidence rules out this hypothesis, as a larger pore diameter does not correlate with a more stable electrode. Actually, the correlation is the opposite. If the clogging of the pores was the reason for the deactivation of the electrode, electrodes with bigger pore diameters would be more stable, as it is harder for larger pores to be clogged than smaller ones.

The third hypothesis relates to deactivation through passivation. Passivation occurs due to the irreversible formation of non-reactive species [8] and loss of electrical conductivity because of an isolating $Fe(OH)_2$ layer with an increased electrical resistance [52]. Both smaller pore size and larger surface area enhance the contact between iron (or iron oxides) and carbon phases. This better contact reduces electrical resistance, hence, enhancing conductivity and reactivity of the metallic oxide phase. In the case of crystal size (Fig. 5d), an insulating layer, as proposed by Figueredo-Rodríguez et al., can cover smaller crystallites more easily, and hence the positive correlation [53]. The low value of the correlation coefficient is explained by the exceptional performance of S-Fe_2O_3-TAR-air, which is caused by its textural properties and the

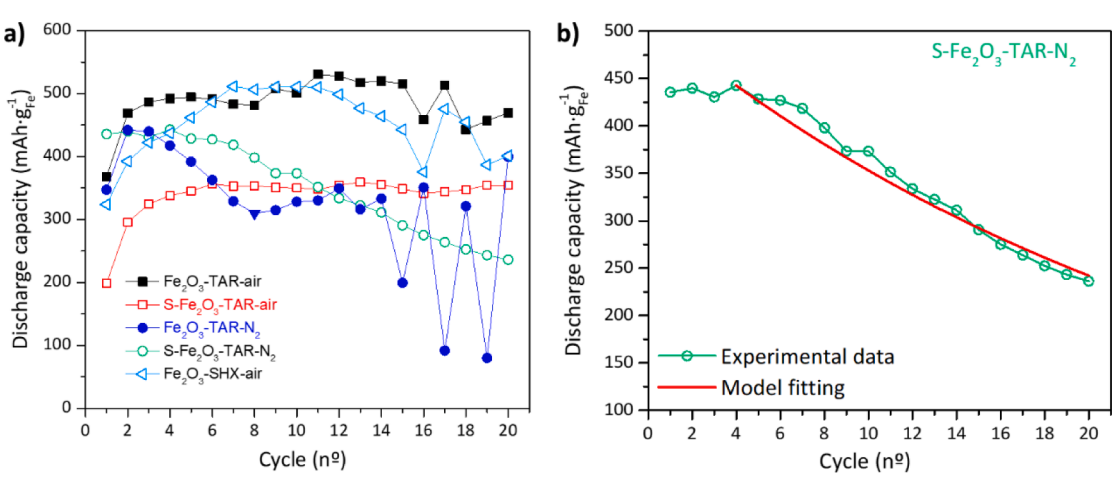

Fig. 4. (a) Discharge capacity of the electrodes along 20 charge-discharge cycles. Charge rate: 0.4 C, discharge rate: 0.2 C. (b) Comparison between the experimental data and the model from Eq. (5) for the electrode S-Fe_2O_3-TAR-N_2.

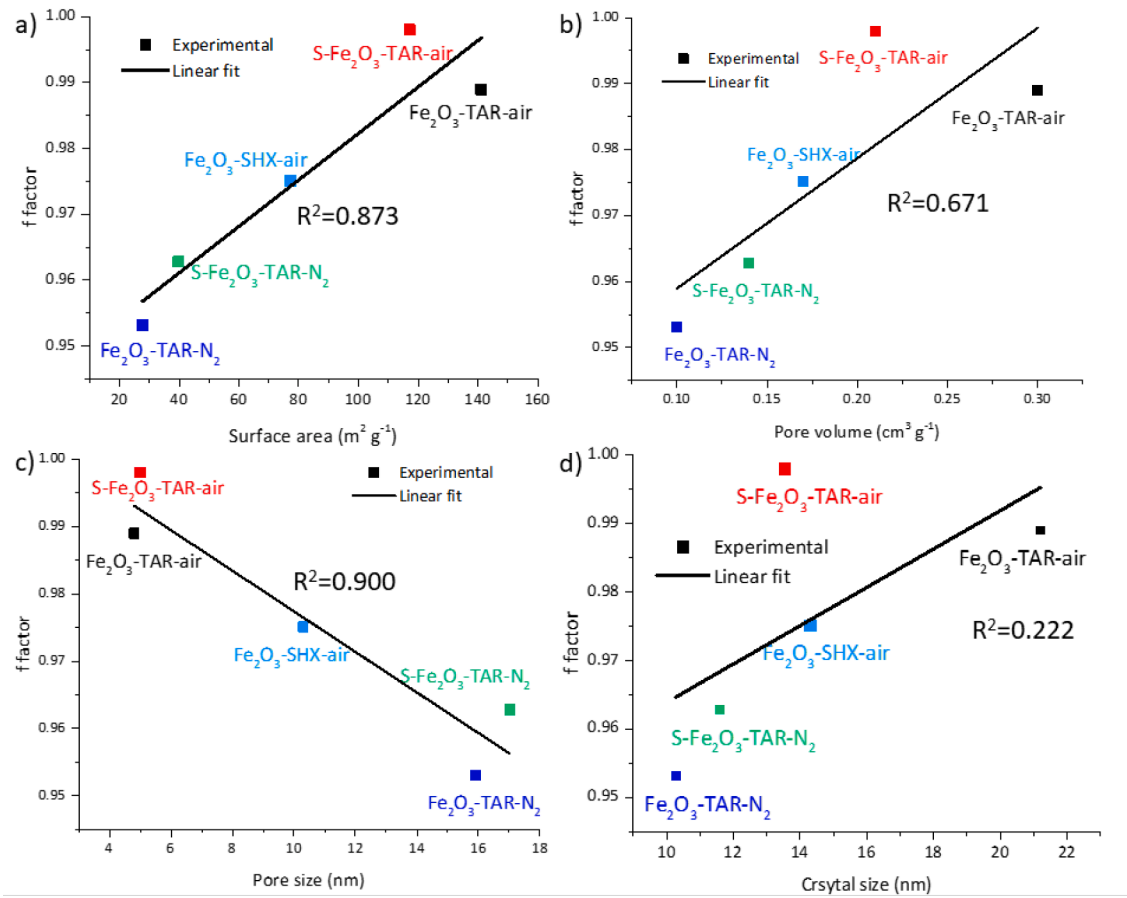

Fig. 5. Stability factors of the different electrodes *vs.* (a) Surface area; (b) Pore volume; (c) Average pore size; and (d) Average crystal size.

presence of sulphur, as will be discussed later.

To test this last hypothesis, we performed electrochemical impedance spectroscopy (EIS) studies of the different electrodes after the first charge-discharge cycle and after 15 cycles (Figs. 6 and S13) and modelled the equivalent circuit of the different phenomena occurring during the second charge step (Eq. (1) in right-to-left direction). The Nyquist diagrams show the typical "tilted", "flattened" semicircle of an electrochemical charge transfer process in a porous electrode, followed by the straight diagonal line related to diffusion impedance – Warburg impedance [54–56]. It can be seen that the Nyquist diagrams of the electrode S-Fe_2O_3-TAR-air (Fig. 6a) are almost identical after 1 cycle and after 15 cycles, while the diagrams of electrode S-Fe_2O_3-TAR-N_2 differ significantly before and after cycling (Fig. 6b) with the semi-circle increasing in diameter, indicating a larger charge transfer resistance.

The equivalent circuit proposed for the reaction (Fig. 7) is in accordance with what Orazem and Tribollet propose for porous electrodes [57]. First, the electrolyte resistance is considered (R1). As the electrolyte is highly concentrated, and the distance from the working to the reference electrode is minimum (< 5 mm) this resistance is low, *circa* 70 mΩ.

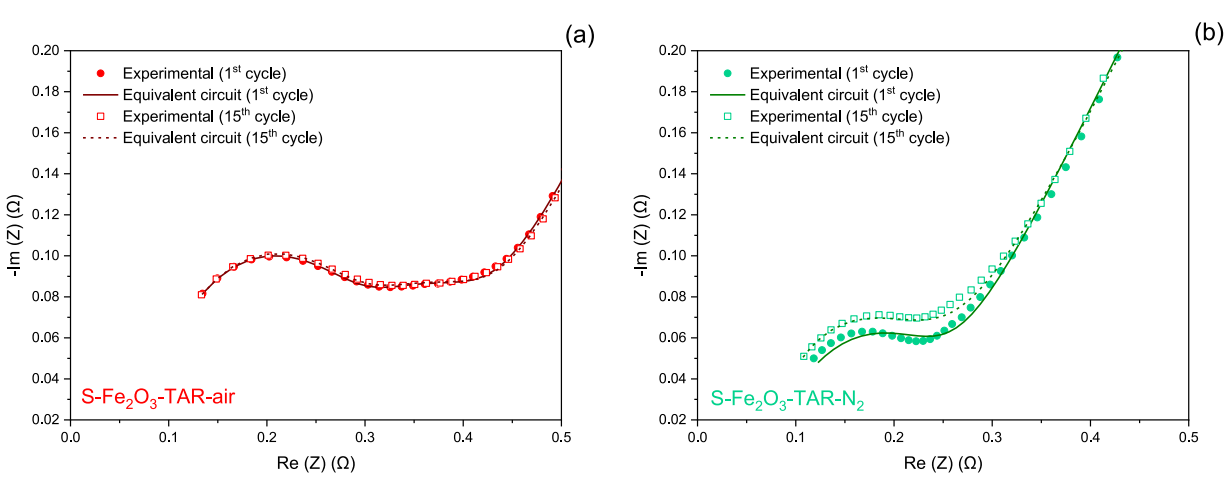

Fig. 6. Nyquist diagrams of electrochemical impedance spectroscopy studies performed at −1.16 V *vs.* Hg|HgO for electrodes: (a) S-Fe_2O_3-TAR-air and (b) S-Fe_2O_3-TAR-N_2.

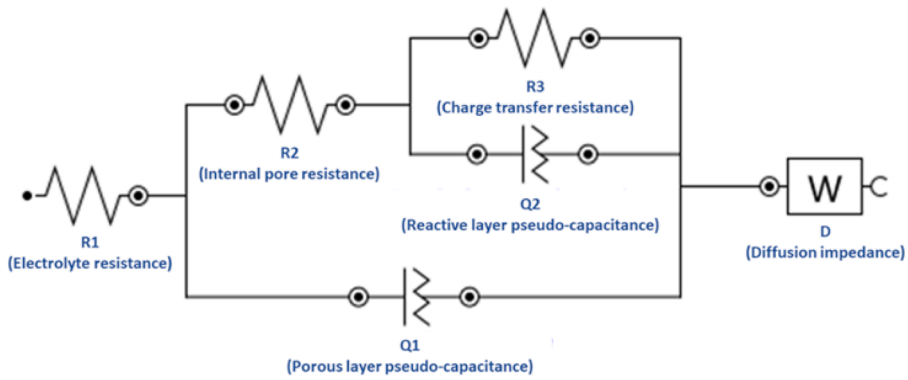

Fig. 7. Proposed equivalent circuit for the reduction of iron (II) hydroxide to iron in porous electrodes.

Then, as the concentration of the electrolyte inside the pores is not the same as in the bulk of the electrolyte, there is an electric resistance inside the pores (R2). This resistance is in parallel with the electrical double layer capacitance of the external surface of the porous layer (Q1). The internal pore resistance is in series with the charge transfer resistance (R3), which is also in parallel with the capacitance of the reactive layer (Q2). Finally, there is the impedance related to the diffusion of reactants and products from the liquid to the surface (D).

The fitted parameters (Table 6) show that, after 15 cycles, the charge transfer resistance (R3) of the electrode S-Fe_2O_3-TAR-air increases from 69.1 mΩ to 72.0 mΩ, which is only a 4.2% increment. On the other hand, in the electrode manufactured with S-Fe_2O_3-TAR-N_2, the charge transfer resistance (R3) increases almost sevenfold, from 18.7 to 127 mΩ. This is consistent with the stability studies, which show a much faster deactivation of the S-Fe_2O_3-TAR-N_2 electrode. A higher charge transfer resistance, *i.e.* a lower charge transfer admittance, is compatible with the presence of a non-conductive – and hence, non-reactive – covering layer, which is our hypothesis. In the case of S-Fe_2O_3-TAR-air, the large surface area and the small pore size entails a better contact between the carbon conductive phase and the iron hydroxide phase, thus enhancing conductivity and favoring the reduction of the iron hydroxide. In contrast, because of the lower surface area of S-Fe_2O_3-TAR-N_2, the iron (II) hydroxide particles have less contact with carbon, incrementing the electric resistance and being more difficult for it to reduce. Similar trends are observed in electrodes Fe_2O_3-TAR-air and Fe_2O_3-TAR-N_2 (Fig. S13 and Table S3 in the Supporting Information). Coincidently, sample calcined in air shows less variation in the charge transfer resistance (R3). In sample Fe_2O_3-TAR-N_2, the charge transfer resistance increases more than threefold, reaching 175 mV, the highest of all the samples considered.

In addition, it is possible to see that the pore diffusion resistance (R2) is considerably higher in electrode S-Fe_2O_3-TAR-air than in electrode S-Fe_2O_3-TAR-N_2, consistent with the fact that the oxide S-Fe_2O_3-TAR-air has 50% more porosity than S-Fe_2O_3-TAR-N_2 (Table 3), but S-Fe_2O_3-TAR-N_2 has a greater pore diameter, which means less electrolyte conduction resistance inside the pores. More evidence supporting our deactivation hypothesis can be found in post-mortem characterizations. Electrodes S-Fe_2O_3-TAR-air and S-Fe_2O_3-TAR-N_2 were subjected to pre and post-cycling nitrogen physisorption experiments (see Fig. S14 in the Supporting Information).

Table 6
Optimized parameters of equivalent circuit (Fig. 7) for the shown electrodes.

Electrode	S-Fe_2O_3-TAR-air		S-Fe_2O_3-TAR-N_2	
	1 cycle	15 cycles	1 cycle	15 cycles
R1 (mΩ)	67.5	69.2	71.0	71.3
R2 (mΩ)	239	239	159	47.1
R3 (mΩ)	69.1	72.0	18.7	127
Q1 – Y_0 (mS^n)	6.09	5.91	28.4	2.13
Q1 – n	0.823	0.830	0.693	0.998
Q2 – Y_0 (mS^n)	149	153	720	176
Q2 – n	0.887	0.887	0.692	0.513
D – Y_0 ($S^{0.5}$)	1.68	1.70	1.13	1.13

The difference in stability between the sulphur-modified iron oxides (S-Fe_2O_3-TAR) and their non sulphur-modified (Fe_2O_3-TAR) counterparts is also compatible with the passivation due to non-conductive species. Our previous studies [35] showed that the sulphate present in the sulphur-modified iron oxides reduces to sulphide upon cycling. Sulphide has proven to prevent passivation by reacting with iron (II) hydroxide to form FeS, which is a better electric conductor than $Fe(OH)_2$ [58]. As S-Fe_2O_3-TAR-air showed the best stability upon cycling, a long run test of 130 charge-discharge cycles (more than 500 h) was performed with this electrode (Fig. 8). After 7 cycles, the electrode follows the trend of exponential deactivation as in Eq. (5), meaning the model is a good predictor of the long-term behaviour of the electrode. Aside from a few oscillations around cycles 45 and 90 – probably due to the formation of hydrogen bubbles –, the discharge capacity fits the one predicted by the model, and the overall R^2 coefficient is 0.73. The *f* factor calculated for this experiment is 0.997, which is just 0.1% lower than the one calculated for the 20 cycles experiment (shown in Fig. 4). Still, this difference means that, after 100 cycles, the electrode loses 26% of its initial discharge capacity, while the loss would have been only 18% if the long-term stability factor had been 0.998, as was calculated in the short experiment (Fig. 4).

Comparing our electrodes to others reported in literature, we could see that our electrode performs comparatively well to similar formulations. For instance, Paulraj et al. manufactured electrodes that were able to achieve 644 mAh g_{Fe}^{-1} of discharge capacity and lose between 10 and 25% of it after 100 cycles, but using much more complicated formulations, including copper, tin and carbon nanotubes in the electrode and lithium hydroxide in the electrolyte [20]. Other studies focus on shorter cycling, not reaching more than 30 cycles, and showing a less stable behaviour than our electrode [33,59–62]. Other works reporting hundreds of cycles (up to 1200) are based on carbonyl iron, which has shown to be able to retain its capacity for even a few hundred cycles [13,14,18], but with capacities of no more than 300 mAh g_{Fe}^{-1} and always with the addition to the electrode or electrolyte of substances such as bismuth sulphide, sodium sulphide and bismuth oxide. Besides, carbonyl iron requires long activation periods, of even more than a hundred cycles. The only electrode found in literature based on carbonyl iron with a short activation period (25 cycles) and high discharge capacity (up to 650 mAh g_{Fe}^{-1}) is the one manufactured by Figueredo-Rodríguez et al. [53], who only tested 40 cycles. These results place our electrode as an interesting, low-cost, well performing alternative.

4. Conclusions

Iron electrodes were manufactured based on mesoporous sulphur-

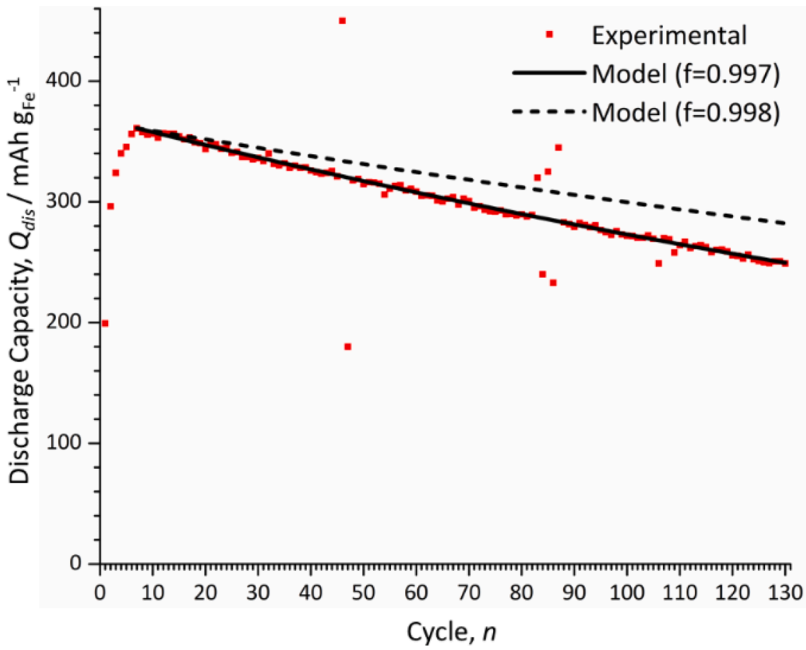

Fig. 8. Extended cycling of the S-Fe_2O_3-TAR-air electrode.

modified iron oxide and commercial carbon black. The physical-chemical features of the iron oxides, especially the textural properties, were tuned upon changing the synthesis conditions. We determined that textural properties, especially surface area and pore size, affect the discharge capacity of the iron oxides. More importantly, these properties have a significant impact on the stability of the electrodes. A large surface area and small pore size were linearly correlated with enhanced stability, because a good contact between the iron oxide and carbon phases was found to be crucial to prevent passivation. Electrochemical impedance spectroscopy studies evidenced that passivation is caused by a non-conductive iron (II) hydroxide layer that inhibits the reduction of this species to metallic iron. The charge transfer resistance in the Fe $(OH)_2$ to Fe reduction increases significantly in the fast-deactivating electrodes. Sulphur-modification was found to have a similar effect as the combination of using an electrode with large surface area and good contact with the carbon phase, as sulphate reduces to sulphide and forms iron (II) sulphide, which replaces iron (II) hydroxide and has a greater conductivity. Our most porous sulphur-doped iron oxide was able to run 130 cycles losing 0.3% of its discharge capacity with each cycle. All these findings provide key insights into both the deactivation mechanism and the physical-chemical properties that could prevent it, advancing one step forward the optimization and design of alkaline iron electrodes.

CRediT authorship contribution statement

Nicolás I. Villanueva-Martínez: Investigation, Methodology, Data curation, Writing – original draft, Supervision, Writing – review & editing. **Cinthia Alegre:** Conceptualization, Writing – review & editing, Data curation, Writing – original draft, Supervision. **Javier Rubín:** Conceptualization, Supervision, Writing – review & editing. **Rachel Mckerracher:** Investigation, Writing – review & editing, Supervision. **Carlos Ponce de León:** Investigation, Resources, Supervision, Writing – review & editing. **Horacio Antonio Figueredo Rodríguez:** Supervision, Writing – review & editing. **María Jesús Lázaro:** Investigation, Funding acquisition, Supervision, Writing – review & editing.

Declaration of Competing Interest

The authors declare that they have no known competing financial interests or personal relationships that could have appeared to influence the work reported in this paper.

Acknowledgements

The authors wish to acknowledge Ministerio de Ciencia e Innovación and Agencia Estatal de Investigación (MCIN/AEI/10.13039/501100011033) for the PID2020-115848RB-C21 grant. The authors also thank the European Union and the NextGeneration EU program for the funding on grant TED2021-130279A-I00. Authors also acknowledge Gobierno de Aragón (DGA) for the financial support to Grupo de Conversión de Combustibles (T06_20R). N. Villanueva acknowledges also DGA for his pre-doctoral contract. The authors would like to acknowledge the use of the Servicio General de Apoyo a la Investigación-SAI, Universidad de Zaragoza. The authors would like to thank Dr. Javier Hernández-Ferrer for his contribution and insights during the analyses of EIS.

Supplementary materials

Supplementary material associated with this article can be found, in the online version, at doi:10.1016/j.electacta.2023.142964.

References

[1] A.G. Olabi, E.T. Sayed, T. Wilberforce, A. Jamal, A.H. Alami, K. Elsaid, S.M. A. Rahman, S.K. Shah, M.A. Abdelkareem, Metal-air batteries–a review, Energies 14 (2021) 1–46, https://doi.org/10.3390/en14217373.

[2] Q. Liu, Z. Pan, E. Wang, L. An, G. Sun, Aqueous metal-air batteries: fundamentals and applications, Energy Storage Mater. 27 (2020) 478–505, https://doi.org/10.1016/j.ensm.2019.12.011.

[3] L. Wang, D. Snihirova, M. Deng, B. Vaghefinazari, W. Xu, D. Höche, S.V. Lamaka, M.L. Zheludkevich, Sustainable aqueous metal-air batteries: an insight into electrolyte system, Energy Storage Mater. 52 (2022) 573–597, https://doi.org/10.1016/j.ensm.2022.08.032.

[4] H. Weinrich, Y.E. Durmus, H. Tempel, H. Kungl, R.A. Eichel, Silicon and iron as resource-efficient anode materials for ambient-temperature metal-air batteries: a review, Materials 12 (2019) 2134, https://doi.org/10.3390/ma121321341-55 (Basel).

[5] R.D. McKerracher, C. Ponce de Leon, R.G.A. Wills, A.A. Shah, F.C. Walsh, A review of the iron-air secondary battery for energy storage, ChemPlusChem 80 (2015) 323–335, https://doi.org/10.1002/cplu.201402238.

[6] H. Weinrich, M. Gehring, H. Tempel, H. Kungl, R.A. Eichel, Impact of the charging conditions on the discharge performance of rechargeable iron-anodes for alkaline

iron air batteries, J. Appl. Electrochem 48 (2018) 451–462, https://doi.org/10.1007/s10800-018-1176-4.
[7] J.O.G. Posada, P.J. Hall, Controlling hydrogen evolution on iron electrodes, Int. J. Hydrog. Energy 41 (2016) 20807–20817, https://doi.org/10.1016/j.ijhydene.2016.04.123.
[8] D.C. Lee, D. Lei, G. Yushin, Morphology and phase changes in iron anodes affecting their capacity and stability in rechargeable alkaline batteries, ACS Energy Lett. 3 (2018) 794–801, https://doi.org/10.1021/acsenergylett.8b00063.
[9] A.B. Hrubiak, V.O. Kotsyubynsky, V.V. Moklyak, B.K. Ostafiychuk, P.I. Kolkovsky, S.V. Fedorchenko, B.I. Rachiy, The electrical conductivity and photocatalytic activity of ultrafine iron hydroxide/oxide systems, Mol. Cryst. Liq. Cryst. 670 (2018) 97–111, https://doi.org/10.1080/15421406.2018.1542070.
[10] R.M. Cornell, U. Schwertmann, Electronic, electrical and magnetic properties and colour. The Iron Oxides: Structure, Properties, Reactions, Occurences and Uses, 2nd ed., Wiley-VCH Verlag GmbH & Co. KGaA, 2003, pp. 111–137, https://doi.org/10.1002/3527602097.
[11] B.T. Hang, M. Eashira, I. Watanabe, S. Okada, J.I. Yamaki, S.H. Yoon, I. Mochida, The effect of carbon species on the properties of Fe/C composite for metal-air battery anode, J. Power Sources 143 (2005) 256–264, https://doi.org/10.1016/j.jpowsour.2004.11.044.
[12] A.S. Rajan, S. Sampath, A.K. Shukla, An *in situ* carbon-grafted alkaline iron electrode for iron-based accumulators, Energy Environ. Sci. 7 (2014) 1110–1116, https://doi.org/10.1039/c3ee42783h.
[13] H. Weinrich, J. Pleie, B. Schmid, H. Tempel, H. Kungl, R.A. Eichel, *In situ* hydrogen evolution monitoring during the electrochemical formation and cycling of pressed-plate carbonyl iron electrodes in alkaline electrolyte, Batter. Supercaps 5 (2022) 3–10, https://doi.org/10.1002/batt.202100415.
[14] A.K. Manohar, C. Yang, S.R. Narayanan, The role of sulfide additives in achieving long cycle life rechargeable iron electrodes in alkaline batteries, J. Electrochem. Soc. 162 (2015) A1864–A1872, https://doi.org/10.1149/2.0741509jes.
[15] B.T. Hang, S.H. Yoon, S. Okada, J. Ichi Yamaki, Effect of metal-sulfide additives on electrochemical properties of nano-sized Fe_2O_3-loaded carbon for Fe/air battery anodes, J. Power Sources 168 (2007) 522–532, https://doi.org/10.1016/j.jpowsour.2007.02.067.
[16] D. Mitra, A.S. Rajan, A. Irshad, S.R. Narayanan, High performance iron electrodes with metal sulfide additives, J. Electrochem. Soc. 168 (2021), 030518, https://doi.org/10.1149/1945-7111/abe9c7.
[17] A.S. Rajan, M.K. Ravikumar, K.R. Priolkar, S. Sampath, A.K. Shukla, Carbonyl-iron electrodes for rechargeable-iron batteries, Electrochem. Energy Technol. 1 (2014) 2–9, https://doi.org/10.1515/eetech-2014-0002.
[18] C. Yang, A.K. Manohar, S.R. Narayanan, A high-performance sintered iron electrode for rechargeable alkaline batteries to enable large-scale energy storage, J. Electrochem. Soc. 164 (2017) A418–A429, https://doi.org/10.1149/2.1161702jes.
[19] B.T. Hang, T. Watanabe, M. Egashira, I. Watanabe, S. Okada, J. ichi Yamaki, The effect of additives on the electrochemical properties of Fe/C composite for Fe/air battery anode, J. Power Sources 155 (2006) 461–469, https://doi.org/10.1016/j.jpowsour.2005.04.010.
[20] A.R. Paulraj, Y. Kiros, M. Chamoun, H. Svengren, D. Noréus, M. Göthelid, B. Skårman, H. Vidarsson, M.B. Johansson, Electrochemical performance and in operando charge efficiency measurements of Cu/Sn-doped nano iron electrodes, Batteries 5 (2019) 1–15, https://doi.org/10.3390/batteries5010001.
[21] P.S. Arunkumar, T. Maiyalagan, S. Kheawhom, S. Mao, Z. Jiang, Effect of carbon material additives on hydrogen evolution at rechargeable alkaline iron battery electrodes, Mater. Sci. Energy Technol. 4 (2021) 236–241, https://doi.org/10.1016/j.mset.2021.06.007.
[22] H.T. Bui, T.M. Vu, Hydrothermal preparation of Fe_2O_3 nanoparticles for Fe-air battery anodes, J. Electron. Mater. 48 (2019) 7123–7130, https://doi.org/10.1007/s11664-019-07522-x.
[23] J. Yao, Y. Liu, H. Zhang, L. Ma, T. Meng, N. Li, J. Jiang, J. Zhu, C.M. Li, Configuring optimal FeS_2@carbon nanoreactor anodes: toward insights into pyrite phase change/failure mechanism in rechargeable Ni-Fe cells, ACS Appl. Mater. Interfaces 11 (2019) 42032–42041, https://doi.org/10.1021/acsami.9b12153.
[24] J.O. Gil Posada, P.J. Hall, Post-hoc comparisons among iron electrode formulations based on bismuth, bismuth sulphide, iron sulphide, and potassium sulphide under strong alkaline conditions, J. Power Sources 268 (2014) 810–815, https://doi.org/10.1016/j.jpowsour.2014.06.126.
[25] B.E. Poling, G.H. Thomson, D.G. Friend, R.L. Rowley, W.V. Wilding, Physical and chemical data, in: D.W. Green (Ed.), Perry's Chemical Engineers' Handbook, 8th ed., McGraw-Hill, 2008 https://doi.org/10.1036/0071511253.
[26] T. Um, S.K. Wilke, H. Choe, D.C. Dunand, Effects of pore morphology on the cyclical oxidation/reduction of iron foams created via camphene-based freeze casting, J. Alloy. Compd. 845 (2020), 156278, https://doi.org/10.1016/j.jallcom.2020.156278.
[27] W.A. Bryant, The importance of physical structure to the capacity of porous iron electrodes, J. Electrochem. Soc. 126 (1979) 1899–1901, https://doi.org/10.1149/1.2128822.
[28] T.S. Balasubramanian, A.K. Shukla, Effect of metal-sulfide additives on charge/discharge reactions of the alkaline iron electrode, J. Power Sources 41 (1993) 99–105, https://doi.org/10.1016/0378-7753(93)85008-C.
[29] J.O.G. Posada, P.J. Hall, Towards the development of safe and commercially viable nickel–iron batteries: improvements to Coulombic efficiency at high iron sulphide electrode formulations, J. Appl. Electrochem. 46 (2016) 451–458, https://doi.org/10.1007/s10800-015-0911-3.
[30] H. Weinrich, M. Gehring, H. Tempel, H. Kungl, R.A. Eichel, Electrode thickness-dependent formation of porous iron electrodes for secondary alkaline iron-air batteries, Electrochim. Acta 314 (2019) 61–71, https://doi.org/10.1016/j.electacta.2019.05.025.
[31] H. Weinrich, M. Gehring, H. Tempel, H. Kungl, R.A. Eichel, Impact of the charging conditions on the discharge performance of rechargeable iron-anodes for alkaline iron–air batteries, J. Appl. Electrochem. 48 (2018) 451–462, https://doi.org/10.1007/s10800-018-1176-4.
[32] A.K. Manohar, C. Yang, S. Malkhandi, G.K.S. Prakash, S.R. Narayanan, Enhancing the performance of the rechargeable iron electrode in alkaline batteries with bismuth oxide and iron sulfide additives, J. Electrochem. Soc. 160 (2013) A2078–A2084, https://doi.org/10.1149/2.066311jes.
[33] A.K. Manohar, S. Malkhandi, B. Yang, C. Yang, G.K. Surya Prakash, S. R. Narayanan, A high-performance rechargeable iron electrode for large-scale battery-based energy storage, J. Electrochem. Soc. 159 (2012) A1209–A1214, https://doi.org/10.1149/2.034208jes.
[34] D. Lei, D.C. Lee, E. Zhao, A. Magasinski, H.R. Jung, G. Berdichevsky, D. Steingart, G. Yushin, Iron oxide nanoconfined in carbon nanopores as high capacity anode for rechargeable alkaline batteries, Nano Energy 48 (2018) 170–179, https://doi.org/10.1016/j.nanoen.2018.03.035.
[35] N. Villanueva, C. Alegre, J. Rubin, H.A. Figueredo-Rodríguez, R.D. McKerracher, C. Ponce De León, M.J. Lázaro, Iron electrodes based on sulfur-modified iron oxides with enhanced stability for iron-air batteries, ACS Appl. Energy Mater. 5 (2022) 13439–13451, https://doi.org/10.1021/acsaem.2c02123.
[36] K. Li, Y. Zhao, M.J. Janik, C. Song, X. Guo, Facile preparation of magnetic mesoporous Fe_3O_4/C/Cu composites as high performance Fenton-like catalysts, Appl. Surf. Sci. 396 (2017) 1383–1392, https://doi.org/10.1016/j.apsusc.2016.11.170.
[37] A. Aharoni, E.H. Frei, M. Schieber, Some properties of γ-Fe_2O_3 obtained by hydrogen reduction of α-Fe_2O_3, J. Phys. Chem. Solids 23 (1962) 545–554, https://doi.org/10.1016/0022-3697(62)90512-7.
[38] R.M. Taylor, Maghemite in soils and its origin II. Maghemite syntheses at ambient temperature and pH 7, Clay Miner. 10 (1974) 299–310, https://doi.org/10.1180/claymin.1974.010.4.08.
[39] C. Li, Z. Deng, C. Wei, G. Fan, X. Li, M. Li, Y. Wang, Production of low-sulfur hematite by hydrothermal oxydrolysis of ferrous sulfate, Hydrometallurgy 178 (2018) 294–300, https://doi.org/10.1016/j.hydromet.2018.05.012.
[40] N.N. Greennwood, T.C. Gibb, Mössbauer Spectroscopy, Chapman and Hall Ltd., London, 1971.
[41] J. Gust, J. Suwalski, Use of Mössbauer spectroscopy to study reaction products of polyphenols and iron compounds, Corrosion 50 (1994) 355–365.
[42] J. de Oñate Martínez, C.D. Aguila, J.F. Bertrán, E.R. Ruíz, C.P. Vergara, R. R. Malherbe, Tribochemical reactions of erionite and Na-LTA zeolites with Fe2 (SO4) 3.5 H2O: a mössbauer study, Hyperfine Interact. 73 (1992) 371–375.
[43] J. Rouquerol, F. Rouquerol, P. Llewellyn, G. Maurin, K.S.W. Sing, Adsorption by Powders and Porous Solids: Principles, Methodology and Applications, Academic Press, 2013.
[44] S. Lowell, J.E. Shields, M.A. Thomas, M. Thommes, Characterization of Porous Solids and Powders: Surface Area, Pore Size and Density, Springer Science & Business Media, 2006.
[45] M. Thommes, K. Kaneko, A.V. Neimark, J.P. Olivier, F. Rodriguez-Reinoso, J. Rouquerol, K.S.W. Sing, Physisorption of gases, with special reference to the evaluation of surface area and pore size distribution (IUPAC Technical Report), Pure Appl. Chem. 87 (2015) 1051–1069, https://doi.org/10.1515/pac-2014-1117.
[46] J. Du, J. Bao, X. Fu, C. Lu, S.H. Kim, Mesoporous sulfur-modified iron oxide as an effective Fenton-like catalyst for degradation of bisphenol A, Appl. Catal. B Environ. 184 (2016) 132–141, https://doi.org/10.1016/j.apcatb.2015.11.015.
[47] B. Meyer, Elemental sulfur, Chem. Rev. 76 (1976) 367–388, https://doi.org/10.1021/cr60301a003.
[48] B. McDonald, J. Rice, J. Stewart, Decomposition characteristics of an elemental sulfur doped polysulfide based ramjet fuel, Combust. Flame 176 (2017) 1–11, https://doi.org/10.1016/j.combustflame.2016.10.012.
[49] H. Weinrich, J. Come, H. Tempel, H. Kungl, R.A. Eichel, N. Balke, Understanding the nanoscale redox-behavior of iron-anodes for rechargeable iron-air batteries, Nano Energy 41 (2017) 706–716, https://doi.org/10.1016/j.nanoen.2017.10.023.
[50] B. Miiller-Ziilow, R. Lacmann, M.A. Schneeweiss, Topological aspects of iron corrosion in alkaline solution by means of scanning force microscopy (SFM), Surf. Sci. 311 (31) (1994) 153–158.
[51] D.M. Dražić, C.S. Hao, The anodic dissolution process on active iron in alkaline solutions, Electrochim. Acta 27 (1982) 1409–1415, https://doi.org/10.1016/0013-4686(82)80031-5.
[52] B.T. Hang, D.H. Thang, Effect of additives on the electrochemical properties of Fe_2O_3/C nanocomposite for Fe/air battery anode, J. Electroanal. Chem. 762 (2016) 59–65, https://doi.org/10.1016/j.jelechem.2015.12.012.
[53] H.A. Figueredo-Rodríguez, R.D. McKerracher, C. Ponce de León, F.C. Walsh, Improvement of negative electrodes for iron-air batteries: comparison of different iron compounds as active materials, J. Electrochem. Soc. 166 (2019) A107–A117, https://doi.org/10.1149/2.1071816jes.
[54] H. Nara, T. Yokoshima, T. Osaka, Technology of electrochemical impedance spectroscopy for an energy-sustainable society, Curr. Opin. Electrochem. 20 (2020) 66–77, https://doi.org/10.1016/j.coelec.2020.02.026.
[55] N. Ogihara, Y. Itou, T. Sasaki, Y. Takeuchi, Impedance spectroscopy characterization of porous electrodes under different electrode thickness using a symmetric cell for high-performance lithium-ion batteries, J. Phys. Chem. C 119 (2015) 4612–4619, https://doi.org/10.1021/jp512564f.
[56] L.M. Gassa, J.R. Vilche, M. Ebert, K. Jüttner, W.J. Lorenz, Electrochemical impedance spectroscopy on porous electrodes, J. Appl. Electrochem. 20 (1990) 677–685, https://doi.org/10.1007/BF01008882.

[57] M.E. Orazem, B. Tribollet, Chapter 9: equivalent circuit analogs. Electrochemical Impedance Spectroscopy, 2nd ed., John Wiley & Sons, Inc., Hoboken, New Jersey, 2008, pp. 154–162.

[58] Q. Wang, Y. Wang, Overcoming the limiting step of Fe_2O_3 reduction via *in situ* sulfide modification, ACS Appl. Mater. Interfaces 8 (2016) 10334–10342, https://doi.org/10.1021/acsami.6b01737.

[59] H. Kitamura, L. Zhao, B.T. Hang, S. Okada, J.I. Yamaki, Effect of binder materials on cycling performance of Fe_2O_3 electrodes in alkaline solution, J. Power Sources 208 (2012) 391–396, https://doi.org/10.1016/j.jpowsour.2012.02.051.

[60] B.T. Hang, H. Hayashi, S.H. Yoon, S. Okada, J. Ichi Yamaki, Fe_2O_3-filled carbon nanotubes as a negative electrode for an Fe-air battery, J. Power Sources 178 (2008) 393–401, https://doi.org/10.1016/j.jpowsour.2007.12.012.

[61] A. Ito, L. Zhao, S. Okada, J.I. Yamaki, Synthesis of nano-Fe_3O_4-loaded tubular carbon nanofibers and their application as negative electrodes for Fe/air batteries, J. Power Sources 196 (2011) 8154–8159, https://doi.org/10.1016/j.jpowsour.2011.05.043.

[62] B.T. Hang, T. Watanabe, M. Eashira, S. Okada, J.I. Yamaki, S. Hata, S.H. Yoon, I. Mochida, The electrochemical properties of Fe_2O_3-loaded carbon electrodes for iron-air battery anodes, J. Power Sources 150 (2005) 261–271, https://doi.org/10.1016/j.jpowsour.2005.02.028.

SUPPORTING INFORMATION

Investigation of the properties influencing the deactivation of iron electrodes in iron-air batteries

Nicolás I. Villanueva-Martínez[1], Cinthia Alegre[1,], Javier Rubin[2,3], Rachel Mckerracher[4], Carlos Ponce de León[4], Horacio Antonio Figueredo Rodríguez[5], María Jesús Lázaro[1,*]*

[1]Instituto de Carboquímica, Consejo Superior de Investigaciones Científicas. C/. Miguel Luesma Castán, 4, 50018, Zaragoza (Spain)
[2] Instituto de Nanociencia y Materiales de Aragón (INMA), CSIC-Universidad de Zaragoza, 50009, Zaragoza (Spain)
[3] Departamento de Ciencia y Tecnología de Materiales y Fluidos, Universidad de Zaragoza, 50018 Zaragoza (Spain)
[4] Electrochemical Engineering Laboratory, Energy Technology Research Group, Faculty of Engineering and Physical Sciences, University of Southampton, Highfield Campus, University Road, Southampton, SO17 1BJ, United Kingdom
[5] Escuela de Ingeniería y Ciencias, Tecnológico de Monterrey, Campus Ciudad de México, 14380, Tlalpan, CDMX, México
*Corresponding authors: C.A. (cinthia@icb.csic.es); M.J.L. (mlazaro@icb.csic.es)

S1.- Electrode manufacturing scheme

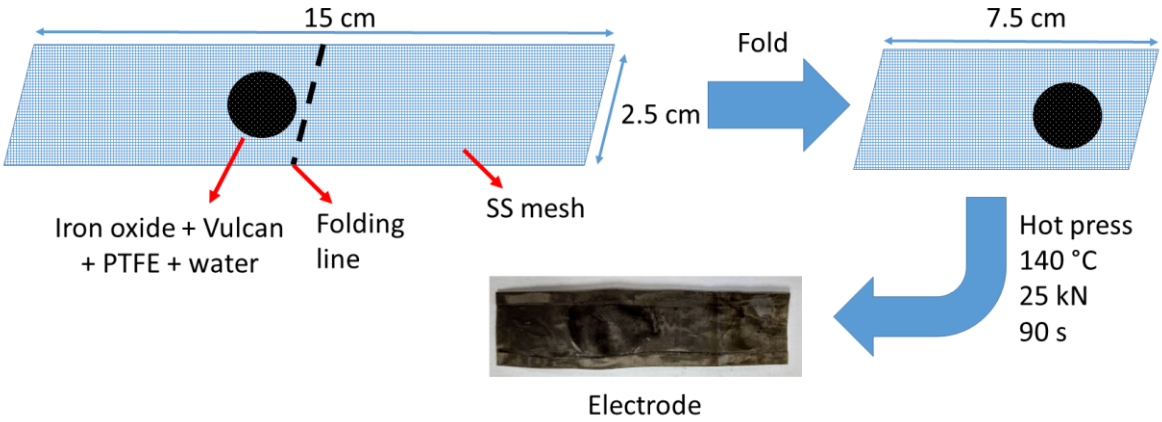

Figure S1. *Scheme of the process of electrode manufacturing.*

S2.- Mössbauer spectroscopy

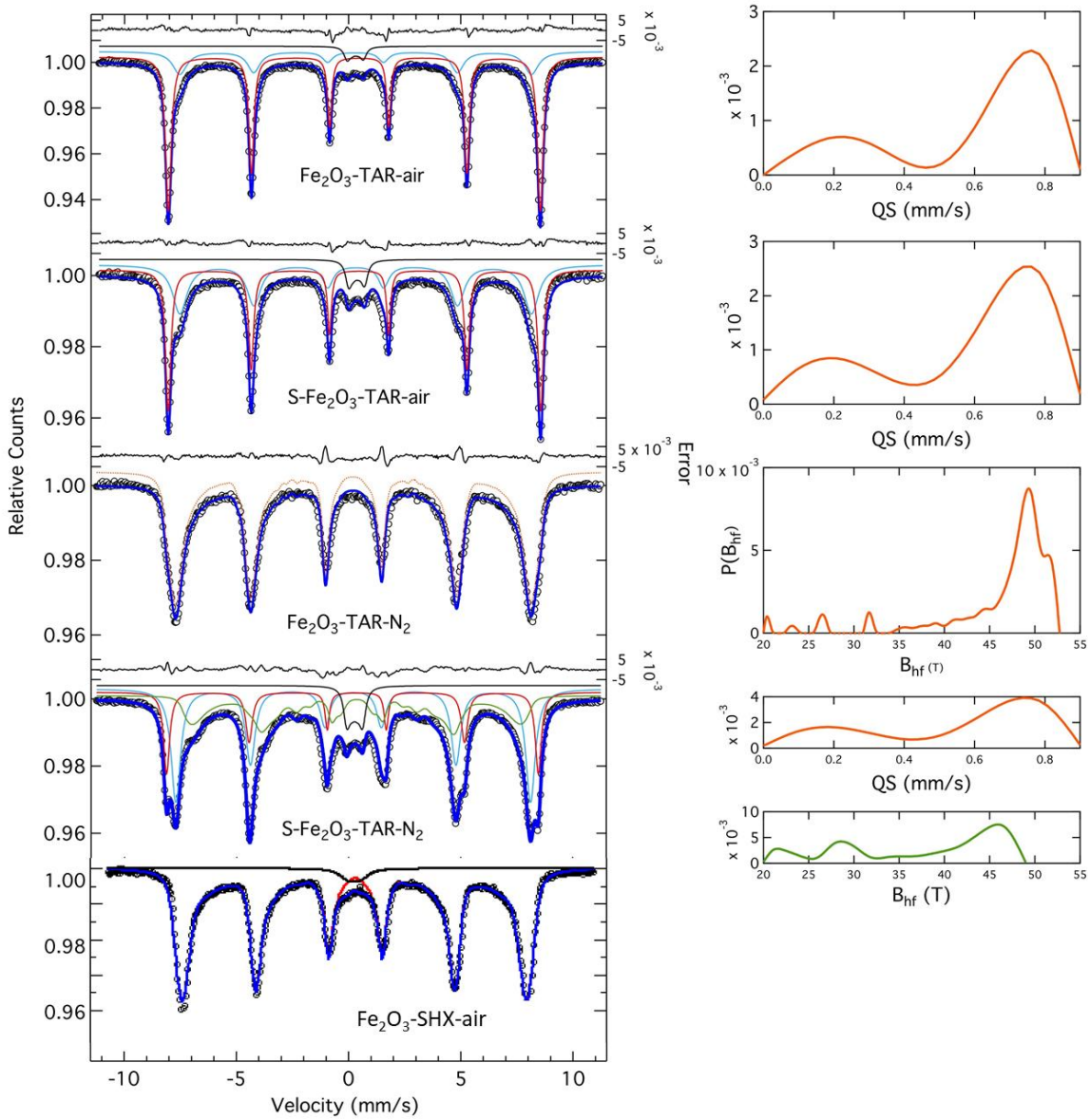

Figure S2. *Mössbauer effect spectra of the studied iron oxides with fitted components (left panel) and distribution of doublets and sextets (right panel) as explained in the manuscript.*

Table S1. *Fitted parameters of the Mössbauer spectra using WinNormos software. Isomer shifts (δ) given with respect to α-Fe. Errors in brackets. For distributions, the average value of δ is given. Max1 and max2 indicate the maxima in the distribution values of quadrupole splitting Δ (doublets) or hyperfine field B_{hf} (sextets).*

		Fe_2O_3-TAR-AIR	S-Fe_2O_3-TAR-AIR	Fe_2O_3-TAR-N_2	S-Fe_2O_3-TAR-N_2
Hematite	**δ (mm/s)**	0.362(1)	0.362(1)		0.266
	2ε (mm/s)	–0.217(1)	–0.204(1)		–0.193
	B_{hf} (T)	51.58(1)	51.64(1)		51.55
	fwhm (mm/s)	0.223(2)	0.213(3)		0.233
	A (%)	69.0(4)	47.5(4)		19.3(4)
Maghemite	**δ (mm/s)**	0.310(3)	0.313(2)		0.203
	2ε (mm/s)	0*	0*		0*
	B_{hf} (T)	48.76(4)	48.75(3)		49.19
	fwhm (mm/s)	0.55(1)	0.57(1)		0.51
	A (%)	27.1(4)	46.4(4)		42.2(7)
Dist. Doublet	**<δ> (mm/s)**	0.28(2)	0.34(1)		0.27
	Δ(max1) (mm/s)	0.22(2)	0.20(2)		0.18
	Δ(max2) (mm/s)	0.76(2)	0.75(2)		0.74
	fwhm (mm/s)	0.294*	0.294*		0.294*
	A (%)	2.9(7)	6(1)		6.1(3)
Dist. Sextet	**<δ> (mm/s)**			0.21(1)	0.35(2)
	2ε (mm/s)			0.011(1)	–0.05(1)
	B_{hf}(max1) (T)			49.2(5)	45.8(5)
	B_{hf}(max2) (T)			51.5(5)	28.5(5)
	fwhm (mm/s)			0.294*	0.344*
	A (%)			100	32(1)

S3.- Determination of crystallite size

The size of the crystallites of each phase, hematite and maghemite, was determined as follows. The powder-diffractograms were fitted by the Rietveld method using FullProf software [1]. In the fits we used the Thompson-Cox-Hastings (TCH) pseudo-Voigt shape for reflections [2]. Instead of the full width of the reflection and pseudo-Voigt mixing parameter, the parametrization of the TCH pseudo-Voigt function allows to calculate the Gaussian and Lorentzian widths, which can be readily identified with crystallite-size effects, microstrains and instrumental resolution broadening. The integral breadth corresponding to size effects finally gives the crystallite size through the Scherrer formula, thus excluding contributions from the instrumental resolution. No strain contribution to the reflections broadening was considered in the present case. The method is described in detail in [1].

Table S2. *Relative molar fractions of iron in hematite and maghemite in %, assuming identical recoilless fractions for both oxides. The values for Fe_2O_3-TAR-N_2 were obtained by fitting the distribution of hyperfine values above 45 T with two Gaussians. The area of the Gaussian centered at ≈51 T yields the contribution of hematite; the rest of the distribution is then assigned to maghemite.*

	Hematite	**Maghemite**
Fe_2O_3-TAR-air	72	28
S-Fe_2O_3-TAR-air	51	49
Fe_2O_3-TAR-N_2	12	88
S-Fe_2O_3-TAR-N_2	21	79

[1] Rodriguez-Carvajal, J., FULLPROF: a program for Rietveld refinement and pattern matching analysis, in: Satell. Meet. Powder Diffr. XV Congr. IUCr (Vol. 127), 1990. Rodriguez-Carvajal, J., Physica B (1993), 192, 55. https://www.ill.eu/sites/fullprof/index.html.

[2] Thompson, P., Cox, D. E., & Hastings, J. B. (1987). Rietveld refinement of Debye–Scherrer synchrotron X-ray data from Al2O3. Journal of Applied Crystallography, 20(2), 79–83. doi:10.1107/s0021889887087090

S4.- Nitrogen physisorption

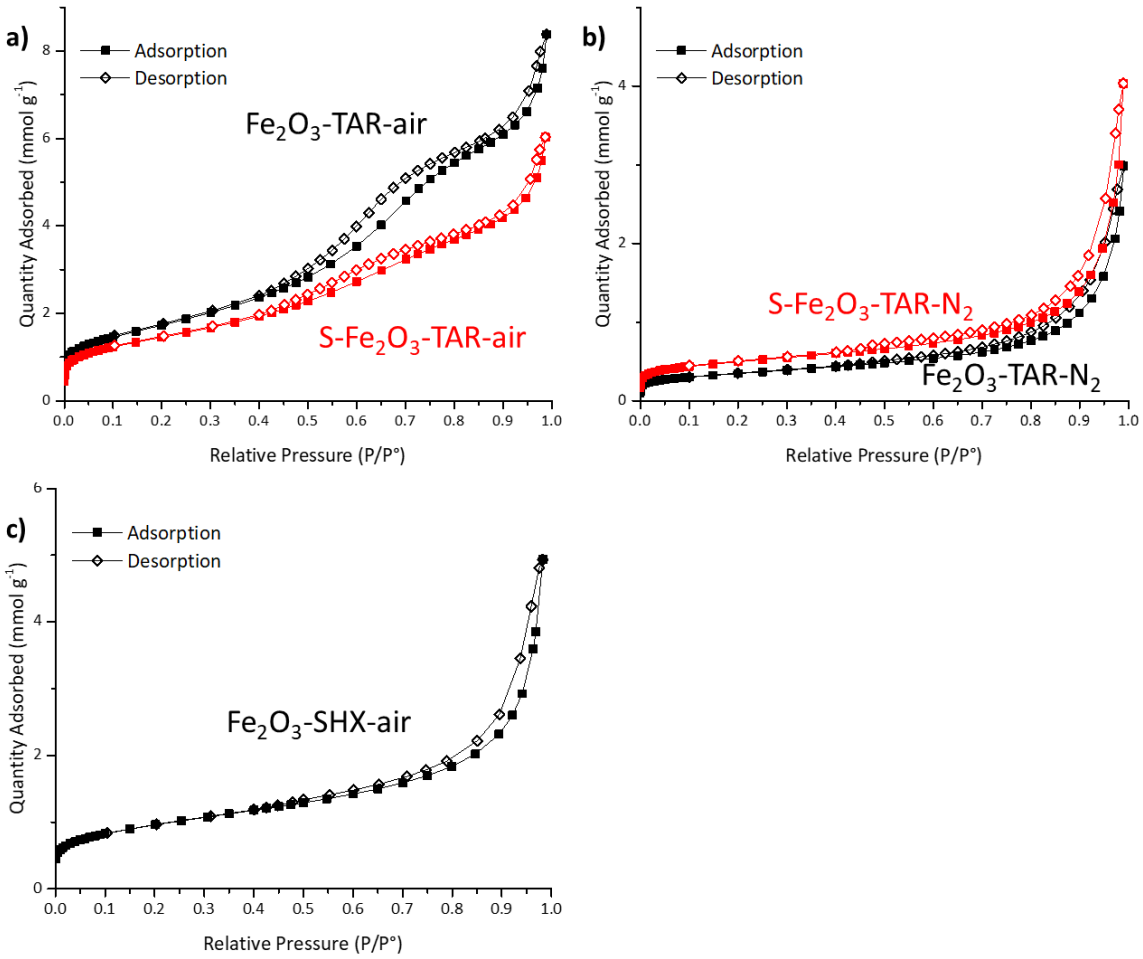

Figure S3. *Nitrogen physisorption isotherms at 77 K over a) Fe_2O_3-TAR-air and S-Fe_2O_3-TAR-air, b) Fe_2O_3-TAR-N_2 and S-Fe_2O_3-TAR-N_2, and c) Fe_2O_3-SHX-air.*

S5.- XPS spectra

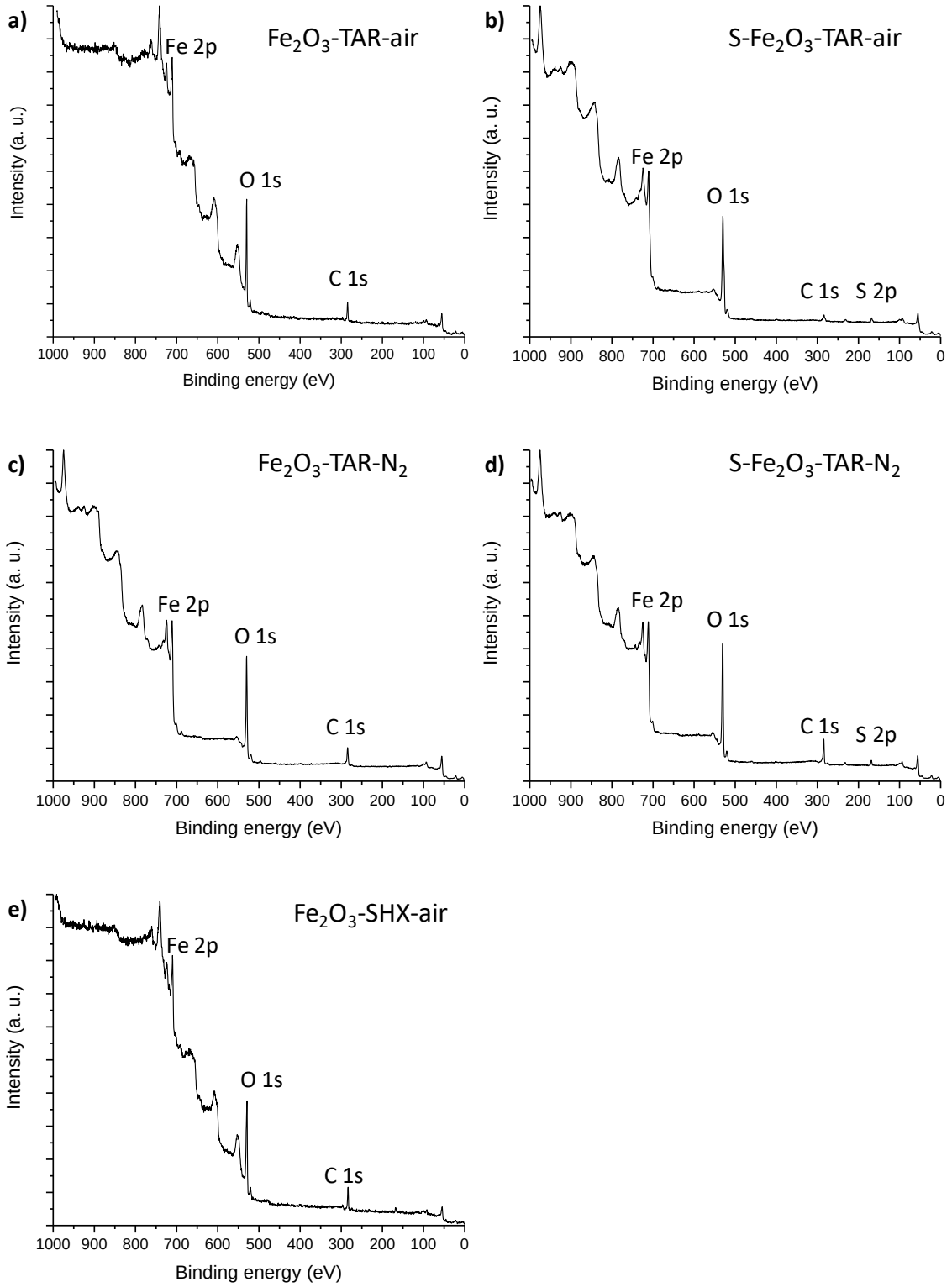

Figure S4. *XPS spectra of samples: a) Fe_2O_3-TAR-air, b) S-Fe_2O_3-TAR-air, c) Fe_2O_3-TAR-N_2, d) S-Fe_2O_3-TAR-N_2, and e) Fe_2O_3-SHX-air. Carbon percentages are overestimated because of adventitious carbon.*

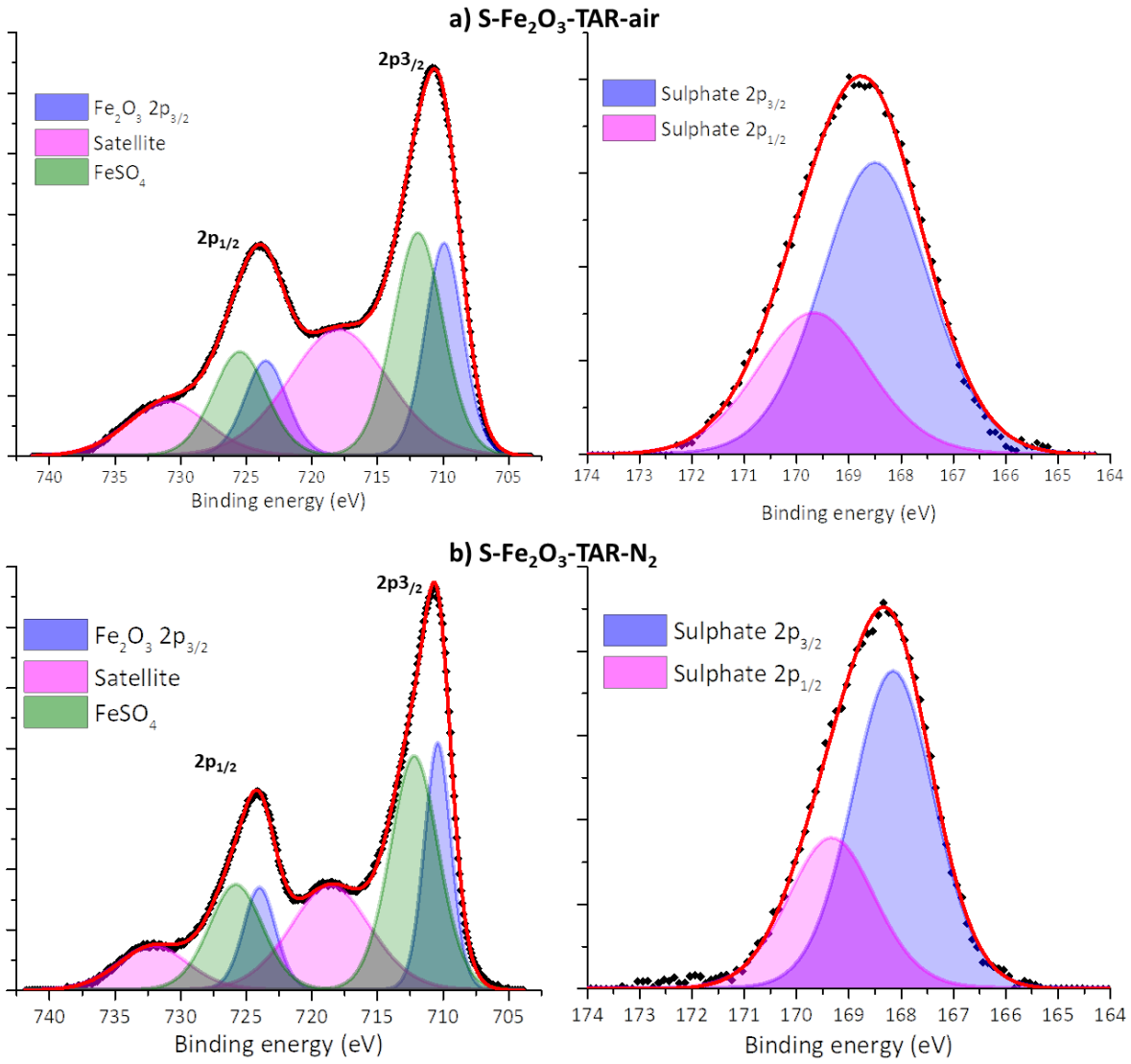

Figure S5. *XPS spectra of orbitals Fe2p (left) and S2p (right) of samples: a) S-Fe_2O_3-TAR-air, and b) S-Fe_2O_3-TAR-N_2*

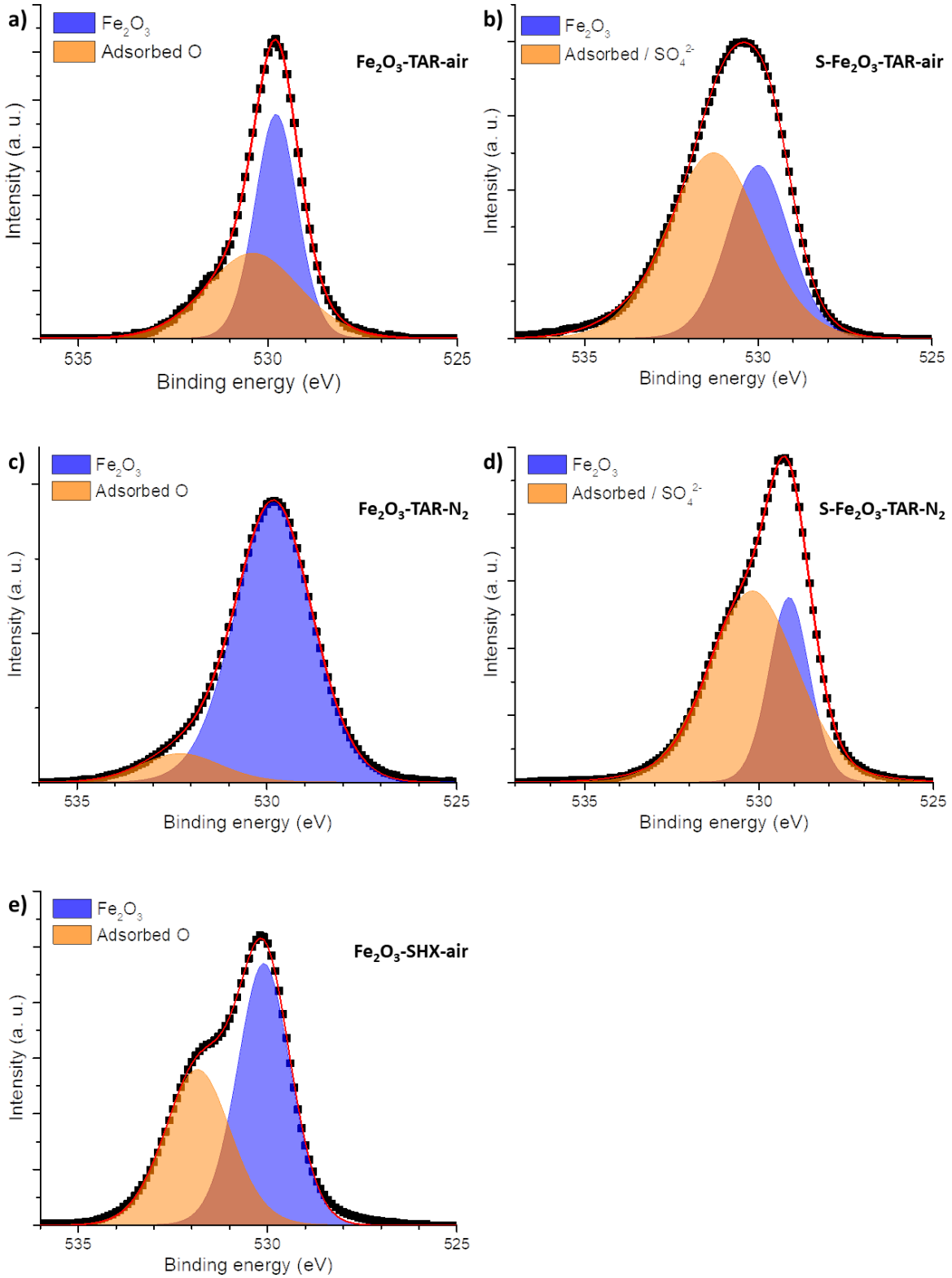

Figure S6. *XPS spectra of orbital O1s of samples: a) Fe_2O_3-TAR-air, b) S-Fe_2O_3-TAR-air, c) Fe_2O_3-TAR-N_2, d) S-Fe_2O_3-TAR-N_2, and e) Fe_2O_3-SHX-air*

S6.- FESEM and TEM/STEM images of the iron oxides

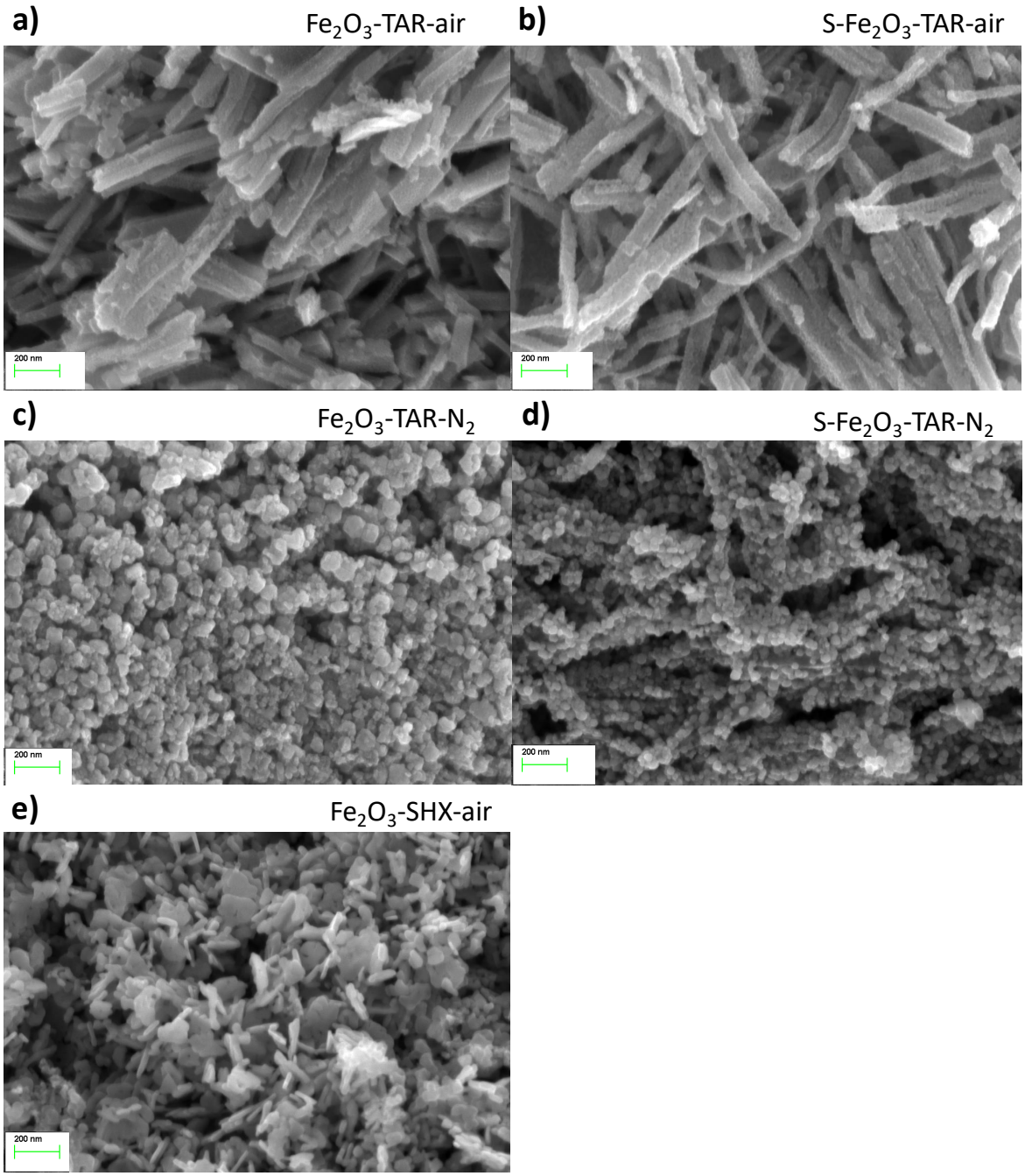

Figure S7. FE*SEM micrographs at 50k magnification of iron oxides a) Fe_2O_3-TAR-air, b) S-Fe_2O_3-TAR-air, c) Fe_2O_3-TAR-N_2, d) S-Fe_2O_3-TAR-N_2, and e) Fe_2O_3-SHX-air*

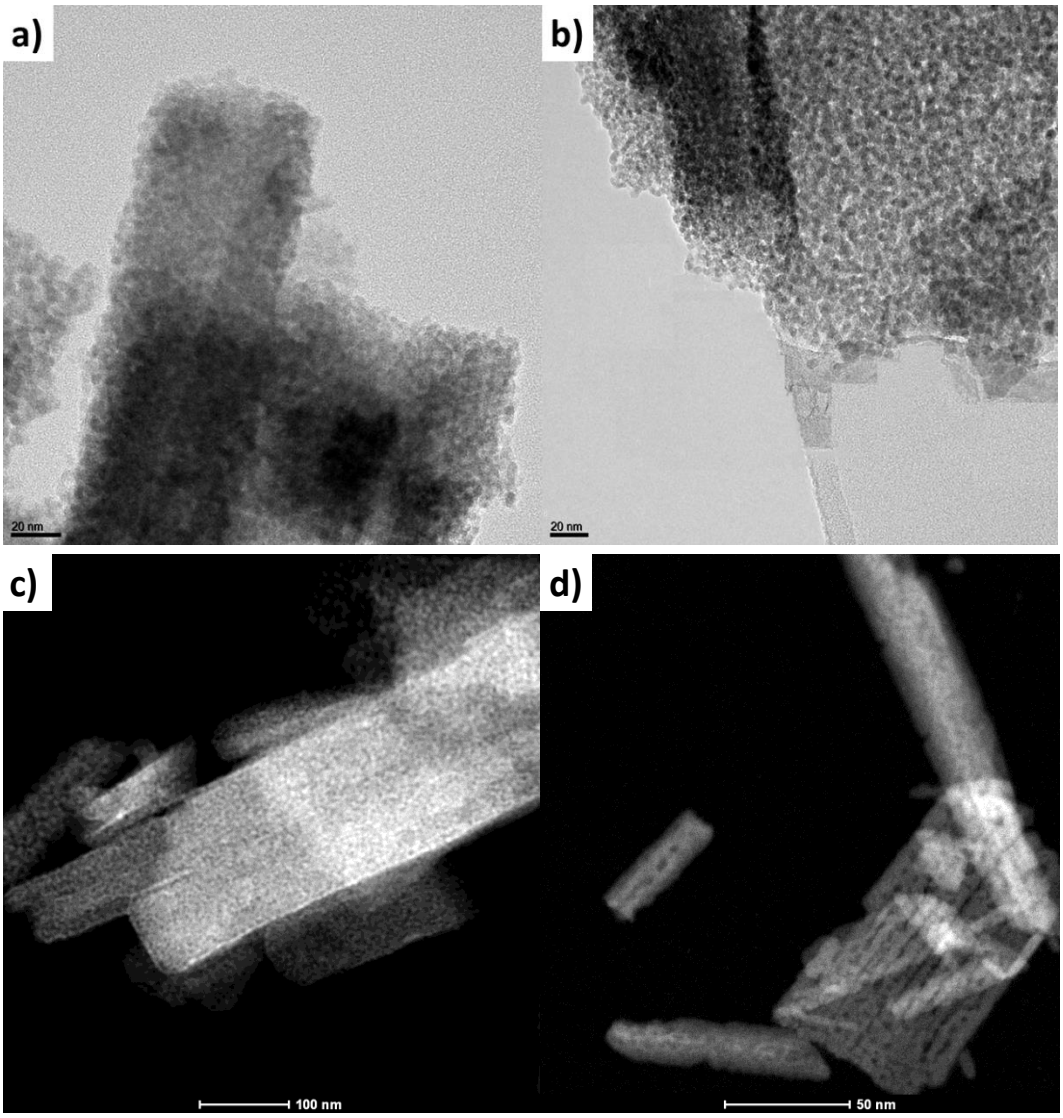

Figure S8. *TEM micrographs of iron oxides a) Fe_2O_3-TAR-air, b) S-Fe_2O_3-TAR-air. STEM images for c) Fe_2O_3-TAR-air, d) S-Fe_2O_3-TAR-air.*

S7.- Electrochemical reactions on the electrodes and electrodes deactivation

During charge (dotted lines), all of the composites show a first plateau at around -0.95 V *vs* Hg|HgO, associated to the reduction of iron (III) to iron (II), and a second longer plateau where both the reduction of iron (II) to metallic iron and the HER take place at -1.18 V *vs* Hg|HgO. When discharging (solid lines), the plateau corresponding to the oxidation of Fe to $Fe(OH)_2$ is visible at around -0.92 V *vs* Hg|HgO and the plateau of the formation of iron (III) appears between -0.75 and -0.70 V *vs* Hg|HgO. Two interesting facts related to all of the electrodes must be noted: first, that both discharge plateaus are roughly the same length. While the stoichiometry of the reactions indicates that two electrons are transferred in the first step and only one in the second and so, the first discharge plateau should be twice the length of the second one. This means that not all the iron (II) hydroxide molecules are reducing to metallic iron and oxidizing to $Fe(OH)_2$ again. The second remarkable fact is that the second discharge plateau appears to be divided into two: a first shorter plateau and a second longer one. This suggests that the oxidation of $Fe(OH)_2$ to FeOOH or Fe_2O_3 occurs through an intermediary, probably Fe_3O_4.

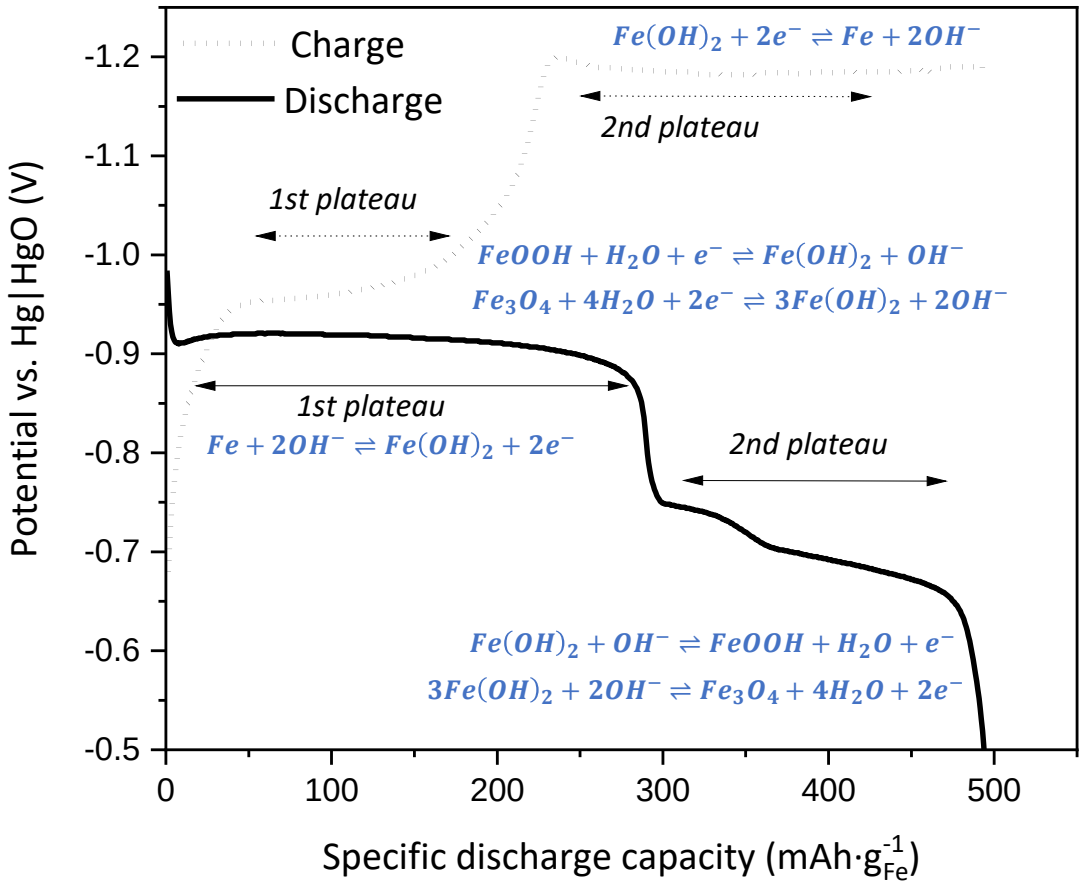

Figure S9. *Detail of the processes of charge and discharge of an iron oxide electrode.*

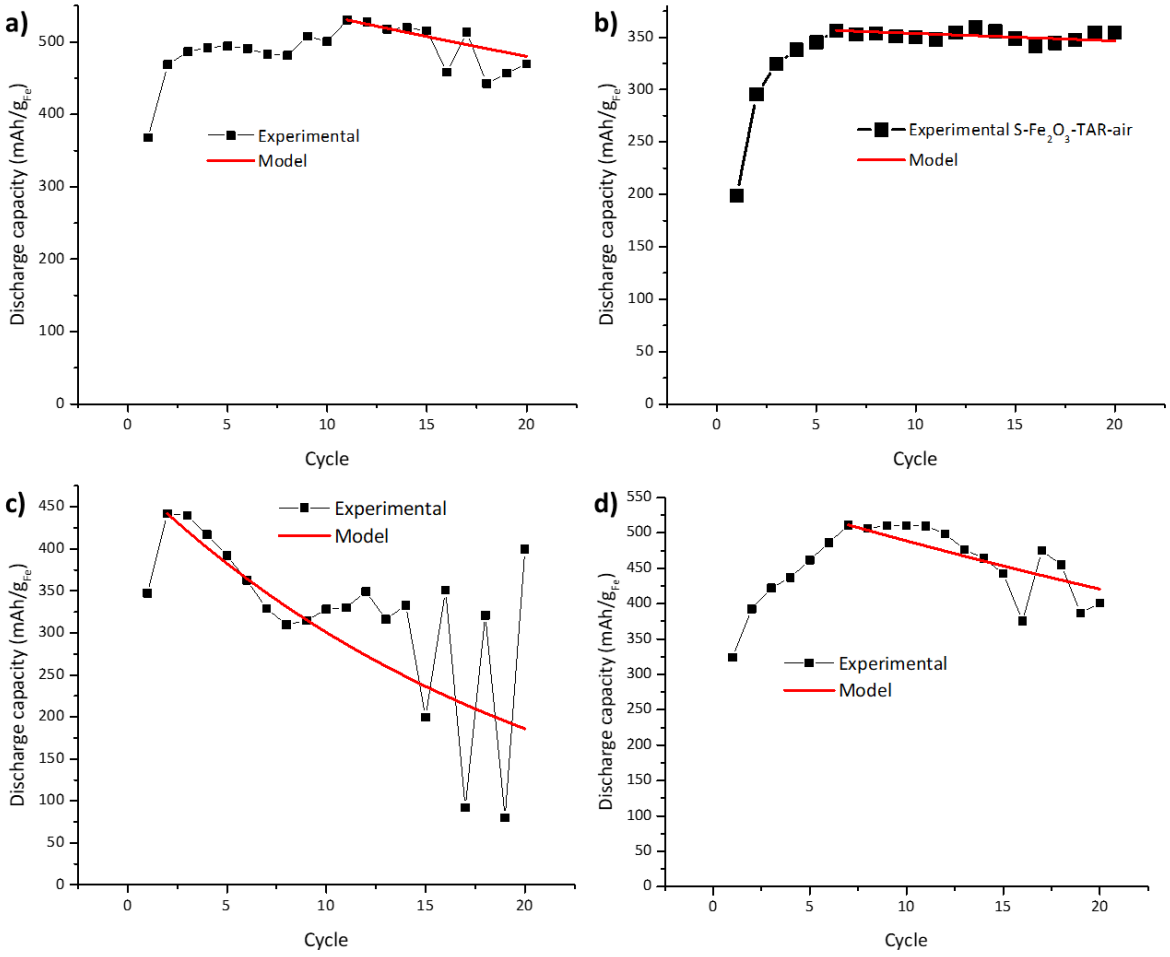

Figure S10. *Model applied to the discharge capacity of electrodes a) Fe_2O_3-TAR-air, b) S-Fe_2O_3-TAR-air, c) Fe_2O_3-TAR-N_2, and d) Fe_2O_3-SHX-air*

S8.- Post-mortem XPS analyses

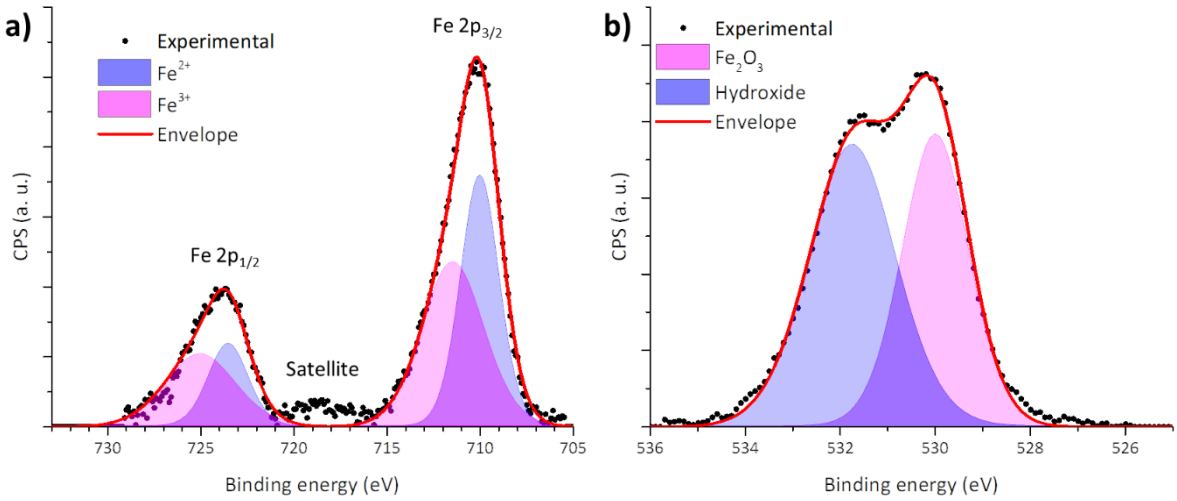

Figure S11. Post-mortem XPS analyses of orbitals a) Fe2p and b) O1s of electrode Fe_2O_3-TAR-N_2.

S8.- Influence of the physical-chemical properties on rate capability

The rate capability of the electrodes S-Fe_2O_3-TAR-air and S-Fe_2O_3-TAR-N_2 was tested performing charge-discharge cycles at C-rates of 0.8 - 0.4 C and 1.6 C - 0.8 C. The electrode S-Fe_2O_3-TAR-N_2, with lower porosity and surface area, is more affected by higher C-rates, as its f factor decreases from 0.962 to 0.891 when increasing the charge-discharge rates from 0.4 - 0.2 C to 1.6 - 0.8 C. This effect is not as strong in electrode S-Fe_2O_3-TAR-air (f factor barely decreases, from 0.976 to 0.970).

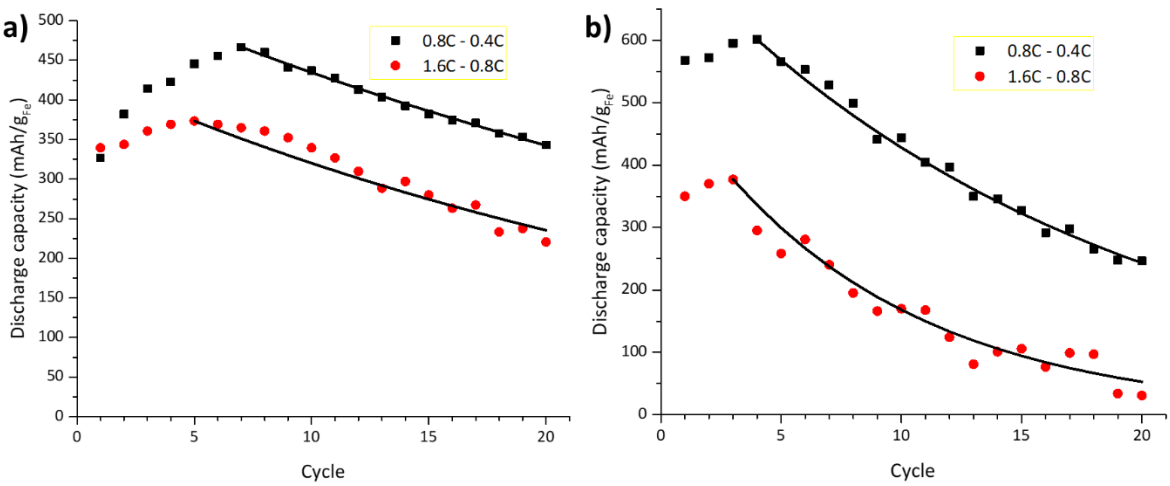

Figure S12. *Model applied to the discharge capacity of electrodes a) S-Fe_2O_3-TAR-air and, b) S-Fe_2O_3-TAR-N_2 at higher C-rates.*

S9.- Additional EIS data

The equivalent circuit fitted to the Nyquist diagrams of samples Fe_2O_3-TAR-air and Fe_2O_3-TAR-N_2 is the same as in Figure 7 in the main text. The Nyquist diagram and fitted parameters of Fe_2O_3-TAR-air show little variability, with the charge transfer resistance increasing *ca.* 10% after 15 cycles. Fe_2O_3-TAR-N_2, by contrast, shows an increment of 120 mV, more than threefold.

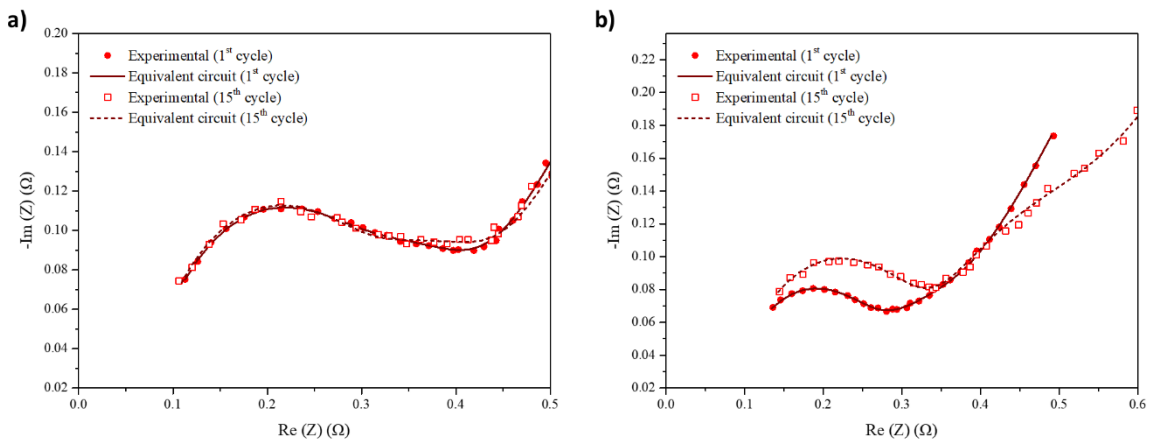

Figure S13. *Nyquist diagrams of EIS tests after 1 and after 15 cycles of electrodes: a) Fe_2O_3-TAR-air and b) Fe_2O_3-TAR-N_2*

Table S3. *Optimized parameters of equivalent circuit (**Figure 7** in the main text) for the electrodes in Figure S13.*

Electrode	Fe_2O_3-TAR-air		Fe_2O_3-TAR-N_2	
	1 cycle	15 cycles	1 cycle	15 cycles
R1 (mΩ)	64.0	63.2	71.0	73.1
R2 (mΩ)	251	255	202	157
R3 (mΩ)	63.4	69.0	55.3	175
Q1 – Y_0 (mS^n)	10.5	6.36	19.28	9.56
Q1 – n	0.849	0.853	0.785	0.772
Q2 – Y_0 (mS^n)	147	161	467	448
Q2 – n	0.872	0.894	0.790	0.810
D – Y_0 ($S^{0.5}$)	1.81	1.74	1.70	1.53

S9.- Post-mortem textural characterization

Figure S14 shows the N_2 physisorption obtained for two electrodes, considering a fresh electrode (without cycling) and an electrode cycled 20 times. Both of the tested electrodes (S-Fe_2O_3-TAR-air and S-Fe_2O_3-TAR-N_2) showed a similar decrease in their surface area and pore volume, as the iron oxides expanded, occupying the pores of the carbon matrix. This phenomenon was investigated by Yang *et al.,* [3]. Coincidently with what they found, the electrode S-Fe_2O_3-TAR-air showed a greater decline in pore size (see Table S4), from 14.1 nm to 6.8 nm, while S-Fe_2O_3-TAR-N_2 average pore diameter increased from 13.8 nm to 16.6 nm. This indicates a better utilization and better contact between the carbon and iron phases in S-Fe_2O_3-TAR-air electrode, and thus, a greater stability.

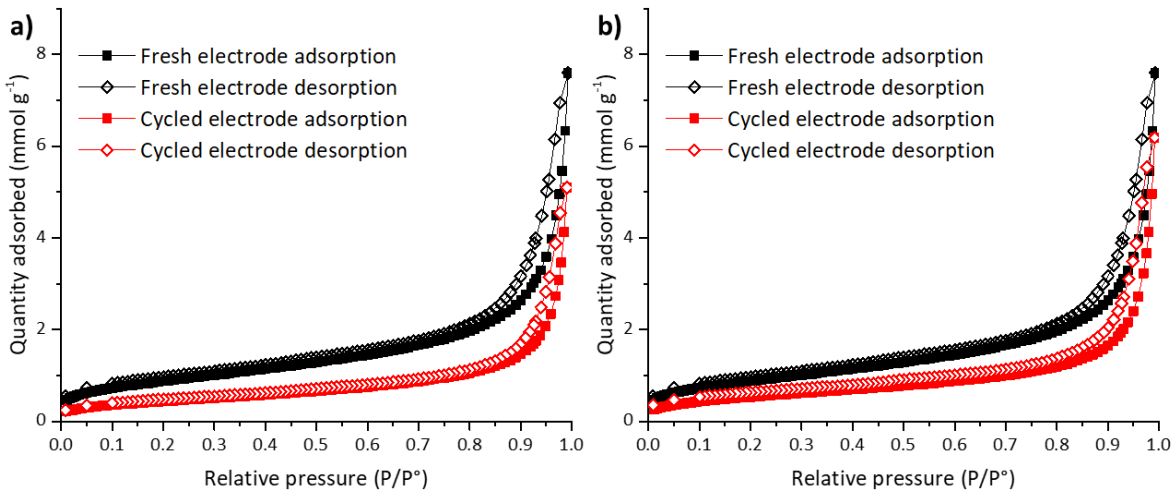

Figure S14. *Adsorption isotherms of electrodes: a) S-Fe_2O_3-TAR-air, and b) S-Fe_2O_3-TAR-N_2; before cycling and after 20 cycles.*

Table S4. *Textural properties of the fresh and cycled electrodes.*

Electrode	BET surface area (m^2 g^{-1})	Pore volume (cm^3 g^{-1})	BJH desorption avg. pore size (nm)
S-Fe_2O_3-TAR-air fresh	72	0.31	14.1
S-Fe_2O_3-TAR-air 20 cycles	36	0.18	6.8
S-Fe_2O_3-TAR-N_2 fresh	72	0.26	13.8
S-Fe_2O_3-TAR-N_2 20 cycles	44	0.21	16.6

[3] Yang, C., Manohar, A. K., & Narayanan, S. R. (2017). A high-performance sintered iron electrode for rechargeable alkaline batteries to enable large-scale energy storage. *Journal of The Electrochemical Society*, *164*(2), A418. doi: 10.1149/2.1161702je

Artículo 3

Villanueva-Martínez, N. I., Alegre, C., Martínez-Visús, I., & Lázaro, M. J. (2023). Bifunctional oxygen electrocatalysts based on non-critical raw materials: Carbon nanostructures and iron-doped manganese oxide nanowires. *Catalysis Today*, *420*, 114083.

DOI: 10.1016/j.cattod.2023.114083

Catalysis Today 420 (2023) 114083

Contents lists available at ScienceDirect

Catalysis Today

journal homepage: www.elsevier.com/locate/cattod

Bifunctional oxygen electrocatalysts based on non-critical raw materials: Carbon nanostructures and iron-doped manganese oxide nanowires

N.I. Villanueva-Martínez [a], C. Alegre [a,*], I. Martínez-Visús [b,c], M.J. Lázaro [a,*]

[a] Instituto de Carboquímica, CSIC, C/. Miguel Luesma Castán, 4, 50018 Zaragoza, Spain
[b] Instituto de Nanociencia y Materiales de Aragón (INMA), CSIC - Universidad de Zaragoza, Zaragoza 50018, Spain
[c] Chemical and Environmental Engineering Department, Universidad de Zaragoza, Zaragoza 50018, Spain

ARTICLE INFO

Keywords:
Bifunctional catalysts
Carbon nanofibers
Manganese oxide
Oxygen reduction
Oxygen evolution

ABSTRACT

Alkaline metal-air batteries are unique systems for energy storage. These devices require a bifunctional catalyst in the positive electrode that must perform both the oxygen evolution and reduction reactions (OER and ORR, respectively). Generally, cobalt-based oxides are employed as air electrodes; however, cobalt is a critical raw material. Future battery devices will mandatorily need non-critical raw materials based on highly abundant metals. Here we investigate the feasibility of iron-doped manganese oxide in the form of nanowires (Fe-MONW) combined with carbon nanofibers. MnO_2 is known for being active for the ORR, however its activity towards the OER is not yet fully understood. Carbon nanofibers (CNF) on the other hand, provide the necessary electrical conductivity to the catalytic system. Simple methods and economic materials are employed to synthesize the Fe-MONW/CNF composites. Our results show that there is a synergistic effect between CNF and MONW, especially for the ORR, which manifests in an increase in the number of exchanged electrons– from 2.9 to 3.5 – and a shift in the onset potential of 70 mV. Doping MONW with iron further enhances the catalytic activity, for both the ORR and OER. Fe ions generate defects in the manganese oxide structure, favoring the adsorption of oxygen and eventually enhancing the catalytic activity. Fe-doped-MONW shows onset potentials for OER comparable to the benchmark catalyst, IrO_2. The improvement on the catalytic activity is particularly evident in terms of the reversibility gap, ΔE. ΔE is the difference between the potential when the current density is 10 mA cm^{-2} in OER and the half-wave potential for the ORR, being a fundamental parameter to assess the performance of metal-air batteries. The reversibility gap for the best catalyst, 5Fe-MONW/CNF, is ΔE = 922 mV (140 mV lower than non-doped MONW/CNF and between 160 and 320 mV lower than the individual components, MONW and CNF). Endurance tests show remarkable stability of the iron-doped MONW/CNF, with a stable potential and an even lower ΔE of 800 mV for *ca.* 20 h of operation (charge-discharge cycles at ± 10 mA cm^{-2}).

1. Introduction

The interest of the scientific community in metal-air batteries (MABs) is continuously increasing since MABs are considered promising energy storage devices. MABs present high theoretical energy densities (from 1000 Wh kg^{-1} of Fe-air batteries to 11.000 Wh kg^{-1} of Li-O_2 batteries) [1,2]. A wide variety of abundant metals can be used as anodes, *e.g.*, Fe, Zn, Mg, Al, or Si, which is of high interest since the supply chain of batteries' raw materials is a significant concern [3–5]. An additional advantage of metal-air batteries is that certain metal anodes, like Fe or Zn, operate in aqueous alkaline media, with lower toxicity (compared to organic electrolytes) and favoring the use of low-cost non-noble metals for the air electrode [5,6]. The air electrode of aqueous metal-air batteries is responsible for reducing oxygen (during the discharge of the battery) and oxidizing water (during the charge), carrying out the widely known couple "oxygen reduction and oxygen evolution reactions (ORR/OER)" [7,8]. It is generally acknowledged that oxygen electrocatalysis is a major challenge for researchers, given the sluggish kinetics and multiple steps of these reactions. Besides, the OER entails a further challenge, the high operating potential (> 1.5 V vs. RHE), producing the electrochemical corrosion of the electrode components [9,10]. These features force research into the quest for highly active, durable, and bifunctional catalysts.

From noble metals to transition metals, several catalysts have been

* Corresponding authors.
E-mail addresses: cinthia@icb.csic.es (C. Alegre), mlazaro@icb.csic.es (M.J. Lázaro).

https://doi.org/10.1016/j.cattod.2023.114083
Received 30 November 2022; Received in revised form 24 February 2023; Accepted 5 March 2023
Available online 9 March 2023

investigated in the last years for metal-air batteries [11–16]. Among non-noble metals, cobalt-based oxides with structures such as spinels or perovskites are widely known for their bifunctionality for ORR/OER [8, 17–22]. However, due to its use in lithium-ion cathodes, cobalt is a critical raw material, with increasing demand and availability concerns. Low-cost alternative metals with high activity are then sought to avoid the use of cobalt in these devices.

Manganese oxides have been investigated as an alternative to cobalt-based catalysts, due to their promising activities, particularly for the ORR, and more recently, with good performances for the OER [23–25]. Yin et al., in a recent review, summarized the main advantages of MnO_2-based catalysts such as the diversity of nanostructures that they can present (tubes, sheets, rods, wires) and different crystallinity (α-, β-, γ-, σ- and λ-MnO_2) what confers them a high surface-area utilization and a rich redox chemistry [26,27]. All these features provide them with an interesting compromise of activity and stability [28]. Gu et al. investigated several manganese nanostructures, determining that manganese nanowires have the best features as ORR/OER catalysts, however, at the expense of using ionic liquids [29]. Some authors have proved that doping MnO_2 with Ni, Fe, or Co is beneficial for their activity towards ORR and OER [28]. However, the low conductivity of these oxides is often an issue for further application. For this reason, the mixture of manganese-based oxides with conductive carbon materials has been recently investigated [30]. Previous reports in the literature have shown good performances combining MnO_2 with graphene, carbon nanotubes, or carbon nanospheres [4,31–33]. For example, Levy et al. employed CNT to improve the activity of MnO_2-catalysts for Li-O_2 batteries. Miao et al. combined MnO_2 with nitrogen-doped graphene as a flexible air electrode for solid-state zinc-air batteries [34].

Here we propose the use of highly-graphitic CNFs as a conductive additive for enhanced ORR/OER bifunctional catalysts based on low-cost iron doped-manganese oxide nanowires. Low-cost catalysts based on non-critical-raw materials are essential for developing economic and sustainable energy storage electrochemical devices such as metal-air batteries or regenerative fuel cells, requiring both bifunctionality and durability.

2. Experimental

2.1. Materials and methods

All the chemicals employed were purchased as high-purity reagents and used as received. The synthesis of manganese oxide nanowires consisted in an easily scalable, low-cost hydrothermal process previously established by Xiao et al. [35]. Briefly, 0.63 g of $KMnO_4$ (99%, Panreac) and 1.4 mL of HCl (37%, Fluka) were mixed and magnetically stirred for 30 min in 50 mL of deionized water. Afterward, the former solution was transferred to a Teflon-lined stainless steel autoclave, placed in an oven for 12 h at 120°C or 140°C. Once the autoclave cooled down, the brown precipitate obtained was collected and washed with deionized water in a centrifuge until the waste water had a neutral pH. The obtained powder was dried overnight at 65°C to obtain the manganese oxide nanowires, named MONW-X, where X is the temperature of the autoclave, either 120°C or 140°C. The same procedure was employed to obtain iron-doped manganese oxide nanowires by adding different amounts (28, 56, or 84 mg) of $FeCl_3$ (97%, Sigma-Aldrich) in the precursor solution, aiming to obtain nominal loadings of 2, 5, and 7 wt%. Fe-doped MONW will be named as X-Fe-MONW, where X is the actual Fe loading determined by ICP.

Once obtained, MONW and Fe-doped MONW were mechanically mixed with highly-graphitic carbon nanofibers obtained by catalytic decomposition of methane, as described in previous reports [36]. Briefly, 300 mg of a Ni:Cu:Al_2O_3 (78:8:16 at. ratio) catalyst were introduced in a fix-bed vertical quartz reactor, flowing H_2 for 1 h at 550°C. Subsequently, temperature was risen up to 700°C under N_2 atmosphere. Then CH_4 was flowed through the reactor for 3 h to proceed with its catalytic decomposition, yielding the carbon nanofibers (CNF). To obtain the Fe-MONW/CNF composites, equal amounts of MONW or Fe-MONW and CNF were placed in an agate vase with 7 agate balls (5 mm diameter), and 10 mL of ethanol, and ball-milled for 1 h at 100 rpm. The resulting mixture was dried overnight at 65°C.

2.2. Materials characterization

CNF, MONW, and Fe-MONW were fully characterized by several solid-state characterization techniques. Powder X-Ray Diffraction (XRD) was performed with a Bruker AXS D8 Advance diffractometer employing Cu Kα radiation and a θ–θ configuration. Crystal size was calculated by applying the Scherrer equation to the main peaks of the diffractogram. The determination of the crystallographic phases was carried out through Rietveld refinement. The morphology of MONW and CNF was investigated by both transmission (TEM) and scanning (SEM) electron microscopy. TEM images were acquired with a Tecnai F30 microscope operated at 300 kV. The samples were ultrasonically dispersed in ethanol for 15 min and then placed in a Cu carbon grid. SEM images were obtained with a Hitachi 3400-N microscope with the powdered samples directly placed on a carbon tape. Textural features of MONW were assessed through nitrogen physisorption at − 196°C in Micromeritics ASAP 2020. The amount of iron was determined by inductively coupled plasma combined with atomic emission spectrometry (ICP-AES) using an Xpectroblue-EOP-TI FMT26 spectrometer. This technique was also employed to determine the amount of nickel in the carbon nanofibers (CNF). In addition, the carbon and hydrogen content of CNF was determined by elemental analysis (EA) in a Thermo Flash 1112 analyzer (Thermoscientific Waltham). Finally, the chemical speciation of manganese oxides was determined by X-Ray photoelectron spectroscopy in an ESCA Plus Omicron spectrometer equipped with Mg (1253.6 eV) anode, 225 W (20 mA, 15 kV) power and using Casa XPS as software for the deconvolution of the peaks. Components were fitted with a Gaussian-Lorentzian (70%−30%) curve and a Shirley function was used for the baseline.

2.3. Electrochemical tests

The activity of MONW/CNF and Fe-doped MONW/CNF composites was investigated towards the critical reactions for the air electrode in an alkaline solution, *i.e.*, the oxygen reduction and the oxygen evolution reactions. The electrochemical experiments were carried out in a three-electrode cell, using a graphite rod as counter-electrode, a reversible hydrogen electrode as the reference electrode in the tests performed in KOH 0.1 M, and a Hg|HgO reference electrode in the tests performed in KOH 6 M. An ink composed of 5 mg of the catalyst under study, 10 μL of binder (Nafion solution 10 wt%., Alfa-Aesar), and 490 μL of ethanol (HPLC grade, Alfa Aesar) was prepared and deposited, drop by drop, on top of a rotating disk electrode (RDE), with a glassy carbon tip of 5 mm (diameter). A catalyst loading of 1018 μg cm^{-2} was obtained. The catalytic activity was assessed by applying linear sweep voltammetry (LSV) from 1.0 to 0.2 V *vs.* RHE to investigate the ORR, with a scan rate of 5 mV s^{-1} and varying rotating speeds from 400 to 2500 rpm and flowing O_2 in the electrolyte solution (0.1 M KOH, prepared from high-purity KOH, 99.99%, Alfa Aesar, and ultrapure water, Milli-Q, 18.2 MΩ cm). Before the ORR, LSV in nitrogen atmosphere was performed in the same potential range and used as baseline, subtracted to the oxygen-LSV. The OER was carried out with LSV from 1.0 to 1.9 V *vs.* RHE at the same scan rate and 1600 rpm of rotating speed to remove the evolved oxygen from the electrode. Endurance tests were carried out to investigate the stability of the catalysts, consisting in 50 cycles comprising 3 min at 1 mA cm^{-2} and 3 min at − 1 mA cm^{-2} at 1600 rpm rotation speed. Besides, a Gas Diffusion Electrode (GDE) was prepared by spray-coating a 1.6 cm diameter carbon paper piece with an ink of the same characteristics as the one of the RDE. A coverage of 0.71 mg cm^{-2} was achieved. Fifteen ORR-OER cycles of 5 h each and current densities of − 10 mA cm^{-2} and

10 mA cm^{-2}, respectively, were performed. The system of these tests used KOH 6 M as an electrolyte and a Hg|HgO reference electrode.

3. Results and discussion

3.1. Materials characterization

The chemical composition of carbon nanofibers was investigated with elemental analysis (EA) and inductive-coupled plasma spectroscopy (ICP). Carbon nanofibers contain solely carbon (89 wt%), hydrogen (1 wt%), and nickel (7.3 wt%, determined from ICP), from the CNF-growth catalyst. The high carbon content is consistent with what was observed during the growth of the CNF, as 300 mg of Ni:Cu:Al_2O_3 catalyst yielded approximately 3 g of CNF [36]. The chemical composition of manganese oxide nanowires was investigated by ICP, as shown in Table 1. MONW-120 and MONW-140 have almost identical compositions (58–59 wt% Mn and around 6 wt% K), indicating that the difference in the studied temperatures has a negligible impact on the composition of the nanowires. Potassium in the MONW comes from $KMnO_4$ employed during the synthesis. This potassium is present as K_2MnO_4 [35], so the amount of potassium correlates with the amount of manganese (VI), as will be discussed later. The total amount of Mn and K in the MONW nanowires is *ca.* 65%. Since no other elements are found in these materials, the amount of oxygen in the MONW can be determined (by difference), being *ca.* 35 wt%. Considering the stoichiometric formula of MnO_2, 36.8% is oxygen, close to 35% of our MONW. Fe-MONW show a lower Mn content (around 50 wt%), that decreases with increasing amount of iron, and more importantly, the K content decreases sharply, compared to the non-doped counterparts. Iron percentages in the Fe-MONW (2, 5.3, and 6.6 wt%) are close to the nominal loadings pursued (2, 5, and 7 wt%). These samples also show a higher amount of oxygen in their composition (calculated by difference): 39.6, 38.3, and 40.2 wt% in 2Fe-MONW-120, 5Fe-MONW-120, and 7Fe-MONW-120, respectively. This greater oxygen content can be related to their capacity to adsorb oxygen, as will be discussed in the next paragraphs, related to XPS analyses.

The chemical composition of MONW and Fe-MONW was also analyzed by XPS (Fig. S1 in Supporting Information). Table 2 reports the chemical composition of the MONW and Fe-MONW obtained from the deconvolution of the XPS spectra.

The elements found on the surface of the nanowires were O, Mn, K, and Fe. MONW-120 and MONW-140 differ in the amount of manganese and oxygen. The O:Mn atomic ratio is reported in Table 3, being 4:3 for MONW-120 and 3:1 for MONW-140. This significant difference could be explained by the adsorbed oxygen [37]. According to Xiao et al. [38], the synthesis of the nanorods at temperatures higher than 120 °C results in the "dissolution or etching of the extremes of the nanorods", slowly transforming them into nanotubes. In the high-resolution SEM images (Fig. S2a), we observed open ends in MONW-140, evidencing the dissolution/etching previously mentioned. These open ends could be responsible for the enhanced oxygen adsorption in MONW-140.

Potassium content determined by XPS (Table 2) ranges around 2–4 at % (corresponding to 3–6 wt% as shown in Table S1, being similar to the bulk content reported in Table 1). On the contrary, iron is found in excess on the surface of Fe-MONW (*ca.* 9–10 at% corresponding to 20 wt %, Table S1) compared to the bulk (see Table 1, from 2 to 6 wt%).

Iron-doped nanowires Fe-MONW present average O:Mn ratio around 6:1 and O:Me ratio (Me = Mn+Fe) of *ca.* 3.3:1, as reported in Table 3. This indicates that iron favours oxygen adsorption, as will be discussed later. Another interesting finding concerns iron concentration. 2Fe-MONW-120 has an atomic bulk concentration (reported in Table S2) of ~1 at% and a surface concentration of 8.9 at% (Table 2). 5Fe-MONW-120 with a bulk concentration of iron of 2.5 at%, presents a higher iron surface concentration, 10.4 at%. However, a further increase in the iron bulk concentration does not mean a further increase in the surface concentration, and consequently, 7Fe-MONW-120 has an iron surface concentration of 9.8 at%. These data suggest that iron tends to accumulate on the surface of the manganese oxide nanowires until a point of saturation. This is relevant since surface chemistry tends to affect catalytic processes severely.

The high-resolution spectra of the manganese 2p orbital are shown in Fig. 1**a** and Fig. S3**.** The Mn peak shows two $2p_{3/2}$ components: one around 642.0 eV, ascribed to MnO_2 (Mn (IV)) and one around 644.3 eV, ascribed to K_2MnO_4 (Mn (VI)). Biesinger et al. reported that pure MnO_2 samples show a peak at lower binding energy, corresponding to Mn (III), which is not observed in our samples [39]. This fact, together with the presence of Mn (VI), means that the reduction of $KMnO_4$ during the synthesis is incomplete. The amount of Mn (VI) on the surface is consequently related to the amount of potassium, as can be seen in 5Fe-MONW-120 (Fig. 1c) and 7Fe-MONW-120 (Fig. S3c), having a lower concentration of both surface potassium (around 2 at%, Table 2) and Mn (VI) (around 7–9 at%).

The analysis of the O 1s orbital allows the identification of the oxygen species present on the surface of the nanowires (Figs. 1b and 1d, and Fig. S4). Two peaks were identified: one at ~529.5 eV, corresponding to lattice oxygen – either bond to Mn or Fe (peaks of manganese and iron oxide appear at almost the same binding energy [40]) and, another one around 531.1 eV, which corresponds to adsorbed oxygen, OH^- groups or oxygen vacancies [41] (Fig. 1b). Since samples with a larger oxygen content also have a more significant oxygen surface content, it is fair to assume that this peak at around 531.1 eV is in fact adsorbed oxygen. Following this idea, the lattice to adsorbed oxygen ratio is higher in MONW-120 than in MONW-140 – 65:35 and 57:43, respectively –, which helps to explain the observed difference in the manganese to oxygen ratio observed in these samples. The amount of adsorbed oxygen in the Fe-MONW is even higher, with a 50:50 ratio of lattice to adsorbed oxygen ratio in the three iron-doped manganese

Table 1
Elemental composition determined by ICP-OES of the synthesized materials.

Material	wt%			
	Manganese	Iron	Nickel	Potassium
CNF	-	-	7.3	-
MONW-120	58	-	-	6.1
MONW-140	59	-	-	6.7
2Fe-MONW-120	52	2.0	-	6.4
5Fe-MONW-120	53	5.3	-	3.4
7Fe-MONW-120	51	6.6	-	2.2

Table 2
Surface composition of the synthesized materials measured by XPS.

Material	Atomic %			
	O	Mn	Fe	K
MONW-120	55.2	41.9	-	2.9
MONW-140	72.1	23.5	-	4.4
2Fe-MONW-120	74.1	13.1	8.9	3.9
5Fe-MONW-120	74.9	12.5	10.4	2.2
7Fe-MONW-120	75.3	13.0	9.8	1.9

Table 3
O:Mn atomic ratio in the bulk (determined from ICP) and on the surface (determined from XPS).

Material	O:Mn bulk ratio	O:Mn surface ratio	O:Me surface (Me = Mn+Fe)
MONW-120	2.1:1	4:3	4:3
MONW-140	2:1	3:1	3:1
2Fe-MONW-120	2.6:1	5.7:1	3.4:1
5Fe-MONW-120	2.5:1	6:1	3.3:1
7Fe-MONW-120	2.7:1	5.8:1	3.3:1

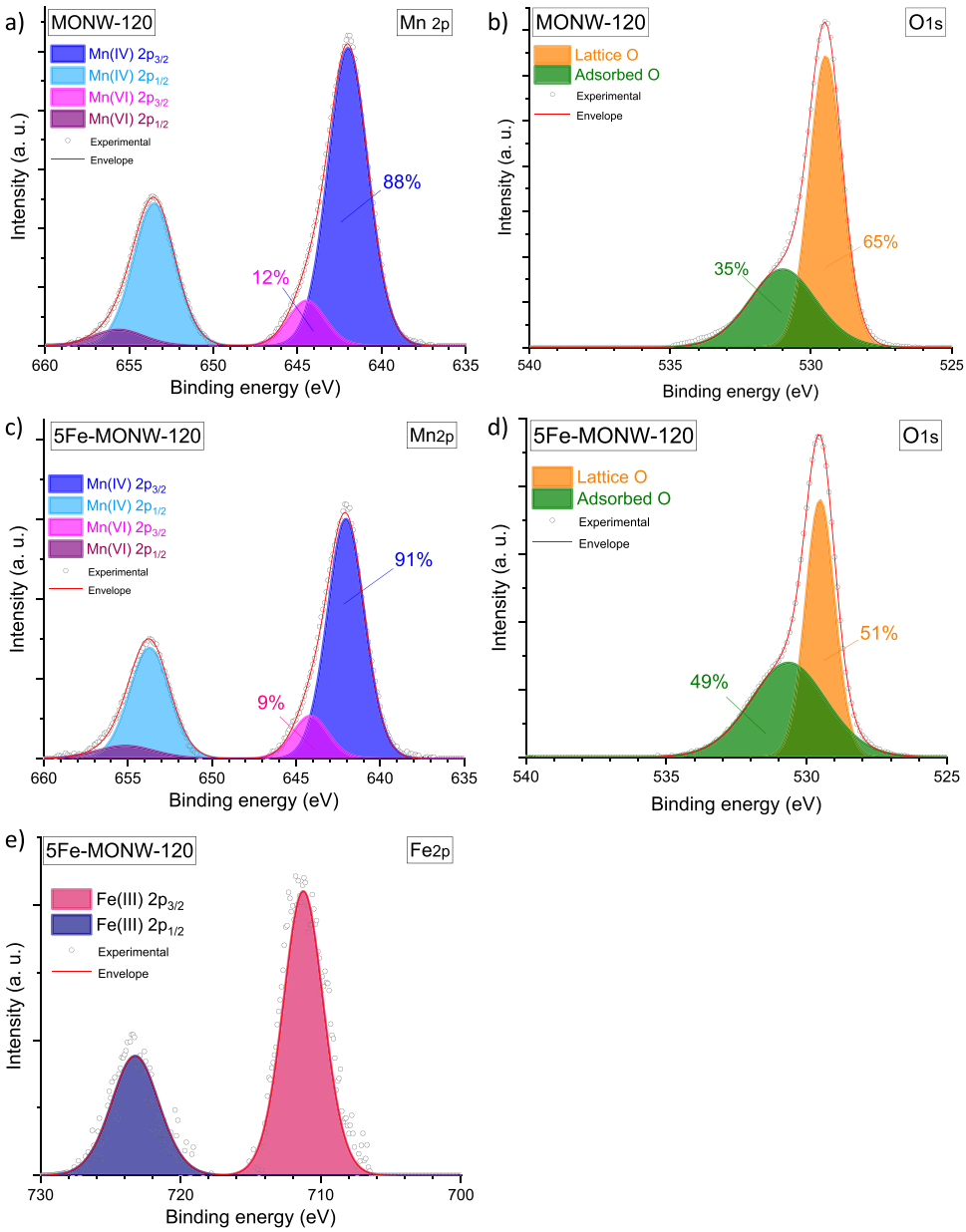

Fig. 1. High-resolution XPS spectra of orbitals a) Mn 2p and b) O 1s, in MONW-120; c) Mn 2p, d) O 1s and e) Fe 2p, in 5Fe-MONW-120. Baseline subtracted in all the spectra.

oxide nanowires (Fig. 1d and Fig. S4). In iron-containing samples, the Fe 2p orbital was also analyzed (Fig. 1e and Fig. S5). The position of the main iron peaks in 2Fe-MONW-120, 5Fe-MONW-120, and 7Fe-MONW-120 at around 711.5 eV allows us to infer that the iron species has a + 3 oxidation state, such as Fe_2O_3 or FeOOH [40]. The lack of a satellite peak between the $2p_{3/2}$ and $2p_{1/2}$ components and the gap between them of approximately 12.5 eV is similar to the goethite XPS spectrum [42]. These Fe^{3+} ions create oxygen vacancies in the MnO_2 lattice, which can enhance the catalytic activity of MnO_2 towards ORR, as reported by Li et al. [43].

XRD studies revealed the crystalline structures of the MnO_2 nanowires (Fig. 2). The only crystalline phase observed, obtained applying Rietveld refinement, was α-MnO_2 (JCPDS: 00–044–0141) confirming that iron ions are inserted in the manganese oxide lattice.

The addition of iron diminishes the size of the MnO_2 crystallite, increasing the number of defects, as reported in Table 4. This can be deducted from the progressive widening of the diffraction peaks with increasing amounts of iron (Fig. 2), particularly appreciable at the (211) peak at 37°. It must be remarked that the inclusion of Fe ions in the α-MnO_2 structure is not reflected as a shift of the peak position in the diffractogram. The similar ionic radius of Fe^{3+} and Mn^{4+} (73 and 67 pm, respectively [44]) means that interplanar distances are not significantly modified, and Bragg angles do not change. The defects induced in the lattice by ferric ions are related to oxygen vacancies due to their lower charge with respect that of Mn^{4+} ions. Thse defects are not caused by the strain ascribed to the different size between ions.

From the crystallite size values, the dislocation density (δ) can be calculated by applying Eq. (1), also reported in Table 4. The dislocation density increases with increasing iron content. The dislocation density represents the concentration of defects in a crystal and is defined as the length of dislocation lines per volume [44,45]:

$$\delta = \frac{1}{D^2} \tag{1}$$

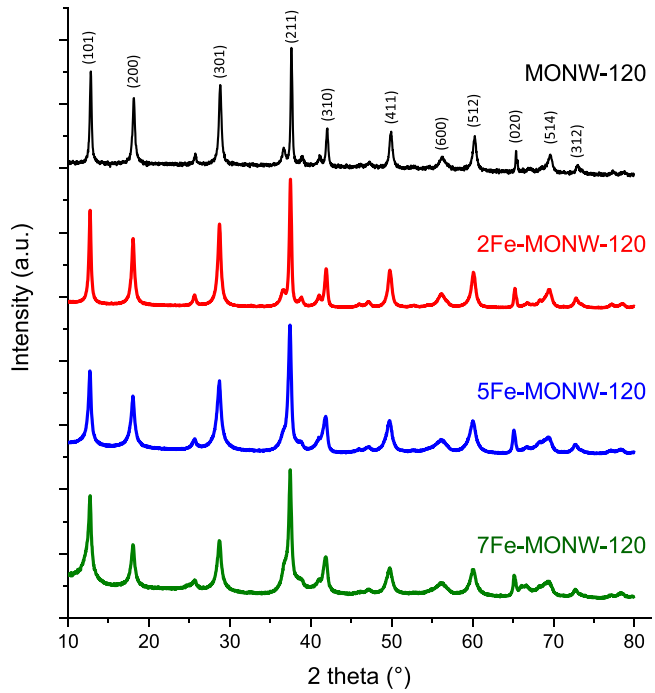

Fig. 2. XRD pattern of manganese oxide nanowires and iron-doped manganese oxide nanowires synthesized at 120°C. Miller indexes for α-MnO_2 are referenced within the figure [47,48].

Table 4
XRD parameters (crystal size and dislocation density).

Material	Crystallite size / nm	Dislocation density / 10^{-4} nm^{-2}
MONW-120	37.0	7.3
2Fe-MONW-120	23.3	18.4
5Fe-MONW-120	16.1	38.6
7Fe-MONW-120	14.6	46.9

XRD pattern was also obtained for CNF (Fig. S6a), where the only observable crystalline phases are graphitic carbon and metallic nickel. Highly graphitic carbon nanofibers are good electrical conductors and can enhance electrochemical reactions [46].

The textural properties of CNF, MONW and MONW/CNF composites were studied by nitrogen physisorption at 77 K (Fig. S7, and Table S3). Carbon nanofibers show a BET surface area of 94 m^2 g^{-1} in accordance with previous studies [49,50]. In the case of the MONW, the synthesis temperature does not have a significant effect on the textural properties, as MONW-120 and MONW-140 present surface area values of 23 m^2 g^{-1} and 24 m^2 g^{-1}, respectively. Doping with iron did not significantly affect the textural properties of MONW. Fe-MONW presented surface area values in the same range (20–26 m^2 g^{-1}) as their non-doped counterparts.

SEM and TEM images of the composites show the morphology of both CNF and MONW (Fig. 3). Carbon nanofibers have a fishbone structure, as ascertained from Fig. 3a, and diameters around 50 nm, as appreciated in Fig. 3b. Fig. 3c shows a bunch of MONW, highly cross-linked, with a needle-like shape. Fig. 3d shows an image at higher magnification of an isolated MONW, with *ca.* 35 nm diameter and from 50 to 100 nm long. TEM images of the composite (Figs. 3e and 3f) show a good contact between the manganese oxide and the carbon phases, which is essential, as will be discussed in the next section. No iron particles were detected in the HR-TEM of the Fe-MONW, which confirms that iron is embedded in the MnO_2 lattice. Figs. 3g and 3h show the particle size distribution for the MONW-120 in terms of both nanowire diameter (Fig. 3g) and nanowire length (Fig. 3h). The statistical distribution was obtained by measuring over 130 nanowires. The average nanowire diameter is around 75 nm, whereas the length is usually around 100 nm. In addition, no significant morphological differences were observed between the nanowires synthesized at 120 °C or 140 °C, as shown in Figs. S2b and S2c.

3.2. Electrochemical characterization

3.2.1. Activity towards oxygen reduction and evolution reactions

The performance of the catalysts towards ORR and OER was assessed by linear sweep voltammetry (Fig. 4a). The onset potentials for ORR (E_{ORR}) and OER (E_{OER}) were calculated as the potential when the current density reaches − 0.1 mA cm^{-2} and 1 mA cm^{-2}, respectively. Based on these values, the onset overpotentials for ORR (η_{ORR}) and OER (η_{OER}), reported in Fig. 4b, were also calculated taking into consideration the standard O_2 reduction potential, 1.23 V. Another important parameter to assess the performance of these bifunctional catalysts is the reversibility gap, ΔE, also reported in Fig. 4b. This value is fundamental for the performance of the final metal-air battery device, since it directly influences the faradaic efficiency. ΔE is usually defined as the difference between the potential at which OER reaches 10 mA cm^{-2} (E_{10}) and the half-wave potential for the ORR (E_{HWP}). This will be the one used in this manuscript. Other works in the literature report ΔE as the difference between the potential for the OER at 10 mA cm^{-2} and the potential for the ORR at − 1 mA cm^{-2} [34,51].

MONW-120/CNF composite catalyst was tested against the CNF and MONW (Fig. 4a). The polarization curves show a synergistic effect between the manganese oxide nanowires (MONW) and the carbon nanofibers (CNF), which is especially notorious in ORR. MONW/CNF composites show an onset potential shifted towards more positive values with respect the CNF (70 mV shift) and a higher limiting current density (−5 mA·cm^{-2} for the composite *versus* −4 mA·cm^{-2} for the individual components). On the other hand, CNF and MONW-120/CNF composite show almost the same behaviour for the OER. CNF have a 7.3 wt% of nickel in their composition, responsible for the catalytic activity towards the OER. To confirm this, carbon nanofibers were leached with hot hydrochloric acid (2 h, 60 °C, under sonication) and tested again for ORR and OER (see LSV in Fig. S8 in the supporting information). Acid-leached CNF has a slightly lower activity towards both ORR and OER with respect to the pristine CNF. Thus, the onset potential for the OER for acid-leached CNF shifts more than 50 mV and for ORR more than 25 mV *versus* CNF, due to the presence of the catalytically active nickel particles.

Fig. 4b shows the reversibility gap *(left Y axis)* and the onset overpotentials for both the ORR and OER *(right Y axis),* confirming the synergistic effect of the CNF with the MONW-120. It is evident that the MONW/CNF composites have lower ΔE gaps than the individual phases (CNF or MONW), mainly due to the poor activity of CNF towards ORR and of MONW towards OER.

The number of electrons transferred during the ORR was calculated applying the Levich equation (Eq. 2) to the polarization curves:

$$j_L = 1.95nFAC^*_{O_2}D^{1.5}_{O_2}\nu^{-1/6}f^{-0.5} \quad (2)$$

Where j_L is the current density at the diffusional limit (E = 0.2 V *vs.* RHE), n is the number of electrodes transferred (2 for oxygen reduction to H_2O_2 and 4 to OH^-), F is the Faraday constant (96485 C/mol), A is the area of the electrode (0.196 cm^2), $C^*_{O_2}$ is the saturation concentration of oxygen in the electrolyte (1.21 mol m^{-3}), D_{O_2} is the diffusivity of oxygen in the electrolyte (1.87 * 10^{-9} m^2 s^{-1}), ν is the cinematic viscosity of the electrolyte solution (10^{-6} m^2 s^{-1}) and f is the rotation frecuency of the electrode, in Hz. The ORR goes through a mechanism of 2.7 electrons for MONW-120 and 2.9 electrons for the CNF. In the composites (MONW/CNF), the number of electrons increases up to 3.4 for MONW-120/CNF and 3.5 for MONW-140/CNF. These increase in the number of electrons confirms the synergistic effect between the MONW and the CNF. The

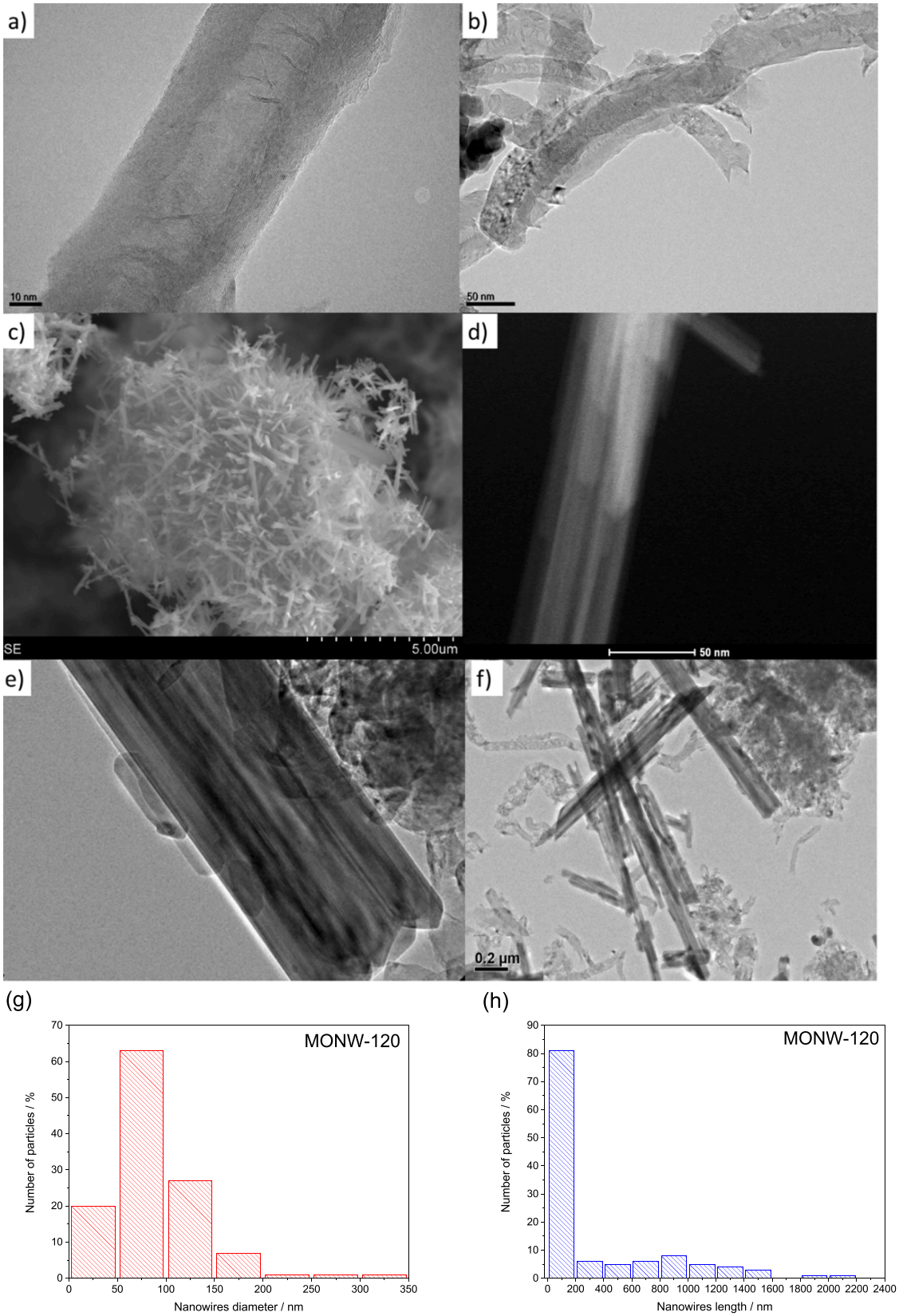

Fig. 3. a) HR-TEM image of a single carbon nanofiber. b) TEM image of carbon nanofibers. c) SEM image of MONW-120. d) STEM image of a single manganese oxide nanowire (MONW-120). e) TEM image of the composite MONW-120/CNF and f) TEM image of the composite 5Fe-MONW-120/CNF, g) Particle size distribution for MONW-120 in terms of the average nanowire diameter and h) Particle size distribution for MONW-120 in terms of the average nanowire length.

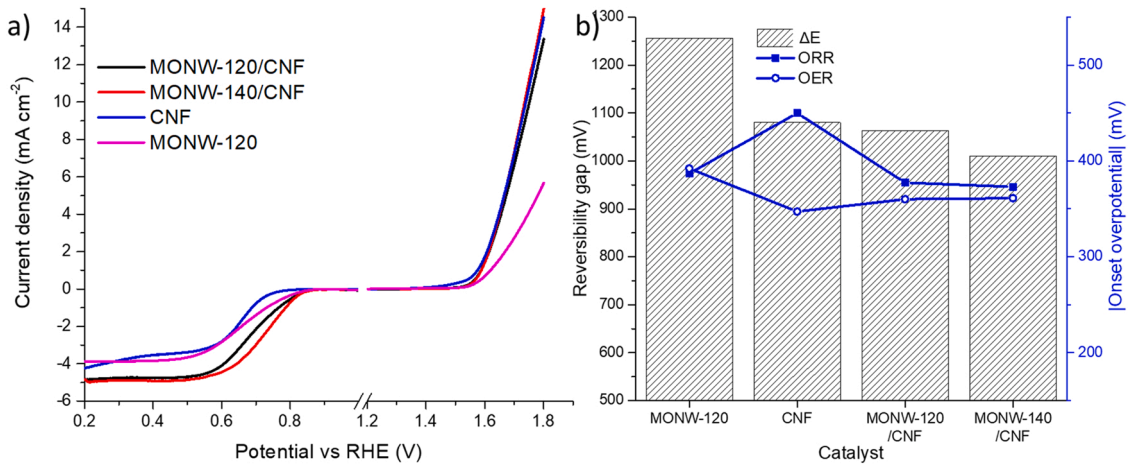

Fig. 4. a) Polarization curves of the MONW/CNF composites, CNF and MONW materials, in a RDE at 1600 rpm in KOH 0.1 M. b) Summary of the performance of the catalysts in terms of overpotential towards OER/ORR and reversibility gap, ΔE.

textural properties of the carbon nanofibers provide a surface where oxygen can be adsorbed and then reduced. In any case, the number of electrons for our catalysts are lower than the theoretical maximum of 4 – achieved by the benchmark Pt/C catalyst – but still means than 75% of the oxygen reduction occurs *via* the hydroxide intermediate and only 25% *via* the peroxide route. These results were corroborated by applying the Levich equation to different rotation speeds (Fig. S9 and Fig. S10).

Tafel slopes (m_T) at low current density (<2 mA cm^{-2}) and exchange current densities (j_0) were also obtained in order to compare the catalysts and gain insight into the mechanisms of the reactions. To obtain the kinetic current density – *i.e.,* the intrinsic current density – the Koutecky-Levich approach was used (Eq. 3):

$$\frac{1}{j} = \frac{1}{j_k} + \frac{1}{j_L} \tag{3}$$

Where j is the observed current density (after subtracting the background) and j_k is the kinetic current density to be determined.

Fig. 5**a** shows the Tafel plots for ORR, that range between 53 and 134 mV dec^{-1}, with MONW-120/CNF presenting the lowest value. The benchmark catalyst, Pt/C, has a higher slope of 84 mV dec^{-1}, but also a much higher exchange current density of 4.2 * 10^{-4} mA cm^{-2} against the 9.1 * 10^{-9} mA cm^{-2} of the catalyst MONW-120/CNF. The synergistic effect between CNF and MONW is also reflected in their Tafel slope values, 76 mV dec^{-1} for the CNF and 134 mV dec^{-1} for the MONW, with respect to the MONW/CNF composite presenting 53 mV dec^{-1}.

According to the literature [17,52–54], the fundamental steps ascribed to the reduction of oxygen in alkaline media are the following:

$$M + O_2 \rightleftharpoons MO_2 \tag{4}$$

$$MO_2 + e^- \rightleftharpoons MO_2^- \tag{5}$$

$$MO_2^- + H_2O \rightleftharpoons MO_2H + OH^- \tag{6}$$

$$MO_2H + e^- \rightleftharpoons MO + OH^- \tag{7}$$

$$MO + H_2O + e^- \rightleftharpoons MOH + OH^- \tag{8}$$

$$MOH + e^- \rightleftharpoons M + OH^- \tag{9}$$

M is an adsorption site in the catalyst. According to Shinagawa et al. [55], when the second step (Eq. 5) is the rate-determining step (RDS), a Tafel slope of 120 mV dec^{-1} should be expected. The Tafel slope for ORR in the material MONW-120 is 134 mV dec^{-1}, so it is a fair assumption that the semi-reaction from Eq. 5 is the rate-determining step over manganese nanowires. Taking a closer look at Eq. 5, a more significant amount of adsorbed oxygen (MO_2) should increase its rate, so materials with a higher ability to adsorb oxygen would yield faster ORR. This might explain why MONW-140/CNF has a better half-wave potential for the ORR than MONW-120/CNF, even though they have similar onset potentials. As was shown in the previous section, MONW-140 has a better ability to adsorb oxygen than MONW-120. The 53 mV dec^{-1} slopes of composites MONW-120/CNF suggest that reaction (7) could be the RDS, as a 40 mV dec^{-1} followed by a 120 mV dec^{-1} is expected when

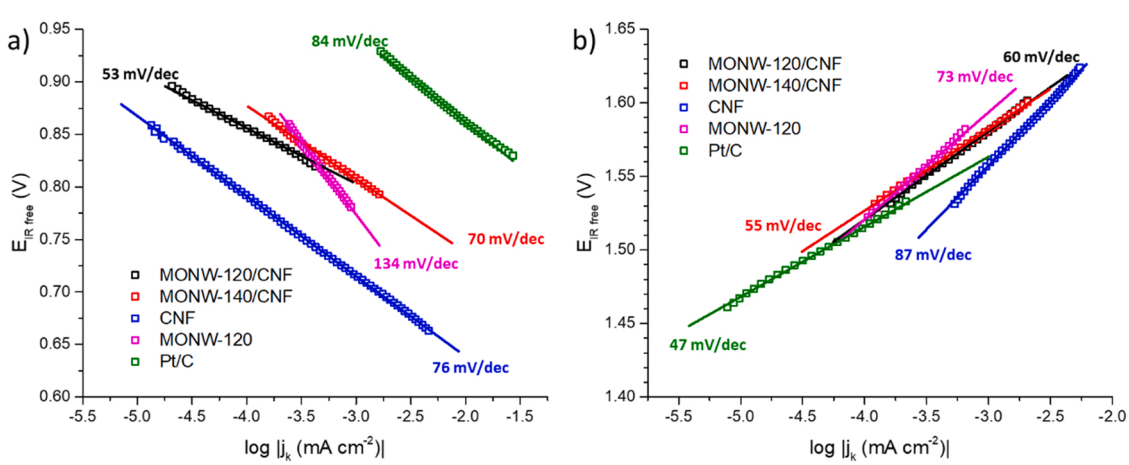

Fig. 5. Tafel plots for a) ORR and b) OER for CNF, MONW-120 and MONW/CNF-composites.

this is the case. Electrochemical Impedance Spectra (EIS) studies were carried out to gain a deeper insight about the RDS of ORR. See Fig. S11 in Supporting Information.

Fig. 5**b** shows the Tafel slope for the OER. The benchmark IrO_2 catalyst has a notably superior performance with a value of 47 mV dec^{-1}, while composites MONW-120/CNF and MONW-140/CNF show slopes of 60 and 55 mV dec^{-1}, respectively. In this reaction, the synergistic effect is less evident but still observable, as the Tafel slopes of CNF and MONW-120 are similar (73 and 87 mV dec^{-1} respectively), but slightly higher than those of the composites. As previously stated, nickel on CNF is active for the OER. MONW shows poorer electrochemical activity than CNF in the polarization curves and a lower Tafel slope. This is explained by the higher exchange current density of CNF, 1.7 * 10^{-4} *versus* MONW-120, 1.0 * 10^{-5} mA cm^{-2}, mainly due to the larger surface area of the CNF.

The commonly accepted route for oxygen evolution in alkaline electrolyte is the following:

$$M + OH^- \rightleftharpoons MOH + e^- \tag{10}$$

$$MOH + OH^- \rightleftharpoons MO + H_2O + e^- \tag{11}$$

$$MO + OH^- \rightleftharpoons MOOH + e^- \tag{12}$$

$$MOOH + OH^- \rightleftharpoons MOO^- + H_2O \tag{13}$$

$$MOO^- \rightleftharpoons M + O_2 + e^- \tag{14}$$

According to the same study cited before [55], a Tafel slope of 40 mV dec^{-1} followed by a higher slope of around 120 mV dec^{-1} – as the one obtained with IrO_2 – is a sign of reaction 12 being the OER rate-determining step. The slopes obtained with the rest of the catalysts, around 60 mV dec^{-1} followed by a higher slope at higher overpotentials, imply that the fourth step (reaction 13) is the rate-determining step.

Due to the close results obtained with MONW-120/CNF and MONW-140/CNF and their interesting electrochemical behaviour, iron-doped manganese oxide nanowires were synthesized at 120 °C and then mixed with CNF to obtain iron-doped composites, Fe-MONW-120 (Fig. 6).

Doping with iron has a beneficial effect on the activity of the composites, since all Fe-MONW-120/CNF composites show superior activity to both reactions in terms of onset potential and current density. The number of exchanged electrons, obtained from K-L plots, does not change upon doping, in comparison to MONW/120-CNF, being 3.4 for all the iron-doped composites. As previously stablished in Section 3.1, iron-doped manganese oxide nanowires have defects, mainly oxygen vacancies, that act like active sites for ORR and OER. These defects are also responsible for the enhanced capacity to adsorb oxygen and OH^-, which is crucial for oxygen reduction [25]. The catalyst with a 5 wt% Fe shows the best activity for both ORR/OER with the lowest onset overpotential and, the lowest ΔE value, 922 mV. ΔE is 140 mV lower compared to the non-doped counterpart (MONW-120/CNF), corroborating the outstanding effect of doping with iron in the electrochemical activity. 5Fe-MONW-120 presents the highest iron surface concentration among the three iron-doped nanowires. Besides, it has a similar amount of defects to 7Fe-MONW-120, but a slightly higher surface area, which are sufficient to enhance the catalytic activity of 5Fe-MONW with respect other samples.

Benchmark catalysts are not bifunctional, Pt/C is not a good catalyst for the OER and IrO_2 is not active for the ORR. For this reason, they were tested independently for their corresponding reactions, and ΔE was not determined. Taking this into account, the differences in activity of benchmark materials with our catalysts were compared in terms of onset overpotential for ORR and OER, and E_{hw} for the ORR. For the OER, 5Fe-MONW-120/CNF and 7Fe-MONW-120/CNF have onset overpotentials practically equal to IrO_2 (only 5 and 3 mV higher) . On the other hand, for the ORR, 5Fe-MONW-120/CNF and 7Fe-MONW-120/CNF present onset overpotentials 147 mV and 155 mV higher than Pt/C, as expected, since Pt/C is an excellent catalyst for the ORR. It must be noted that the number of exchanged electrodes– calculated by Koutecky-Levich equation – does not significantly change in the Fe-MONW/CNF catalysts. This suggests that iron in the manganese structure does not change the mechanism of the reaction but somewhat changes the activation energy of the steps of oxygen reduction.

Table 5 compares all the previously cited electrochemical parameters for ORR and OER over each catalyst. The difference between the composites for ORR is more evident when comparing the half-wave potentials. These values are 687, 736, 765, and 735 mV for MONW-120/CNF, 2Fe-MONWFe-120/CNF, 5Fe-MONW-120/CNF, and 7Fe-MONW-120/CNF, respectively. 5Fe-MONW-120/CNF presents a half-wave potential 30 mV more positive than 7Fe-MONW-120/CNF. This is also the case when comparing the E_{hwp} of 5Fe-MONW-120/CNF *versus* Pt/C, presenting a difference of 110 mV

Tafel slopes were also obtained for the iron-doped composites (Fig. 7). For ORR, the four composites show similar Tafel slopes, with the undoped composite having the lowest one, 53 mV dec^{-1}. On the other hand, 5Fe-MONW120/CNF – the most active composite for ORR – has a slightly higher Tafel slope, 68 mV dec^{-1}, but an exchange current density 1.8 * 10^{-6} mA cm^{-1}, two orders of magnitude higher than the non-doped composite and two orders of magnitude lower than the Pt/C

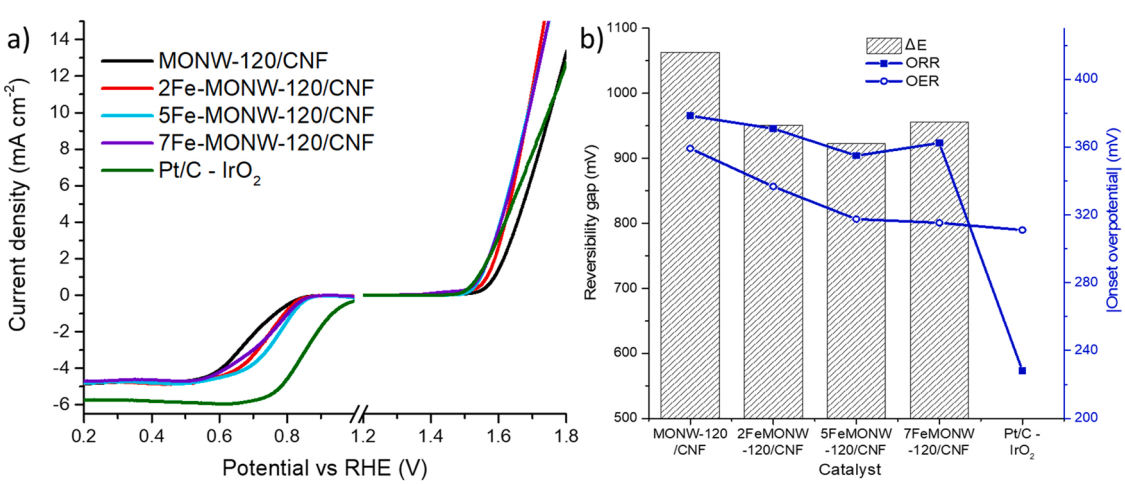

Fig. 6. a) ORR-OER polarization curves of the iron-doped MONW/CNF composites, in a RDE at 1600 rpm in KOH 0.1 M. b) Summary of the performance of the catalysts in terms of overpotential towards OER/ORR and reversibility gap, ΔE. Benchmark catalysts are also included for the sake of comparison: Pt/C for the ORR, and IrO_2 for the OER.

Table 5
Electrochemical parameters obtained from Figs. 4, 5, 6 and 7 for all the tested catalysts.

Catalyst	Oxygen Reduction Reaction						Oxygen Evolution Reaction				ΔE (V)
	E_{hwp} (V *vs.* RHE)	η_{ORR} (mV)	j_L (mA cm^{-2})	*n*	$j_{0,ORR}$ (mA cm^{-2})	$m_{T,ORR}$ (mV dec^{-1})	E_{10} (V *vs.* RHE)	η_{OER} (mV)	$j_{0,OER}$ (mA cm^{-2})	$m_{T,OER}$ (mV dec^{-1})	
CNF	0.66	450	4.2	2.9	$1.8 * 10^{-10}$	76	1.74	347	$1.7 * 10^{-4}$	87	1.08
MONW-120	0.66	387	3.9	2.7	$4.9 * 10^{-10}$	134	1.90	392	$1.0 * 10^{-5}$	73	1.24
MONW-120/CNF	0.69	377	4.8	3.4	$9.1 * 10^{-9}$	53	1.75	360	$1.4 * 10^{-6}$	60	1.06
MONW-140/CNF	0.73	373	4.9	3.5	$8.1 * 10^{-7}$	70	1.74	361	$4.2 * 10^{-7}$	55	1.01
2Fe-MONW-120/CNF	0.74	371	4.8	3.4	$2.4 * 10^{-7}$	63	1.69	331	$1.1 * 10^{-6}$	55	0.95
5Fe-MONW-120/CNF	0.77	355	4.8	3.4	$1.8 * 10^{-6}$	68	1.69	317	$8.5 * 10^{-7}$	51	0.92
7Fe-MONW-120/CNF	0.73	362	4.8	3.4	$4.0 * 10^{-6}$	74	1.69	315	$1.3 * 10^{-5}$	63	0.96
Pt/C – IrO_2	0.88	208	5.7	4.0	$4.2 * 10^{-4}$	84	1.75	312	$1.0 * 10^{-7}$	47	-

E_{hwp} = Half-wave potential;; η_{ORR} = onset overpotential for the ORR (difference between the standard reduction potential and the potential at which ORR reaches −0.1 mA cm^{-2}); j_L = limiting current density; n = number of exchanged electrons; i_0 = exchange current density, $m_{T,ORR}$ = Tafel slope for the ORR; E_{10} = potential at 10 mA cm^{-2}; η_{OER} = onset overpotential for the OER (difference between the potential at which OER reaches 1 mA cm^{-2} and the standard reduction potential); $m_{T,OER}$ = Tafel slope for the OER. ΔE = reversibility gap, calculated as $E_{10} - E_{hwp}$.

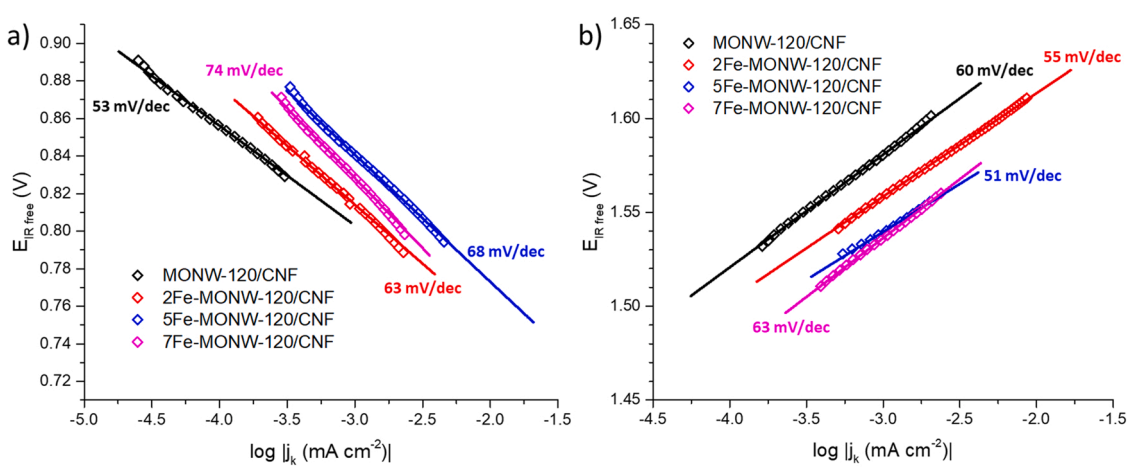

Fig. 7. Tafel plots for a) ORR and b) OER of the iron-doped MONW/CNF composites.

catalyst. There is a trend between the amount of iron and the Tafel slopes, with the slope increasing with the iron percentage, up to 74 mV dec^{-1} in the 7% iron composite. The Tafel slopes for the oxygen evolution show even less variability, with the composite 5Fe-MONW-120/CNF exhibiting a slope very close to that of the benchmark catalyst, 51 mV dec^{-1}. Only 12 mV dec^{-1} of difference separates the Tafel slopes of this catalyst and that of the most active composite OER, 7Fe-MONW-120/CNF. The latter, however, has one order-of-magnitude higher exchange current density, $1.3 * 10^{-5}$ against $8.5 * 10^{-7}$ mA cm^{-2}. These values are similar to what is found in literature, where values around 60 mV dec^{-1} are generally observed for OER over Mn catalysts [35,56, 57].

A comparison between our best catalyst (5Fe-MONW-120/CNF) and several reported catalysts in the literature is presented in Table 6. Catalysts based on similar formulations, employing both manganese and carbon and other catalysts based on non-critical materials have been selected (only studies performed in KOH 0.1 M were included). Our catalyst performs relatively well in terms of reversibility against this kind of materials, as ΔE in literature ranges from 0.71 to 1.20 V. Catalysts obtained by Zhan et al. [58] and by Ma et al. [59], for example, show a reversibility gap of 0.85 V. However, those materials include the synthesis of graphene oxide by Hummer's method and the use of formamide, respectively, with the economical, practical and environmental concerns associated to those methods. The catalyst with the lowest reversibility gap we found in the literature [60], on its side, uses reagents like dioxane in its synthesis, with similar issues. Other Mn-based catalyst with low ΔE rely on the use of cobalt-based formulations, that are not desirable either.

3.2.2. *Stability tests*

Accelerated degradation endurance tests were performed to screen the durability of the best catalyst 5Fe-MONW-120/CNF over cycling (Fig. 8). The tests were carried out over the same RDE at 400 rpm, with negative and positive current densities of 1 mA cm^{-2}. The test comprised 50 cycles of 3 min charging (OER) and 3 min discharging (ORR). At the beginning, the estimated overpotentials for OER (η_{OER}) and ORR (η_{ORR}) are 317 and 418 mV, and the reversibility gap is 735 mV, in accordance with the one calculated from the polarization curve in Fig. 6. The OER overpotential slowly increases from 317 to 331 mV in the 50th cycle. The ORR, on its side, showed a decrease in the potential by cycle 27, having an average overpotential increase of 12 mV over the entire test. Adjusting linear models to the change in

Table 6
Comparison between electrochemical parameters for the best catalyst in this work and non-critical-materials catalysts found in literature.

Catalyst	Ref.	E_{hwp} (V *vs.* RHE)	E_{10} (V *vs.* RHE)	ΔE (V)
5Fe-MONW-120/CNF	**This work**	**0.77**	**1.69**	**0.92**
$MnCo_2O_4$@C	[61]	0.80	1.66	0.89
Electronic and defective $CaMnO_3$ nanotubes	[62]	0.76	1.70	0.94
Iron-doped manganese oxide nanorods	[35]	0.69	1.89	1.20
Single Fe atom on S, N-Codoped Nanocarbon	[63]	0.84	1.64	0.80
Ni-Fe layer double hydroxide @ rGO	[58]	0.63	1.48	0.85
Atomically dispersed Fe *via* Ni neighbouring	[59]	0.84	1.69	0.85
Fe/Ni dual-active sites anchored in honeycomb porous carbon material	[64]	0.87	1.59	0.71
N-doped graphene with topological defects	[65]	0.78	1.71	0.93
N, S co-doped oxygen-functionalized Vulcan XC/72	[66]	0.81	1.58	0.77
NiO-Mn_2O_3-carbon dots catalyst	[67]	0.84	1.53	0.69
Mn-Fe-Ni oxides supported on multiwall carbon nanotubes	[68]	0.81	1.57	0.76
Ni|MnO interfaces over carboxylic-functionalized carbon nanofibers	[69]	0.83	1.58	0.75
Manganese MOF @reduced graphene oxide nanocomposite	[70]	0.98	1.84	0.86
Ultrahin amorphous MnO_2-C (prawn shell derived)	[71]	0.97	1.59	0.77

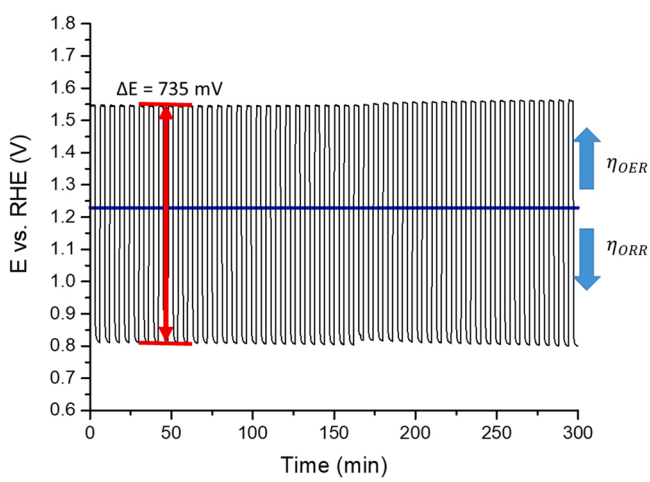

Fig. 8. a) Chronopotentiometric cycles over catalyst 5Fe-MONW-120/CNF. Test carried out at ± 1 mA cm^{-2} for 3 min for each reaction.

overpotential, in average, the OER overpotential increases 0.26 mV per cycle and the ORR overpotential increases 0.10 mV per cycle, evidencing that 5Fe-MONW-120/CNF shows a really stable behavior.

Long endurance tests, shown in Fig. 9, at higher current densities were performed in GDE to test the catalyst under more demanding and realistic conditions, namely, ± 10 mA cm^{-2} for both OER and ORR and 2.5 h for each reaction. For the first four cycles (20 h of operation), 5Fe-MONW-120/CNF shows a reasonably stable behavior, with the overpotentials for both OER and ORR increasing very slowly. However, at the end of the fourth oxygen reduction cycle, a significant increase in the overpotential – manifested as a sharp fall (for the ORR) and increase (for the OER) of the measured potential – is appreciated. After this sudden change, the overpotential for ORR increases slowly but steadily. In contrast, the overpotential for OER stays constant until the fourteenth-fifteenth cycle when another sharp increase can be seen. This sharp variation of the potential can be due to the excessive formation of oxygen bubbles, partially covering the electrode area, which could affect to the measuring of the potential with respect to the reference potential. This could entail a higher applied current to the electrode, eventually causing a higher electrode degradation. As a result, for the first four cycles (first 20 h of operation), the reversibility gap **(**Fig. 9**b)** stays below 850 mV, reaching 950 mV during cycles 5–13 and exceeding 1000 mV after. The combination of a sudden but sharp loss of activity (*e.g.,* between cycles 4 and 5) and a sustained but slower deactivation suggests two different deactivation causes or mechanisms acting simultaneously. Post-mortem XRD analysis was performed in the GDE electrode to investigate if a change in the crystalline phases of the electrode could be responsible for the deactivation of the electrode **(**Fig. S12**)**. No change in the crystal phases, crystallinity, or crystal size could be observed, so the formation of bubbles in the electrode, affecting the reference potential, could explain the deactivation, as previously mentioned.

4. Conclusions

Bifunctional easy-synthesis oxygen catalysts composites based on iron-doped (2–7% wt.) manganese oxide nanowires (Fe-MONW) and carbon nanofibers (CNF) were tested as electrodes for alkaline oxygen evolution (OER) and reduction (ORR) reactions. The Fe-MONW/CNF composites show an enhanced activity compared to their individual phases (CNF and MONW) and onset potentials similar to the benchmark catalysts, especially for OER. Doping with iron reduced the onset overpotential for both ORR and OER, leading to a decrease in the reversibility gap of *ca.* 140 mV, reaching as low as 922 mV. The overpotential for OER decreased monotonically with the amount of iron in the studied range, while the overpotential for ORR reached an optimal at 5% wt. Physical-chemical characterization determined that iron creates vacancies in the MnO_2 lattice, which increases its catalytic activity by favoring the adsorption of oxygen. The analysis of the Tafel slopes reveals that combining CNF and MONW changes the rate-determining step of the reaction. However, this does not occur by doping MONW with iron (Tafel slopes do not change significantly). Endurance tests were also carried out with mild and challenging conditions for the 5Fe-doped MONW/CNF composite, which presented remarkable stability, with a stable potential for over 20 h, keeping the reversibility gap around 800 mV, which is an outstanding result, taking into account the higher current density employed (more challenging conditions).

The synergy between the iron-doped manganese nanostructure and the carbon nanofiber leads to a remarkable reversibility and enhanced performance for the oxygen reduction (ORR) and evolution (OER) reactions, along with a remarkable stability, a key issue for the future implementation of this kind of devices.

CRediT authorship contribution statement

N.I. Villanueva-Martínez is responsible for the investigation, conducting the research and investigation process, specifically performing the experiments, and data collection. Also N.I. Villanueva-Martínez is responsible for data curation and writing of the draft. C. Alegre is responsible for the conceptualization, planning and execution of the research activity including mentorship as well as for the critical review of the data curation and the writing of the draft. I. Martínez-Visús is responsible for conducting the research, performing the synthesis of materials. M.J. Lázaro is responsible for management and coordination for the research activity planning and execution, as well as responsible for the acquisition of the financial support for the project leading to this publication, and for the critical review of the manuscript. All authors have supervised and critically revised the writing of the manuscript.

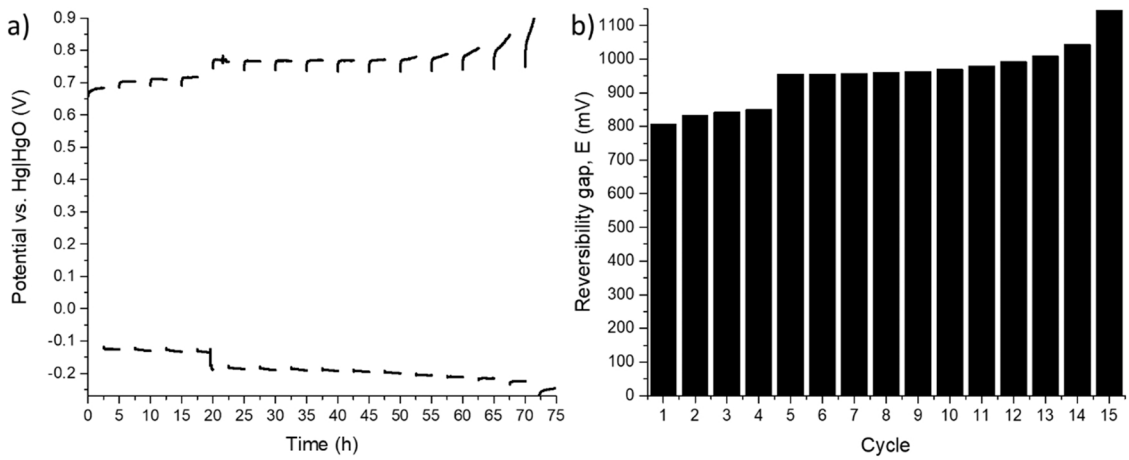

Fig. 9. a) Chronopotentiometric cycles and b) reversibility gap for each cycle for durability tests over catalyst 5Fe-MONW-120/CNF in GDE. Test carried out at ± 10 mA cm^{-2} and 2.5 h for each reaction in 6 M KOH.

Declaration of Competing Interest

The authors declare that they have no known competing financial interests or personal relationships that could have appeared to influence the work reported in this paper.

Data Availability

Data will be made available on request.

Acknowledgments

The authors wish to acknowledge the grant PID2020-115848RB-C21 funded by MCIN/AEI/10.13039/501100011033. Authors also acknowledge Gobierno de Aragón (DGA) for the financial support to Grupo de Conversión de Combustibles (T06_20R). N. Villanueva-Martínez also acknowledges DGA for his pre-doctoral contract.

Appendix A. Supporting information

Supplementary data associated with this article can be found in the online version at doi:10.1016/j.cattod.2023.114083.

References

[1] W.J. Kwak, D. Rosy, C. Sharon, H. Xia, L.R. Kim, P.G. Johnson, L.F. Bruce, Y. K. Nazar, A.A. Sun, M. Frimer, S.A. Noked, D. Freunberger, Aurbach, Lithium-oxygen batteries and related systems: potential, status, and future, ACS Appl. Mater. Interfaces 120 (14) (2020) 6626–6683, https://doi.org/10.1021/acs.chemrev.9b00609.

[2] Q. Liu, Z. Pan, E. Wang, L. An, G. Sun, Aqueous metal-air batteries: fundamentals and applications, Energy Storage Mater. 27 (2020) 478–505, https://doi.org/10.1016/j.ensm.2019.12.011.

[3] A. Kraytsberg, Y. Ein-Eli, The impact of nano-scaled materials on advanced metal-air battery systems, Nano Energy 2 (2013) 468–480, https://doi.org/10.1016/j.nanoen.2012.11.016.

[4] N.R. Levy, P. Tereshchuk, A. Natan, R. Haas, D. Schröder, J. Janek, P. Jakes, R. A. Eichel, Y. Ein-Eli, Hybridization of carbon nanotube tissue and MnO2 as a generic advanced air cathode in metal–air batteries, J. Power Sources 514 (2021), 230597, https://doi.org/10.1016/j.jpowsour.2021.230597.

[5] H. Weinrich, Y.E. Durmus, H. Tempel, H. Kungl, R.-A. Eichel, Silicon and iron as resource-efficient anode materials for ambient-temperature metal-air batteries, A Rev., Mater. Vol. 12 (2019) 2134, https://doi.org/10.3390/MA12132134.

[6] Y. Li, J. Lu, Metal-air batteries: will they be the future electrochemical energy storage device of choice? ACS Energy Lett. 2 (6) (2017) 1370–1377, https://doi.org/10.1021/acsenergylett.7b00119.

[7] H. Li, L. Ma, C. Han, Z. Wang, Z. Liu, Z. Tang, C. Zhi, Advanced rechargeable zinc-based batteries: recent progress and future perspectives, Nano Energy 62 (2019) 550–587, https://doi.org/10.1016/J.NANOEN.2019.05.059.

[8] X. Cai, L. Lai, J. Lin, Z. Shen, Recent advances in air electrodes for Zn-air batteries: electrocatalysis and structural design, Mater. Horiz. 4 (2017) 945–976, https://doi.org/10.1039/c7mh00358g.

[9] N.-T. Suen, S.-F. Hung, Q. Quan, N. Zhang, Y.-J. Xu, H.M. Chen, Electrocatalysis for the oxygen evolution reaction: recent development and future perspectives, Chem. Soc. Rev. 46 (2017) 337–365, https://doi.org/10.1039/C6CS00328A.

[10] M. Shao, Q. Chang, J.-P. Dodelet, R. Chenitz, Recent advances in electrocatalysts for oxygen reduction reaction, Chem. Rev. 116 (2016) 3594–3657, https://doi.org/10.1021/acs.chemrev.5b00462.

[11] C. Alegre, E. Modica, C. Lo Vecchio, S. Siracusano, A.S. Aricò, V. Baglio, Pd supported on Ti-suboxides as bifunctional catalyst for air electrodes of metal-air batteries, Int. J. Hydrog. Energy 41 (2016) 19579–19586, https://doi.org/10.1016/j.ijhydene.2016.03.095.

[12] R.D. McKerracher, H.A. Figueredo-Rodríguez, C. Ponce de León, C. Alegre, V. Baglio, A.S. Aricò, F.C. Walsh, A high-performance, bifunctional oxygen electrode catalysed with palladium and nickel-iron hexacyanoferrate, Electrochim. Acta 206 (2016) 127–133, https://doi.org/10.1016/j.electacta.2016.04.090.

[13] C. Alegre, S. Siracusano, E. Modica, A.S. Aricò, V. Baglio, Titanium–tantalum oxide as a support for Pd nanoparticles for the oxygen reduction reaction in alkaline electrolytes, Mater. Renew. Sustain. Energy 7 (2018) 8, https://doi.org/10.1007/s40243-018-0114-z.

[14] A.A. Gewirth, J.A. Varnell, A.M. Diascro, Nonprecious metal catalysts for oxygen reduction in heterogeneous aqueous systems, Chem. Rev. 118 (2018) 2313–2339, https://doi.org/10.1021/acs.chemrev.7b00335.

[15] R. Wang, Z. Chen, N. Hu, C. Xu, Z. Shen, J. Liu, Nanocarbon-based electrocatalysts for rechargeable aqueous Li/Zn-Air batteries, ChemElectroChem 5 (2018) 1745–1763, https://doi.org/10.1002/celc.201800141.

[16] Q. Wei, Y. Fu, G. Zhang, S. Sun, Rational design of carbon-based oxygen electrocatalysts for zinc–air batteries, Curr. Opin. Electrochem. 4 (2017) 45–59, https://doi.org/10.1016/J.COELEC.2017.09.006.

[17] X. Ge, A. Sumboja, D. Wuu, T. An, B. Li, F.W.T. Goh, T.S.A. Hor, Y. Zong, Z. Liu, Oxygen reduction in alkaline media: from mechanisms to recent advances of catalysts, ACS Catal. 5 (2015) 4643–4667, https://doi.org/10.1021/acscatal.5b00524.

[18] C. Alegre, E. Modica, M. Rodlert-Bacilieri, F.C. Mornaghini, A.S. Aricò, V. Baglio, Enhanced durability of a cost-effective perovskite-carbon catalyst for the oxygen evolution and reduction reactions in alkaline environment, Int. J. Hydrog. Energy 42, Issue 46, (2017), 28063-28069. doi:10.1016/j.ijhydene.2017.03.216.

[19] C. Alegre, C. Busacca, A. Di Blasi, O. Di Blasi, A.S.S. Aricò, V. Antonucci, E. Modica, V. Baglio, Electrospun carbon nanofibers loaded with spinel-type cobalt oxide as bifunctional catalysts for enhanced oxygen electrocatalysis, J. Energy Storage 23 (2019) 269–277, https://doi.org/10.1016/J.EST.2019.04.001.

[20] J.M. Luque-Centeno, M.V. Martínez-Huerta, D. Sebastián, G. Lemes, E. Pastor, M. J. Lázaro, Bifunctional N-doped graphene Ti and Co nanocomposites for the oxygen reduction and evolution reactions, Renew. Energy 125 (2018) 182–192, https://doi.org/10.1016/J.RENENE.2018.02.073.

[21] P. Stelmachowski, A.H.A. Monteverde Videla, T. Jakubek, A. Kotarba, S. Specchia, The Effect of Fe, Co, and Ni Structural Promotion of Cryptomelane (KMn8O16) on the Catalytic Activity in Oxygen Evolution Reaction, Electrocatalysis 9 (2018) 762–769, https://doi.org/10.1007/s12678-018-0488-9.

[22] A. Kostuch, J. Gryboś, P. Indyka, L. Osmieri, S. Specchia, Z. Sojka, K. Kruczała, Morphology and dispersion of nanostructured manganese-cobalt spinel on various carbon supports: The effect on the oxygen reduction reaction in alkaline media, Catal. Sci. Technol. 8 (2018) 642–655, https://doi.org/10.1039/c7cy02228j.

[23] H. Osgood, S.V. Devaguptapu, H. Xu, J. Cho, G. Wu, Transition metal (Fe, Co, Ni, and Mn) oxides for oxygen reduction and evolution bifunctional catalysts in alkaline media, Nano Today 11 (2016) 601–625, https://doi.org/10.1016/J.NANTOD.2016.09.001.

[24] A.B. Haruna, K.I. Ozoemena, Manganese-based bifunctional electrocatalysts for zinc-air batteries, Curr. Opin. Electrochem. 21 (2020) 219–224, https://doi.org/10.1016/J.COELEC.2020.02.021.

[25] L. Tian, X. Zhai, X. Wang, J. Li, Z. Li, Advances in manganese-based oxides for oxygen evolution reaction, J. Mater. Chem. A 8 (2020) 14400–14414, https://doi.org/10.1039/d0ta05116k.
[26] J. Deng, S. Fang, Y. Fang, Q. Hao, L. Wang, Y.H. Hu, Multiple roles of graphene in electrocatalysts for metal-air batteries, Catal. Today 409 (2023) 2–22, https://doi.org/10.1016/j.cattod.2022.01.003.
[27] M.F.P. Duarte, I.M. Rocha, J.L. Figueiredo, C. Freire, M.F.R. Pereira, CoMn-LDH@carbon nanotube composites: Bifunctional electrocatalysts for oxygen reactions, Catal. Today 301 (2018) 17–24, https://doi.org/10.1016/j.cattod.2017.03.046.
[28] M. Yin, H. Miao, R. Hu, Z. Sun, H. Li, Manganese dioxides for oxygen electrocatalysis in energy conversion and storage systems over full pH range, J. Power Sources 494 (2021), 229779, https://doi.org/10.1016/j.jpowsour.2021.229779.
[29] Y. Gu, G. Yan, Y. Lian, P. Qi, Q. Mu, C. Zhang, Z. Deng, Y. Peng, MnIII-enriched α-MnO2 nanowires as efficient bifunctional oxygen catalysts for rechargeable Zn-air batteries, Energy Storage Mater. 23 (2019) 252–260, https://doi.org/10.1016/j.ensm.2019.05.006.
[30] H. Singh, M. Marley-Hines, S. Chakravarty, M. Nath, Multi-walled carbon nanotube supported manganese selenide as a highly active bifunctional OER and ORR electrocatalyst, J. Mater. Chem. A 10 (2022) 6772–6784, https://doi.org/10.1039/d1ta09864k.
[31] J. Melder, S. Mebs, P.A. Heizmann, R. Lang, H. Dau, P. Kurz, Carbon fibre paper coated by a layered manganese oxide: a nano-structured electrocatalyst for water-oxidation with high activity over a very wide pH range, J. Mater. Chem. A 7 (2019) 25333–25346, https://doi.org/10.1039/C9TA08804K.
[32] H. Miao, B. Chen, S. Li, X. Wu, Q. Wang, C. Zhang, Z. Sun, H. Li, All-solid-state flexible zinc-air battery with polyacrylamide alkaline gel electrolyte, J. Power Sources 450 (2020), 227653, https://doi.org/10.1016/J.JPOWSOUR.2019.227653.
[33] T. Zhang, Z. Li, L. Wang, P. Sun, Z. Zhang, S. Wang, Spinel MnCo2O4 nanoparticles supported on three-dimensional graphene with enhanced mass transfer as an efficient electrocatalyst for the oxygen reduction reaction, ChemSusChem 11 (2018) 2730–2736, https://doi.org/10.1002/CSSC.201801070.
[34] C. Alegre, C. Busacca, A. Di Blasi, O. Di Blasi, A.S. Aricò, V. Antonucci, V. Baglio, Electrocatalysis of oxygen on bifunctional nickel-cobaltite spinel, ChemElectroChem 7 (2020) 124–130, https://doi.org/10.1002/celc.201901584.
[35] A. Mathur, A. Halder, One-step synthesis of bifunctional iron-doped manganese oxide nanorods for rechargeable zinc-air batteries, Catal. Sci. Technol. 9 (2019) 1245–1254, https://doi.org/10.1039/c8cy02498g.
[36] D. Sebastián, I. Suelves, R. Moliner, M.J. Lázaro, The effect of the functionalization of carbon nanofibers on their electronic conductivity, Carbon 48 (2010) 4421–4431, https://doi.org/10.1016/j.carbon.2010.07.059.
[37] Y. Ma, R. Wang, H. Wang, J. Key, S. Ji, Control of MnO2 nanocrystal shape from tremella to nanobelt for ehancement of the oxygen reduction reaction activity, J. Power Sources 280 (2015) 526–532, https://doi.org/10.1016/j.jpowsour.2015.01.139.
[38] W. Xiao, D. Wang, X.W. Lou, Shape-controlled synthesis of MnO2 nanostructures with enhanced electrocatalytic activity for oxygen reduction, J. Phys. Chem. C. 114 (2010) 1694–1700, https://doi.org/10.1021/jp909386d.
[39] M.C. Biesinger, B.P. Payne, A.P. Grosvenor, L.W.M. Lau, A.R. Gerson, R.S.C. Smart, Resolving surface chemical states in XPS analysis of first row transition metals, oxides and hydroxides: Cr, Mn, Fe, Co and Ni, Appl. Surf. Sci. 257 (2011) 2717–2730, https://doi.org/10.1016/j.apsusc.2010.10.051.
[40] D. Briggs, Handbook of X-ray Photoelectron Spectroscopy, in: C.D. Wanger, W. M. Riggs, L.E. Davis, J.F. Moulder, G. E.Muilenberg (Eds.), Physical Electronics Division, Perkin-Elmer Corp., Eden Prairie, Minnesota, USA, 1979, 190 pp., Surf. Interface Anal. 3 (1981) v–v. doi:10.1002/sia.740030412.
[41] V.P. Santos, M.F.R. Pereira, J.J.M. Órfão, J.L. Figueiredo, The role of lattice oxygen on the activity of manganese oxides towards the oxidation of volatile organic compounds, Appl. Catal. B Environ. 99 (2010) 353–363, https://doi.org/10.1016/j.apcatb.2010.07.007.
[42] H. Abdel-Samad, P.R. Watson, An XPS study of the adsorption of chromate on goethite (α-FeOOH), Appl. Surf. Sci. 108 (1997) 371–377, https://doi.org/10.1016/S0169-4332(96)00609-5.
[43] L. Li, X. Feng, Y. Nie, S. Chen, F. Shi, K. Xiong, W. Ding, X. Qi, J. Hu, Z. Wei, L. J. Wan, M. Xia, Insight into the Effect of Oxygen Vacancy Concentration on the Catalytic Performance of MnO2, ACS Catal. 5 (2015) 4825–4832, https://doi.org/10.1021/acscatal.5b00320.
[44] E. Hastuti, A. Subhan, P. Amonpattaratkit, M. Zainuri, S. Suasmoro, The effects of Fe-doping on MnO2: phase transitions, defect structures and its influence on electrical properties, RSC Adv. 11 (2021) 7808–7823, https://doi.org/10.1039/d0ra10376d.
[45] D. Mondal, B.K. Paul, S. Das, D. Bhattacharya, D. Ghoshal, P. Nandy, K. Das, S. Das, Synthesis and Property of Copper-Impregnated α-MnO2 Semiconductor Quantum Dots, Langmuir 34 (2018) 12702–12712, https://doi.org/10.1021/acs.langmuir.8b01745.
[46] D. Sebastián, I. Suelves, R. Moliner, M.J. Lázaro, The effect of the functionalization of carbon nanofibers on their electronic conductivity, Carbon 48 (15) (2010) 4421–4431, https://doi.org/10.1016/j.carbon.2010.07.059.
[47] M.S. Ahn, R. Ahmad, J.Y. Yoo, Y.B. Hahn, Synthesis of manganese oxide nanorods and its application for potassium ion sensing in water, J. Colloid Interface Sci. 516 (2018) 364–370, https://doi.org/10.1016/j.jcis.2018.01.081.
[48] J. Jia, P. Zhang, L. Chen, The effect of morphology of α-MnO2 on catalytic decomposition of gaseous ozone, Catal. Sci. Technol. 6 (2016) 5841–5847, https://doi.org/10.1039/c6cy00301j.
[49] J.C. Ruiz-Cornejo, D. Sebastián, M.J. Lázaro, Synthesis and applications of carbon nanofibers: a review, Rev. Chem. Eng. 36 (2020) 493–511, https://doi.org/10.1515/revce-2018-0021.
[50] D. Sebastián, A.G. Ruiz, I. Suelves, R. Moliner, M.J. Lázaro, On the importance of the structure in the electrical conductivity of fishbone carbon nanofibers, J. Mater. Sci. 48 (2013) 1423–1435, https://doi.org/10.1007/s10853-012-6893-1.
[51] C. Alegre, C. Busacca, A. Di Blasi, O. Di Blasi, A.S. Aricò, V. Antonucci, V. Baglio, Toward more efficient and stable bifunctional electrocatalysts for oxygen electrodes using FeCo2O4/carbon nanofiber prepared by electrospinning, Mater. Today, Energy 18 (2020), https://doi.org/10.1016/j.mtener.2020.100508.
[52] A. Holewinski, S. Linic, Elementary mechanisms in electrocatalysis: revisiting the ORR tafel slope, J. Electrochem. Soc. 159 (2012) H864–H870, https://doi.org/10.1149/2.022211jes.
[53] M. Shao, P. Liu, R.R. Adzic, Superoxide anion is the intermediate in the oxygen reduction reaction on platinum electrodes, J. Am. Chem. Soc. 128 (2006) 7408–7409.
[54] J.S. Spendelowa, A. Wieckowski, Electrocatalysis of oxygen reduction and small alcohol oxidation in alkaline media, Phys. Chem. Chem. Phys. 9 (2007) 2654–2675.
[55] T. Shinagawa, A.T. Garcia-Esparza, K. Takanabe, Insight on Tafel slopes from a microkinetic analysis of aqueous electrocatalysis for energy conversion, Sci. Rep. 5 (2015) 1–21, https://doi.org/10.1038/srep13801.
[56] F. Cheng, T. Zhang, Y. Zhang, J. Du, X. Han, J. Chen, Enhancing electrocatalytic oxygen reduction on MnO2 with vacancies, Angew. Chem. - Int. Ed. 52 (2013) 2474–2477, https://doi.org/10.1002/anie.201208582.
[57] F. Cheng, Y. Su, J. Liang, Z. Tao, J. Chen, MnO2-based nanostructures as catalysts for electrochemical oxygen reduction in alkaline media, Chem. Mater. 22 (2010) 898–905, https://doi.org/10.1021/cm901698s.
[58] T. Zhan, Y. Zhang, X. Liu, S.S. Lu, W. Hou, NiFe layered double hydroxide/reduced graphene oxide nanohybrid as an efficient bifunctional electrocatalyst for oxygen evolution and reduction reactions, J. Power Sources 333 (2016) 53–60, https://doi.org/10.1016/j.jpowsour.2016.09.152.
[59] M. Ma, A. Kumar, D. Wang, Y. Wang, Y. Jia, Y. Zhang, G. Zhang, Z. Yan, X. Sun, Boosting the bifunctional oxygen electrocatalytic performance of atomically dispersed Fe site via atomic Ni neighboring, Appl. Catal. B Environ. 274 (2020), 119091, https://doi.org/10.1016/j.apcatb.2020.119091.
[60] B. Guo, J. Guo, W. Yang, X. Tian, X. Wang, Z. Xiang, M. Wu, Highly dispersed iron/nickel dual-sites in hierarchical porous carbon materials as high-performance bifunctional oxygen electrocatalysts for Zn-air batteries, Renew. Energy 201 (2022) 117–124, https://doi.org/10.1016/j.renene.2022.11.036.
[61] C. Shenghai, S. Liping, K. Fanhao, H. Lihua, Z. Hui, Carbon-coated MnCo2O4 nanowire as bifunctional oxygen catalysts for rechargeable Zn-air batteries, J. Power Sources 430 (2019) 25–31, https://doi.org/10.1016/j.jpowsour.2019.05.029.
[62] S. Peng, X. Han, L. Li, S. Chou, D. Ji, H. Huang, Y. Du, J. Liu, S. Ramakrishna, Electronic and defective engineering of electrospun CaMnO3 nanotubes for enhanced oxygen electrocatalysis in rechargeable Zinc–air batteries, Adv. Energy Mater. 8 (2018), 1800612, https://doi.org/10.1002/aenm.201800612.
[63] J. Zhang, M. Zhang, Y. Zeng, J. Chen, L. Qiu, H. Zhou, C. Sun, Y. Yu, C. Zhu, Z. Zhu, Single Fe atom on hierarchically porous S, N-codoped nanocarbon derived from porphyra enable boosted oxygen catalysis for rechargeable Zn-air batteries, Small 15 (2019) 1900307, https://doi.org/10.1002/smll.201900307.
[64] B. Guo, J. Guo, W. Yang, X. Tian, X. Wang, Z. Xiang, M. Wu, Highly dispersed iron/nickel dual-sites in hierarchical porous carbon materials as high-performance bifunctional oxygen electrocatalysts for Zn-air batteries, Renew. Energy 201 (2022) 117–124, https://doi.org/10.1016/j.renene.2022.11.036.
[65] Y. Liu, K. Sun, X. Cui, B. Li, J. Jiang, Defect-rich, graphenelike carbon sheets derived from biomass as efficient electrocatalysts for rechargeable zinc-air batteries, ACS Sustain. Chem. Eng. 8 (2020) 2981–2989, https://doi.org/10.1021/acssuschemeng.9b07621.
[66] S. Zhou, J. Zang, H. Gao, X. Tian, P. Tian, S. Song, Y. Wang, Deflagration method synthesizing N, S co-doped oxygen-functionalized carbons as a bifunctional catalyst for oxygen reduction and oxygen evolution reaction, Carbon 181 (2021) 234–245, https://doi.org/10.1016/j.carbon.2021.05.034.
[67] C. Shao, F. Liao, W. Zhu, Y. Zhang, M. Ma, J. Yang, K. Yin, M. Shao, B. Jiang, Carbon dots bridge NiO and Mn2O3 as highly efficient bifunctional oxygen electrocatalysts for rechargeable zinc-air batteries, Appl. Surf. Sci. 596 (2022), 153642, https://doi.org/10.1016/j.apsusc.2022.153642.
[68] D.M. Morales, M.A. Kazakova, S. Dieckhöfer, A.G. Selyutin, G.V. Golubtsov, W. Schuhmann, J. Masa, Trimetallic Mn-Fe-Ni oxide nanoparticles supported on multi-walled carbon nanotubes as high-performance bifunctional ORR/OER electrocatalyst in alkaline media, Adv. Funct. Mater. 30 (2020) 1905992, https://doi.org/10.1002/adfm.201905992.
[69] D. Ji, J. Sun, L. Tian, A. Chinnappan, T. Zhang, W.A.D.M. Jayathilaka, R. Gosh, C. Baskar, Q. Zhang, S. Ramakrishna, Engineering of the heterointerface of porous carbon nanofiber–supported nickel and manganese oxide nanoparticle for highly efficient bifunctional oxygen catalysis, Adv. Funct. Mater. 30 (2020) 1910568, https://doi.org/10.1002/adfm.201910568.
[70] A. Wahab, N. Iqbal, T. Noor, S. Ashraf, M.A. Raza, A. Ahmad, U.A. Khan, Thermally reduced mesoporous manganese MOF @reduced graphene oxide nanocomposite as bifunctional electrocatalyst for oxygen reduction and evolution, RSC Adv. 10 (2020) 27728–27742, https://doi.org/10.1039/d0ra04193a.
[71] X. Xiao, W. Zhang, H. Zhao, L. Li, P. Deng, Y. Wu, S. Luo, B. Chen, Ultrathin amorphous MnO2 modified prawn shells-derived porous carbon towards robust oxygen electrocatalyst for rechargeable Zn-air battery, Ceram. Int. 48 (5) (2022) 6506–6511, https://doi.org/10.1016/j.ceramint.2021.11.195.

Supporting information

Bifunctional oxygen electrocatalysts based on non-critical raw materials: carbon nanostructures and iron-doped manganese oxide nanowires

N.I. Villanueva-Martínez[1], C. Alegre[1,*], I. Martínez-Visús[2,3], M.J. Lázaro[1,*]

[1]Instituto de Carboquímica, CSIC. C/. Miguel Luesma Castán, 4. 50018 Zaragoza

[2]Instituto de Nanociencia y Materiales de Aragón (INMA), CSIC

Universidad de Zaragoza, Zaragoza 50018, Spain

[3]Chemical and Environmental Engineering Department

Universidad de Zaragoza, Zaragoza 50018, Spain

*Corresponding authors: cinthia@icb.csic.es; mlazaro@icb.csic.es

Table S1. Surface composition of MONW and Fe-MONW measured by XPS expressed as weight percentage.

Material	Weight %			
	O	Mn	Fe	K
MONW-120	26.8	69.8	-	3.4
MONW-140	44.1	49.3	-	6.6
2Fe-MONW-120	46.4	28.2	19.4	6.0
5Fe-MONW-120	47.0	26.9	22.8	3.4
7Fe-MONW-120	47.4	28.1	21.5	2.9

** Atomic percentages transformed to wt. percentages.*

Table S2. Bulk composition expressed as atomic percentage, obtained from ICP.

Material	Atomic %			
	O	Mn	Fe	K
MONW-120	64.9	30.6	-	4.5
MONW-140	63.3	31.7	-	5.1
2Fe-MONW-120	68.4	26.1	1.0	4.5
5Fe-MONW-120	67.6	27.2	2.7	2.5
7Fe-MONW-120	69.5	25.7	3.3	1.6

** Weight percentages transformed to at. percentages.*

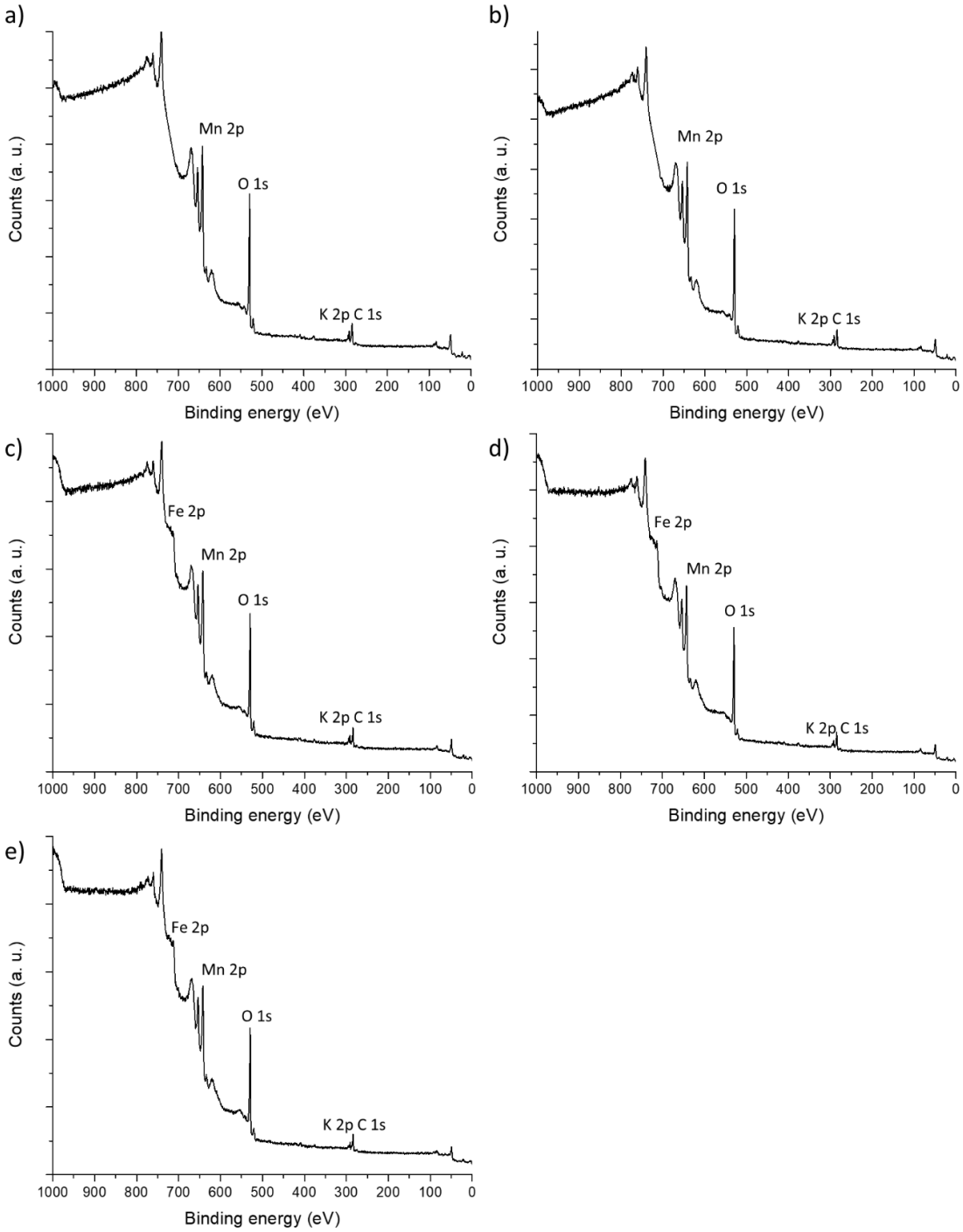

Figure S1. XPS spectra of pattern of nanowires a) MONW-120, b) MONW-140, c) 2FeMONW-120, d) 5FeMONW-120 and e) 7FeMONW-120. ** Adventitious carbon (not coming from MONW samples). Adventitious carbon is a thin layer of carbonaceous material usually found on the surface of most air exposed samples.*

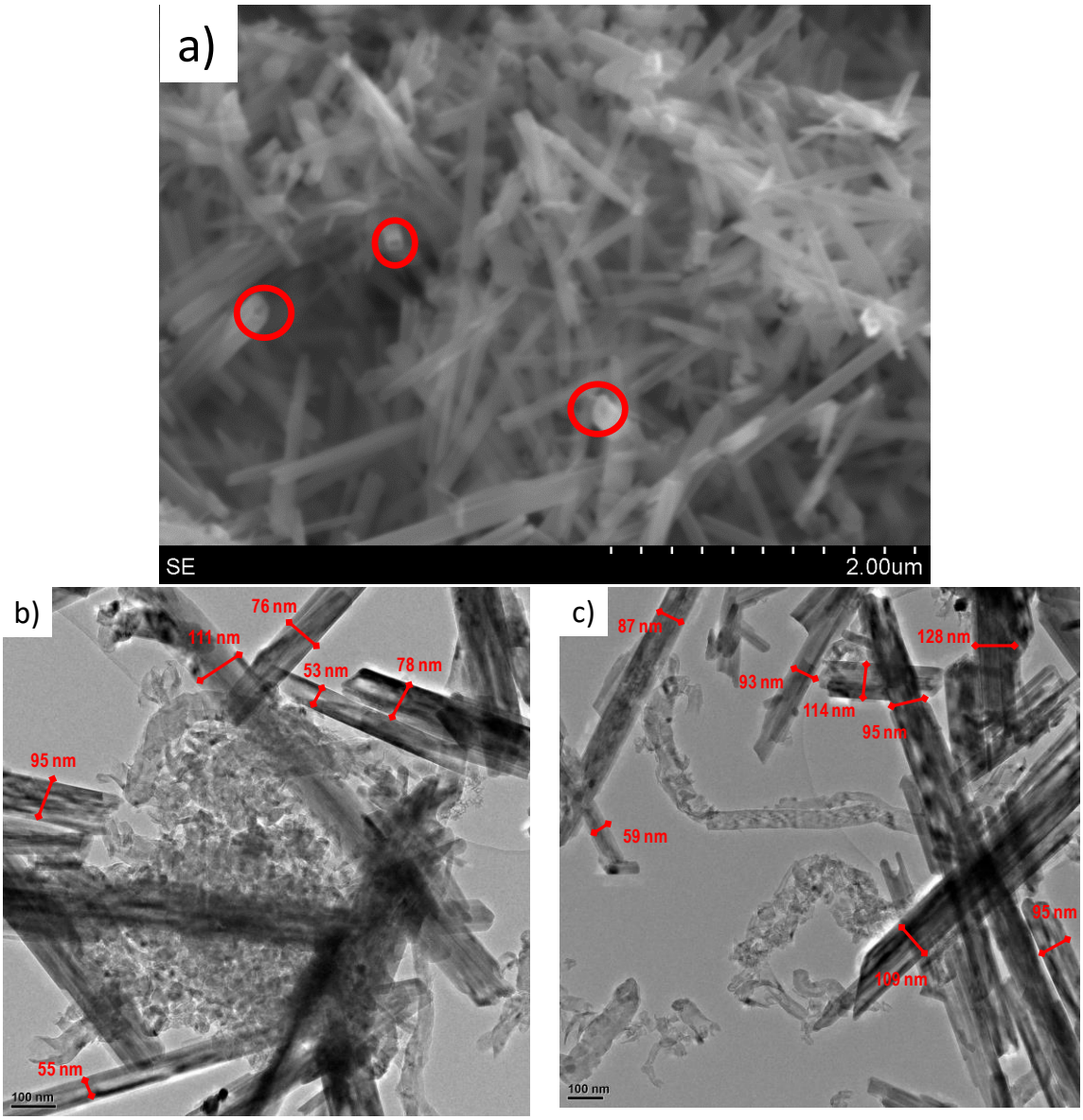

Figure S2. (a) High-resolution SEM image of MONW-140 at 23000x magnification. Red circles indicate the openings in the extreme of the nanowires. TEM-image for (b) MONW-120/CNF and for c) MONW-140/CNF. Red lines indicate the diameter of the nanowires.

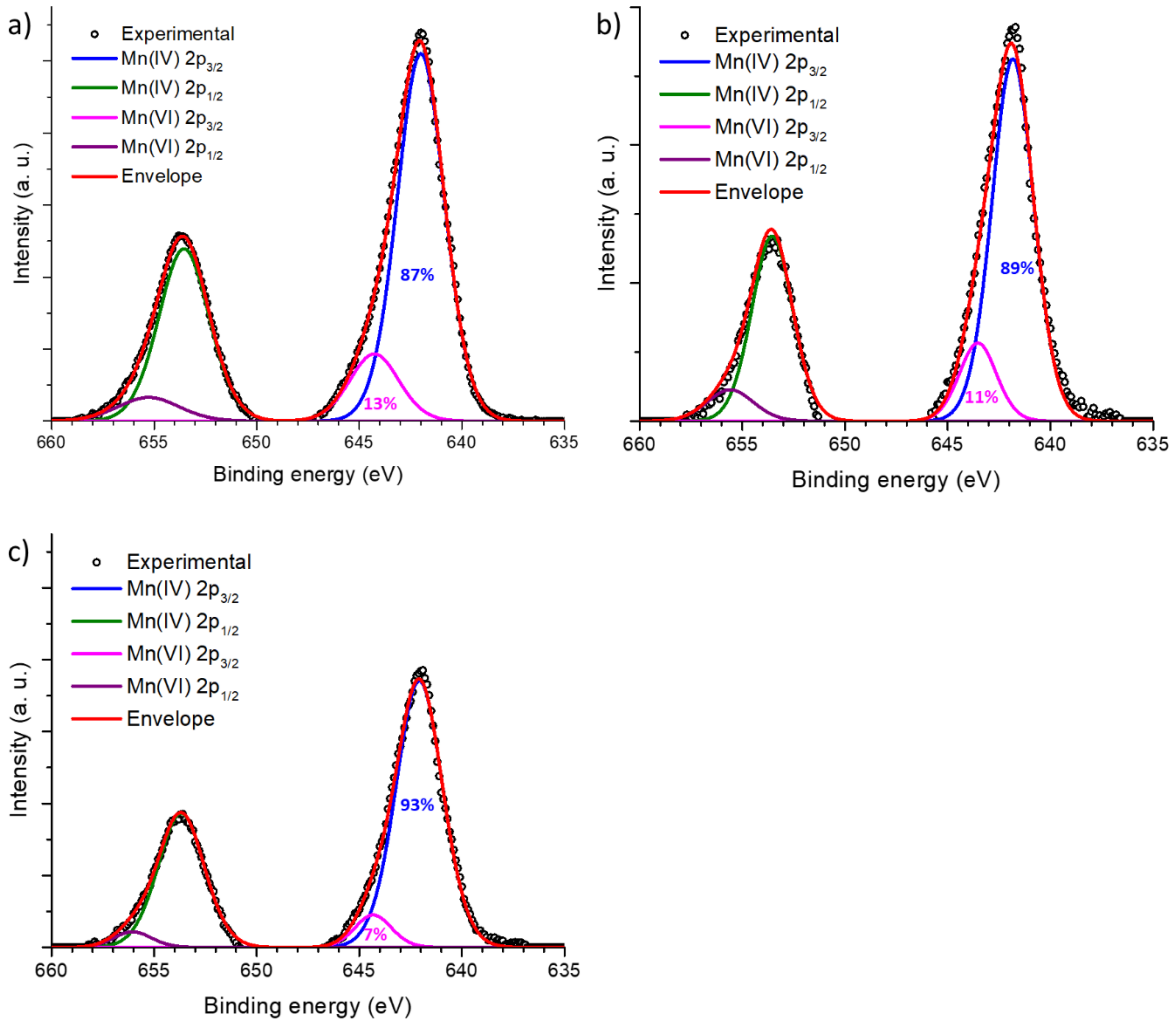

Figure S3. High-resolution XPS spectra of Mn 2p orbital of samples a) MONW-140, b) 2Fe-MONW-120, c) 7Fe-MONW-120.

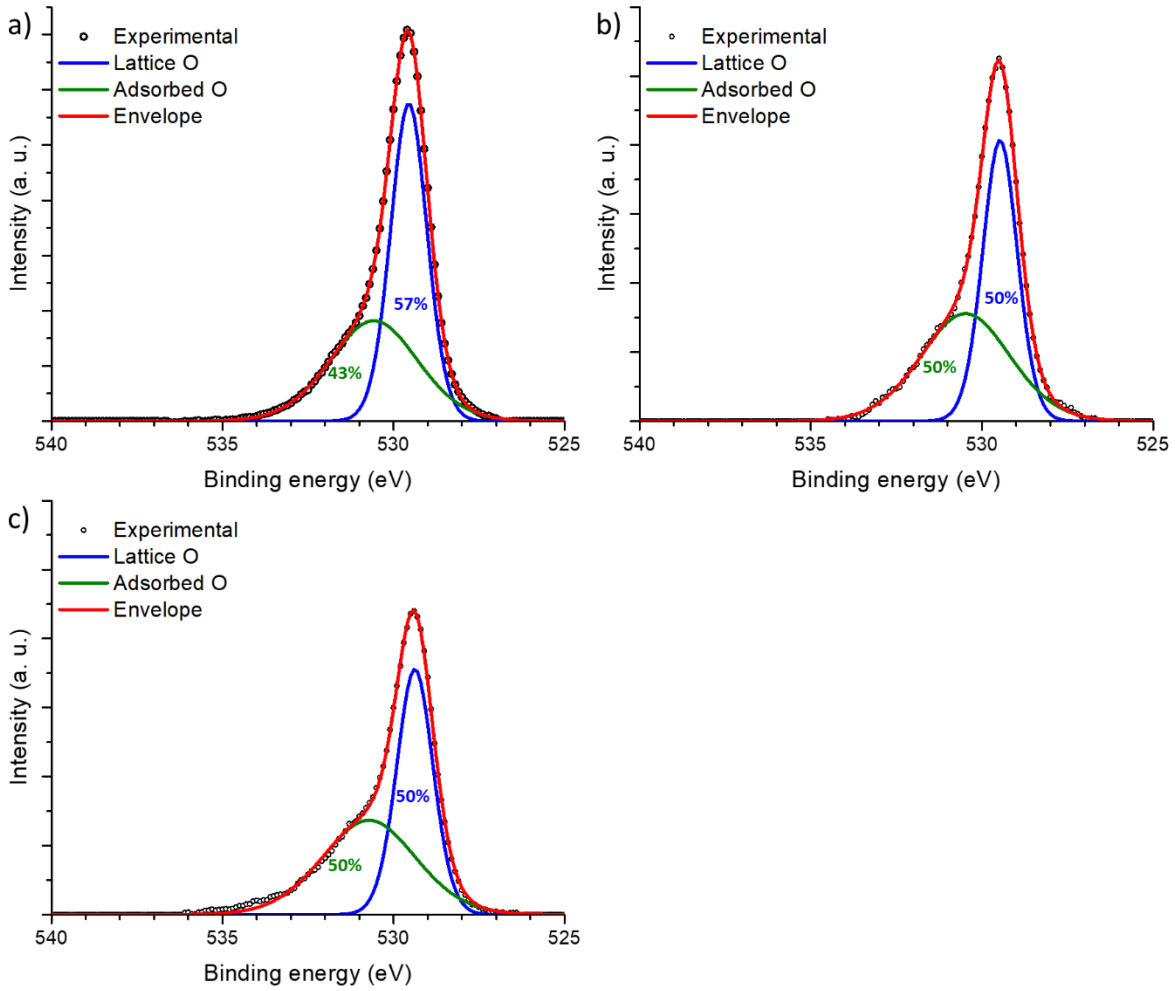

Figure S4. High-resolution XPS spectra of O 1s orbital of samples a) MONW-140, b) 2Fe-MONW-120, c) 7Fe-MONW-120.

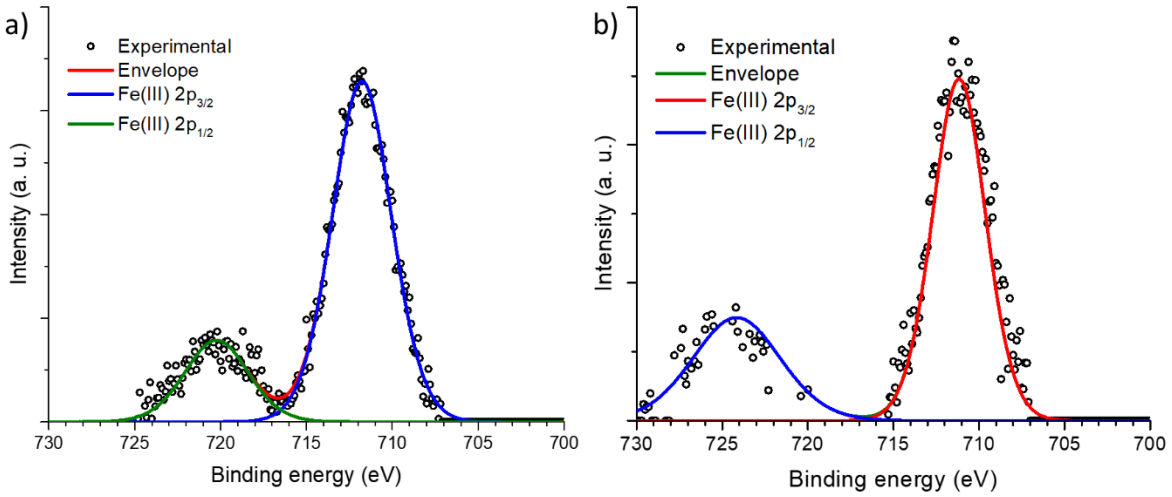

Figure S5. High-resolution XPS spectra of Fe 2p orbital of samples a) 2Fe-MONW-120, and b) 7Fe-MONW-120.

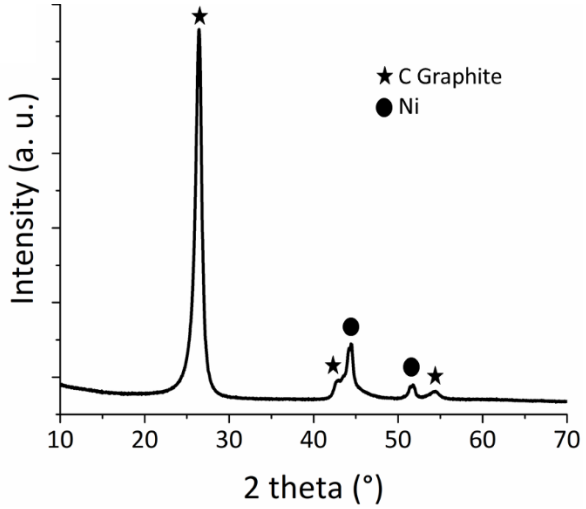

Figure S6. Diffractogram of CNF

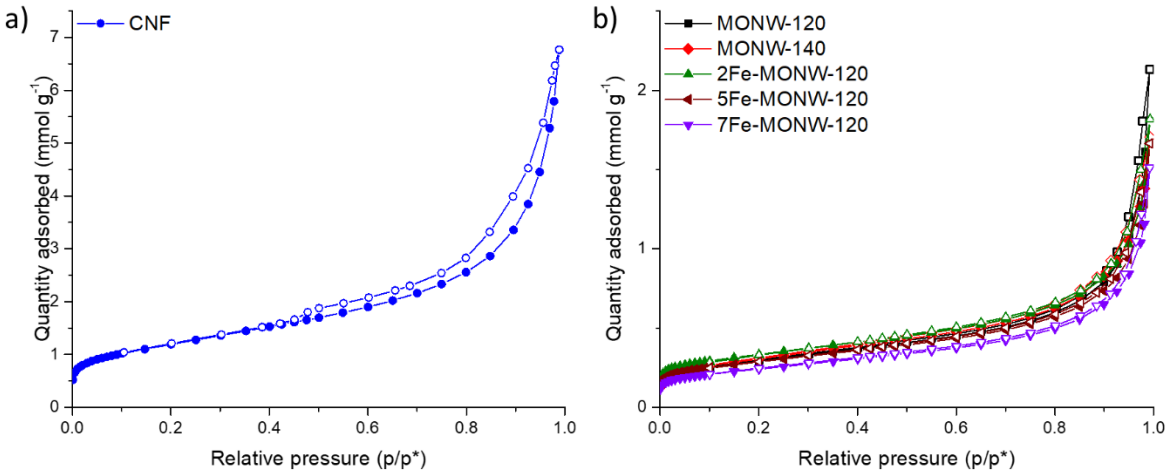

Figure S7. Nitrogen @ 77 K physisorption isotherms over a) carbon nanofibers and b) MnO_2 nanowires.

Table S3. Textural properties of the synthesized materials.

Material	BET Surface area (cm^2 g^{-1})	Single point pore volume (cm^3 g^{-1})	BJH average pore size (nm)	t-plot micropore volume (cm^3 g^{-1})
CNF	93	0.23	10.0	0.009
MONW-120	23	0.07	13.5	0.003
MONW-140	24	0.06	11.0	0.004
2Fe-MONW-120	26	0.06	13.2	0.005
5Fe-MONW-120	22	0.06	13.7	0.003
7Fe-MONW-120	20	0.05	13.6	0.002

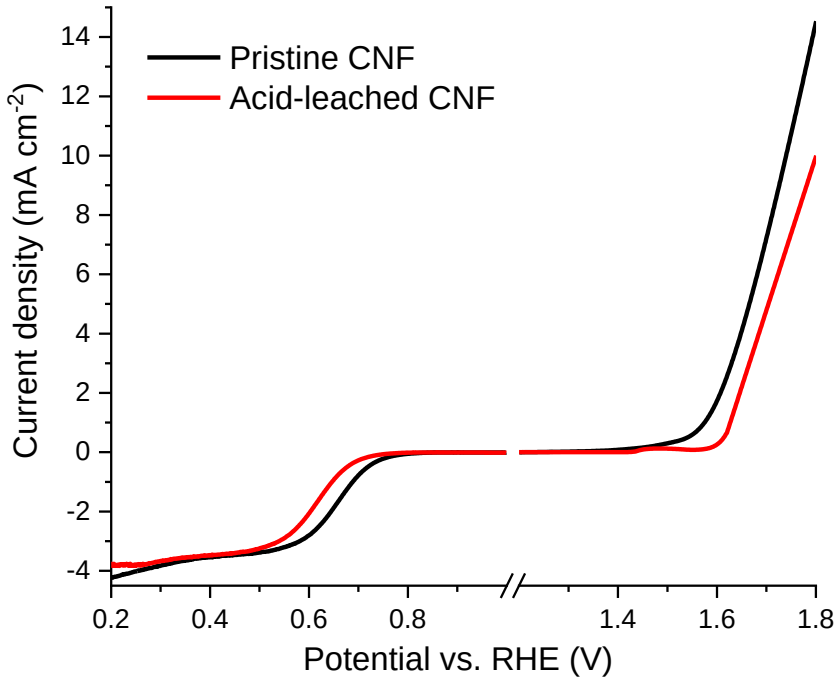

Figure S8. Polarization curves toward the ORR and the OER for pristine carbon nanofibers and acid-leached carbon nanofibers.

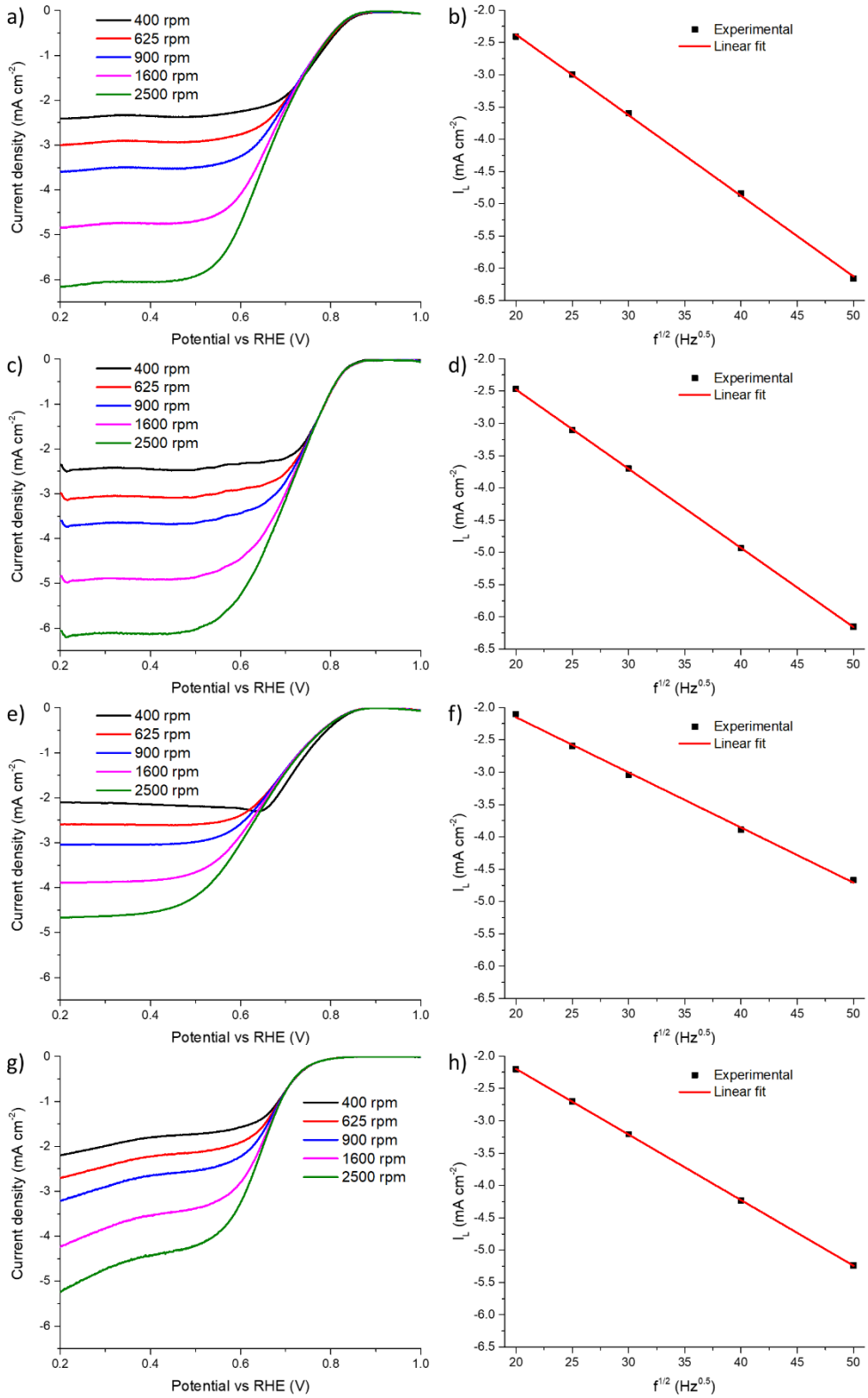

Figure S9. LSV of ORR at different rotation speeds and Levich plots, respectively, obtained with catalysts: a, b) MONW-120/CNF; c, d) MONW-140/CNF; e, f) MONW-120; and g, h) CNF.

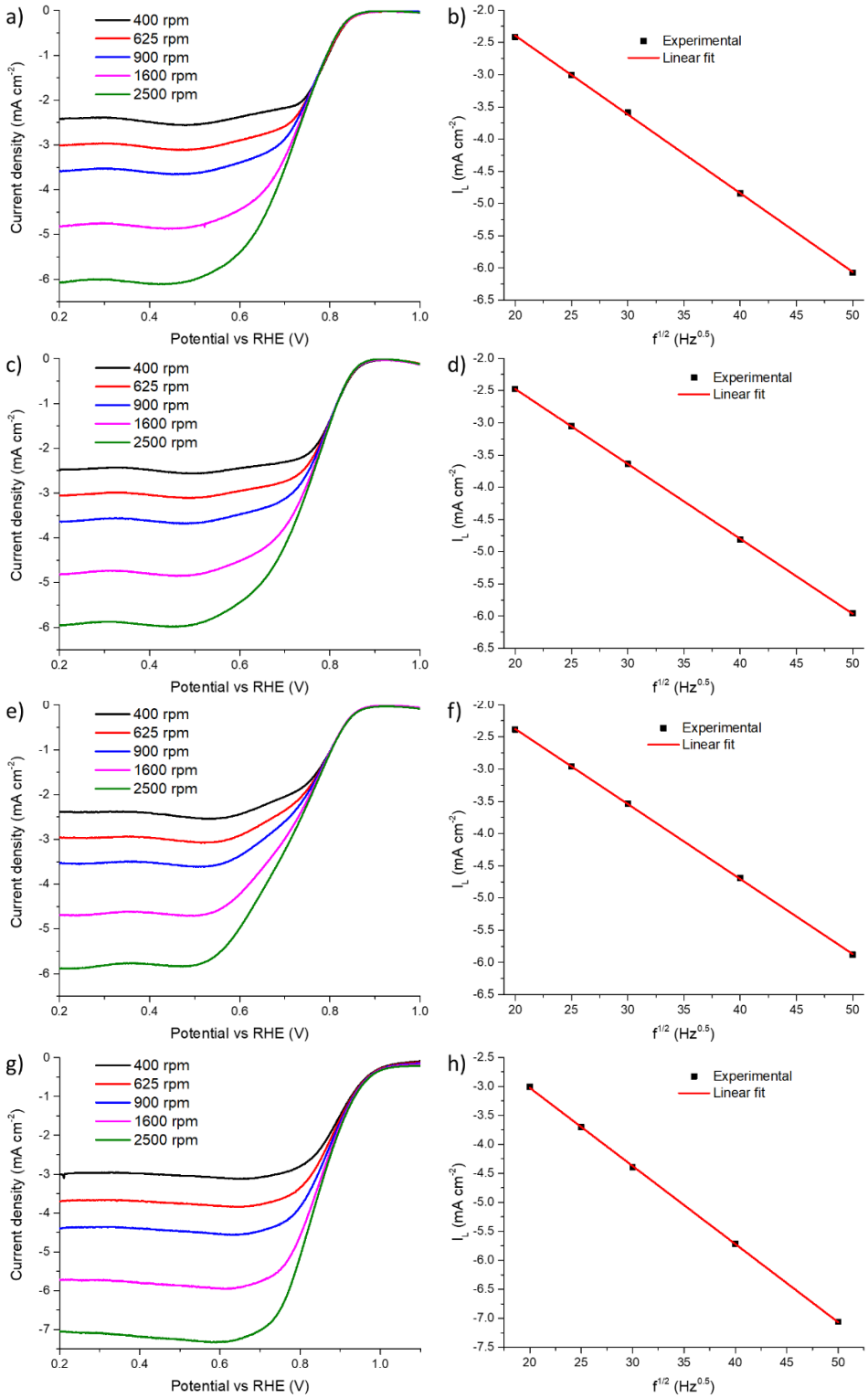

Figure S10. LSV of ORR at different rotation speeds and Levich plots, respectively, obtained with catalysts: a, b) 2Fe-MONW-120/CNF; c, d) 5Fe-MONW-120/CNF; e, f) 7Fe-MONW-120/CNF; and g, h) Pt/C.

To gain more insight, we performed electrochemical impedance spectroscopy **(Figure S11)** over MONW-120/CNF in a GDE at -0.1 V *vs.* Hg|HgO. The 45° slope at the beginning of the electrochemical circle in the Nyquist plot **(Figure S11a)** indicates the presence of a Gerischer element, characteristic of a non-electrochemical reaction. In fact, according to reference [54] in the main text, reaction 7 (in the main text) can sometimes be divided into two sub-steps (equations 7a and 7b):

$$MO_2H + e^- \rightleftharpoons MOOH^- \quad (7a)$$

$$MOOH^- \rightleftharpoons MO + OH^- \quad (7b)$$

An equivalent circuit was fitted to the experimental data **(Figure S11b).** The circuit includes the mentioned Gerischer element, which can be attributed to the non-electrochemical desorption of hydroxyl ion (equation 7b).

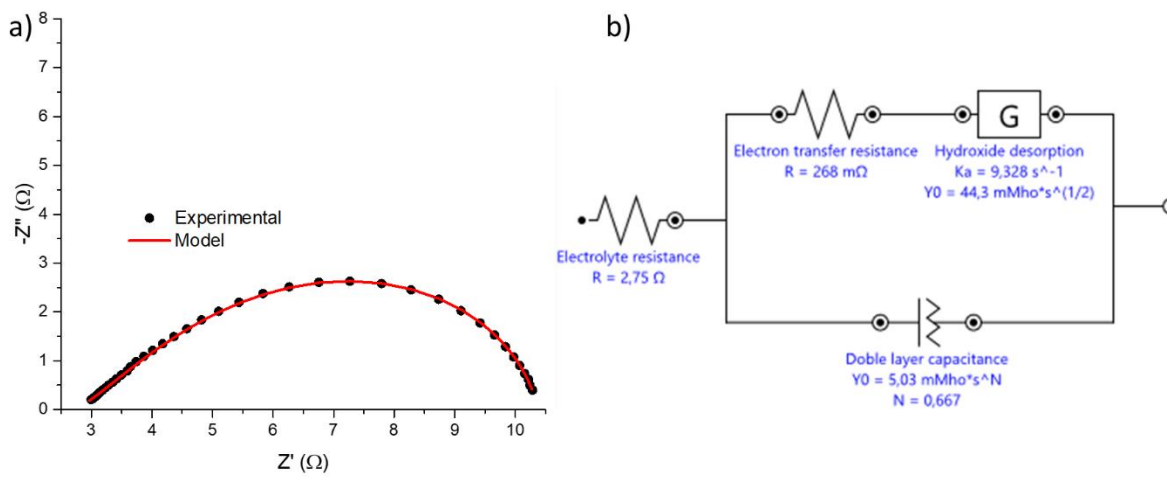

Figure S11. a) Nyquist diagram for ORR (-0.1 V *vs.* Hg|HgO) over catalyst MONW-120/CNF. b) Proposed equivalent circuit.

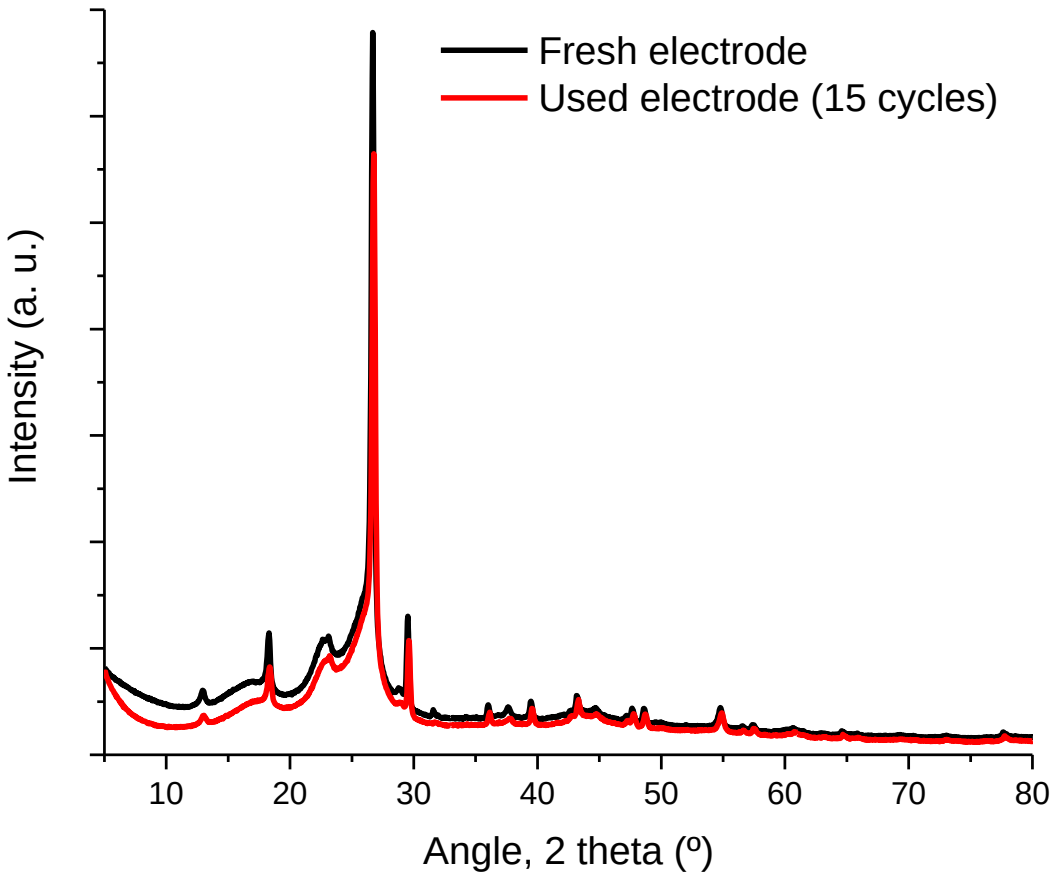

Figure S12. XRD analysis of the fresh GDE and used GDE. 5Fe-MONW-120/CNF electrode cycled 15 times at 10 mA cm^{-2} and -10 mA cm^{-2} for 2.5 hour each in KOH 6M.

Artículo 4

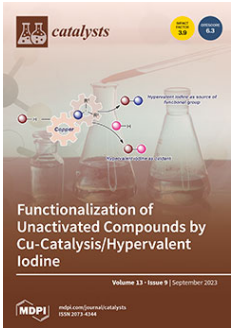

Villanueva-Martínez, N. I., Alegre, C., Sebastián, D., Orozco, N., & Lázaro, M. J. (2023). On the Effect of the Nature of Carbon Nanostructures on the Activity of Bifunctional Catalysts Based on Manganese Oxide Nanowires. *Catalysts*, *13*(9), 1240.

DOI: 10.3390/catal13091240

catalysts

MDPI

Article

On the Effect of the Nature of Carbon Nanostructures on the Activity of Bifunctional Catalysts Based on Manganese Oxide Nanowires

Nicolás Ignacio Villanueva-Martínez, Cinthia Alegre *, David Sebastián, Nataly Orozco and María Jesús Lázaro *

Instituto de Carboquímica–CSIC, Calle Miguel Luesma Castán, 4, 50018 Zaragoza, Spain; nvillanueva@icb.csic.es (N.I.V.-M.); dsebastian@icb.csic.es (D.S.)
* Correspondence: cinthia@icb.csic.es (C.A.); mlazaro@icb.csic.es (M.J.L.)

Abstract: Manganese oxide nanowires (MONW) combined with carbon nanostructures were synthesized using three different carbon materials, and their effect on the activity towards Oxygen Reduction Reaction (ORR) and Oxygen Evolution Reaction (OER) was investigated in alkaline electrolytes. The carbon structures were carbon nanofibers (CNF), multiwall carbon nanotubes (CNT) and reduced graphene oxide (rGO). Both MONW and carbon nanostructures were characterized by X-ray diffraction, scanning and transmission electron microscopy, N_2 physisorption and X-ray photoelectron spectroscopy. The electrochemical activity was assessed in a three-electrode cell. Composite MONW/CNF showed the best activity towards ORR, and MONW/rGO exhibited the highest activity towards OER of the series. The addition of the carbon nanostructures to MONW increased the number of electrons transferred in the ORR, indicating a synergistic effect between the carbon and manganese oxide structures due to changes in the reaction pathway. The analysis of Tafel slopes and electrochemical impedance spectroscopies showed that carbons and MONW catalyze different steps of the reactions, which explains the better activity of the composites. This led us to synthesize a MONW/rGO-CNF composite, where rGO-CNF is a hybrid carbon material. Composite MONW/rGO-CNF showed an improved activity towards ORR, close to the benchmark Pt/C catalyst, and activity towards OER, close to MONW/rGO, and better than the benchmark IrO_2 catalyst. It also showed remarkable stability in challenging operation conditions.

Keywords: bifunctional catalysts; carbon nanostructures; manganese oxide; oxygen reduction; oxygen evolution

check for updates

Citation: Villanueva-Martínez, N.I.; Alegre, C.; Sebastián, D.; Orozco, N.; Lázaro, M.J. On the Effect of the Nature of Carbon Nanostructures on the Activity of Bifunctional Catalysts Based on Manganese Oxide Nanowires. *Catalysts* **2023**, *13*, 1240. https://doi.org/10.3390/catal13091240

Academic Editor: Ermete Antolini

Received: 23 July 2023
Revised: 18 August 2023
Accepted: 24 August 2023
Published: 26 August 2023

1. Introduction

Bifunctional air electrodes have gained increased interest over the last years due to their relevance to sustainable energy devices, including regenerative fuel cells and metal-air batteries [1,2]. These bifunctional air electrodes are responsible for the oxygen evolution reaction (OER) and oxygen reduction reaction (ORR), which are known for their sluggish kinetic reactions due to the complex $4e^-$ mechanisms governing them [3,4]. Noble metals such as Pt/C and IrO_2 or RuO_2 have been widely studied and are considered the most active catalysts for ORR and OER, respectively. However, these catalysts are not bifunctional: Pt shows very poor activity towards OER, and neither IrO_2 nor RuO_2 are active for the ORR [5,6]. Amongst noble metals, Pd displays high activity towards both reactions [7–9], but its cost is even higher than that of Pt, a reason that encourages the search for another kind of catalyst.

In the last decade, great efforts have been devoted to the search for bifunctional catalysts based on non-noble transition metals. Cobalt-based catalysts, either in the form of spinels, perovskites or mixed oxides, are reported as the most active bifunctional catalysts for ORR and OER [10–13]. However, due to the increased use of lithium-ion batteries, cobalt

has become a critical raw material, not being interesting from an economic or ethical point of view. This fact has motivated the quest for alternative catalysts based on non-critical raw materials, such as Fe, Ni or Mn.

Some reviews have reported interesting performances towards ORR and OER for manganese-based catalysts. Manganese oxides exist in different oxidation states (MnO, Mn_3O_4, Mn_2O_3, MnO_2, MnOOH) and nanostructures (cubic [14], layered [15], spinels [16], etc.). Among them, nanowires have been reported as efficient nanostructures providing high activity for the electrocatalysis of oxygen reactions due to their structure favoring cavities with MnO_6 octahedra disposed on the edge and corner-linked [17,18].

One challenge concerning not only manganese oxides but transition metal-based catalysts in general, is their low electrical conductivity [19]. To overcome this issue, transition metal-based catalysts are generally mixed with carbon materials. Several studies have reported the use of manganese oxide combined with diverse carbon materials, from graphene-based materials to carbon nanotubes/carbon nanofibers, mesoporous carbons doped with heteroatoms, etc. For example, catalysts like Ni-MnO over graphene aerogel [20], Co/Mn oxide intertwined with carbon nanotubes [21] and Pd-MnO_2/carbon nanotubes [22] have achieved bifunctionalities (differences between the potentials for OER and ORR) in the 0.8–0.9 V range. Poux et al. synthesized La-Sr-Mn perovskites/pyrolytic carbon composites [23] and concluded that carbon not only increases the electrical conductivity of the catalyst but also increases the surface area and favors oxygen adsorption, thus enhancing ORR. In a previous work [24], we observed that combining iron-doped manganese oxide nanowires with carbon nanofibers generated a synergistic effect that was ascribed to both an increase in the conductivity of the catalyst and to enhanced oxygen adsorption, eventually favoring ORR.

In the last years, several studies have achieved good activities for OER and OER using manganese oxides and carbon materials in combination. For example, He et al. [25] synthesized MnO_x/carbon nanotubes composites that showed bifunctional potential difference (between the OER potential at 10 mA cm^{-2} and the ORR half-wave potential) of 0.91 or 0.92 V and onset potentials for ORR of 0.83 or 0.84 V vs. RHE and for OER of 1.54 V or 1.58 V vs. RHE, depending on the oxidation state of Mn. Their Tafel slopes ranged between 83 and 114 mV dec^{-1} for ORR. Other studies with doped manganese oxides and doped carbon nanostructures show interesting results. One case is the catalyst developed by Niu et al. [26], who combined Co-doped MnO and N-doped carbon nanowires to obtain a highly active catalyst for both OER and ORR. The onset potentials, respectively, were 1.46 and 0.96 V vs. RHE, respectively. They also obtained a half-wave potential for ORR of 0.85 V vs. RHE and a potential for 10 mA cm^{-2} in OER of 1.49 V vs. RHE, totalizing 0.64 V of bifunctional gap difference. Their co-doped material even achieved Tafel slopes low as 74 and 53 mV dec^{-1} for ORR and OER, respectively.

Studies assessing manganese oxides with carbon materials usually evaluate one individual species, so there is not a straightforward comparison nor a proper evaluation of the effect of the carbon material on the activity of manganese-based catalysts. For this reason, the present manuscript investigates the performance of manganese oxide in the form of nanowires (the most active proven structure for ORR/OER) combined with three carbon nanostructures: carbon nanofibers, carbon nanotubes and reduced graphene oxide, assessing how these carbon materials affect the activity for OER and ORR of manganese oxide nanowires. In addition, a carbon hybrid structure, graphene nanofibers, is proposed in order to maximize the activity of the manganese oxide nanowires, taking advantage of the main properties of the individual carbon nanostructures.

2. Results

2.1. Physical-Chemical Characterization

TEM micrographs (Figure 1) allowed us to study the arrangement and morphology of the carbon nanostructures. CNFs (Figure 1a) have micron-size lengths and diameters around 50 nm, with a fishbone morphology (Figure 1d). CNTs (Figure 1b,e) have wider

diameters, ca. 60–70 nm, and are shorter than CNFs but still have lengths longer than 1 µm. CNTs are multiwall type, as can be seen in Figure 1e. In addition, graphitic carbon particles around the iron catalyst can also be observed. rGO shows the typical sheet-like morphology, as shown in Figure 1c,f, where single sheets can be observed, presenting wrinkles, which are a product of the defects that are produced during the graphene oxide thermal reduction [27,28]. Figure S1 (Supporting Information, Section S1) shows SEM and TEM micrographs of MONW. The manganese oxide nanowires have square cross-sections and widths ranging between 60 and 100 nm. Their length can reach up to several microns. TEM and SEM micrographs of the composites (Figure 1g–i) show the good mixing between the phases, with several contact points between the carbon materials and MONW.

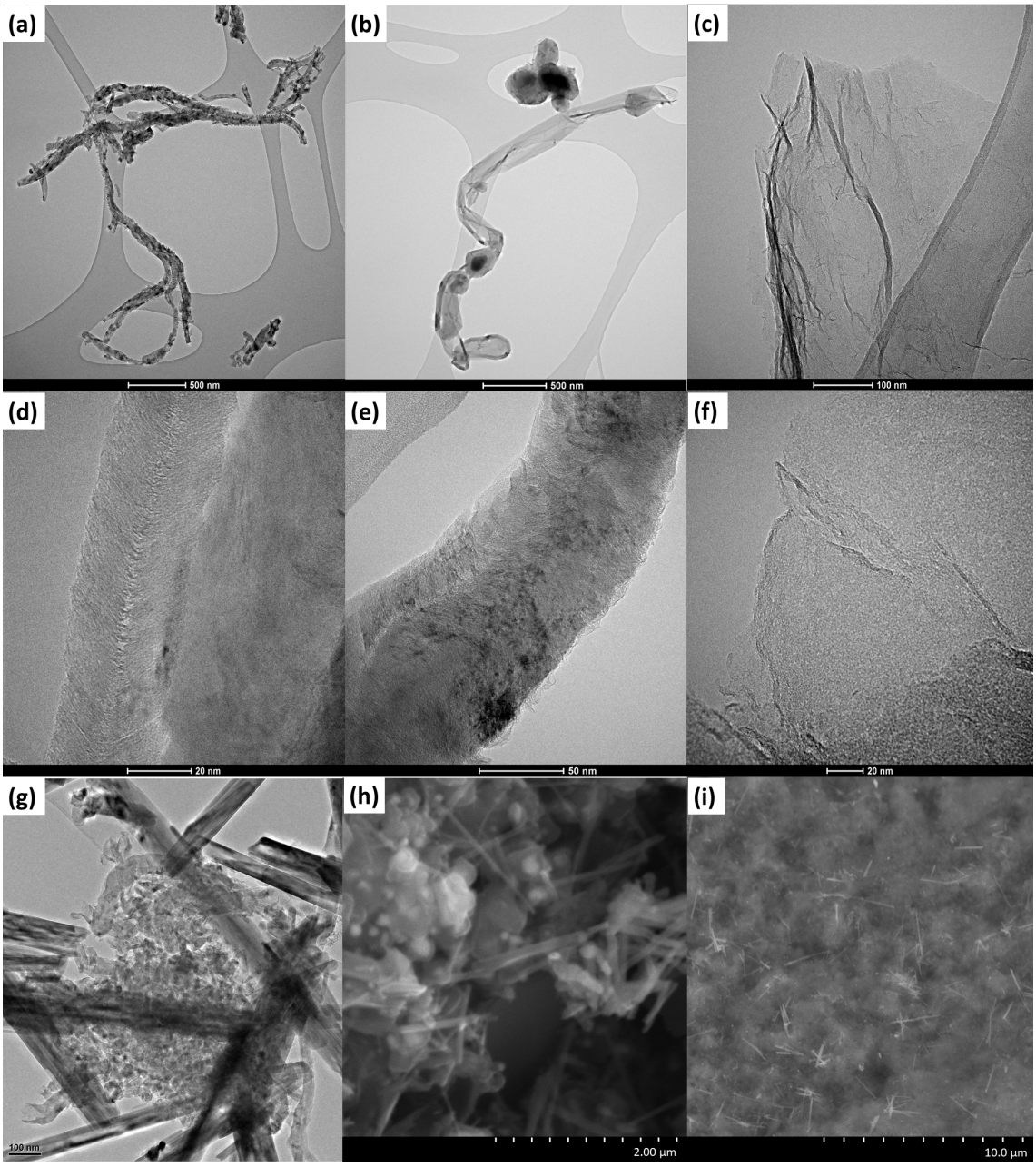

Figure 1. TEM micrographs of CNF (**a**,**d**), CNT (**b**,**e**), rGO (**c**,**f**) and composite MONW/CNF (**g**). SEM images of composites MONW/CNT and MONW/rGO (**h**,**i**).

XRD analyses (Figure 2a) revealed the crystalline structure of the carbon materials. CNF and CNT show a highly graphitic structure, with the characteristic peak of graphite

(JCPDS 75-2078) at 2θ = 26.5° and 26.6°, respectively, attributed to the (002) reflection. These values indicate interplanar distances of 0.337 and 0.335 nm and graphitization degrees of 80% and 100%, respectively. In the case of rGO, the interplanar distance is much higher, 0.347 nm (position of the peak at 25.65°), mainly due to the presence of oxygen functional groups, as can be interpreted from the 5 wt% of oxygen content in this sample (Table 1). Still, this value is far from the typical 0.8–0.9 nm layer separation distance of graphene oxide [29–31], and no peak at 2θ = 10° was observed. The position of the peak agrees with others reported in the literature [32,33]. Other peaks ascribed to graphitic carbon are (100) in the three carbon materials and (004) in CNF and CNT [30]. The (004) peak is not visible in rGO due to its low number of layers. Carbons CNF and CNT also show reflection planes characteristic of the catalyst metals. In CNF, planes (111) and (200) at 44.5° and 51.8°, respectively, corresponding to metallic nickel (JCPDS 04-850) are also observed [34], while CNT shows peaks ascribed to (110) and (200) metallic iron (JCPDS 06-0696) [35], but also to martensite, an iron–carbon alloy (JCPDS 04–003-1419) [36].

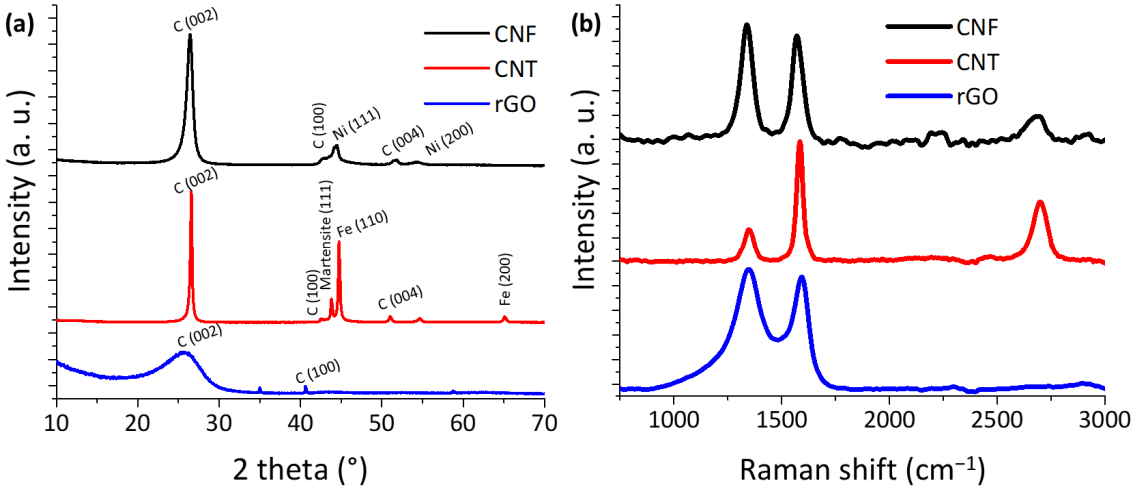

Figure 2. (**a**) X-ray diffractograms and (**b**) Raman spectra of the carbon materials.

Table 1. Chemical composition and textural properties of the carbon materials.

	Chemical Composition (wt%)				Textural Properties	
Material	**Carbon**	**Oxygen**	**Iron ***	**Nickel ***	S_{BET} ($m^2\ g^{-1}$)	V_{pore} ($cm^3\ g^{-1}$)
CNF	92.5	-	-	7.3	95	0.24
CNT	76.5	-	23.5	-	11	0.04
rGO	92.9	5.6 **	-	-	175	0.70

* Iron and nickel percentages determined by ICP. ** Oxygen content for rGO determined from EA.

The number of layers comprising carbon nanotubes and reduced graphene oxide was determined by applying Scherrer's equation to the (002) peak. The crystallite size (in the 002 direction) of CNT is approximately 34 nm, which allows us to estimate that carbon nanotubes have 100 layers (or walls), in agreement with TEM micrographs, as the crystallite size calculated by XRD approximately corresponds to the radius of multiwall carbon nanotubes. rGO presents an average crystallite size of 15 nm, corresponding to 4.5 layers, also in good agreement with the TEM micrographs. XRD analysis of MONW is presented in Figure S2 (Section S1). The only present phase is α-MnO_2, and the crystallite size obtained by applying Scherrer's equation to the main peak (211 planes at 37°) is 37 nm. The reflection planes were obtained from JCPDS (α-MnO_2, 00−044−0141) and matched other works found in the literature [37]. MONW were also analyzed using X-ray photoelectron spectroscopy (Figure S3). Mn2p spectra show two $2p_{3/2}$ peaks, at 642.0 eV, ascribed to Mn^{4+}

in MnO_2 (≈88%) [38], and at 644.3 eV, ascribed to Mn^{6+} in K_2MnO_4 (≈12%) [39]. The O1s orbital can be decomposed into two peaks: one at 539.5 eV, corresponding to lattice oxygen (≈65%), and another one at 531.1 eV, ascribed to adsorbed oxygen or water (≈35%) [40].

Raman spectroscopy (Figure 2b) was used to investigate the structural defects of the carbon nanostructures. All of them show the characteristic G band: CNF at 1570 cm^{-1}, CNT at 1585 cm^{-1} and rGO at 1593 cm^{-1}. The D band, associated with defects, mainly sp3 carbon atoms, is also visible in the three samples, being especially intense in CNF and rGO, with I_D/I_G ratios of 1.1 and 1.4, respectively, while CNT has a much smaller amount of defects as can be inferred from its I_D/I_G ratio = 0.4. CNF and CNT also exhibit the 2G band at 2681 and 2700 cm^{-1}, respectively, whereas this band is not visible in rGO due to its low amount of layers. The intensity of the 2G band is especially high in CNT because of the high number of layers.

Elemental analysis and ICP were used to investigate the composition of the carbon materials. CNFsF are comprised of 92 wt% carbon and 7 wt% nickel, which is consistent with the catalytic decomposition of methane. An amount of 300 mg of $NiCuAl_2O_3$ catalyst yielded approximately 3 g of CNF, indicating that the amount of catalyst should be less than 10 wt% in the final material. CNT, on the other hand, presents a higher amount of metal, around a quarter of the total weight of the sample. Indeed, 300 mg of iron oxide yielded ca. 1.2 g of CNT. rGO has a C:O mass ratio of 17 (atomic ratio of 22), indicating a good—but not complete—reduction of the graphene oxide.

The textural properties of the different carbon nanostructures were studied using nitrogen physisorption (Figure 3, Table 1). All isotherms (Figure 3a) show a hysteresis cycle—type IIb or IV according to the IUPAC classification—characteristic of small particles or crystal aggregates with mesopore-size voids between them [41]. The surface area was calculated with the Brunauer–Emmett–Teller (BET) model (Table 1), being 175 m^2 g^{-1}, 95 m^2 g^{-1} and 11 m^2 g^{-1} for rGO, CNF and CNT, respectively. The low surface area of CNT is explained by the graphitic carbon particles formed together with the nanotubes, the high number of walls of the tubes and the large amount of iron in this sample. The textural characteristics of MONW are displayed in Figure S4 (Section S1, in the Supplementary Materials). MONW also present a type IV adsorption isotherm, indicative of mesoporosity, with a surface area of 23 m^2 g^{-1} and a pore size distribution, including meso- and macropores.

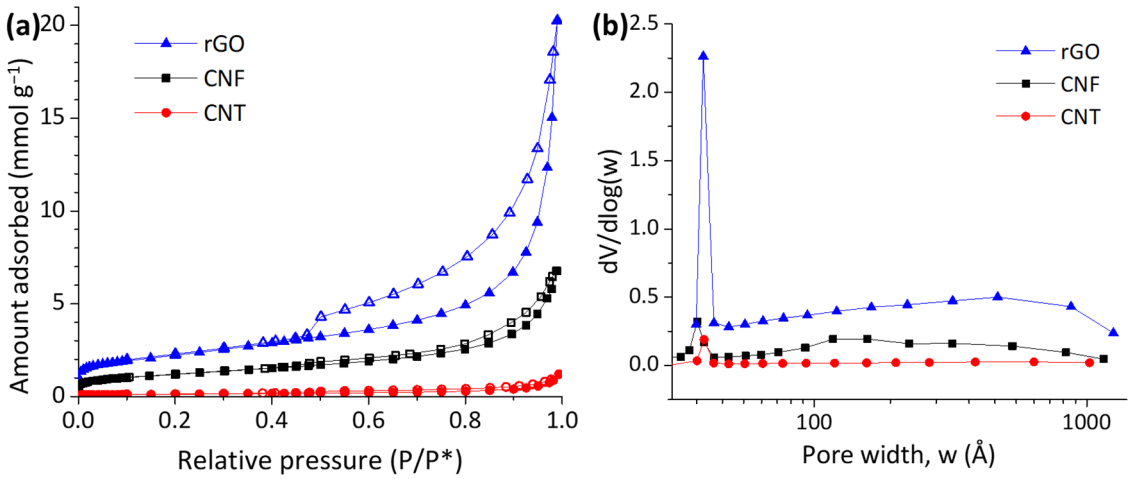

Figure 3. Nitrogen physisorption isotherm (**a**) and BJH (Barrett–Joyner–Halenda Model) pore size distribution (**b**) of the carbon materials.

Pore size distributions were obtained by applying the BJH method to the desorption branch of the isotherms, revealing that carbon nanostructures present pores in the 4–5 nm range. Consistently with the pore size distribution and surface areas, rGO has the highest pore volume of all samples, 0.70 cm^3 g^{-1}, followed by 0.24 cm^3 g^{-1} of CNF and 0.04 cm^3 g^{-1}

of CNT. CNF and rGO also display a small fraction of microporosity, with micropore areas of 17 and 29 m^2 g^{-1}, respectively, and micropore volumes of 0.009 and 0.017 cm^3 g^{-1}.

2.2. Effect of the Carbon Nanostructure on the Catalytic Activity towards the Oxygen Reduction and Evolution Reactions

Linear sweep voltammetries (Figure 4) performed in the ranges 1.2–0.2 V for ORR and 1.1–1.8 V vs. RHE for OER were carried out to investigate the catalytic activity of MONW/C composites, alongside evaluating their reversibility towards ORR/OER. Table 2 collects the main electrochemical parameters derived from the LSV curves, such as the onset potential for both ORR and OER ($E_{ORR,\ onset}$ being the potential at −0.1 mA cm^{-2} current density and $E_{OER,\ onset}$ the potential at 1 mA cm^{-2} current density), half-wave potential for the ORR ($E_{1/2}$), the limiting current density (j_d), the number of exchanged electrons for the ORR (n), the potential for the OER at 10 mA cm^{-2} (E_{10}) and the potential gap between ORR and OER.

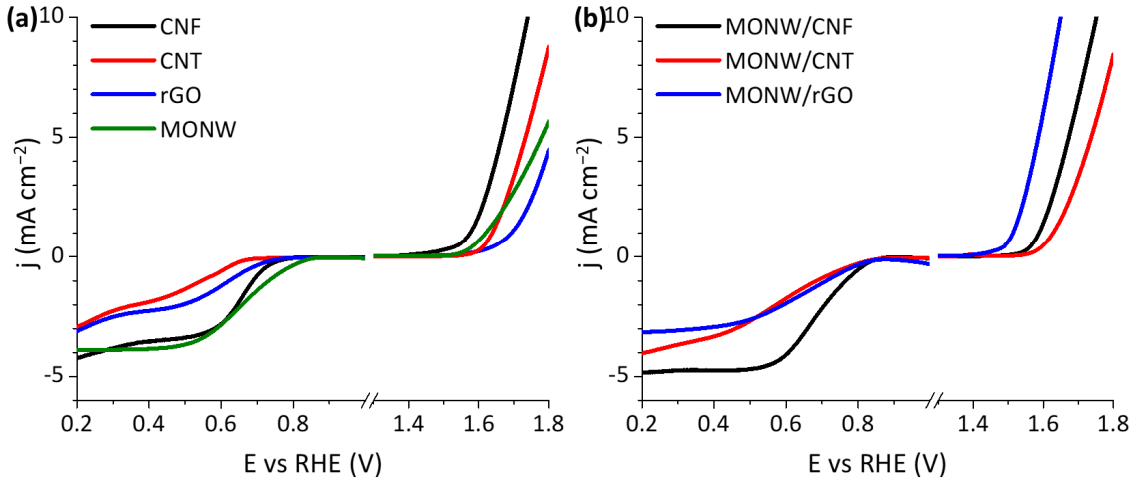

Figure 4. ORR and OER LSVs over (**a**) carbon materials and manganese oxide; (**b**) composite MONW/C catalysts. Experiments were carried out on an RDE at 1600 rpm.

Table 2. Electrocatalytic parameters obtained for the individual carbon nanostructures and for MONW/C composites.

Catalyst	Oxygen Reduction Reaction				Oxygen Evolution Reaction		Reversibility ORR/OER
	$E_{ORR,onset}$ (V vs. RHE)	j_d (mA cm^{-2})	$E_{1/2}$ (V vs. RHE)	n	$E_{OER,onset}$ (V vs. RHE)	E_{10} (V vs. RHE)	ΔE * (V)
CNF	0.78	−4.23	0.66	2.9	1.58	1.74	1.08
CNT	0.68	−2.90	0.48	2.9	1.64	1.82	1.34
rGO	0.76	−3.06	0.57	3.0	1.69	1.92	1.35
MONW	0.84	−3.89	0.66	2.7	1.62	1.90	1.24
MONW/CNF	0.85	−4.84	0.69	3.4	1.59	1.75	1.06
MONW/CNT	0.82	−4.02	0.57	3.8	1.63	1.83	1.25
MONW/rGO	0.83	−3.15	0.64	3.4	1.51	1.65	1.01

* ΔE was calculated by subtracting the half-wave potential for the ORR from the potential at 10 mA cm^{-2} for the OER ($\Delta E = E_{10} - E_{1/2}$).

Figure 4a reveals that CNF (without MONW) is the most active carbon material for both the OER and the ORR, with a similar LSV for the ORR to the individual MONW. This excellent catalytic behavior is due to the presence of nickel in the CNF, an active metal towards both ORR and OER, alongside the outstanding electrical conductivity of the carbon

material. In a previous work [24], we showed that acid-leached carbon nanofibers also hold a considerable, yet slightly lower, catalytic activity towards ORR and non-negligible activity towards OER. As was discussed in Section 2.1, CNF, although still presenting a small amount of nickel (<2 wt%), has a large amount of structural defects, which have been reported as active sites [42]. This is consistent with what has been reported in the literature regarding acid-leached carbon nanofibers showing activity for ORR and OER [43,44]. CNT also shows a decent OER activity due to the presence of Fe; however, its performance towards the ORR is the lowest of the series, which could be due to the low amount of defects (acting as active sites for ORR) since this sample is the most graphitic one. Acid-leached CNTs were tested to assess the activity of the carbon nanostructure (Figure S5). It can be observed that the activity towards ORR barely reduces, while the activity towards OER shows a more significant decrease in activity, with the onset overpotential increasing 66 mV. The mild effect of leaching on the activity of CNT can be explained by the encapsulation of Fe particles in a graphitic matrix under a high number of layers (as explained by XRD and seen in TEM), which does not allow them to act as catalytic active sites. This is why other iron-over-carbon catalysts in the literature show better activities towards OER [45] or ORR [46]. rGO shows the lowest ORR/OER performance on its own. On the other hand, the catalytic activity of MONW without any carbon material is good for the ORR but not for the OER, highlighting the need for a carbon nanostructure to maximize the catalytic activity of Mn oxide sites by enhancing the electrical conductivity. The onset potentials for the ORR follow the trend CNT < rGO < CNF < MONW, and for the OER, the trend is rGO > CNT > MONW > CNF.

Upon combination of MONW with the different carbon nanostructures (Figure 4b), there is a clear improvement in the catalytic activity of the individual manganese oxide nanowires, as can be ascertained from both the parameters displayed in Table 2 and the curves of Figure S6 in the Supporting Information (Section S2.1), comparing each MONW/C composite with its individual components. This highlights the importance of adding carbon for an enhanced activity for the oxygen evolution reaction. On the other hand, for the ORR, there is only a synergistic effect between Mn and C in the case of using CNF. Neither the combination of MONW with rGO nor with CNT provides a more active catalyst, which could be ascribed to a worsened interaction between these carbonaceous materials with the metal oxide active phase. As previously explained, CNT possesses a highly graphitic character and a low surface area, which could hinder the carbon–metal interaction. On the other hand, in the case of MONW/rGO, its low performance for the ORR might be explained by the large difference in surface area between carbon and manganese oxide phases. As the surface area of reduced graphene oxide is approximately seven times greater than that of the manganese oxide nanowires, most of the exposed area of the catalyst is rGO and not MONW. The poor mixing between the two materials can be seen in the SEM micrograph displayed in (Figure 1i).

In general, the electrochemical parameters shown in Table 2 reveal a positive shift of the onset potential for the ORR between 70 and 150 mV and between 30 and 90 mV for the half-wave potential for the MONW/C composites with respect to the individual carbon nanostructures.

Comparing the activity of the composite catalysts (MONW/C: CNF, CNT and rGO in Figure 4b), both MONW/CNF and MONW/rGO show an excellent OER activity, and MONW/CNF also exhibits an outstanding ORR performance. The MONW/CNT composite is the least active one for both ORR/OER, probably due to a worsened interaction between Mn and C due to the lower surface area of CNTs, the low amount of defects, and we cannot discard some effect due to the encapsulation of the iron particles with the carbon matrix.

The synergistic effect between C and MONW for the OER is also reflected in the improvement of the ΔE value, around 70 to 200 mV lower for the MONW/C composites than for the individual components. This reveals that adding carbon to manganese-based catalysts is a good strategy to improve the reversibility of systems operating on ORR/OER.

Both MONW/rGO and MONW/CNF show the lowest values of ΔE (1.01 and 1.06 V, respectively), mainly due to their superior performance towards OER (lower E_{10}). The composite MONW/CNT has the highest ΔE of all the composites, as it presents the lowest activities towards both ORR and OER.

The number of exchanged electrons for the ORR was assessed by applying the Koutecky–Levich (K-L) approach in the diffusional limit of the LSVs performed at different rotation speeds (400, 625, 900, 1600 and 2500 rpm). Further details can be found in the Supporting information (Section S2.3, Figures S7 and S8). The K-L plots for both carbon nanostructures and composites (MONW/C, C: CNF, CNT, rGO) are shown in Figure 5, and all the electrochemical parameters obtained from the LSVs are gathered in Table 2. CNF, CNT, rGO and MONW exhibit the exchange of ca. 3 electrons in the diffusional limit of ORR (2.9, 2.9, 3.0 and 2.7, respectively), indicating that oxygen is reduced to both hydroxide and peroxide. Despite not having the highest number of electrons transferred, CNF is more active than the other materials in the diffusional limit, as is corroborated by the intercept on the *Y*-axis at a lower value (higher kinetic current at 0.2 V vs. RHE). The superior performance of nanofibers can be explained by their physical-chemical properties: the presence of nickel from the catalyst [24], their relatively high surface area and the amount of structural defects acting as active sites [42].

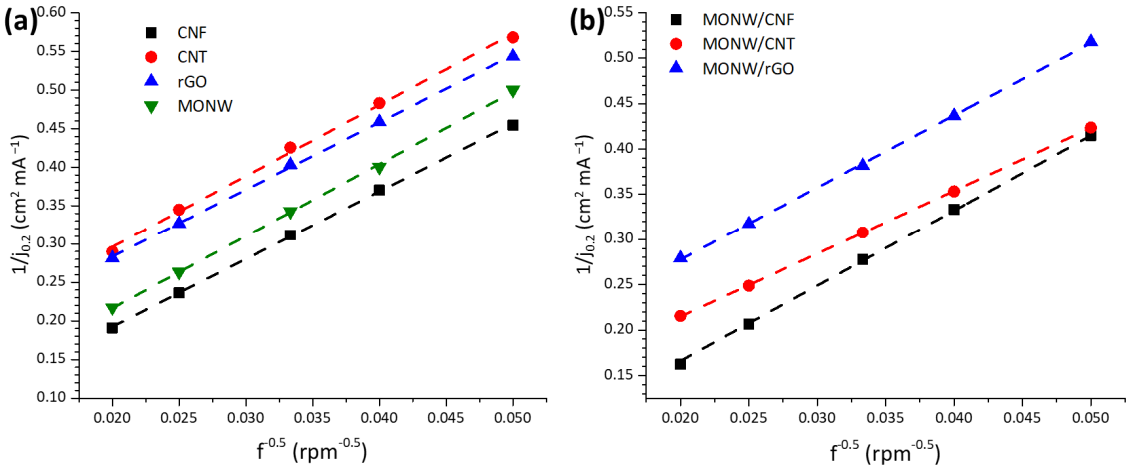

Figure 5. Koutecky–Levich plots at E = 0.2 V vs. RHE of (**a**) carbon materials and manganese oxide and (**b**) composite catalysts.

MONW/C composites exhibit a higher number of exchanged electrons than the individual carbon materials. The largest synergistic effect in terms of transferred electrons is observed in the composite MONW/CNT, as it exhibits 3.8 transferred electrons. This number, however, must be analyzed cautiously, as the LSV at 1600 rpm (Figure 4b) suggests the diffusional limit has not yet been reached at 0.2 V. In the case of MONW/CNF and MONW/rGO, the number of electrons is slightly lower, with 3.4, meaning 70% of hydroxide formation. However, the high intercept of the MONW/rGO curve with the *Y*-axis (Figure 5b, blue triangles) indicates a low intrinsic current density at 0.2 V vs. RHE, only 8.4 mA cm^{-2}, which is due to the poor interaction between the carbon phase and the metallic phases, as previously explained.

Two paths have been described in the literature for oxygen reduction over manganese catalysts [47]. The first mechanism is the four-electron reaction that yields OH^-. Since the surface of metal oxide electrodes in a strongly alkaline medium is covered by adsorbed OH species [48,49], the first step involves the displacement of OH to adsorb one O_2 molecule with the acceptance of one electron (Equation (1)). The adsorbed OO is then protonated (Equation (2)), and after that, a hydroxide anion is released, and a single oxygen atom

remains adsorbed (Equation (3)). Finally, the adsorbed oxygen is protonated to obtain a hydroxyl group adsorbed to the manganese oxide (Equation (4)).

$$Mn(OH)_{ads} + O_{2(aq)} + e^- \rightleftharpoons Mn(O_2)_{ads} + OH^- \quad (1)$$

$$Mn(O_2)_{ads} + H_2O + e^- \rightleftharpoons Mn(OOH)_{ads} + OH^- \quad (2)$$

$$Mn(OOH)_{ads} + e^- \rightleftharpoons Mn(O)_{ads} + OH^- \quad (3)$$

$$Mn(O)_{ads} + H_2O + e^- \rightleftharpoons Mn(OH)_{ads} + OH^- \quad (4)$$

Oxygen can also be reduced to peroxide in a two-electron pathway. The first two steps are the same as in the four-electron mechanism (Equations (1) and (2)). The adsorbed peroxyl then desorbs as hydroperoxide and is replaced by hydroxide (Equation (5)). This happens because the energy is not enough to break the O=O bond.

$$Mn(OOH)_{ads} + OH^- \rightleftharpoons Mn(OH)_{ads} + HO_2{}^- \quad (5)$$

The peroxide can degrade non-electrochemically to water and oxygen (Equation (6)) or react electrochemically with another adsorbed OH group to yield adsorbed oxygen and 2 hydroxide ions (Equation (7)) and then reduce to hydroxide following equation Equation (4), completing a "2 + 2" mechanism. The difference between the four-electron and the 2+2 electron pathways is that the first one is dissociative, and the latter is associative.

$$2HO_2{}^- \rightleftharpoons O_2 + 2OH^- \quad (6)$$

$$Mn(OH)_{ads} + HO_2{}^- + e^- \rightleftharpoons Mn(O)_{ads} + 2OH^- \quad (7)$$

In both mechanisms, the rate-determining step is the electrochemical adsorption of oxygen. In fact, in a previous work [24], we showed that the ability of manganese oxide to adsorb oxygen plays a key role in the ORR kinetics. The four-electron and the two-electron pathways compete, as the operation potentials are lower than the standard reduction potentials for the two mechanisms (1.23 V vs. RHE and 0.77 V vs. RHE, respectively). As a result, the number of electrons is between 2 and 4 (2.7 in MONW at 0.2 V vs. RHE). By operating at a less negative potential, i.e., calculating the number of exchanges by the Koutecky–Levich method at 0.4 V vs. RHE, it increases to 3.7 (Figure S9, Section S2.3). This happens because the overpotential is too low for the 2-electron pathway. As the standard potential for peroxide reduction in alkaline electrolyte is 1.71 V vs. RHE, the potentials at which the number of electrons are calculated (either 0.2 or 0.4 V vs. RHE) should imply a rapid reduction of the peroxide if it re-adsorbs. Consequently, the amount of hydroperoxide that reduces to hydroxide does not depend on the potential—but, rather, on the rates at which hydroperoxide degrades into oxygen (Equation (6)) and at which it re-adsorbs on the catalyst.

The activity of the catalysts was also assessed by analyzing Tafel slopes for both ORR and OER. Further details can be obtained in the Supporting Information. To obtain the Tafel slopes in ORR, the intrinsic current density was estimated using the Koutecky–Levich method (Equation S1 in Supporting information). The effective overpotential (η_{eff}) was calculated according to Equation (8):

$$\eta_{eff} = E - E^0 - IR \quad (8)$$

where E is the measured potential, E^0 is the standard potential at the electrolyte concentration (1.23 V vs. RHE), I is the measured current, and R is the electrolyte resistance, calculated using Newman's equation [35]. Figure 6 shows the Tafel slopes obtained for ORR (Figure 6a) and OER (Figure 6b) for the MONW/C composites, and Figure S10 (Section S2.4 in the Supporting Information) shows the Tafel slopes for the individual components,

carbon nanostructures and MONW. The Tafel parameters for all the catalysts are collected in Table 3.

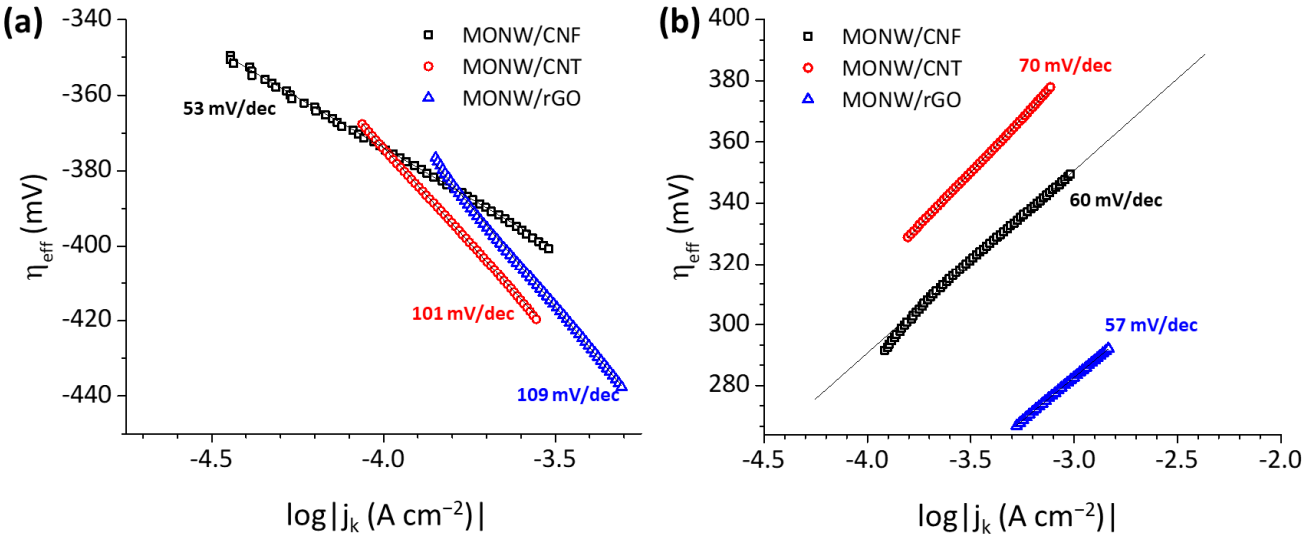

Figure 6. ORR (**a**) and OER (**b**) Tafel plots of composite catalysts. Experiments carried out over a RDE at 1600 rpm.

Table 3. Kinetic parameters obtained from the Tafel slopes for the different catalysts.

Catalyst	Oxygen Reduction Reaction		Oxygen Evolution Reaction	
	j_0 (mA cm^{-2})	Tafel Slope (mV dec^{-1})	j_0 (mA cm^{-2})	Tafel Slope (mV dec^{-1})
CNF	1.8×10^{-10}	76	1.7×10^{-4}	87
CNT	6.8×10^{-11}	88	8.5×10^{-6}	38
rGO	3.5×10^{-10}	86	4.3×10^{-4}	131
MONW	4.9×10^{-10}	136	1.0×10^{-5}	73
MONW/CNF	9.1×10^{-9}	53	1.4×10^{-6}	60
MONW/CNT	2.0×10^{-8}	101	3.3×10^{-6}	70
MONW/rGO	4.8×10^{-8}	109	1.0×10^{-5}	57

The superior performance of MONW/CNF for the ORR is also evident in its low Tafel slope, 53 mV dec^{-1}, while MONW/CNT and MONW/rGO exhibit approximately double that value (ca. 100 mV dec^{-1}). The synergistic effect between CNF and MONW can be appreciated in the composite having a lower Tafel slope than the materials on their own. In the case of OER, the three composites have similar Tafel slopes, ranging from 57 to 70 mV dec^{-1}. However, the MONW/rGO composite has an exceptional exchange current density (j_0) of 1.0×10^{-5} mA cm^{-2}, one order of magnitude higher than the 1.4×10^{-6} mA cm^{-2} of MONW/CNF and the 3.3×10^{-6} mA cm^{-2} corresponding to MONW/CNT. When analyzing the Tafel slopes of the carbon materials, it is possible to observe that the exchange current density of rGO for OER is 4.3×10^{-4} mA cm^{-2}, a higher value than the rest of the catalysts. This suggests that reduced graphene oxide provides the largest surface where the OH^- anions can adsorb and then be oxidized over the manganese oxide nanowires.

Tafel slopes also provide information about the mechanism of the reactions and are closely related to the kinetics [50], especially to the rate-determining steps of ORR and OER. As previously stated, in Mn-based catalysts, the rate-determining step for ORR is assumed to be the hydroxide-displacement oxygen adsorption. In fact, the obtained 136 mV dec^{-1} in MONW is close to the theoretical 120 mV dec^{-1} calculated as the Tafel slope when the first electron transfer is the rate-limiting step [51]. In contrast, carbon materials studied

in this work show ORR Tafel slopes closer to 60 than to 120 mV dec^{-1} (especially CNF, Figure S10), suggesting that the rate-limiting step is the protonation of adsorbed O_2^- rather than the first electron transfer [51,52]. This way, catalyst MONW/CNF, for example, has two phases that are able to catalyze different steps of the reaction pathway, explaining its better performance than the separate phases. In the case of OER, the reverse of the four-electron ORR pathway was considered as the predominant mechanism (inverse of Equations (1)–(4)). The Tafel slope of MONW (73 mV dec^{-1}) suggests that the third step (inverse of Equation (2)) is the rate-limiting step on this material [53]. In rGO, on the other hand, the Tafel slope of 131 mV dec^{-1} suggests that the first step, i.e., the protonation of an adsorbed hydroxyl group (inverse of Equation (4)), which has a theoretical Tafel slope of 120 mV dec^{-1} [54]. As in the case of ORR, the different phases show the ability to catalyze different steps of the reaction pathway.

2.3. Catalytic Activity towards the Oxygen Reduction and Evolution Reactions for a Composite Material between Mn Oxide and Hybrid Carbon Nanostructure

Taking into account that the composite catalyst based on CNF (MOWN/CNF) was the most active towards ORR while the one based on rGO (MONW/rGO) was the most active towards OER, hybrid carbon materials composed of rGO and CNF were investigated, aimed to take advantage of both carbon nanostructures towards an enhanced MONW/C catalyst.

Two synthetic strategies were evaluated to obtain the hybrid carbon material. The first strategy consisted of mechanical mixing of the two carbon nanostructures CNF and rGO (25 wt% CNF and 25 wt% rGO) with 50 wt% MONW. This process yielded a material named MONW/mm[rGO-CNF] that, just like the three original composites, was comprised of 50% carbon material and 50% manganese oxide nanowires and tested in the same conditions as the others. However, this strategy was not successful since the catalytic activity for ORR and OER was not remarkable, as can be seen in the Supporting Information (Figure S11, Section S2.5 in Supporting Information).

The second strategy consisted of synthesizing a hybrid carbon material by growing carbon nanofibers in an rGO matrix (rGO-CNF) in order to obtain an intimate mixture at the nanoscale of the two carbon phases. To do so, nickel nanoparticles, acting as CNF growth sites, were deposited on rGO, which was subsequently treated in a CH_4 atmosphere, following a similar method to the one reported in a previous work [55]. TEM images of this hybrid carbon are shown in Figure 7, where the presence of irregular nanofilaments is advised together with an amorphous carbon phase from rGO. At high magnification (Figure 7b), the graphitic layers corresponding to the nanofilaments can be clearly observed, which follow a platelet structure with an irregular surface. This hybrid rGO-CNF presents a BET surface area of 380 m^2 g^{-1}, much higher than the individual counterparts (95 m^2 g^{-1} for CNF and 175 m^2 g^{-1} for rGO, see Table 1), as a result of the separation of graphenic layers from rGO due to the intercalation of nanofilaments. Figure 7c shows a SEM image of the composite MONW/CNF-rGO, where a good contact between the carbon and MnO_2 phases is visible, with manganese oxide nanowires inserted between the carbon nanofibers.

To produce the catalyst, the rGO-CNF hybrid material was mixed in a planetary mill with manganese oxide nanowires in a 1:1 mass ratio following the same procedure as the other carbon materials. The composite material was named as MONW/rGO-CNF. Figure 8 shows the LSVs of the hybrid carbon composited with manganese oxide, compared to MONW/rGO and MONW/CNF, and with benchmark catalysts for ORR and OER: Pt supported on carbon, and IrO_2, respectively.

The most remarkable result is that the catalyst MONW/rGO-CNF presents an improved activity for the ORR compared to CNF- and rGO-supported MONW. The number of exchanged electrons is higher, 3.7 (see Table 4), and the onset and half-wave potentials are more than 50 mV more positive than the other MONW/C catalysts.

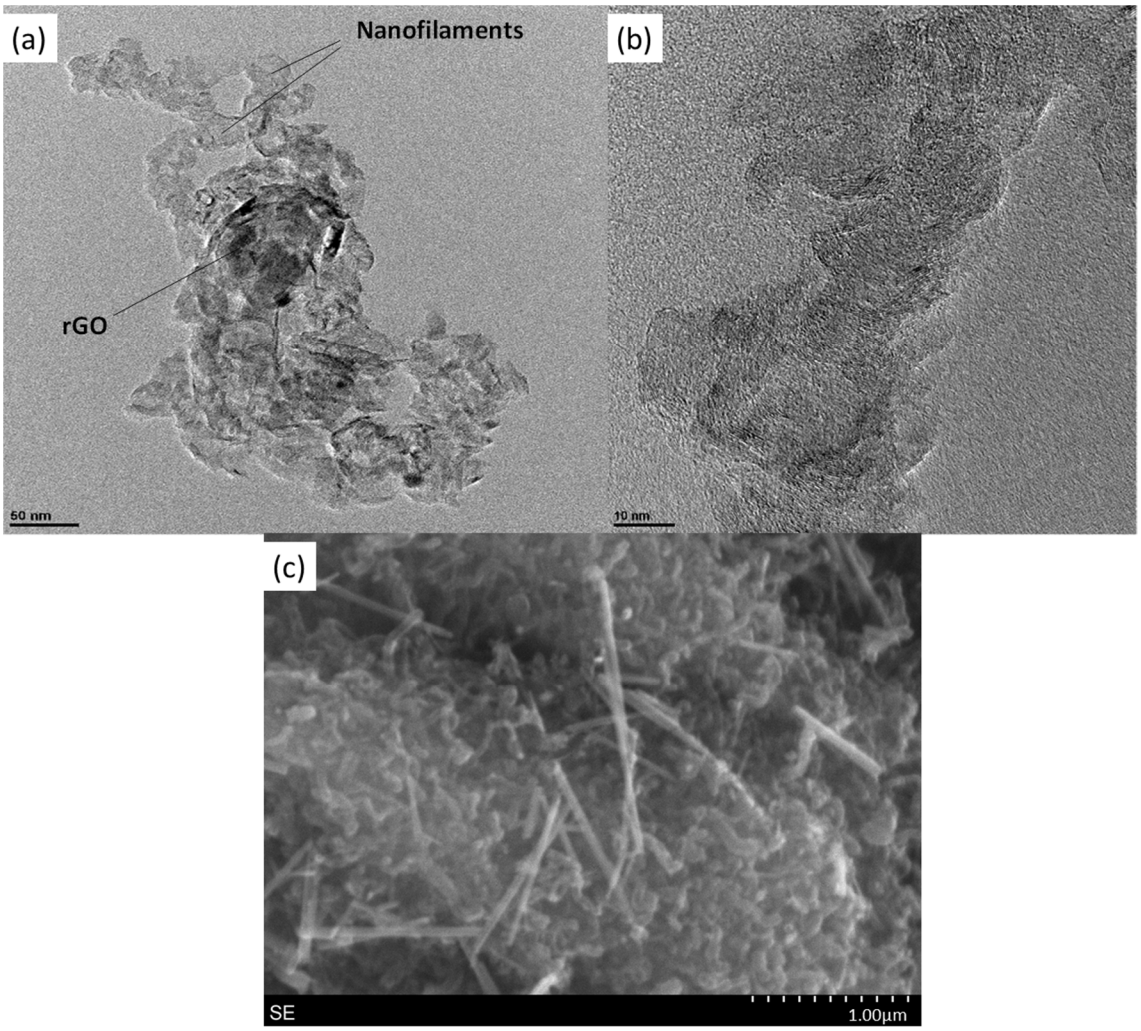

Figure 7. TEM (**a**,**b**) and SEM (**c**) micrographs of rGO-CNF composite produced by growing CNF on the surface of rGO.

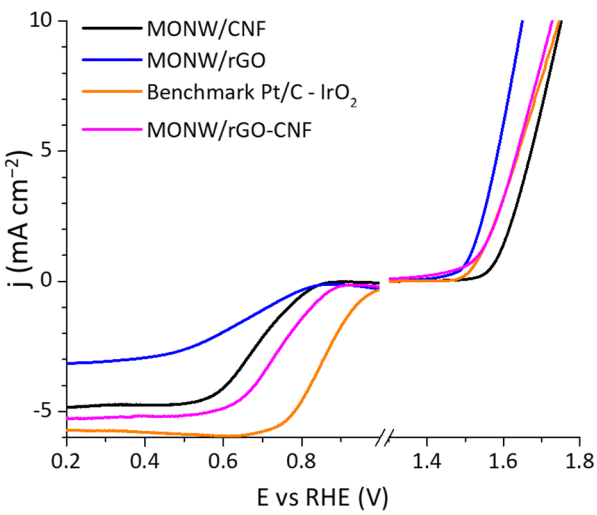

Figure 8. ORR and OER LSVs of selected catalysts. Experiments carried out in a RDE at 1600 rpm.

Table 4. Electrocatalytic parameters obtained for rGO-CNF, MONW/rGO-CNF, the benchmark catalysts, and similar catalysts from literature.

Catalyst	Oxygen Reduction Reaction				Oxygen Evolution Reaction		Reversibility ORR/OER	Ref.
	$E_{ORR, onset}$ † (V vs. RHE)	j_d @ 1600 rpm (mA cm^{-2})	$E_{1/2}$ (V vs. RHE)	n	$E_{OER, onset}$ † (V vs. RHE)	E_{10} (V vs. RHE)	ΔE (V)	
rGO-CNF	0.79	−3.80	0.69	2.9	1.58	1.76	1.07	This work
MONW/rGO-CNF	0.90	−5.26	0.74	3.7	1.54	1.73	0.99	This work
Pt/C–IrO_2	1.02	−5.72	0.85	4	1.53	1.75	-	This work
MnO_x/CNTs	0.85 *	−4.90	0.77 *	3.6	1.58 *	0.91 *	0.91 *	[25]
MnO_2-$C_{(ultrathin\ amorphous)}$	0.97	−5.81	0.81	4	1.45	1.59	0.78	[56]
α-$MnO_{2(cryptomelane)}$/Vulcan	0.88 *	−4.1	0.79 *	4	1.58 *	1.73 *	0.94 *	[57]
Mn-MOF @rGO	1.09 *	−2.03	0.98 *	-	1.75 *	1.84 *	0.86 *	[58]
Mn_xO_y/N-carbon	0.85	−5.0	0.77	-	1.61	1.68	0.91	[59]
MnO_x/S-carbon	0.94	−4.5	0.81	3.7	1.33 *	1.62 *	0.81 *	[60]

* IR corrected. - Not reported or not relevant. † Onset potentials for OER and ORR according to the definitions of this work.

Table 4 also compares our catalyst with some similar materials based on manganese and carbon found in the literature. It is possible to see that our catalyst MONW/rGO-CNF has an interesting activity. Some materials, like those in [25,57,58], show reversibility gaps up to 0.13 V lower, but these differences must be considered with caution, as their results are reported corrected by IR, unlike in this work. It is interesting to note that the material by He et al. [25] has a relatively high activity, even though it uses carbon nanotubes, suggesting that the CNT used in this study have low activity due to their high number of layers and low surface area, rather than the cause being the structure of CNT. The work by Wahab et al. [58], uses reduced graphene oxide and contrary to our findings, their material has an extraordinary activity for ORR, but lower activity than our MONW/rGO-CNF material. The referenced work uses a metal-organic framework (MOF) with manganese supported over reduced graphene oxide, which may result in different interactions between the carbon and metallic phases. Moreover, the MOF as a catalyst with rGO showed extremely limited activity towards ORR, which reinforces our idea that it is a combination of graphitic carbon phases and manganese phases responsible for the high activity of the catalysts rather than the carbon phase just working as a conductive additive.

The good ORR activity of the composite reveals a synergistic effect that must comprise the three phases: the two carbons and the manganese oxide, which can be derived from the analysis of the separated phases (see Figure S6d). As stated before, oxygen reduction on rGO involves the transfer of 2.9 electrons, indicating partial reduction to peroxide. However, some works have shown that peroxyl can adsorb over the edges of graphene layers [38]. Therefore, and most probably, the superior number of electrons exchanged in MONW/rGO-CNF is explained by a 2+2 mechanism. We propose that the reduction of hydroperoxide (Equation (9)) can take place between two adsorbed species (Equations (9) and (10)).

$$C + HO_2^- \rightleftharpoons C(OOH)_{ads} + e^- \quad (9)$$

$$Mn(OH)_{ads} + C(OOH)_{ads} + 2e^- \rightleftharpoons Mn(O)_{ads} + 2OH^- \quad (10)$$

In this case, the hydroxyperoxide anion electrochemically adsorbs over a carbon edge site, either on rGO or CNF. It is crucial for this mechanism to take place to ensure good contact between carbon and manganese phases. A possible explanation for the superior performance of MOWN/rGO-CNF over that of the rest of the carbon composites is that graphene oxide provides a large surface area where peroxyl can adsorb, and CNF improves the contact between the carbon and manganese phases. In this regard, Poux et al. [23] synthesized composites containing La-Sr-Mn perovskites and pyrolitic carbon and reached the conclusion that carbon enhances the activity of the perovskites in two different ways: first, it improves the electrical conductivity from the current collector to the outside layers

of the perovskite, and second, it provides a large area where oxygen can adsorb and begin to reduce. Despite these two effects are definitively important, they are not enough by themselves to explain the increase in electrons exchanged during ORR. Our proposed explanation can deal with this observation.

Even though composite MONW/rGO-CNF has a slightly lower activity for OER than MONW/rGO, especially at high current densities, it holds especially well against the benchmark catalyst, IrO_2. They have an almost identical onset potential, but the composite has a 20 mV lower E_{10}, which may be a consequence of the good conductivity of carbon materials in comparison to metallic oxides. Therefore, composite MONW/rGO-CNF has a good compromise in activity towards ORR and OER, and consequently, it exhibits the lowest value of reversibility gap amongst the tested catalysts, with 0.99 V (see Table 3).

The activity of the MONW/rGO-CNF hybrid catalyst was also assessed, analyzing Tafel slopes for both ORR and OER, compared to the benchmark catalysts, as shown in Figure 9 and Table 5.

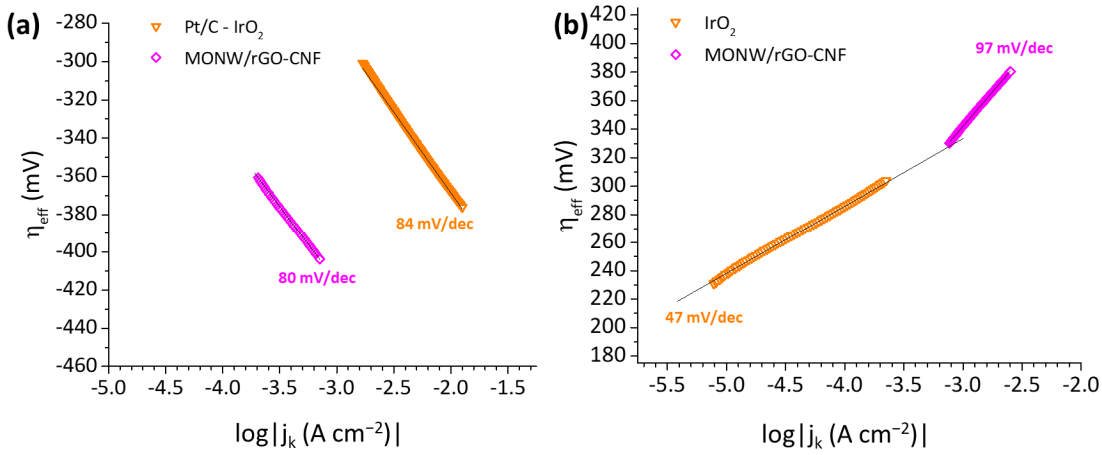

Figure 9. ORR (**a**) and OER (**b**) Tafel plots of hybrid MONW/rGO-CNF composite and benchmark catalysts.

Table 5. Kinetic parameters obtained from the Tafel slopes for rGO-CNF, MONW/rGO-CNF and benchmark catalysts.

Catalyst	Oxygen Reduction Reaction		Oxygen Evolution Reaction	
	j_0 (mA cm^{-2})	Tafel Slope (mV dec^{-1})	j_0 (mA cm^{-2})	Tafel Slope (mV dec^{-1})
rGO-CNF	2.6×10^{-12}	42	4.6×10^{-4}	98
MONW/rGO-CNF	6.3×10^{-6}	80	2.9×10^{-6}	97
Pt/C–IrO_2	4.2×10^{-4}	84	1.0×10^{-7}	47

Tafel slopes for ORR also reveal the superior behavior of the benchmark catalyst. Even though it is not the catalyst with the lowest slope, it has a superior exchange current density (j_0), as is evident from the position of the data in the graph. Pt/C has a j_0 of 4.2×10^{-4} mA cm^{-2}, two orders of magnitude higher than the MONW/rGO-CNF composite, 6.3×10^{-6} mA cm^{-2}, which has a comparable Tafel slope. None of our carbon-manganese catalysts can match the high activity of the well-dispersed, high surface-area Pt/C catalyst towards ORR. In the case of the OER, the benchmark material has the lowest Tafel slope (half that of MONW/rGO-CNF); however, composite MONW/rGO (Figure 6) has a higher j_0, explaining its better activity. Although the ORR activity of the MONW/rGO-CNF is significantly lower than that of Pt/C, its good performance (bifunctionality) for both ORR and OER makes it an interesting choice due to the lower cost and abundance of manganese compared to Pt.

The low ORR Tafel slope of hybrid carbon rGO-CNF of only 42 mV dec^{-1} (Figure S10a) is indicative that, in this material, the second electron transfer limits the kinetics of the reaction. In this case, it is possible to see that the different phases have the ability to catalyze the different steps of the reaction and yield the most active of the synthesized catalysts.

The hypothesis of different phases catalyzing different steps of the reaction was studied through EIS (Figure 10). Figure 10a shows the Nyquist plot for ORR for MONW. A large transfer resistance can be observed over a single semicircle. The equivalent circuit is visible inside the plot. By contrast, the Nyquist plot of ORR for the MONW/rGO-CNF catalyst can be modeled by a series of two RQ elements (resistance in parallel with a constant phase element). Despite the presence of two resistances, their lower values result in a lower total charge transfer resistance, in agreement with the higher activity observed for this catalyst. More interestingly, the presence of a series of two RQ elements suggests the transfer of two electrons or, at least, two processes with similar rates, indicating that there is no single rate-determining step for ORR for this catalyst, contrary to what happens in the MONW catalyst. The large difference in the admittance of the constant phase elements in the circuit in Figure 10b suggests that the two different electron transfers could take place over different surfaces, in agreement with our hypothesis.

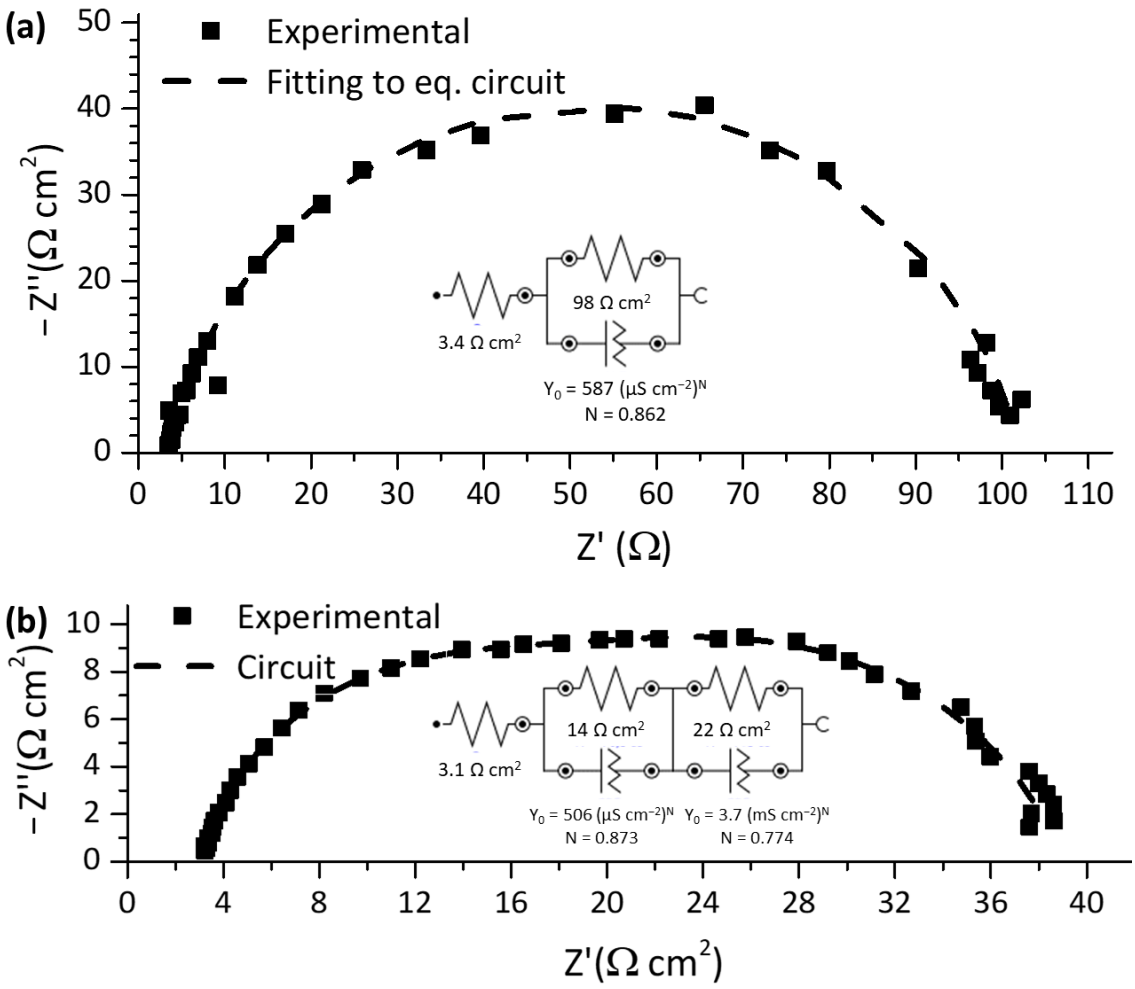

Figure 10. Nyquist diagrams for ORR, EIS tests at E_j = 1 for: (**a**) MONW; and (**b**) MONW/rGO-CNF.

2.4. Stability Studies

The durability and resistance to degradation of the MONW/CNF, MONW/rGO and MONW/rGO-CNF catalysts were assessed in an endurance test at ±10 mA cm^{-2} for 20 h in a gas-diffusion electrode in 6 M KOH (Figure 11). Catalyst MONW/rGO-CNF

shows remarkable stability, with the potential for OER increasing an average of 1.9 mV per hour of operation and the overpotential for ORR increasing less than 1 mV per hour. The overpotential for ORR (corrected by the ohmic potential loss, which was obtained from electrochemical impedance spectroscopy, see Figure S13) is around 450 mV and for OER, ca. 330 mV in the first cycle, resulting in a potential gap between ORR and OER at 10 mA cm^{-2} (IR free) of ca. 780 mV. This is consistent with what was observed during the LSVs (Table 3), as the observed onset potential for OER was lower than for ORR in those conditions. The stability of the catalyst towards OER is especially remarkable since it is considerably better than the benchmark IrO_2 catalyst. Gebreslase et al. [61] showed that after only 5 h of operation at 10 mA cm^{-2} in 1 M KOH, the IrO_2 catalyst began to quickly lose activity.

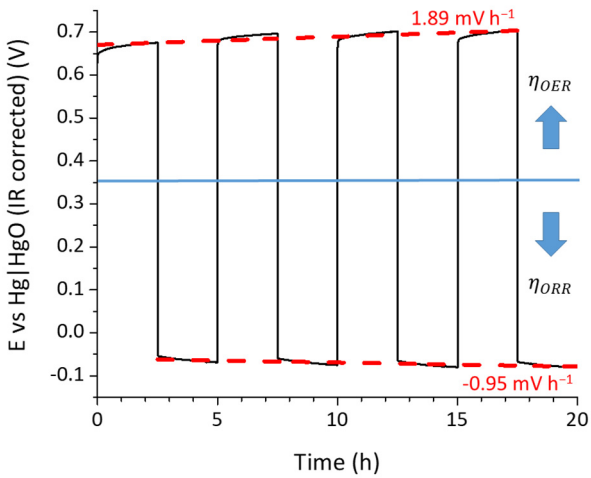

Figure 11. Endurance test carried out over a GDE with catalyst MONW/rGO-CNF in 6 M KOH. Potentials corrected for IR.

Figure S12 (Section S2.6 in Supporting Information) shows the endurance test for MONW/CNF and MONW/rGO, alongside the comparison with MONW/rGO-CNF. Catalyst MONW/CNF is also significantly stable, showing an increase in overpotential of 1.8 mV h^{-1} for ORR and 4.2 mV h^{-1} for OER, but exhibits a wider gap between the potentials for OER and ORR. Catalyst MONW/rGO has a good performance at the beginning, especially for OER, but quickly starts to deactivate, incrementing its overpotential at a rate of 2.1 mV h^{-1} for ORR and 11.3 mV h^{-1} for OER. By the end of the 20 h, the difference of potentials in this catalyst is almost 1100 mV.

3. Materials and Methods

3.1. Catalysts Synthesis

Manganese oxide nanowires (MONW) were synthesized following a procedure described elsewhere [24]. Briefly, 100 mL of an aqueous solution with 1.26 g of potassium permanganate (99%, Sigma-Aldrich, St. Louis, MO, USA) and 2.8 mL of concentrated hydrochloric acid (37% wt., Fluka) was stirred at room temperature for 30 min and then transferred to an autoclave at 120 °C for 12 h. A brown precipitate formed, which was washed with 2 L of deionized water (DI) and dried overnight at 70 °C.

Carbon nanofibers (CNF) and nanotubes (CNT) were obtained by catalytic decomposition of methane, varying the synthesis catalyst and temperature. The catalyst for CNF was based on $NiCuAl_2O_3$, as described by Sebastián et al. [62], and for CNT, Fe_2O_3 nanoparticles (<50 nm) obtained from Sigma-Aldrich. The catalysts were reduced with a 10 mL min^{-1} flow of hydrogen at 550 °C for CNF and at 700 °C for CNT. Subsequently, the temperature was raised under a flow of nitrogen up to 700 °C for CNF and 900 °C for CNT, after which a flow of 50 mL min^{-1} of methane was passed through the reactor for 3 h.

Reduced graphene oxide was synthesized by the Tour's method [63]. Briefly, 120 mL of concentrated sulphuric acid (98% Labkem) and 13.3 mL of phosphoric acid (85% Panreac) were mixed in a flask. After cooling, 1 g of graphite (Sigma-Aldrich) was added to the mixture under stirring. An amount of 6 g of $KMnO_4$ (99%, Sigma-Aldrich) was added slowly under stirring. The flask was then kept at 50 °C under stirring for 18 h. After that period, the mixture was poured over 135 mL of DI water ice, obtaining a brownish solution that was stirred for 30 min at 95 °C and then left to cool to room temperature. A solution of H_2O_2 (30% wt., 8 mL) was poured drop by drop, and then the mixture was placed in an ultrasound bath for 30 min to exfoliate the graphite oxide layers. Finally, the graphene oxide (GO) dispersion was washed and centrifuged repeatedly until a neutral pH was achieved, and the collected solid was dried overnight at 65 °C. The graphene oxide was reduced at 800 °C in a nitrogen atmosphere for 2 h to obtain reduced graphene oxide (rGO).

The carbon materials and MONW were mixed in a planetary ball mill in a 1:1 mass ratio, with a rotation speed of 100 rpm and using ethanol as a dispersing agent. The obtained composites were named MONW/C, where C is CNF, CNT or rGO.

A hybrid carbon material (rGO-CNF) was also synthesized by growing nanofibers in reduced graphene oxide. To do this, 0.7 g of GO was dispersed in 140 mL of water, and a solution of 1.48 g of $Ni(NO_3)_2 \cdot 6H_2O$ in 68 mL of water was added dropwise. The pH of the mixture was then raised to 5 with NaOH, and a solution with 0.38 g of $NaBH_4$ in 204 mL of water was slowly added. The solid was then filtered, washed with abundant water and dried overnight at 60 °C. This Ni oxide on GO material was introduced in a tubular quartz reactor, reduced in H_2 at 550 °C for one hour and then CH_4 was passed at 700 °C for one hour for the growth of CNF by catalytic decomposition on Ni particles.

3.2. Physical-Chemical Characterization

MONW and carbon materials were characterized using solid-state characterization techniques. The crystalline structures of the materials were investigated using powder X-Ray Diffraction (XRD). The equipment used was a Bruker AXS D8 Advance diffractometer (Billerica, MA, USA), which has a Cu Kα radiation source and a θ–θ configuration. The interplanar distances were obtained using Bragg's equation, and the number of graphitic planes was obtained by dividing the 002 crystal size (obtained from Scherrer's equation) by the interplanar distance. The determination of the crystallographic phases was carried out through Rietveld refinement. The morphology of MONW and carbon nanostructures was investigated by both transmission (TEM) and scanning (SEM) electron microscopy. TEM images were acquired with a Tecnai F30 microscope (Thermofisher, Waltham, Massachusetts, Estados Unidos operated at 300 kV. The samples were ultrasonically dispersed in ethanol for 15 min and then placed in a Cu carbon grid. SEM images were obtained with a Hitachi 3400-N microscope (Hitachi Ltd., Tokyo, Japan) with the powdered samples directly placed on a carbon tape. Textural features of MONW were assessed through nitrogen physisorption at −196 °C in Micromeritics ASAP 2020 (Norcross, GA, USA). The amount of metals in the samples was determined by inductively coupled plasma combined with atomic emission spectrometry (ICP-AES) using an Xpectroblue-EOP-TI FMT26 spectrometer (SPECTRO Analytical Instruments, Kleve, Germany). In addition, the carbon and hydrogen content of carbon materials was determined by elemental analysis (EA) in a Thermo Flash 1112 analyzer (Thermoscientific, Waltham, MA, USA).

3.3. Electrochemical Characterization

All the electrochemical tests were carri, ed out in a three-electrode cell connected to an Autolab potentiostat/galvanostat (Metrohm 302N, Metrohm Hispania, Madrid, Spain). The activity of the electrocatalysts was assessed through linear sweep voltammetries (LSVs) in a 0.1 M KOH electrolyte, using a reversible hydrogen electrode as the reference electrode and a graphite rod as the counter electrode. The working electrode was a glassy carbon rotating disk electrode (RDE, 5 mm diameter), on top of which a fine layer of the catalyst was deposited. To do so, an ink was prepared dispersing 5 mg of the catalyst and 10 μL of

Nafion (10% wt., Sigma-Aldrich, St. Louis, MO, USA) in 490 μL of ethanol under sonication and then deposited over the RDE in order to achieve a loading of 1 mg cm^{-2}. The LSVs to evaluate the ORR were performed in the range 1.2–0.2 V vs. RHE at a sweeping rate of 5 mV s^{-1} in oxygen-saturated electrolyte and at different rotation speeds (400, 625, 900, 1600 and 2500 rpm). Prior to the ORR LSVs, blank LSVs in nitrogen-saturated electrolyte were complete in the same potential range and used as a baseline. OER tests were carried out at 1600 rpm in the 1.1–1.8 V vs. RHE potential range at 5 mV s^{-1} of scan rate. Electrochemical impedance spectroscopy (EIS) tests were executed at the potential at which current had a magnitude of 1 mA cm^{-2} for both ORR (E_j = 1) and OER, with a sine wave of 10 mV of amplitude and in the range between 10 kHz and 100 mHz, acquiring ten points per decade. Endurance tests were carried out over a gas diffusion electrode of 0.5 cm^2 of exposed area in the strong basic electrolyte (6 M KOH). An ink of the same characteristics as the one of the RDE was sprayed over carbon paper, achieving a coverage of ca. 800 μg cm^{-2}. The reference electrode was a Hg | HgO electrode in 1 M KOH. Consecutive cycles (OER/ORR) of 2.5 h for each reaction at a current density of ±10 mA cm^{-2} were run.

4. Conclusions

Three different carbon nanostructures (carbon nanofibers, carbon nanotubes and reduced graphene oxide) were synthesized and mixed with manganese oxide nanowires to obtain bifunctional oxygen electrocatalysts. The type of carbon employed in the catalyst had an important effect on the activity, being the catalyst synthesized with CNF the most active towards ORR and the catalyst with rGO the most active towards OER, even surpassing the performance of the benchmark IrO_2 catalyst. Catalysts with CNT showed poor activity for both reactions, which was ascribed to their low surface area and lack of structural defects. The Koutecky–Levich plots show that the MONW/C catalysts have an increased number of electrons transferred in comparison to the phases on their own, indicating a synergistic effect that goes beyond just increasing conductivity or enhancing surface area but also changes the pathway of the reaction. The analysis of Tafel plots and electrochemical impedance spectroscopy allowed us to conclude that carbon and manganese oxide phases can catalyze different steps of the reaction pathways, and thus, by mixing them, a catalyst with lower energetic barriers for the reactions could be obtained. With this information in mind, we synthesized a hybrid rGO-CNF material and mixed it with MONW, which showed increased activity towards ORR in comparison to MONW/CNF and a closer activity towards OER than that of catalyst MONW/rGO. The hybrid MONW/rGO-CNF catalyst was tested in demanding conditions in a gas diffusion electrode (6 M KOH, at ±10 mA cm^{-2}) and showed remarkable stability for 20 h of operation, maintaining less than 0.77 V of difference between the potentials for OER and ORR (IR corrected) under the mentioned conditions. This work proves that the structure of carbon materials used as an additive in manganese bifunctional oxygen catalysts plays a key role in both the mechanisms of the reactions and the performance of the catalysts and that this can be exploited to rationally design catalysts with enhanced activity and/or bifunctionality.

Supplementary Materials: The following supporting information can be downloaded at https://www.mdpi.com/article/10.3390/catal13091240/s1. S1. Additional physical-chemical characterization of manganese oxide nanowires; S1.1. Morphology; Figure S1. (a) TEM and (b) SEM micrographs for MONW; S1.2. X-Ray diffraction; Figure S2. Diffractogram of MONW; S1.3. X-ray photoelectron spectroscopy; Figure S3. XPS spectra of orbitals: (a) Mn2p and (b) O1s of MONW; S1.4. Nitrogen physisorption; Figure S4. (a) Nitrogen physisorption for MONW at 96 K and, (b) Pore size distribution (BJH desorption); S2. Additional electrochemical characterization of manganese oxide nanowire–carbon composites; S2.1 Effect of acid-leaching on carbon nanotubes; Figure S5. Comparison between the catalytic activities of pristine carbon nanotubes and acid-leached carbon nanotubes (CNT-AL); S2.2. Comparison between the single materials and the composite catalysts; Figure S6. Comparison between the catalytic activities of carbon materials and their composites: (a) CNF, (b) CNT, (c) rGO and, (d) rGO-CNF; S2.3. Koutecky–Levich plots; Table S1. Parameters and properties of the electrochemical system used in the Levich equation; Figure S7. LSVs at 400, 625, 900, 1600 rpm

rotation speed of materials: (a) CNF, (b) CNT, (c) rGO and, (d) MONW; Figure S8. LSVs at 400, 625, 900, 1600 rpm rotation speed of materials: (a) MONW/CNF, (b) MONW/CNT and, (c) MONW/rGO; Figure S9. Koutecky–Levich plots at E = 0.4 V vs. RHE of carbon materials and manganese oxide; S2.4. Tafel plots; S2.5. Electrochemical characterization of composite MONW/mm[rGO-CNF]; Figure S11. Comparative performance of composite MONW/mm[rGO-CNF] with respect to MONW/C catalysts; S2.6. Durability tests; Figure S12. Endurance test carried out over a GDE with catalysts (a) MONW/CNF and (b) MONW/rGO in 6M KOH. Potentials corrected for IR; Figure S13. Nyquist diagrams (top: ORR, bottom: OER) for EIS tests for MONW/CNF-rGO.

Author Contributions: Conceptualization, N.I.V.-M., C.A. and D.S.; methodology, N.I.V.-M., C.A. and D.S.; validation, N.I.V.-M. and N.O.; formal analysis, N.I.V.-M., C.A. and D.S.; investigation, N.I.V.-M., C.A., D.S. and N.O.; resources, C.A. and M.J.L.; data curation, N.I.V.-M. and N.O.; writing—original draft preparation, N.I.V.-M.; writing—review and editing, C.A. and D.S.; visualization, N.I.V.-M. and N.O.; supervision, C.A. and M.J.L.; project administration, C.A., D.S. and M.J.L.; funding acquisition, C.A., D.S. and M.J.L. All authors have read and agreed to the published version of the manuscript.

Funding: The authors wish to acknowledge Ministerio de Ciencia e Innovación and Agencia Estatal de Investigación (MCIN/AEI/10.13039/501100011033) for the PID2020-115848RB-C21 grant. The authors also thank the European Union and the NextGeneration EU program for the funding of grant TED2021-130279A-I00. The authors also acknowledge Gobierno de Aragón (DGA) for the financial support to Grupo de Conversión de Combustibles (T06_20R). N. Villanueva also acknowledges DGA for his pre-doctoral contract. The authors would like to acknowledge the use of the Servicio General de Apoyo a la Investigación-SAI, Universidad de Zaragoza.

Data Availability Statement: The data presented in this study are available on request from the corresponding author.

Conflicts of Interest: The authors declare no conflict of interest.

References

1. McKerracher, R.D.; Ponce de Leon, C.; Wills, R.G.A.; Shah, A.A.; Walsh, F.C. A Review of the Iron-Air Secondary Battery for Energy Storage. *Chempluschem* **2015**, *80*, 323–335. [CrossRef]
2. Wang, Y.; Leung, D.Y.C.; Xuan, J.; Wang, H. A review on unitized regenerative fuel cell technologies, part B: Unitized regenerative alkaline fuel cell, solid oxide fuel cell, and microfluidic fuel cell. *Renew. Sustain. Energy Rev.* **2017**, *75*, 775–795. [CrossRef]
3. Xie, X.; Du, L.; Yan, L.; Park, S.; Qiu, Y.; Sokolowski, J.; Wang, W.; Shao, Y. Oxygen Evolution Reaction in Alkaline Environment: Material Challenges and Solutions. *Adv. Funct. Mater.* **2022**, *32*, 2110036. [CrossRef]
4. Shao, Y.; Jiang, Z.; Zhang, Q.; Guan, J. Progress in Nonmetal-Doped Graphene Electrocatalysts for the Oxygen Reduction Reaction. *ChemSusChem* **2019**, *12*, 2133–2146. [CrossRef] [PubMed]
5. Yang, C.J. An impending platinum crisis and its implications for the future of the automobile. *Energy Policy* **2009**, *37*, 1805–1808. [CrossRef]
6. Minke, C.; Suermann, M.; Bensmann, B.; Hanke-Rauschenbach, R. Is iridium demand a potential bottleneck in the realization of large-scale PEM water electrolysis? *Int. J. Hydrog. Energy* **2021**, *46*, 23581–23590. [CrossRef]
7. Alegre, C.; Stassi, A.; Modica, E.; Lo Vecchio, C.; Aricò, A.S.; Baglio, V. Investigation of the activity and stability of Pd-based catalysts towards the oxygen reduction (ORR) and evolution reactions (OER) in iron-air batteries. *RSC Adv.* **2015**, *5*, 25424–25427. [CrossRef]
8. McKerracher, R.D.; Alegre, C.; Baglio, V.; Aricò, A.S.; Ponce De León, C.; Mornaghini, F.; Rodlert, M.; Walsh, F.C. A nanostructured bifunctional Pd/C gas-diffusion electrode for metal-air batteries. *Electrochim. Acta* **2015**, *174*, 508–515. [CrossRef]
9. Alegre, C.; Modica, E.; Lo Vecchio, C.; Sebastián, D.; Lázaro, M.J.; Aricò, A.S.; Baglio, V. Carbon Nanofibers as Advanced Pd Catalyst Supports for the Air Electrode of Alkaline Metal-Air Batteries. *Chempluschem* **2015**, *80*, 1384–1388. [CrossRef]
10. Zhao, Q.; Yan, Z.; Chen, C.; Chen, J. Spinels: Controlled Preparation, Oxygen Reduction/Evolution Reaction Application, and beyond. *Chem. Rev.* **2017**, *117*, 10121–10211. [CrossRef]
11. Alegre, C.; Modica, E.; Aricò, A.S.; Baglio, V. Bifunctional oxygen electrode based on a perovskite/carbon composite for electrochemical devices. *J. Electroanal. Chem.* **2018**, *808*, 412–419. [CrossRef]
12. Rashkova, V.; Kitova, S.; Konstantinov, I.; Vitanov, T. Vacuum evaporated thin films of mixed cobalt and nickel oxides as electrocatalyst for oxygen evolution and reduction. *Electrochim. Acta* **2002**, *47*, 1555–1560. [CrossRef]
13. Indra, A.; Menezes, P.W.; Sahraie, N.R.; Bergmann, A.; Das, C.; Tallarida, M.; Schmeißer, D.; Strasser, P.; Driess, M. Unification of catalytic water oxidation and oxygen reduction reactions: Amorphous beat crystalline cobalt iron oxides. *J. Am. Chem. Soc.* **2014**, *136*, 17530–17536. [CrossRef]
14. Hazarika, K.K.; Goswami, C.; Saikia, H.; Borah, B.J.; Bharali, P. Cubic Mn_2O_3 nanoparticles on carbon as bifunctional electrocatalyst for oxygen reduction and oxygen evolution reactions. *Mol. Catal.* **2018**, *451*, 153–160. [CrossRef]

15. Wang, Y.; Yang, D.; Li, S.; Zhang, L.; Zheng, G.; Guo, L. Layered copper manganese oxide for the efficient catalytic CO and VOCs oxidation. *Chem. Eng. J.* **2019**, *357*, 258–268. [CrossRef]
16. Yang, S.; Wang, Z.; Cao, Z.; Mao, X.; Shi, M.; Li, Y.; Zhang, R.; Yin, Y. Facile synthesis of well dispersed spinel cobalt manganese oxides microsphere as efficient bi-functional electrocatalysts for oxygen reduction reaction and oxygen evolution reaction. *J. Alloys Compd.* **2017**, *721*, 482–491. [CrossRef]
17. Gu, Y.; Yan, G.; Lian, Y.; Qi, P.; Mu, Q.; Zhang, C.; Deng, Z.; Peng, Y. MnIII-enriched α-MnO_2 nanowires as efficient bifunctional oxygen catalysts for rechargeable Zn-air batteries. *Energy Storage Mater.* **2019**, *23*, 252–260. [CrossRef]
18. Chatenet, M.; Pollet, B.G.; Dekel, D.R.; Dionigi, F.; Deseure, J.; Millet, P.; Braatz, R.D.; Bazant, M.Z.; Eikerling, M.; Staffell, I.; et al. Water electrolysis: From textbook knowledge to the latest scientific strategies and industrial developments. *Chem. Soc. Rev.* **2022**, *51*, 4583–4762. [CrossRef]
19. Jiang, J.; Li, Y.; Liu, J.; Huang, X.; Yuan, C.; Lou, X.W. Recent advances in metal oxide-based electrode architecture design for electrochemical energy storage. *Adv. Mater.* **2012**, *24*, 5166–5180. [CrossRef]
20. Fu, G.; Yan, X.; Chen, Y.; Xu, L.; Sun, D.; Lee, J.M.; Tang, Y. Boosting Bifunctional Oxygen Electrocatalysis with 3D Graphene Aerogel-Supported Ni/MnO Particles. *Adv. Mater.* **2018**, *30*, 1704609. [CrossRef]
21. Xu, N.; Zhang, Y.; Wang, M.; Fan, X.; Zhang, T.; Peng, L.; Zhou, X.D.; Qiao, J. High-performing rechargeable/flexible zinc-air batteries by coordinated hierarchical Bi-metallic electrocatalyst and heterostructure anion exchange membrane. *Nano Energy* **2019**, *65*, 104021. [CrossRef]
22. Xiang, W.; Zhao, Y.; Jiang, Z.; Li, X.; Zhang, H.; Sun, Y.; Ning, Z.; Du, F.; Gao, P.; Qian, J.; et al. Palladium single atoms supported by interwoven carbon nanotube and manganese oxide nanowire networks for enhanced electrocatalysis. *J. Mater. Chem. A* **2018**, *6*, 23366–23377. [CrossRef]
23. Poux, T.; Napolskiy, F.S.; Dintzer, T.; Kéranguéven, G.; Istomin, S.Y.; Tsirlina, G.A.; Antipov, E.V.; Savinova, E.R. Dual role of carbon in the catalytic layers of perovskite/carbon composites for the electrocatalytic oxygen reduction reaction. *Catal. Today* **2012**, *189*, 83–92. [CrossRef]
24. Villanueva-Martínez, N.I.; Alegre, C.; Martínez-Visús, I.; Lázaro, M.J. Bifunctional oxygen electrocatalysts based on non-critical raw materials: Carbon nanostructures and iron-doped manganese oxide nanowires. *Catal. Today* **2023**, *420*, 114083. [CrossRef]
25. He, M.; Jin, X.; Chen, F.; Chen, J.; Min, J.; Duan, H.; Kuang, X.; Li, J.; Wu, Z.; Li, J. Synergistic effect of Mn^{3+} and oxygen vacancy on the bifunctional oxygen electrocatalytic performance of MnOX/CNTs composites. *J. Alloys Compd.* **2023**, *933*, 167728. [CrossRef]
26. Niu, Y.; Teng, X.; Gong, S.; Liu, X.; Xu, M.; Chen, Z. Boosting oxygen electrocatalysis for flexible zinc-air batteries by interfacing iron group metals and manganese oxide in porous carbon nanowires. *Energy Storage Mater.* **2021**, *43*, 42–52. [CrossRef]
27. Cuong, T.V.; Pham, V.H.; Tran, Q.T.; Chung, J.S.; Shin, E.W.; Kim, J.S.; Kim, E.J. Optoelectronic properties of graphene thin films prepared by thermal reduction of graphene oxide. *Mater. Lett.* **2010**, *64*, 765–767. [CrossRef]
28. Liu, T.H.; Gajewski, G.; Pao, C.W.; Chang, C.C. Structure, energy, and structural transformations of graphene grain boundaries from atomistic simulations. *Carbon N. Y.* **2011**, *49*, 2306–2317. [CrossRef]
29. Krishnamoorthy, K.; Veerapandian, M.; Yun, K.; Kim, S.J. The chemical and structural analysis of graphene oxide with different degrees of oxidation. *Carbon N. Y.* **2013**, *53*, 38–49. [CrossRef]
30. Stobinski, L.; Lesiak, B.; Malolepszy, A.; Mazurkiewicz, M.; Mierzwa, B.; Zemek, J.; Jiricek, P.; Bieloshapka, I. Graphene oxide and reduced graphene oxide studied by the XRD, TEM and electron spectroscopy methods. *J. Electron Spectros. Relat. Phenomena* **2014**, *195*, 145–154. [CrossRef]
31. Paulchamy, B.; Arthi, G.; Lignesh, B.D. A Simple Approach to Stepwise Synthesis of Graphene Oxide Nanomaterial. *J. Nanomed. Nanotechnol.* **2015**, *6*, 1000253. [CrossRef]
32. Shen, J.; Hu, Y.; Shi, M.; Lu, X.; Qin, C.; Li, C.; Ye, M. Fast and facile preparation of graphene oxide and reduced graphene oxide nanoplatelets. *Chem. Mater.* **2009**, *21*, 3514–3520. [CrossRef]
33. Saleem, H.; Haneef, M.; Abbasi, H.Y. Synthesis route of reduced graphene oxide via thermal reduction of chemically exfoliated graphene oxide. *Mater. Chem. Phys.* **2018**, *204*, 1–7. [CrossRef]
34. Tientong, J.; Garcia, S.; Thurber, C.R.; Golden, T.D. Synthesis of nickel and nickel hydroxide nanopowders by simplified chemical reduction. *J. Nanotechnol.* **2014**, *2014*, 193162. [CrossRef]
35. Hosseynizadeh Khezri, S.; Yazdani, A.; Khordad, R. Pure iron nanoparticles prepared by electric arc discharge method in ethylene glycol. *EPJ Appl. Phys.* **2012**, *59*, 30401. [CrossRef]
36. Lu, X.; Qin, Z.; Zhang, Y.; Wang, X.; Li, F.; Ding, B.; Hu, Z. Study of the paramagnetic-antiferromagnetic transition and the $\gamma \rightarrow \varepsilon$ martensitic transformation in Fe-Mn alloys. *J. Mater. Sci.* **2000**, *35*, 5597–5603. [CrossRef]
37. Mathur, A.; Halder, A. One-step synthesis of bifunctional iron-doped manganese oxide nanorods for rechargeable zinc-air batteries. *Catal. Sci. Technol.* **2019**, *9*, 1245–1254. [CrossRef]
38. Shen, Y.; Zhu, Y.; Sunarso, J.; Guan, D.; Liu, B.; Liu, H.; Zhou, W.; Shao, Z. New Phosphorus-Doped Perovskite Oxide as an Oxygen Reduction Reaction Electrocatalyst in an Alkaline Solution. *Chem. A Eur. J.* **2018**, *24*, 6950–6957. [CrossRef]
39. Briggs, D. Handbook of X-ray Photoelectron Spectroscopy C. D. Wanger, W.M. Riggs, L.E. Davis, J.F. Moulder and G. E.Muilenberg Perkin-Elmer Corp., Physical Electronics Division, Eden Prairie, Minnesota, USA, 1979. 190 pp. $195. *Surf. Interface Anal.* **1981**, *3*, v. [CrossRef]
40. Santos, V.P.; Pereira, M.F.R.; Órfão, J.J.M.; Figueiredo, J.L. The role of lattice oxygen on the activity of manganese oxides towards the oxidation of volatile organic compounds. *Appl. Catal. B Environ.* **2010**, *99*, 353–363. [CrossRef]

41. Kabalan, I.; Lebeau, B.; Fadlallah, M.B.; Toufaily, J.; Hamieh, T.; Bellat, J.P.; Daou, T.J. Hierarchical faujasite-type zeolite for molecular decontamination. *J. Nanosci. Nanotechnol.* **2016**, *16*, 9318–9322. [CrossRef]
42. Waki, K.; Wong, R.A.; Oktaviano, H.S.; Fujio, T.; Nagai, T.; Kimoto, K.; Yamada, K. Non-nitrogen doped and non-metal oxygen reduction electrocatalysts based on carbon nanotubes: Mechanism and origin of ORR activity. *Energy Environ. Sci.* **2014**, *7*, 1950–1958. [CrossRef]
43. Ruiz-Cornejo, J.C.; Vivo-Vilches, J.F.; Sebastián, D.; Martínez-Huerta, M.V.; Lázaro, M.J. Carbon nanofiber-supported tantalum oxides as durable catalyst for the oxygen evolution reaction in alkaline media. *Renew. Energy* **2021**, *178*, 307–317. [CrossRef]
44. Ruiz-Cornejo, J.C.; Sebastián, D.; Pardo, J.I.; Martínez-Huerta, M.V.; Lázaro, M.J. Sulfur-doped carbon nanofibers as support for tantalum oxides bifunctional catalysts for the oxygen reduction and evolution reactions. *J. Power Sources* **2022**, *546*, 231988. [CrossRef]
45. Chen, X.; Gao, P.; Liu, H.; Xu, J.; Zhang, B.; Zhang, Y.; Tang, Y.; Xiao, C. In situ growth of iron-nickel nitrides on carbon nanotubes with enhanced stability and activity for oxygen evolution reaction. *Electrochim. Acta* **2018**, *267*, 8–14. [CrossRef]
46. Ahmed, M.S.; Begum, H.; Kim, Y.B. Iron nanoparticles implanted metal-organic-frameworks based Fe–N–C catalysts for high-performance oxygen reduction reaction. *J. Power Sources* **2020**, *451*, 227733. [CrossRef]
47. Stoerzinger, K.A.; Risch, M.; Han, B.; Shao-Horn, Y. Recent Insights into Manganese Oxides in Catalyzing Oxygen Reduction Kinetics. *ACS Catal.* **2015**, *5*, 6021–6031. [CrossRef]
48. Ramaswamy, N.; Mukerjee, S. Influence of inner- and outer-sphere electron transfer mechanisms during electrocatalysis of oxygen reduction in alkaline media. *J. Phys. Chem. C* **2011**, *115*, 18015–18026. [CrossRef]
49. Poux, T.; Bonnefont, A.; Ryabova, A.; Kéranguéven, G.; Tsirlina, G.A.; Savinova, E.R. Electrocatalysis of hydrogen peroxide reactions on perovskite oxides: Experiment versus kinetic modeling. *Phys. Chem. Chem. Phys.* **2014**, *16*, 13595–13600. [CrossRef]
50. Guan, D.; Shi, C.; Xu, H.; Gu, Y.; Zhong, J.; Sha, Y.; Hu, Z.; Ni, M.; Shao, Z. Simultaneously mastering operando strain and reconstruction effects via phase-segregation strategy for enhanced oxygen-evolving electrocatalysis. *J. Energy Chem.* **2023**, *82*, 572–580. [CrossRef]
51. Shinagawa, T.; Garcia-Esparza, A.T.; Takanabe, K. Insight on Tafel slopes from a microkinetic analysis of aqueous electrocatalysis for energy conversion. *Sci. Rep.* **2015**, *5*, 13801. [CrossRef] [PubMed]
52. Roche, I.; Chaînet, E.; Chatenet, M.; Vondrák, J. Carbon-supported manganese oxide nanoparticles as electrocatalysts for the Oxygen Reduction Reaction (ORR) in alkaline medium: Physical characterizations and ORR mechanism. *J. Phys. Chem. C* **2007**, *111*, 1434–1443. [CrossRef]
53. Park, S.; Jiang, T.; Zheng, K.; Lin, Z.; Meng, Y.; Wang, M.; Chen, J.; Chen, W. Ultrafast Thermal Synthesis of Non-Noble Metal-Based Electrocatalysts for Overall Water Splitting. *ACS Appl. Energy Mater.* **2023**, *6*, 5787–5796. [CrossRef]
54. Kapałka, A.; Fóti, G.; Comninellis, C. Determination of the Tafel slope for oxygen evolution on boron-doped diamond electrodes. *Electrochem. Commun.* **2008**, *10*, 607–610. [CrossRef]
55. Sebastián, D.; Alegre, C.; Gálvez, M.E.; Moliner, R.; Lázaro, M.J.; Aricò, A.S.; Baglio, V. Towards new generation fuel cell electrocatalysts based on xerogel-nanofiber carbon composites. *J. Mater. Chem. A* **2014**, *2*, 13713–13722. [CrossRef]
56. Xiao, X.; Zhang, W.; Zhao, H.; Li, L.; Deng, P.; Wu, Y.; Luo, S.; Chen, B. Ultrathin amorphous MnO_2 modified prawn shells-derived porous carbon towards robust oxygen electrocatalyst for rechargeable Zn-air battery. *Ceram. Int.* **2022**, *48*, 6506–6511. [CrossRef]
57. Meng, Y.; Song, W.; Huang, H.; Ren, Z.; Chen, S.Y.; Suib, S.L. Structure-property relationship of bifunctional MnO_2 nanostructures: Highly efficient, ultra-stable electrochemical water oxidation and oxygen reduction reaction catalysts identified in alkaline media. *J. Am. Chem. Soc.* **2014**, *136*, 11452–11464. [CrossRef]
58. Wahab, A.; Iqbal, N.; Noor, T.; Ashraf, S.; Raza, M.A.; Ahmad, A.; Khan, U.A. Thermally reduced mesoporous manganese MOF @reduced graphene oxide nanocomposite as bifunctional electrocatalyst for oxygen reduction and evolution. *RSC Adv.* **2020**, *10*, 27728–27742. [CrossRef]
59. Masa, J.; Xia, W.; Sinev, I.; Zhao, A.; Sun, Z.; Grützke, S.; Weide, P.; Muhler, M.; Schuhmann, W. MnxOy/NC and CoxOy/NC nanoparticles embedded in a nitrogen-doped carbon matrix for high-performance bifunctional oxygen electrodes. *Angew. Chem. Int. Ed.* **2014**, *53*, 8508–8512. [CrossRef]
60. Gao, Y.; Zhao, H.; Chen, D.; Chen, C.; Ciucci, F. In situ synthesis of mesoporous manganese oxide/sulfur-doped graphitized carbon as a bifunctional catalyst for oxygen evolution/reduction reactions. *Carbon N. Y.* **2015**, *94*, 1028–1036. [CrossRef]
61. Gebreslase, G.A.; Sebastián, D.; Martínez-Huerta, M.V.; Lázaro, M.J. Nitrogen-doped carbon decorated-Ni3Fe@Fe3O4 electrocatalyst with enhanced oxygen evolution reaction performance. *J. Electroanal. Chem.* **2022**, *925*, 116887. [CrossRef]
62. Sebastián, D.; Suelves, I.; Moliner, R.; Lázaro, M.J. The effect of the functionalization of carbon nanofibers on their electronic conductivity. *Carbon N. Y.* **2010**, *48*, 4421–4431. [CrossRef]
63. Marcano, D.C.; Kosynkin, D.V.; Berlin, J.M.; Sinitskii, A.; Sun, Z.; Slesarev, A.; Alemany, L.B.; Lu, W.; Tour, J.M. Improved synthesis of graphene oxide. *ACS Nano* **2010**, *4*, 4806–4814. [CrossRef] [PubMed]

SUPPLEMENTARY MATERIALS

On the Effect of the Nature of Carbon Nanostructures on the Activity of Bifunctional Catalysts Based on Manganese Oxide Nanowires

Nicolás Ignacio Villanueva-Martínez, Cinthia Alegre *, David Sebastián, Nataly Orozco and María Jesús Lázaro *

Instituto de Carboquímica–CSIC, Calle Miguel Luesma Castán, 4.,50018 Zaragoza, Spain;
nvillanueva@icb.csic.es (N.I.V.-M.); dsebastian@icb.csic.es (D.S.)
* Correspondence: cinthia@icb.csic.es (C.A.); mlazaro@icb.csic.es (M.J.L.)

S1. Additional physical-chemical characterization of manganese oxide nanowires

S1.1. Morphology

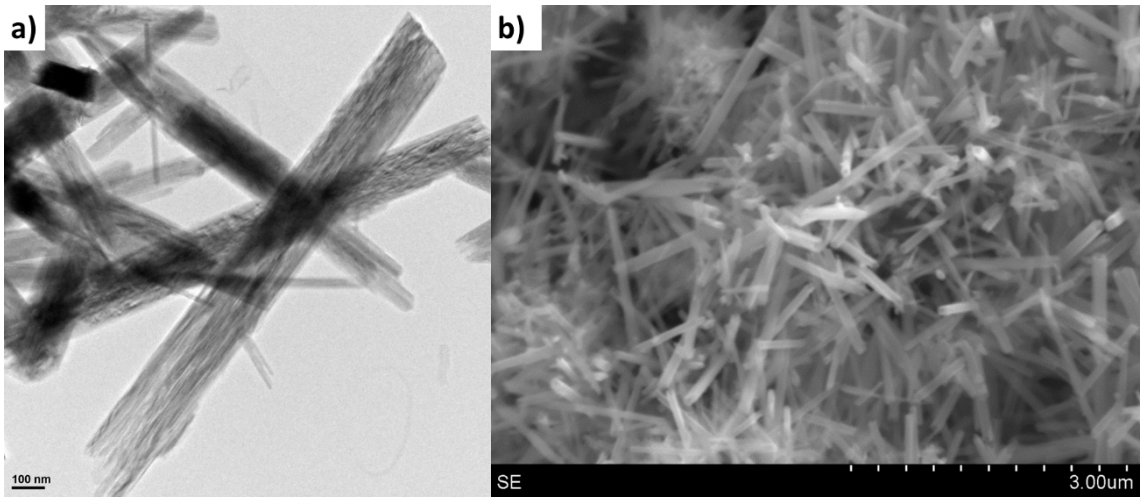

Figure S1. a) TEM and b) SEM micrographs for MONW.

S1.2. X-Ray diffraction

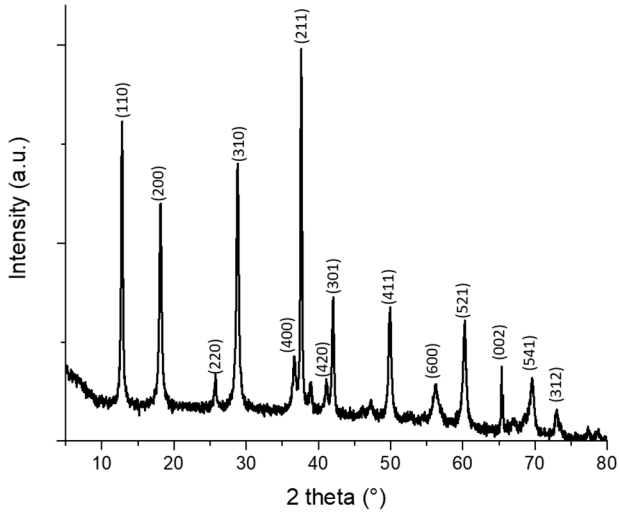

Figure S2. Diffractogram of MONW.

S1.3. X-ray photoelectron spectroscopy

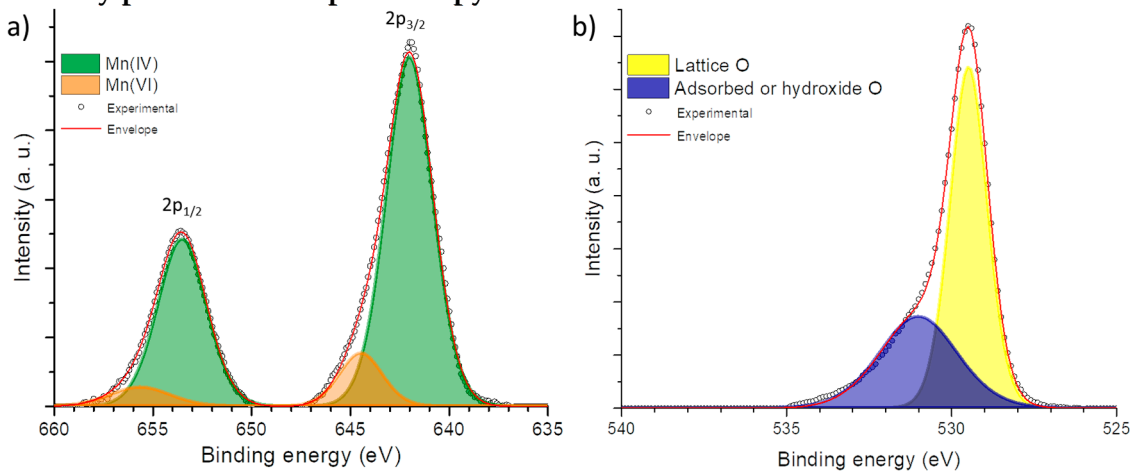

Figure S3. XPS spectra of orbitals: a) Mn2p and b) O1s of MONW.

S1.4. Nitrogen physisorption

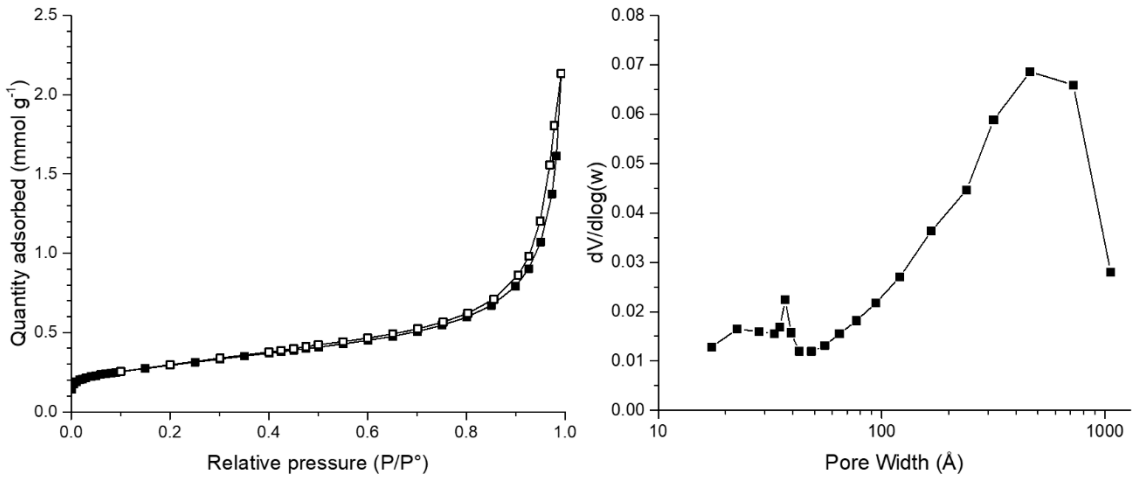

Figure S4. a) Nitrogen physisorption for MONW at 96 K and, b) Pore size distribution (BJH desorption).

S2. Additional electrochemical characterization of manganese oxide nanowire–carbon composites

S2.1 Effect of acid-leaching on carbon nanotubes

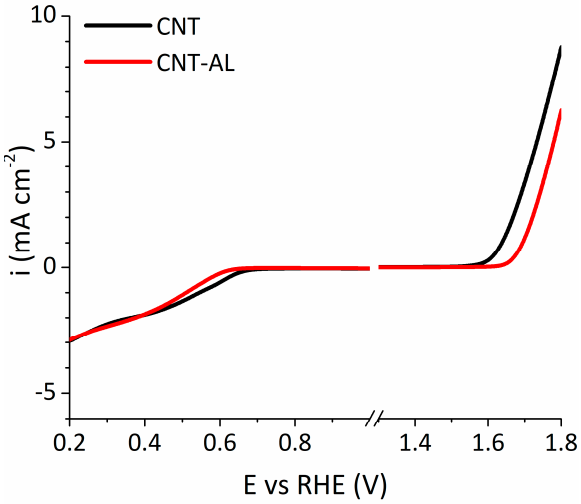

Figure S5. Comparison between the catalytic activities of pristine carbon nanotubes and acid-leached carbon nanotubes (CNT-AL)

S2.2. Comparison between the single materials and the composite catalysts

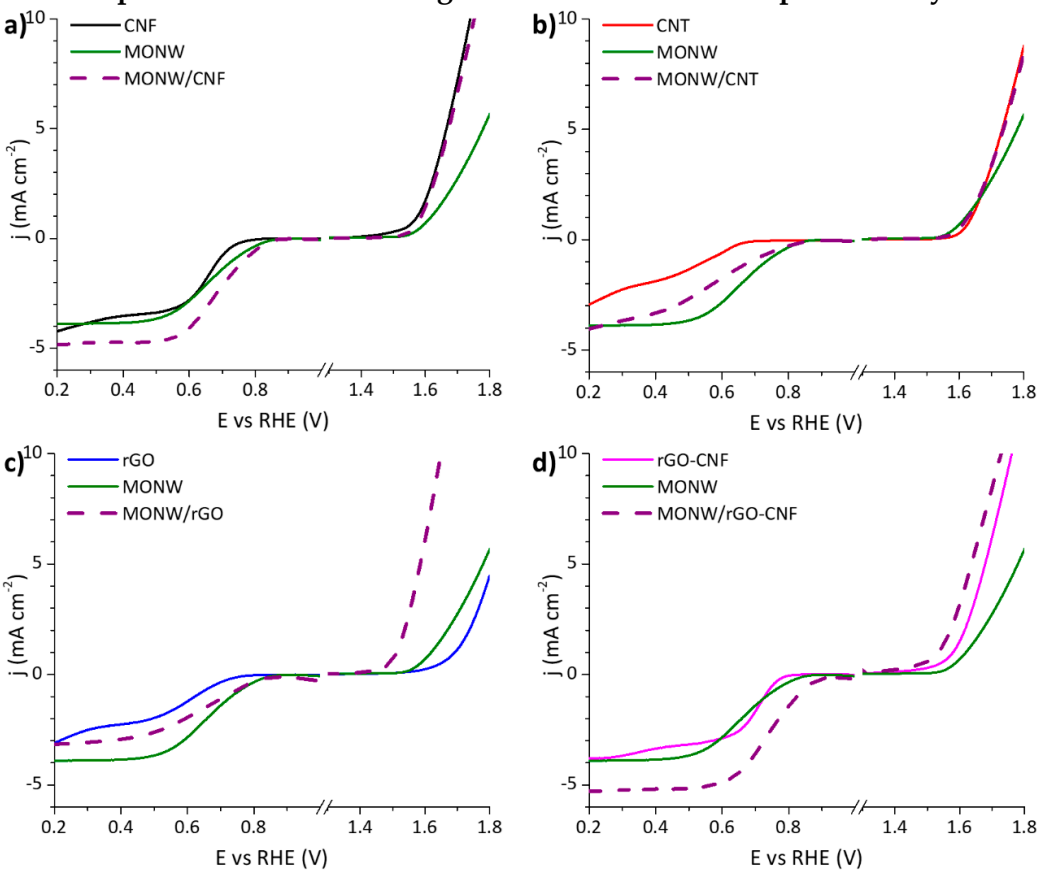

Figure S6. Comparison between the catalytic activities of carbon materials and their composites: a) CNF, b) CNT, c) rGO and, d) rGO-CNF.

S2.3. Koutecky–Levich plots

ORR LSVs were performed at 400, 625, 900, 1600 and 2500 rpm to obtain the number of electrons exchanged in the diffusional limit, using the Koutecky–Levich approach, applying Equation S1:

$$|j|^{-1} = |j_L|^{-1} + |j_k|^{-1} \quad \text{(S1)}$$

Where j is the observed current density at E = 0.2 V *vs*. RHE, j_k is the intrinsic current density and j_L is the limiting current density, estimated using the Levich equation for rotating disk electrodes (Equation S2):

$$j_L = 1.95nFAC_{O_2}^{*}D_{O_2}^{1.5}\nu^{-(1/6)}f^{1/2} \quad \text{(S2)}$$

In the Levich equation, n is the number of electrons transferred in the oxygen reduction reaction, $C_{O_2}^{*}$ is the saturation concentration of oxygen in the electrolyte, D_{O_2} is the diffusivity of oxygen in the electrolyte, ν is the cinematic viscosity of the electrolyte and f is the rotation frequency of the electrode, F is the Faraday constant and A is the disc electrode area. Combining Equations S1 and S2, Equation S3 is obtained:

$$|j|^{-1} = |j_L|^{-1} + m_L f^{-0.5} \quad \text{(S3)}$$

where $m_L = 1/(1.95nFAC_{O_2}^{*}D_{O_2}^{1.5}\nu^{-(1/6)})$.

Plotting the inverse of the observed current density vs. the inverse of the square root of the rotation frequency made it possible to obtain the number of electrons transferred from the slope of the fitted line. The parameters used are summarized in Table S1.

Table S1. Parameters and properties of the electrochemical system used in the Levich equation

Parameter	Value
F	96485 C mol^{-1}
A	1.96 x 10^{-5} m^2
$C_{O_2}^{*}$	1.21 mol m^{-3}
D_{O_2}	1.87 x 10^{-9} m^2 s^{-1}
ν	10^{-6} m^2 s^{-1}

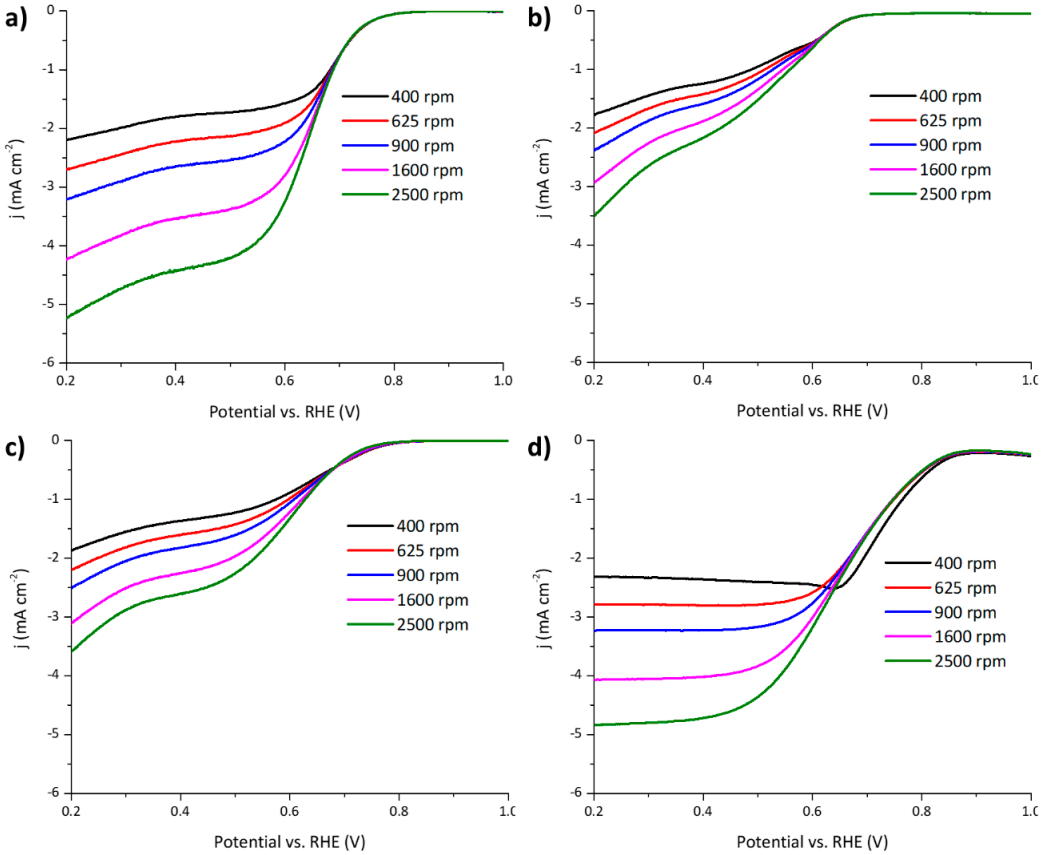

Figure S7. LSVs at 400, 625, 900, 1600 rpm rotation speed of materials: a) CNF, b) CNT, c) rGO and, d) MONW.

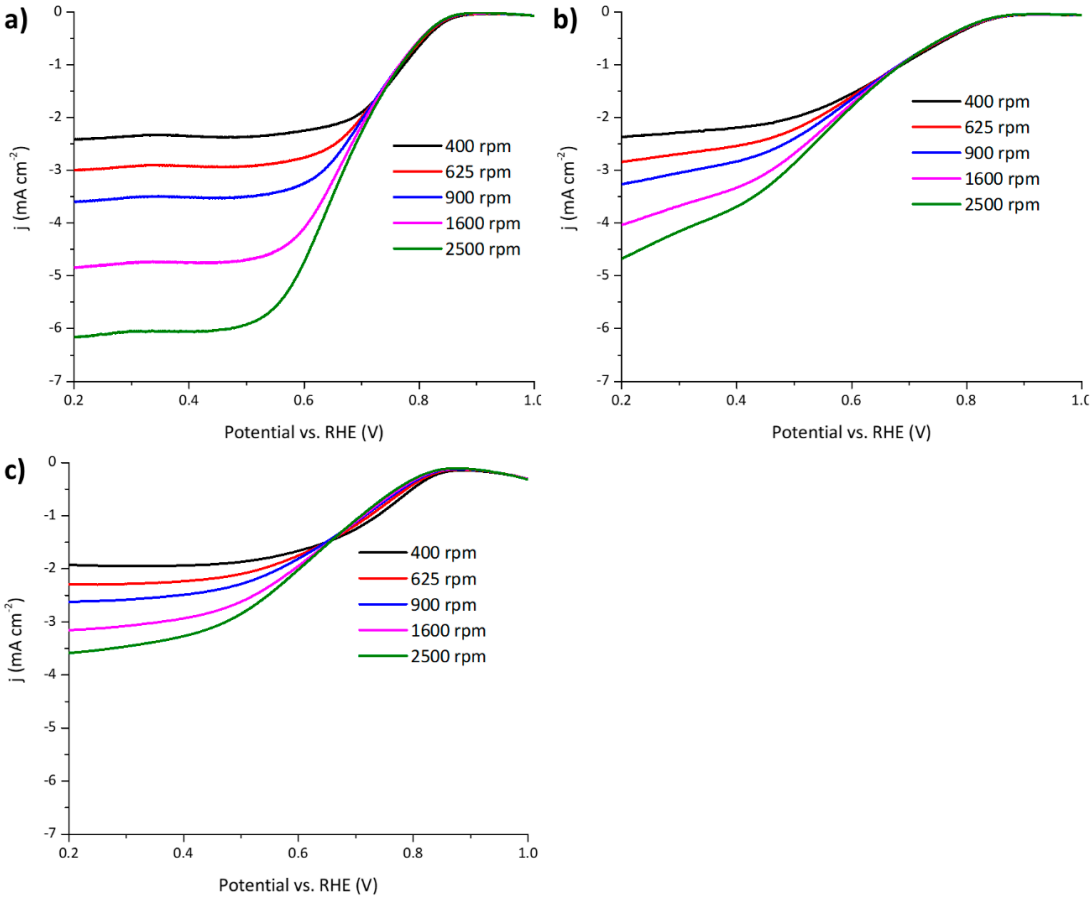

Figure S8. LSVs at 400, 625, 900, 1600 rpm rotation speed of materials: a) MONW/CNF, b) MONW/CNT and, c) MONW/rGO.

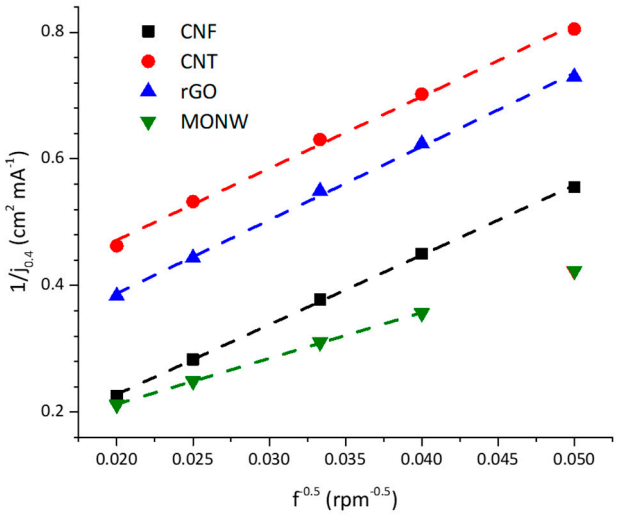

Figure S9. Koutecky–Levich plots at E = 0.4 V vs. RHE of carbon materials and manganese oxide.

S2.4. Tafel plots

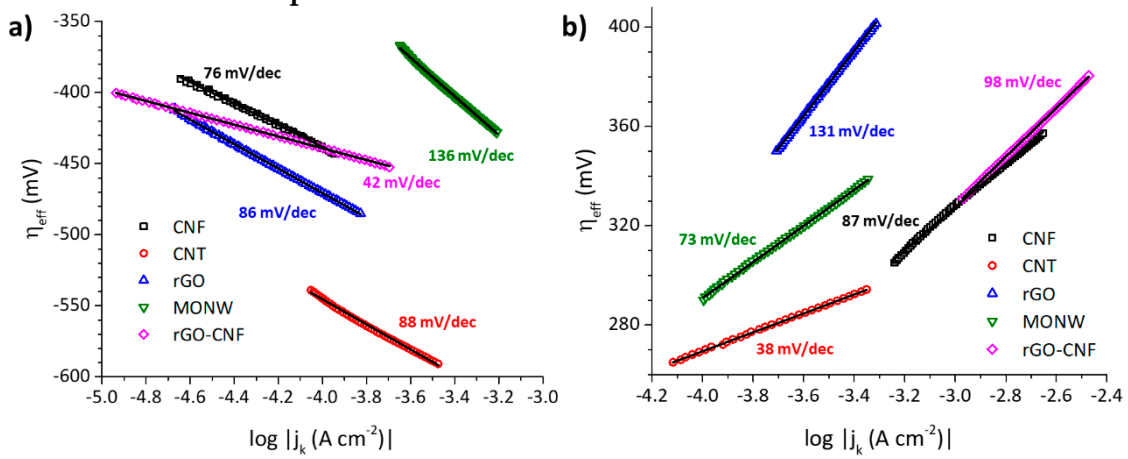

Figure S10. ORR (a) and OER (b) Tafel plots of non-composite catalysts. Experiments carried out over a RDE at 1600 rpm.

S2.5. Electrochemical characterization of composite MONW/mm[rGO-CNF]

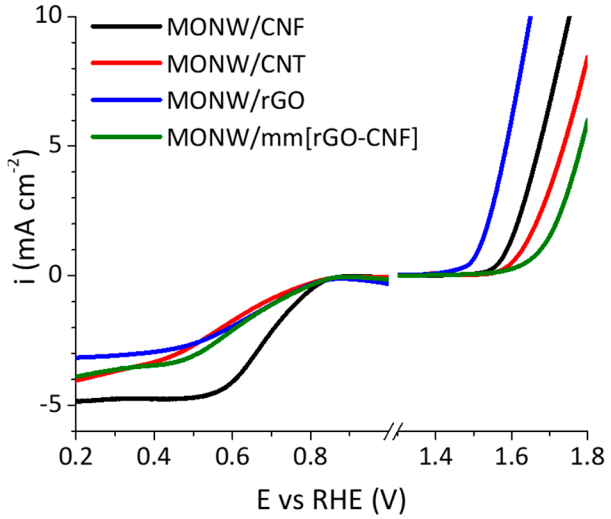

Figure S11. Comparative performance of composite MONW/mm[rGO-CNF] with respect to MONW/C catalysts.

S2.6. Durability tests

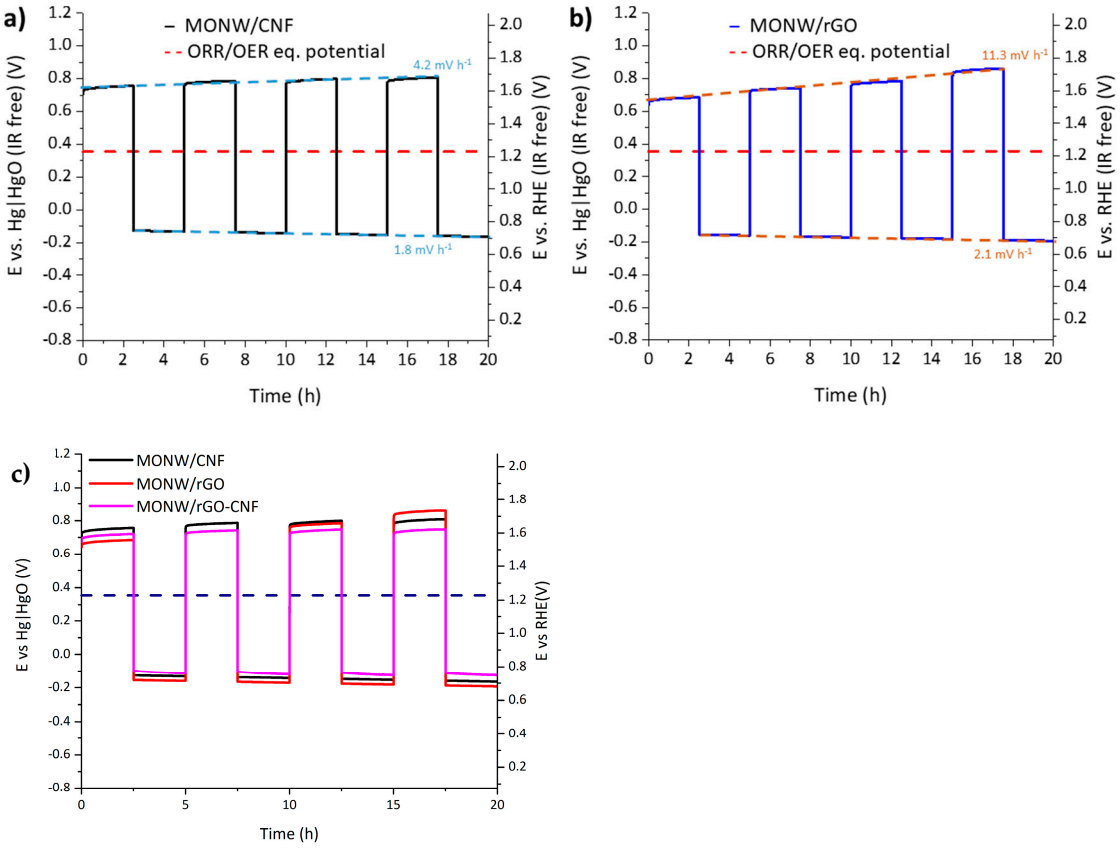

Figure S12. Endurance test carried out over a GDE with catalysts a) MONW/CNF and b) MONW/rGO in 6M KOH. Potentials corrected for IR.

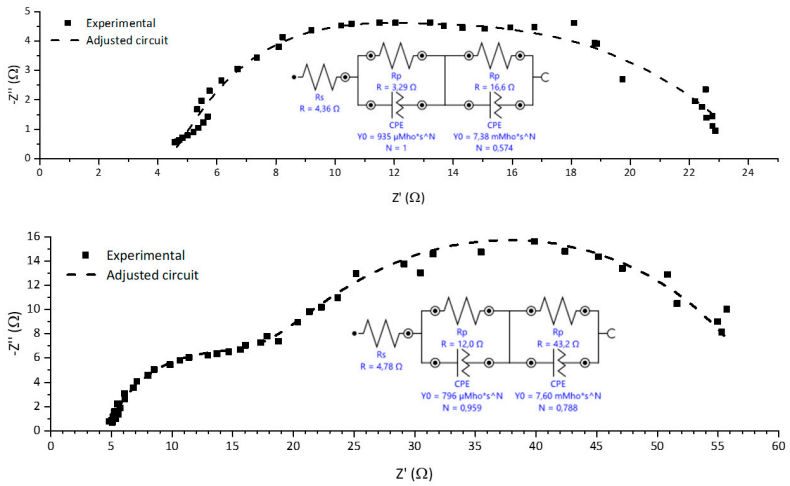

Figure S13. Nyquist diagrams (top: ORR, bottom: OER) for EIS tests for MONW/CNF-rGO.

CAPÍTULO III: DISCUSIÓN GLOBAL DE RESULTADOS

En este capítulo, se presenta un resumen de los principales resultados obtenidos en los artículos que conforman esta tesis doctoral. El capítulo se divide en dos secciones: la primera dedicada a resolver los desafíos que plantea el electrodo negativo de baterías hierro-aire; y la segunda, enfocada a catalizadores bifuncionales para el electrodo de aire.

1. Antecedentes

Los sistemas hierro-aire son una tecnología muy prometedora con el potencial de convertirse en una de las soluciones de almacenamiento de energía más baratas y seguras en el futuro. Tanto el electrodo negativo (electrodo de hierro) como el electrodo positivo (electrodo de aire) de estas baterías presentan una serie de desafíos, aún por resolver, de cara a hacer de esta tecnología una solución comercialmente viable. En la presente tesis se han intentado abordar los principales desafíos de ambos electrodos. En el esquema de la **Figura 1**, se muestra un resumen de cómo se ha organizado la investigación de esta tesis de acuerdo a los desafíos de cada electrodo.

Electrodo negativo	**Electrodo positivo**
Desafíos abordados	**Desafíos abordados**
(i) Pasivación del electrodo (ii) Reacción de evolución de hidrógeno (iii) Cambio de volumen del electrodo	(i) Obtener catalizadores activos y bifuncionales para ORR/OER basados en materiales económicos. (ii) Mejorar la durabilidad del electrodo.
Investigación propuesta	**Investigación propuesta**
Óxidos de hierro mesoporosos modificados con azufre	Catalizadores bifuncionales basados en nanofilamentos de manganeso y nanoestructuras carbonosas
Objetivo	**Objetivo**
(1) Obtener electrodos negativos a base de materiales económicos (Fe_2O_3) con aditivos (S) que ayuden a mejorar la estabilidad de los electrodos. (2) Entender y mejorar las propiedades físico-químicas de los materiales de electrodo que determinan su estabilidad.	(1) Obtener catalizadores bifuncionales de oxígeno basados en materiales económicos (Mn) y estudiar su actividad, reversibilidad y durabilidad. (2) Estudiar el rol de las fases carbonosas en las reacciones de evolución y reducción de oxígeno y estudiar su impacto en el desempeño de los catalizadores

Figura 1. Esquema de la investigación realizada durante esta tesis.

2. Electrodos negativos para baterías hierro-aire basados en óxidos de hierro modificados con azufre

Entre los desafíos a resolver para el electrodo negativo de baterías hierro-aire se encuentran: (i) la pasivación del electrodo, que resulta en la pérdida de capacidad, debido a la formación de especies no conductoras durante los ciclos de carga y descarga; (ii) la reacción de evolución de hidrógeno, una reacción parásita que interfiere con la carga del electrodo y (iii) el cambio de volumen del electrodo, debido a que los productos de descarga (óxidos y (oxi)hidróxidos de hierro) ocupan más volumen que el hierro metálico, lo que puede hacer que se desintegre la estructura del electrodo, además de bloquear los poros e impedir el paso del electrolito [1,2]. En esta tesis, y en los dos trabajos científicos presentados, se abordan las problemáticas descritas.

En el primer artículo, se investiga la viabilidad del óxido de hierro modificado con azufre como electrodo negativo, abordando la evolución de hidrógeno (HER) y la pasivación del

electrodo. En concreto se obtuvieron óxidos de hierro modificados con azufre que se investigaron como electrodos negativos de baterías alcalinas de hierro-aire. La mayoría de los enfoques destinados a inhibir o reducir tanto la HER como la pasivación se basan en ciertos aditivos en el electrolito (como alcanotioles o sales de sulfuro, K_2S, etc.) o sulfuros (FeS, Bi_2S_3) en la composición del electrodo de hierro. Sin embargo, estos enfoques incorporan los aditivos de sulfuro ya sea por molienda de bolas (en la que los aditivos y las especies activas del electrodo se mezclan físicamente) o en el electrolito (añadiendo complejidad al diseño de la celda y contaminando el electrodo de aire, como se estableció recientemente [3]). Además, ciertos aditivos como los basados en bismuto no son deseables ya que el bismuto es una materia prima crítica. Por lo tanto, en esta tesis consideramos que son necesarios nuevos métodos para incorporar dichos elementos inhibidores de la HER. Durante el ciclo de carga de las baterías de hierro-aire, se forma hidrógeno en la superficie de las partículas de hierro; por lo tanto, es muy deseable obtener un material electroactivo de hierro con una distribución adecuada de los elementos inhibidores de HER. Por estas razones, en este trabajo se propuso usar óxidos de hierro como material del electrodo negativo, modificados con azufre durante su síntesis, con el fin de evaluar su viabilidad como electrodos negativos y su efectividad frente a la evolución de hidrógeno y la pasivación.

En el segundo artículo, se investiga el efecto de las propiedades texturales y cristalográficas sobre la estabilidad y capacidad de los electrodos. Para escalar la tecnología de baterías hierro-aire y optimizar las formulaciones de las celdas, es fundamental comprender claramente cómo las propiedades físico-químicas del electrodo influyen en su comportamiento electroquímico, en particular, en su estabilidad. En este trabajo, proponemos por primera vez correlaciones matemáticas entre las propiedades texturales y cristalográficas de los electrodos de hierro y su estabilidad electroquímica. Además, buscamos explicar mediante espectroscopía de impedancia electroquímica (EIS) y caracterización físico-química post-mortem cuáles son las causas de la desactivación de los electrodos y porqué las propiedades físico-químicas influyen en la estabilidad. En este caso, se utilizaron nuevamente óxidos de hierro modificados con azufre (gracias a los buenos resultados obtenidos previamente) si bien se llevó a cabo una modificación del método de síntesis con el fin de obtener óxidos de hierro con una porosidad mayor de la obtenida precedentemente, con el fin de acomodar mejor los cambios de volumen del electrodo durante el ciclado.

En la **Tabla 1** se muestra un esquema resumido de los materiales investigados en ambos artículos.

Tabla 1. Esquema de los materiales investigados para el electrodo negativo y publicaciones resultantes

Electrodo negativo	
Materiales investigados	**Revista, factor de impacto *(Journal Citation Report)*, cuartil**
Óxidos de hierro dopados con azufre obtenidos mediante precipitación con ácido oxálico **(S-Fe_2O_3-OXL)** e hidróxido de sodio **(S-Fe_2O_3-SHX)**	ACS Applied Energy Materials (FI_{2022} = 6,4; $Q1_{\text{Materials Science Multidisc}}$) (Artículo I)
Óxidos de hierro mesoporosos dopados con azufre obtenidos mediante precipitación con ácido tartárico calcinados en aire **(S-Fe_2O_3-TAR-AIR)** o en nitrógeno **(S-Fe_2O_3-TAR-N_2)**	Electrochimica Acta (FI_{2022} = 6,6; $Q2_{\text{MElectrochemistry}}$) (Artículo II)

2.1. Materiales investigados

Se desarrollaron electrodos negativos para baterías hierro-aire basados en composites de negro de carbono comercial y óxidos de hierro porosos. El carbono se usa como aditivo conductor, debido a que los productos de oxidación del hierro (salvo la magnetita) no son buenos conductores eléctricos. Los óxidos de hierro fueron obtenidos mediante 3 métodos de precipitación de sales: precipitación con ácido oxálico, precipitación hidrotermal con hidróxido de sodio y precipitación hidrotermal con ácido tartárico. Los óxidos fueron modificados con azufre agregando tiosulfato de sodio en su síntesis. Se sintetizaron también óxidos de hierro sin modificar con azufre, con el fin de evaluar el efecto de este aditivo en la capacidad de descarga de los electrodos. Los óxidos de hierro fueron calcinados en aire a 350 °C o tratados en nitrógeno a 500 °C. Todas estas variaciones en los procesos de síntesis se llevaron a cabo con el objetivo de obtener óxidos de hierro con diferentes características físico-químicas, tales como estructura cristalina y tamaño de cristal, propiedades texturales o química superficial. La **Tabla 2** resume los óxidos sintetizados y sus condiciones de síntesis. Además, todos estos materiales se compararon con un óxido de hierro comercial suministrado por Sigma-Aldrich (Fe_2O_3, nanopowder, < 50 nm, pureza superior a 99 %), al cual se hará referencia como Fe_2O_3-COM.

Tabla 2. Condiciones de síntesis de los óxidos de hierro para electrodos negativos

Óxido de hierro	Agente precipitante	Tratamiento térmico	Adición de tiosulfato de azufre
Fe_2O_3-OXL-air	Oxalato	Aire 350 °C	No
S-Fe_2O_3-OXL-air	Oxalato	Aire 350 °C	Sí
Fe_2O_3-SHX-air	Hidróxido de sodio	Aire 350 °C	No
S-Fe_2O_3-SHX-air	Hidróxido de sodio	Aire 350 °C	Sí
Fe_2O_3-TAR-air	Ácido tartárico	Aire 350 °C	No
S-Fe_2O_3-TAR-air	Ácido tartárico	Aire 350 °C	Sí
Fe_2O_3-TAR-N_2	Ácido tartárico	Nitrógeno 500 °C	No
S-Fe_2O_3-TAR-N_2	Ácido tartárico	Nitrógeno 500 °C	Sí

2.2. Propiedades físico-químicas

2.2.1. Estructura cristalina

Los óxidos muestran diferencias en sus propiedades químicas, cristalográficas y texturales. Las únicas fases detectadas mediante difracción de rayos X fueron hematita y maghemita, lo que indicó que el hierro se encontró como óxido de hierro (III) (Fe_2O_3). Los óxidos de hierro mostraron tamaños de cristal (d_{crist}) de entre 6 y 21 nm (**Tabla 3**). La temperatura de tratamiento influyó en las propiedades cristalográficas, obteniéndose a mayor temperatura de tratamiento, una mayor proporción de fase maghemita y menores tamaños de cristal. Para corroborar los resultados de XRD, se efectuaron también análisis de espectroscopia Mossbauer (MS). En general, los resultados de MS mostraron concordancia con lo obtenido mediante XRD, tanto en composición de fases cristalinas como en tamaños de cristales.

Tabla 3. Composición química, propiedades cristalográficas y texturales de los óxidos de hierro

Óxido de hierro	Composición química (bulk) (% p/p)	Composición química (superficie) (% at.)	Fases cristalinas	d_{crist} (nm)	S_{BET} ($m^2\ g^{-1}$)	V_{poro} ($cm^3\ g^{-1}$)
Fe_2O_3-COM			100 % maghemita	20,0	39	0.13
Fe_2O_3-OXL-air			79 % hematita 21 % maghemita	17,0	56	0.24
S-Fe_2O_3-OXL-air	58 Fe 4,6 S	21,9 Fe 61,2 O 6,9 S	65 % hematita 35 % maghemita	15,8	56	0.20
Fe_2O_3-SHX-air	57 Fe	21,8 Fe 66,7 O	15 % hematita 85 % maghemita	15,1	77	0.17
S-Fe_2O_3-SHX-air	51 Fe 6,6 S	18,0 Fe 65,4 O 4,8 S	*	6	28,3	0.19
Fe_2O_3-TAR-air	63 Fe < 1 C	22,2 Fe 67.1 O	80 % hematita 20 % maghemita	21,2	141	0.30
S-Fe_2O_3-TAR-air	57 Fe < 1 C 3,5 S	20,4 Fe 65,3 O 4,3 S	65 % hematita 35 % maghemita	13,6	117	0.21
Fe_2O_3-TAR-N_2	65 Fe < 1 C	19,2 Fe 54,4 O	14 % hematita 82 % maghemita	10,3	28	0.10
S-Fe_2O_3-TAR-N_2	64 Fe	15,7 Fe	20 % hematita	11,6	40	0.14

	2,6 C 2,1 S	53,9 O 2,8 S	80 % maghemita			

* En el óxido S-Fe_2O_3-SHX-air, el tamaño de cristalito era demasiado pequeño y no se pudo calcular la proporción de fases ni por XRD ni por MS.

2.2.2. Composición química

Los óxidos de hierro están formados por hierro, oxígeno, azufre (en los modificados con tiosulfato) y trazas de carbono (en las muestras obtenidas mediante precipitación con ácido tartárico). Los análisis ICP indicaron entre un 51 % y un 65 % másico de hierro, mientras que el análisis elemental reveló entre un 2,1 % y 6,6 % de azufre másico. El azufre se encuentra principalmente sobre la superficie y en forma de grupos sulfato, como mostraron los análisis XPS. A modo de ejemplo, se muestra el espectro de XPS de los orbitales Fe 2p y S 2p de la muestra S-Fe_2O_3-OXL-air en la **Figura 2**. La ausencia de sulfuro podría ser interpretada como una desventaja (debido a que son las especies de sulfuro las que han sido reportadas en literatura que previenen la pasivación y HER [4,5]), pero, como se verá más adelante, esto no supuso un problema para el rendimiento de los electrodos

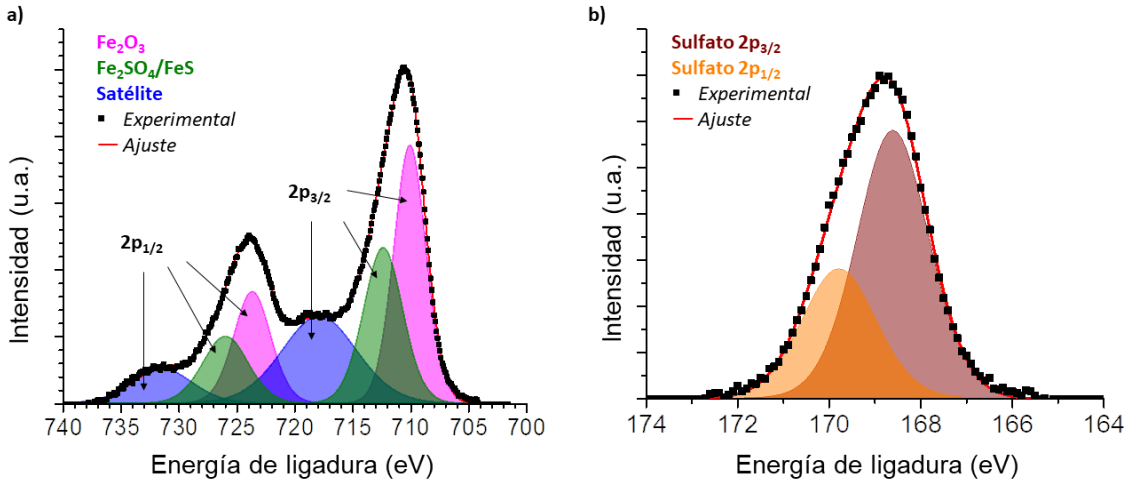

Figura 2. Espectros XPS de los orbitales: a) Fe 2p y b) S 2p del óxido S-Fe2O_3-OXL-air

2.2.3. Propiedades texturales y morfológicas

La **Figura 3** muestra micrografías SEM y FESEM de los óxidos modificados con azufre. S-Fe_2O_3-OXL-air (**Figura 3**a) consiste en aglomerados de paralelepípedos de ancho aproximado 5 micrones. Estas estructuras muestran irregularidades, grietas y fisuras, que se forman durante la descomposición térmica de los iones oxalato. El óxido de hierro S-Fe_2O_3-SHX-air tiene una morfología completamente diferente, con partículas con forma de aguja y algunas esferas (**Figura 3**b). La mesoporosidad observada para este material es consecuencia de los espacios entre estas pequeñas estructuras. El óxido de hierro basado en ácido tartárico y calcinado en aire (**Figura 3**c) muestran una morfología similar a la paja, con poros e irregularidades (formadas

durante la calcinación de la sal orgánica) que aumentan su área superficial, como se explica en el próximo párrafo. El óxido de hierro tratado en nitrógeno (**Figura 3**d) muestran signos de sinterización debido a la mayor temperatura de recocido, con partículas más pequeñas, pero más compactas y cercanas entre sí. Como resultado, hay menos huecos y menos espacio entre partículas, lo que explica el menor volumen de poro y área superficial de estos materiales.

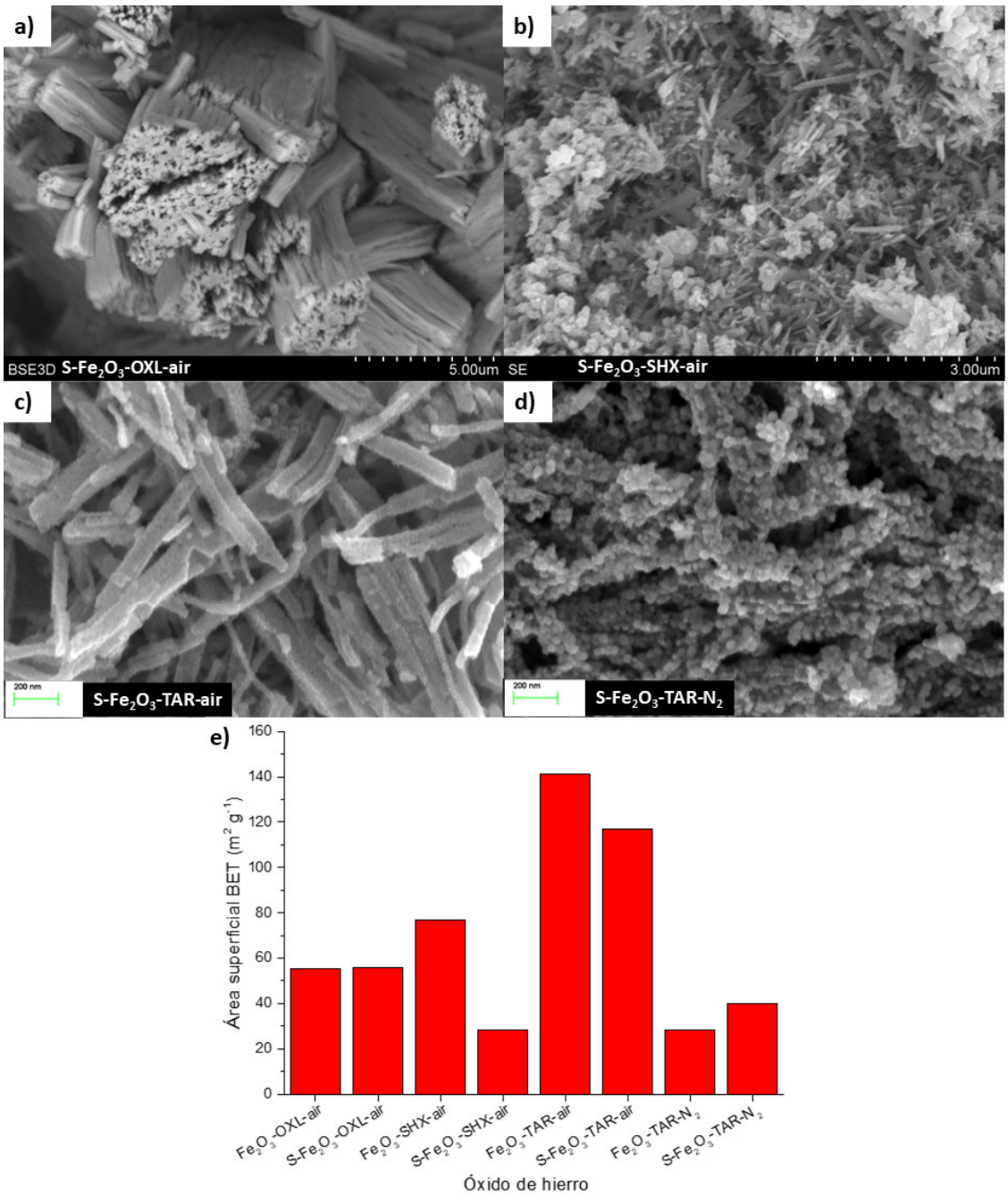

Figura 3. a) Imagen SEM de S-Fe_2O_3-OXL-air. b) Imagen SEM de S-Fe_2O_3-SHX-air. c) Imagen FESEM de S-Fe_2O_3-TAR-air. d) Imagen FESEM de S-Fe_2O_3-TAR-N_2. e) Áreas superficiales de todos los óxidos de hierro sintetizados

Los óxidos calcinados en aire mostraron isotermas de adsorción de nitrógeno tipo IV, con ciclos de histéresis H4, característicos de sólidos mesoporosos con diámetros de poro superiores a 4 nm. Por otro lado, los materiales tratados en nitrógeno a 500 °C exhiben isotermas tipo II con indicios de un ciclo de histéresis H3. Esto sugiere materiales con poca porosidad y espacios vacíos entre partículas pequeñas. Las áreas superficiales de los materiales variaron entre 28 y 141 $m^2 g^{-1}$ (**Figura 3**e) y los volúmenes de poro (V_{poro}) entre 0,13 y 0,30 $cm^3 g^{-1}$ (porosidades de entre 40 % y 61 %), habiéndose obtenido los valores más altos en los óxidos sintetizados mediante precipitación con ácido tartárico y calcinados en aire. En general, los óxidos calcinados en aire tienen mayor área superficial y volumen de poros que los tratados en nitrógeno, debido a que la mayor temperatura de tratamiento genera una rápida descomposición del ion tartrato, lo que colapsa los poros, además de sinterizar las partículas de hierro. Además, el ácido tartárico es una molécula más grande, que deja mayor porosidad al evaporarse que el ácido oxálico, razón por la cual se obtienen óxidos más porosos con esta molécula.

2.3. Evaluación de las propiedades electroquímicas (capacidad de descarga, estabilidad) de los electrodos

2.3.1. Capacidad de descarga

Los electrodos fabricados con los distintos óxidos de hierro se sometieron a 20 ciclos de carga y descarga a velocidades de 0,4 C y 0,2 C, respectivamente, mostrando diferencias en las capacidades de descarga obtenidas. En la **Figura 4** se muestran las capacidades de descarga máxima y promedio de los 20 primeros ciclos para los electrodos de los artículos 1 y 2. Se observa que el óxido de hierro comercial (Sigma-Aldrich) con partículas de diámetro menor a 50 nm, exhibe la capacidad de descarga máxima más alta de todos los electrodos, sin embargo, su bajísima capacidad promedio demuestra que este electrodo se desactiva rápidamente. Por el contrario, los electrodos S-Fe_2O_3-OXL, S-Fe_2O_3-SHX y S-Fe_2O_3-TAR-air muestran menores capacidades máximas, pero sus capacidades promedio son similares, lo que indica que son más estables. En general, los óxidos sintetizados mediante el método del ácido oxálico mostraron una capacidad máxima mayor que los sintetizados mediante el método del ácido tartárico, mientras que estos últimos presentaron diferencias menores entre capacidad máxima y capacidad promedio. Otra observación importante que se puede realizar es que todos los electrodos fabricados con óxidos modificados con azufre mostraron una pérdida de capacidad en 20 ciclos menor a los óxidos sin azufre. En promedio, cada óxido modificado con azufre tiene

una capacidad media de los 20 ciclos equivalente a un 86 % de su capacidad máxima, mientras que los no modificados con azufre (sin considerar el óxido Fe_2O_3-COM, por presentar un valor extremo) muestran una capacidad media de un 73 % de la máxima. Como se mostró en el artículo 1, el sulfato (presente en todos los óxidos sintetizados con tiosulfato de sodio) se reduce a sulfuro en las condiciones de operación del electrodo, especialmente durante la carga siguiendo la serie de reacciones descritas en las ecuaciones 1-3:

$$SO_4^{2-} + H_2O + 2e^- \rightarrow SO_3^{2-} + 2OH^- \qquad E^0 = -0.93\ \mathrm{V}\ vs.SHE \quad (1)$$

$$SO_3^{2-} + 3H_2O + 4e^- \rightarrow S^0 + 6OH^- \qquad E^0 = -0.66\ \mathrm{V}\ vs.SHE \quad (2)$$

$$S^0 + 2e^- \rightarrow S^{2-} \qquad E^0 = -0.48\ \mathrm{V}\ vs.SHE \quad (3)$$

Debido a que el sulfato se encontraba principalmente en la superficie de los óxidos de hierro, como mostraron los análisis XPS, es razonable suponer que el sulfuro formado también se encuentra en la superficie. Así, este sulfuro previene la pasivación del electrodo por especies poco conductoras y/o poco reactivas.

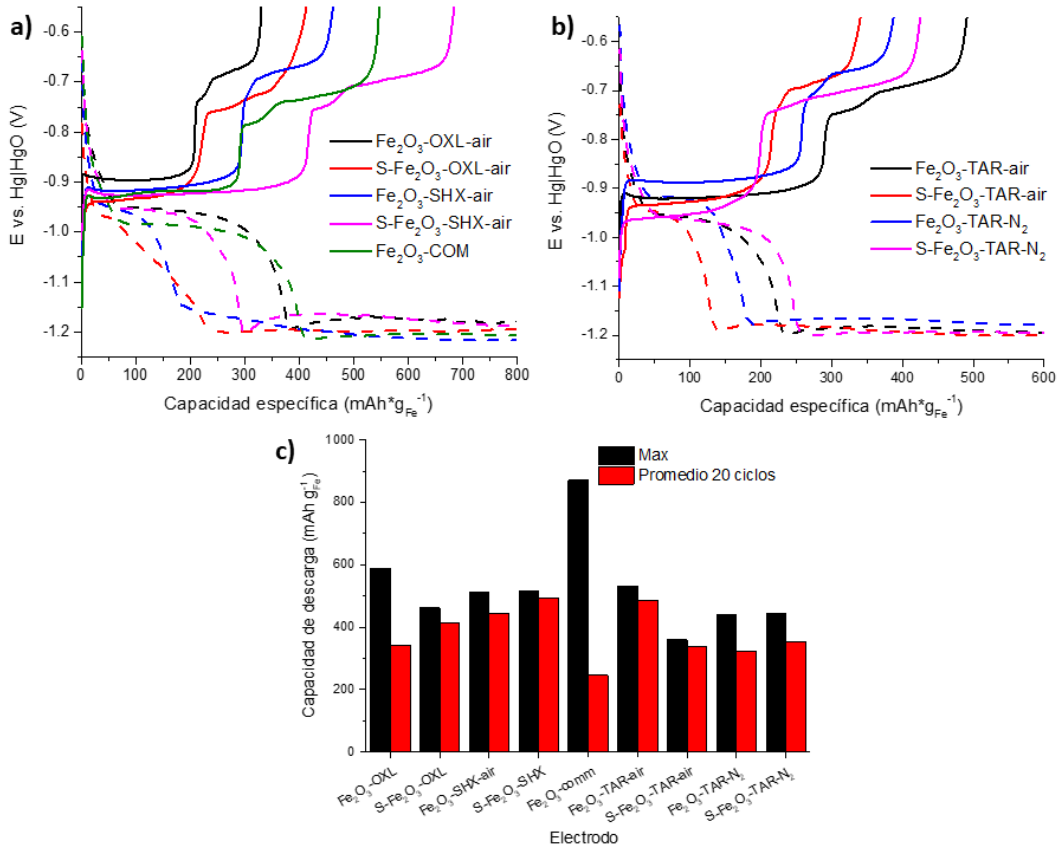

Figura 4. a) Cronopotenciometría del mejor ciclo de carga-descarga de los electrodos basados en Fe_2O_3 obtenidos a partir de ácido oxálico y NaOH, junto con el Fe_2O_3 comercial. b) a) Cronopotenciometría del mejor ciclo de carga-descarga de los electrodos basados en Fe_2O_3 obtenidos a partir de ácido oxálico tartárico. c) Capacidades de descarga máximas y promedio obtenidas con los diferentes electrodos estudiados.

2.3.2. Estabilidad

Una forma de evaluar la estabilidad de los electrodos, introducida en los artículos que conforman esta tesis es el factor de estabilidad. Este factor constituye una novedad que ajusta una curva exponencial a la capacidad de los electrodos y es una forma objetiva de comparar las estabilidades de distintos electrodos, no observada antes en literatura. De acuerdo a este modelo, los electrodos pasan por un periodo de formación, durante el cual su capacidad de descarga aumenta. Una vez superado este periodo, la capacidad disminuye siguiendo una función exponencial, de acuerdo con la ecuación 4:

$$Q_n = Q_i \times f^{n-i} \tag{4}$$

En la ecuación 4, Q es la capacidad de descarga, n es el número del ciclo, i es la cantidad de ciclos de formación y f es el factor de estabilidad, una cantidad adimensional que tiene un valor entre 0 y 1. Un ejemplo del ajuste del modelo de la ecuación 4 a la capacidad de descarga de los electrodos más estables de cada artículo se puede ver en la **Figura 5** (o en las Figuras 6 y 4 de los artículos 1 y 2, respectivamente). El electrodo más estable fue el manufacturado con el óxido de hierro S-Fe_2O_3-TAR-air, cuyo factor de estabilidad fue de 0,998, indicando que pierde aproximadamente un 0,2 % de su capacidad de descarga con cada ciclo, mientras que, de los óxidos sintetizados, el mínimo es el que corresponde al óxido Fe_2O_3-OXL, 0,829).

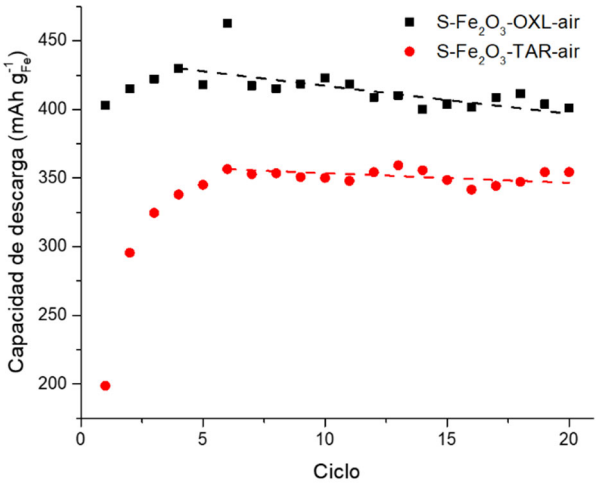

Figura 5. Ajuste del modelo de la ecuación 4 a los electrodos más estables de ambos estudios

En el artículo 1, se observó que el electrodo con mayor factor de estabilidad fue el que contenía azufre y que tuvo mayor área superficial y porosidad. El rol del azufre ya se ha explicado previamente. Sin embargo, quedaba por dilucidar el rol de las propiedades texturales en la estabilidad. Con este objetivo, en el artículo 2 se buscó correlacionar la estabilidad de los electrodos con sus propiedades texturales y cristalográficas (**Figura 6**). Se pudo observar que el

factor f se correlaciona fuertemente con el área superficial, diámetro de poros BJH (d_{poro}) y volumen de poros, mientras que muestra una tendencia positiva con el tamaño de cristal, pero no una correlación precisa. También se probó a correlacionar las propiedades físico-químicas con la capacidad máxima de descarga, donde se observan tendencias si se tratan los óxidos modificados con azufre y los no modificados como grupos separados. Sin embargo, debido a la poca cantidad de datos de cada subgrupo, no se puede hablar de correlación, por lo que se ceñirá el análisis a la estabilidad, obviando la capacidad máxima de descarga.

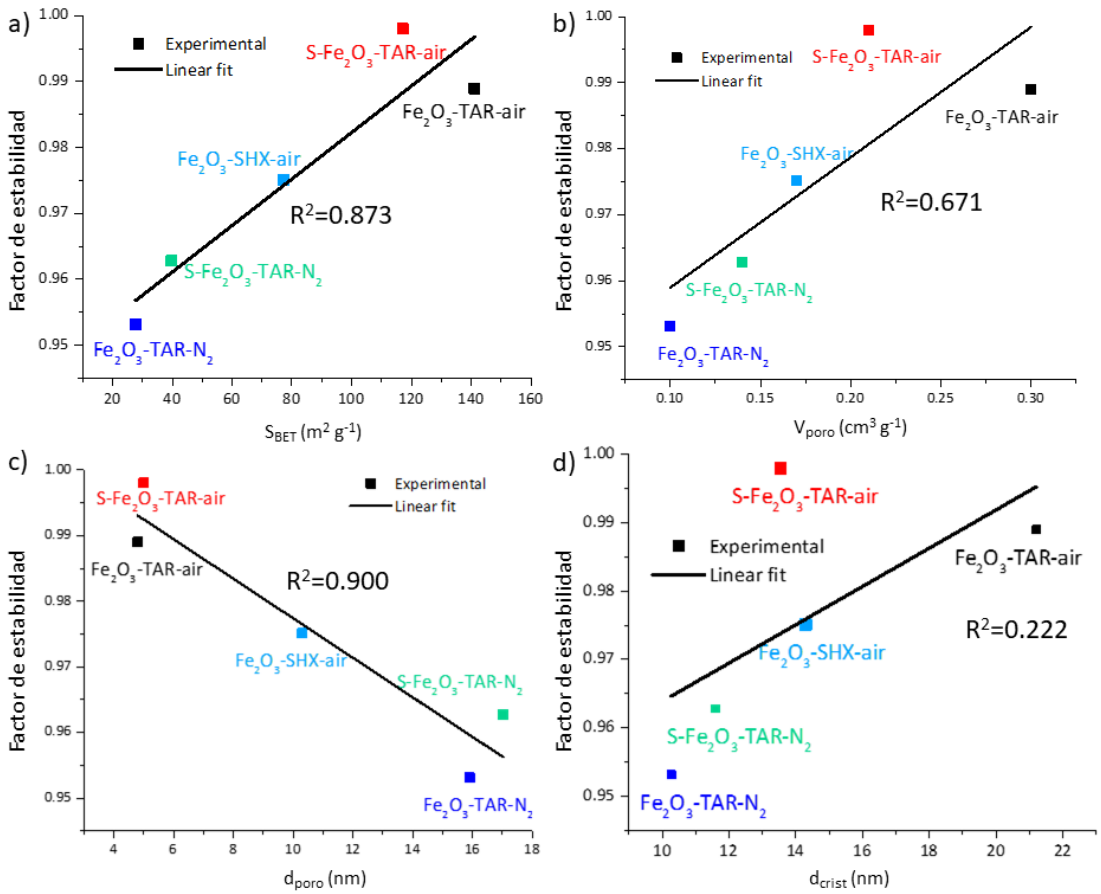

Figura 6. Correlación entre factores de estabilidad y propiedades texturales y cristalográficas,

Para estudiar las causas de la pérdida de capacidad de los electrodos, se efectuaron estudios de espectroscopía de impedancia electroquímica (EIS) al potencial de reducción de $Fe(OH)_2$ a Fe (segundo paso de carga). Estos mostraron que, en los electrodos más estables, la resistencia a la transferencia de carga prácticamente no cambia, sin embargo, esta aumenta hasta 15 veces en los electrodos que sufren más desactivación. Esta evidencia, sumada a las correlaciones encontradas entre propiedades físico-químicas y estabilidad, sugieren que la pérdida de capacidad de descarga es causada por la pasivación del electrodo debida a la formación de una capa no conductora y no reactiva de hidróxido de hierro (II). Tanto la presencia de azufre como las propiedades texturales mejoradas combaten este efecto. El azufre, por la ya

explicada formación de sulfuro y la mayor área superficial y porosidad, porque mejoran el contacto entre las fases carbonosa y metálica, reduciendo la resistencia eléctrica y, de esta forma, aumentando la reactividad.

Los dos electrodos más estables, S-Fe_2O_2-OXL-air y S-Fe_2O_2-TAR-air fueron sometidos a ciclado de larga duración. El electrodo S-Fe_2O_2-OXL fue sometido a 60 ciclos a velocidades de carga y descarga de 0,4 C y 0,2, respectivamente, logrando retener más del 80 % de su capacidad inicial. El electrodo S-Fe_2O_2-TAR-air, por su parte, fue ciclado durante 130 ciclos, perdiendo alrededor de un 20 % de la capacidad inicial (**Figura 7**). Durante los primeros 70 ciclos (350 horas, aproximadamente), el electrodo S-Fe_2O_2-OXL-air tiene mayor capacidad de descarga, pero la mayor estabilidad del electrodo S-Fe_2O_2-TAR-air hace que éste último posea una mayor capacidad a largo plazo.

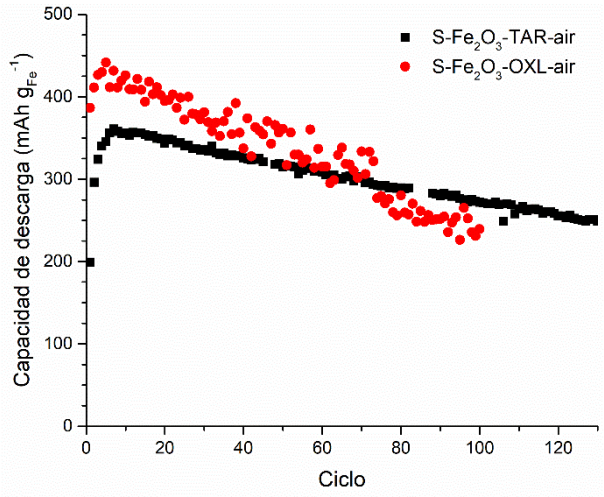

Figura 7. Durabilidad de los electrodos S-Fe_2O_2-TAR-air y S-Fe_2O_2-OXL-air

2.3.3. Capacidad de ciclado a intensidades de corriente elevadas

Dos electrodos fabricados con el óxido S-Fe_2O_3-OXL-air fueron cargados a una tasa de 0,8 C y 1,6 y descargados a una tasa de 0,4 C y 0,8 C, respectivamente. El aumento en las velocidades de carga y descarga resultó en un incremento notable en la capacidad de descarga, especialmente cuando se cargó a 0.8C y descargó a 0.4C. En estas condiciones, el electrodo alcanzó un total de casi 800 mAh g_{Fe}^{-1} de capacidad de descarga, cercano al máximo encontrado en literatura de 900 mAh g_{Fe}^{-1} [6].

Una velocidad de ciclado más alta, es decir, 1,6 C para la carga y 0,8 C para la descarga, no aumenta la capacidad del electrodo tanto como la tasa C intermedia, alcanzándose aproximadamente 600 mAh g_{Fe}^{-1} de capacidad máxima de descarga. Otro efecto del aumento en la tasa de carga y descarga es una reducción en el factor de estabilidad f. A 0,8 C – 0,4 C, el factor

de estabilidad para el electrodo S-Fe_2O_3-OXL-air se reduce de 0,995 a 0,98, mientras que, a velocidades aún más elevadas de carga y descarga, disminuye hasta poco menos de 0,97. De esta forma, variar la velocidad de carga y descarga permite variar entre una operación más estable (a menos velocidades) o una mayor capacidad específica (a velocidades intermedias), como se ve en la **Figura 8**.

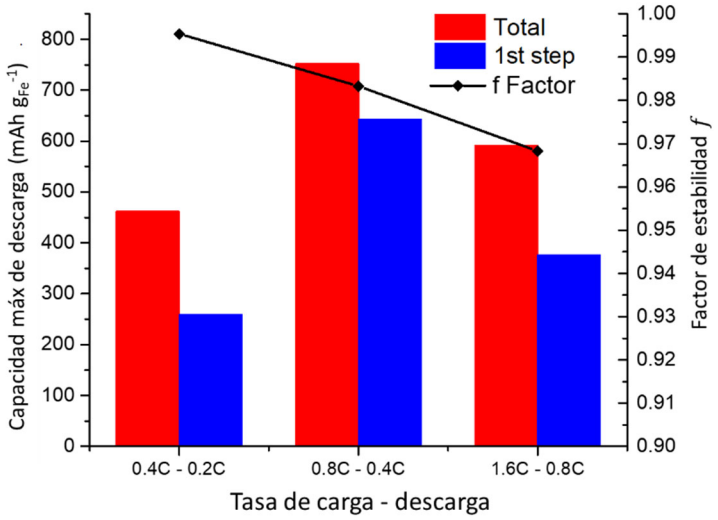

Figura 8. Efecto de la velocidad de ciclado en la capacidad y estabilidad del electrodo S-Fe_2O_3-OXL-air.

3. Catalizadores bifuncionales basados en óxidos de manganeso y estructuras carbonosas para el electrodo positivo

El electrodo positivo de las baterías metal-aire requiere un catalizador bifuncional que debe realizar tanto la reacción de evolución como la de reducción de oxígeno (OER y ORR, respectivamente). Los óxidos a base de cobalto han sido ampliamente investigados como electrodos de aire dada su excelente actividad bifuncional; sin embargo, el cobalto es una materia prima crítica debido a su uso extensivo en baterías de iones de litio. Los dispositivos de batería del futuro necesitarán obligatoriamente materias primas no críticas basadas en metales altamente abundantes. Los óxidos de manganeso han sido investigados como una alternativa a los catalizadores basados en cobalto, debido a sus actividades prometedoras, particularmente para la ORR, y más recientemente, con buenos rendimientos para la OER. Sin embargo, la baja conductividad de estos óxidos suele ser un problema para su posterior aplicación. Por esta razón, la mezcla de óxidos basados en manganeso con materiales de carbono conductores es una opción interesante.

En esta tesis se investigaron nanofilamentos de óxidos de manganeso (MONW) combinados con nanoestructuras carbonosas como nanofibras y nanotubos de carbono y óxido

de grafeno reducido. En el artículo 3, se evalúa la actividad catalítica de los MONW para las reacciones de OER y ORR, además de estudiar el efecto del dopado de estos con hierro. Se evalúa también el efecto que tiene mezclar estos materiales con nanofibras de carbono (CNF). En el artículo 4, se investiga qué efecto tiene cambiar las nanofibras de carbono por otras nanoestructuras como nanotubos de carbono multicapa (CNT) u óxido de grafeno reducido (rGO), se profundiza en el mecanismo de las reacciones y se busca explicar a nivel molecular el efecto sinérgico entre las fases carbono y óxido metálico.

En la **Tabla 4** se muestra un esquema resumido de los materiales investigados en ambos artículos.

Tabla 4. Esquema de los materiales investigados para el electrodo positivo y publicaciones resultantes

Electrodo positivo	
Materiales investigados	**Revista**
Catalizadores bifuncionales basados en nanohilos de Mn y nanofibras de carbono (**Fe-MONW/CNF)**	Catalysis Today (FI_{2021} = 5.3, $Q1_{\text{Applied Chemistry}}$; $Q1_{\text{Chemical Engineering}}$) (Artículo III)
Catalizadores bifuncionales basados en nanohilos de Mn y estructuras nanocarbonosas **(MONW/C, C: rGO, CNT, CNF y rGO-CNF)**	Catalysts (FI_{2022} = 3.9, $Q2_{\text{Physical Chemistry}}$)

3.1. Materiales investigados

En esta tesis se investigaron óxidos de manganeso en forma de nanofilamentos (MONW) dopados con hierro y materiales nanoestructurados de carbono: nanofibras (CNF) y nanotubos de carbono (CNT) y óxido de grafeno reducido (rGO) (ver **Tabla 5**).

Los nanofilamentos de dióxido de manganeso se sintetizaron mediante un método hidrotermal, reduciendo $KMnO_4$ en medio ácido a 120 y 140 °C durante 12 horas. Los nanofilamentos fueron dopados con hierro, agregando $FeCl_3$ a la síntesis, en porcentajes másicos entre 2 y 7 %. Las CNF y CNT se sintetizaron mediante descomposición catalítica de metano. Para las CNF, se empleó un catalizador $Ni:Cu:Al_2O_3$ en razón atómica 78:8:16, obtenido mediante un método de coprecipitación, mientras que para los CNT se emplearon partículas nanométricas de óxido de hierro (III), de diámetro inferior a 50 nm, (Sigma-Aldrich). Los catalizadores para CNF y CNT fueron reducidos a 550 °C y 700 °C en una corriente de hidrógeno, respectivamente, y posteriormente, la descomposición de metano se llevó a cabo a 700 °C y 900 °C, respectivamente. El óxido de grafeno se obtuvo mediante una modificación del método de Hummers [7], conocida como método de Tour [8]. Esta estrategia consiste en la oxidación

química de grafito mediante agente oxidantes fuertes ($KMnO_4$ y H_2SO_4/H_3PO_4) para obtener óxido de grafito, el cual es luego exfoliado en baño de ultrasonidos para obtener óxido de grafeno de pocas capas. El óxido de grafeno es reducido térmicamente en atmósfera inerte a 800 °C para obtener rGO. Los nanofilamentos de manganeso y las nanoestructuras de carbono fueron mezclados en molino de bolas a baja velocidad (100 rpm).

Tabla 5. Materiales sintetizados para el electrodo positivo

Nomenclatura	**Descripción**
Nanofilamentos de MnO_2	
MONW-120	Nanofilamentos de MnO_2 sintetizados a 120 °C
MONW-140	Nanofilamentos de MnO_2 sintetizados a 140 °C
2Fe-MONW-120	Nanofilamentos de MnO_2 sintetizados a 120 °C dopados con 2 % másico de hierro
5Fe-MONW-120	Nanofilamentos de MnO_2 sintetizados a 120 °C dopados con 5 % másico de hierro
7Fe-MONW-120	Nanofilamentos de MnO_2 sintetizados a 120 °C dopados con 7 % másico de hierro
Nanoestructuras de carbono	
CNF	Nanofibras de carbono sintetizadas mediante descomposición catalítica de metano a 700 °C
CNT	Nanotubos de carbono sintetizados mediante descomposición catalítica de metano a 900 °C
rGO	Óxido de grafeno reducido sintetizado por método de Tour y reducción térmica a 800 °C
rGO-CNF	Material híbrido de nanofibras de carbono crecidas mediante descomposición catalítica de metano sobre óxido de grafeno reducido
Composites	
MONW-120/CNF	Composite de MONW-120 y CNF mezclados en molino de bolas en razón másica 1:1
MONW-140/CNF	Composite de MONW-140 y CNF mezclados en molino de bolas en razón másica 1:1
MONW/CNT	Composite de MONW-120 y CNT mezclados en molino de bolas en razón másica 1:1
MONW/rGO	Composite de MONW-120 y rGO mezclados en molino de bolas en razón másica 1:1
MONW/rGO-CNF	Composite de MONW-120 y rGO-CNF mezclados en molino de bolas en razón másica 1:1

3.2. Propiedades físico-químicas

3.2.1. Propiedades cristalográficas, morfológicas y texturales

Los nanofilamentos de Mn tienen sección transversal cuadrada de ancho aproximado 75 nm y varias centenas de largo (**Figura 9** a y b), áreas superficiales alrededor de los 25 $m^2 g^{-1}$ y tienen como única fase cristalina α-MnO_2. La adición de hierro disminuyó el tamaño promedio de cristal, lo que fue interpretado como un aumento de los defectos (**Figura 9**c). Estos defectos no tienen que ver con estrés en la estructura cristalina, ya que el ion Fe^{3+} tiene un radio similar al Mn^{4+}, sino con vacantes de oxígeno debido al menor estado de oxidación del primero con respecto al segundo. No se observaron cambios en las propiedades morfológicas ni cristalográficas con la adición de hierro a la síntesis ni con la variación de la temperatura de síntesis.

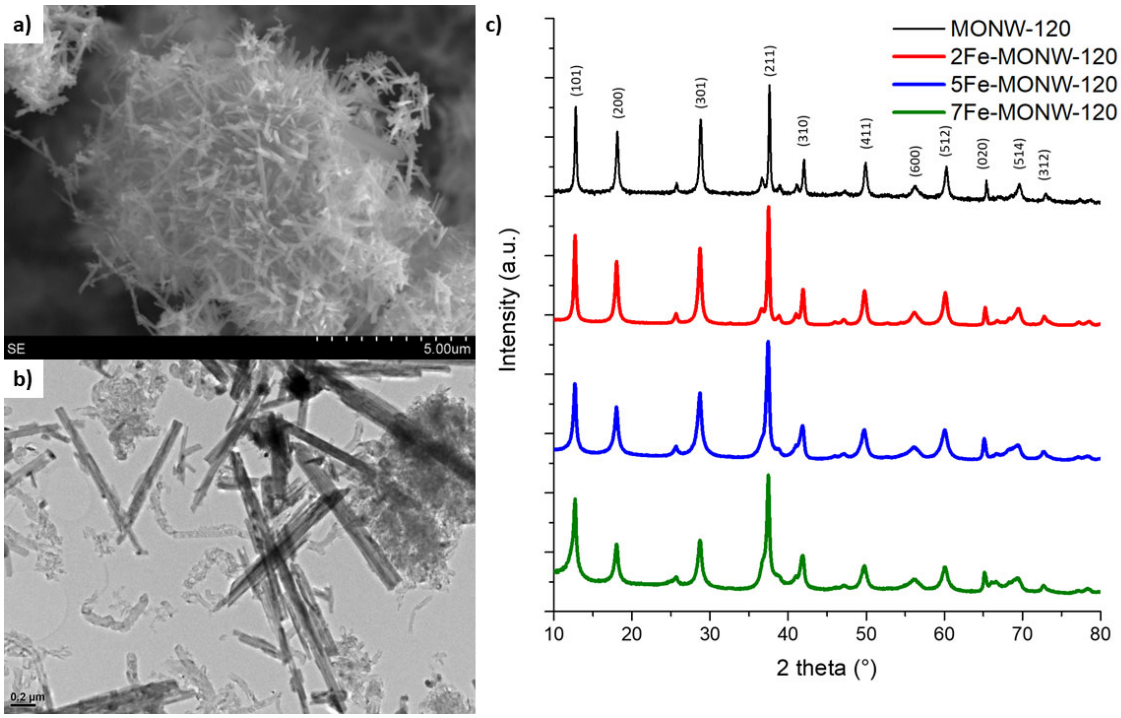

Figura 9. a) Imagen SEM de MONW-120. b) Imagen TEM del composite 5FeMONW-120/CNF. c) Difractograma de los materiales FeMONW-120

Los materiales carbonosos muestran predominancia de la fase grafítica. Las CNF tienen morfología *fishbone* con diámetros de alrededor de 50 nm (**Figura 10**a) y presentan área superficial de 95 $m^2 g^{-1}$. Los CNT son de estructura multicapa, con 100 paredes en promedio, de acuerdo a lo determinado mediante XRD (tamaño de cristal en la dirección 002 de 34 nm). Esto concuerda con las imágenes TEM, en las que se observa un diámetro de aproximadamente 70 nm para los CNT (**Figura 10**b). Debido a su elevado número de capas, los CNT tienen área superficial de sólo 11 $m^2 g^{-1}$. Finalmente, el rGO muestra un tamaño de cristal de 15 nm, lo que

equivale a un promedio de 4,5 capas (**Figura 10**c), y un área superficial de 175 $m^2 g^{-1}$. CNF y rGO tienen una concentración similar de defectos en la estructura grafítica, como se determinó mediante espectroscopía Raman (ratios entre intensidad de las bandas D y G de 1,1 y 1,4, respectivamente). Por el contrario, CNT son altamente grafíticos (I_D/I_G = 0,4) (**Figura 10**d).

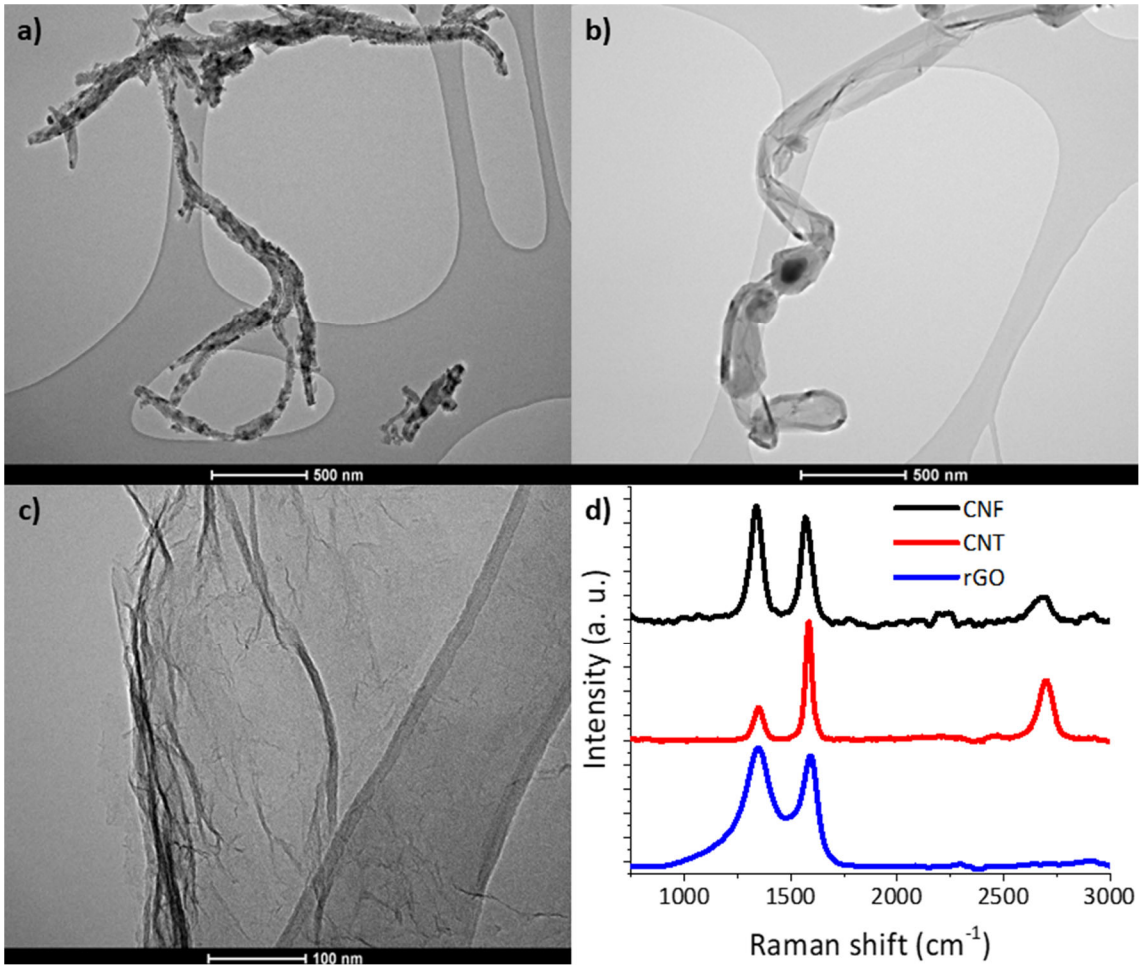

Figura 10. Imágenes TEM de: a) CNF, b) CNT, c) rGO. d) Espectros Raman de los 3 materiales de carbono.

3.2.1.1. Composición química

La composición química de los materiales carbonosos fue investigada mediante análisis elemental (EA) y espectroscopía de plasma acoplado inductivamente (ICP). Las nanofibras de carbono contienen únicamente carbono (89 % en peso), hidrógeno (1 % en peso) y níquel (7 % en peso, determinado por ICP), proveniente del catalizador de crecimiento de CNF. Los CNT, por otro lado, presentan una mayor cantidad de metal, 26 % del peso total de la muestra. El rGO tiene una relación en masa de C:O de 17 (relación atómica de 22), indicando una buena, pero no completa, reducción del óxido de grafeno.

La composición química de los nanofilamentos de óxido de manganeso fue investigada por ICP. MONW-120 y MONW-140 tienen composiciones casi idénticas (58-59 % en peso de Mn

y alrededor de 6 % en peso de K), indicando que la diferencia en las temperaturas estudiadas tiene un impacto insignificante en la composición de los nanofilamentos. El potasio en los MONW proviene del $KMnO_4$ utilizado durante la síntesis que no se ha reducido por completo. Este potasio está presente como K_2MnO_4, por lo que la cantidad de potasio se correlaciona con la cantidad de manganeso (VI). Los Fe-MONW muestran un contenido de Mn más bajo (alrededor del 50 % en peso), que disminuye con el aumento de la cantidad de hierro. Los porcentajes de hierro en los Fe-MONW (2, 5.3 y 6.6 % en peso) se acercan a las cargas nominales perseguidas (2, 5 y 7 % en peso).

La composición química de MONW y Fe-MONW también fue analizada mediante XPS. Los elementos encontrados en la superficie de los nanofilamentos fueron O, Mn, K y Fe. MONW-120, MONW-140 y los tres Fe-MONW obtenidos difieren principalmente en la cantidad de manganeso y oxígeno (**Figura 11**). Estas diferencias significativas podrían explicarse por el oxígeno adsorbido. Los nanofilamentos dopados con hierro muestran una mayor cantidad superficial de oxígeno, lo que se atribuye a su mayor capacidad de adsorber oxígeno debido a las vacantes generadas por el ion Fe^{3+}.

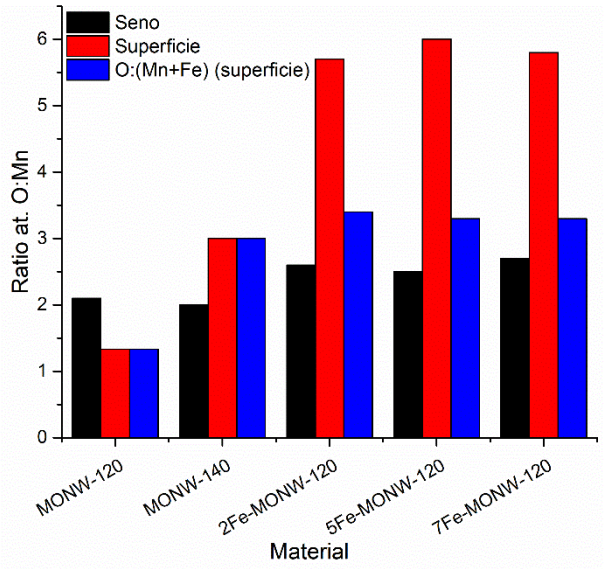

Figura 11. Ratios atómicos O:Mn y O:Me de los FeMONW-120

3.3. Propiedades electroquímicas

3.3.1. Actividad catalítica y reversibilidad hacia las reacciones de reducción y evolución de oxígeno de los MONW, CNF y efecto sinérgico entre las fases

Los resultados de voltametría lineal en KOH 0,1 M de los catalizadores del artículo 3 no dopados con hierro (MONW-120, CNF, MONW-120/CNF, MONW-140/CNF) indican un sobrepotencial de *onset* para la ORR (η_{ORR}) de entre 373 y 450 mV de magnitud (**Figura 12** y

Tabla 6). Se observa, para la ORR, un claro efecto sinérgico entre las fases, al ser el potencial de *onset* para la ORR menos negativo para los composites MONW-120/CNF y MONW-140 CNF que para los materiales MONW-120 y CNF por separado. Este efecto se hace aún más patente al observar los potenciales de semi-onda (E_{hw}) y, también, las corrientes límites (j_d) y número de electrones transferidos en la ORR (n), parámetro que aumenta desde 2,7 y 2,9 para MONW y CNF, respectivamente, hasta 3,4 y 3,5 para MONW-120/CNF y MONW-140/CNF.

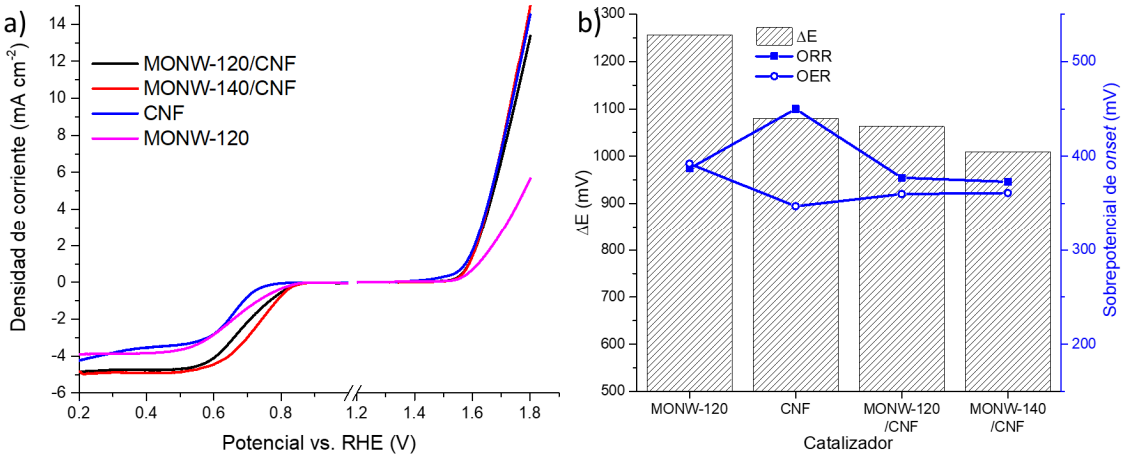

Figura 12. Actividad y reversibilidad de los catalizadores basados en MONW y CNF

Tabla 6. Parámetros de ORR y OER de catalizadores basados en MONW y CNF

Catalizador	ORR				OER		ΔE (V)
	E_{hw} (V *vs.* RHE)	η_{ORR} (mV)	j_d (mA cm^{-2})	n	E_{10} (V *vs.* RHE)	η_{OER} (mV)	
CNF	0.66	450	4.2	2.9	1.74	347	1.08
MONW-120	0.66	387	3.9	2.7	1.90	392	1.24
MONW-120/CNF	0.69	377	4.8	3.4	1.75	360	1.06
MONW-140/CNF	0.73	373	4.9	3.5	1.74	361	1.01

En el caso de la OER, CNF tiene una actividad considerable, lo que se atribuye al níquel presente como catalizador de síntesis y a los defectos de la red carbonosa (aunque las CNF lavadas con ácido aún conservan actividad, como se explica en el artículo 4). De hecho, no se observa un efecto sinérgico como sí ocurre en la ORR, al ser la actividad de los composites prácticamente idéntica a de las CNF. La actividad de MONW hacia la OER es pobre.

3.3.2. Efecto del dopado con hierro

La adición de hierro en los MONW disminuye la magnitud del sobrepotencial para la ORR, alcanzándose un óptimo en 5% de hierro (5Fe-MONW-120/CNF), aunque 7Fe-MONW-

120/CNF presenta prácticamente el mismo potencial de *onset*. Los potenciales de semi-onda, sin embargo, muestran una diferencia mayor entre los composites 5Fe-MONW-120/CNF y 7Fe-MONW-120/CNF, poniendo de manifiesto la mayor actividad catalítica del primero (**Figura 13** y **Tabla 7**). La buena actividad de los nanofilamentos dopados con hierro, más elevada que los no dopados, fue atribuida a la cantidad de defectos en la red cristalina que induce el hierro, al crear vacantes de oxígeno. Estas vacantes promueven la adsorción de oxígeno, incrementando la velocidad de la ORR. Debido a que el número de electrones transferidos no se vio afectado por el dopado con hierro, se puede suponer que éste no afecta al mecanismo de reacción, sólo la velocidad de adsorción y/o la cantidad de oxígeno que se adsorbe sobre la superficie.

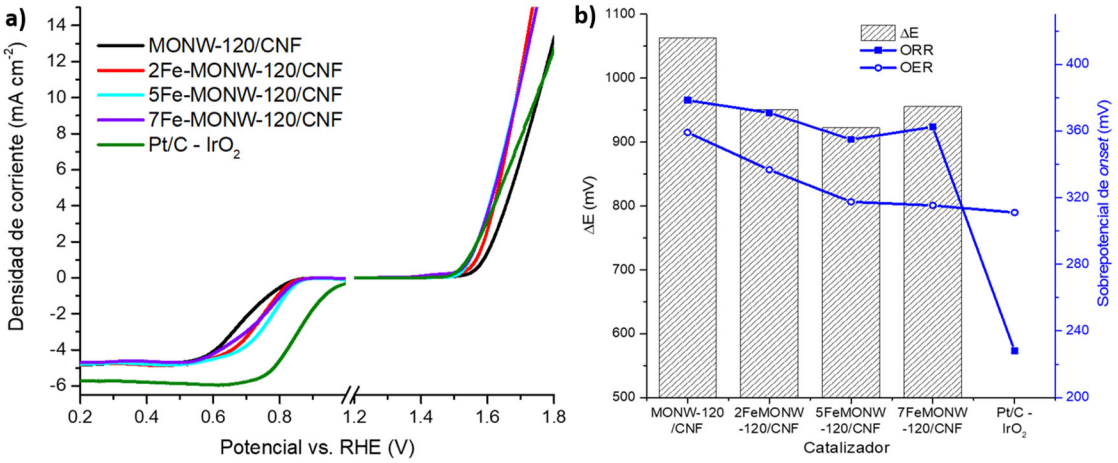

Figura 13. Actividad y reversibilidad de los catalizadores basados en Fe-MONW/CNF y de referencia

Tabla 7. Parámetros de ORR y OER de catalizadores Fe-MONW/CNF

Catalizador	ORR				OER		ΔE (V)
	E_{hw} (V *vs.* RHE)	η_{ORR} (mV)	j_d (mA cm^{-2})	n	E_{10} (V *vs.* RHE)	η_{OER} (mV)	
2Fe-MONW-120	0.74	371	4.8	3.4	1.69	331	0.95
5Fe-MONW-120	0.77	355	4.8	3.4	1.69	317	0.92
7Fe-MONW-120	0.73	362	4.8	3.4	1.69	315	0.96
Pt/C – IrO_2	0.88	208	5.7	4.0	1.75	312	-

En la OER, el sobrepotencial de *onset* tiene un mínimo en el composite 7Fe-MONW-120/CNF, prácticamente idéntico al del catalizador de referencia, IrO_2. Sin embargo, al analizar el potencial E_{10}, los tres composites dopados con hierro muestran un valor menor que IrO_2, indicando una buena actividad para la OER.

La bifuncionalidad de los catalizadores se evaluó a través del parámetro ΔE (**Figura 12**b y **Figura 13**b), correspondiente a la diferencia entre E_{10} en la OER y el potencial de semi-onda para la ORR. Con los catalizadores Fe-MONW/CNF, se obtuvieron valores de ΔE inferiores a 1 V, siendo el mínimo el obtenido con 5Fe-MONW-120/CNF, 0,92 V. Este valor está en un rango medio al ser comparado con valores reportados en literatura para materiales similares (como se observa en la Tabla 6 del artículo 3).

Para complementar el análisis de actividades para la ORR y OER de los catalizadores, se analizaron las pendientes de Tafel. Los valores de las pendientes variaron entre 53 y 134 mV dec^{-1} para la ORR y 51 y 87 mV dec^{-1} para la OER. Un aspecto destacable es que MONW-120 presenta la pendiente de Tafel más alta para la ORR, pero el composite MONW-120/CNF, la menor, reforzando la hipótesis de que existe un efecto sinérgico entre la fase grafítica y la fase de MnO_2.

3.3.3. Efecto de la naturaleza de la fase carbonosa en la actividad de composites MONW/C hacia ORR y OER

Para profundizar en esta hipótesis, en el artículo 4, se probaron 3 materiales de carbono nanoestructurados como catalizadores bifuncionales para ORR-OER: nanofibras de carbono (CNF), nanotubos de carbono multicapa (CNT) y óxido de grafeno reducido (rGO). Estos materiales fueron mezclados con MONW-120 (en adelante, llamado MONW) en molino de bolas para obtener composites, al igual que en el artículo 3 se hizo con CNF.

Los materiales de carbono mostraron una menor actividad hacia la ORR que los MONW (**Figura 14**a y **Tabla 8**), con potenciales de *onset* entre hasta 160 mV más negativos. De los materiales de carbono, las nanofibras mostraron tanto el potencial de *onset* como de semi-onda más positivo. De hecho, a pesar de tener un potencial de *onset* 60 mV más negativo que MONW, CNF tiene prácticamente el mismo potencial de semi-onda. Esto puede deberse a la mayor conductividad eléctrica de las nanofibras de carbono que los óxidos de manganeso. El número de electrones transferidos en el límite difusional, calculado por el método de Koutecky-Levich es prácticamente idéntico para los 3 carbonos, siendo 2,9 o 3,0. Sin embargo, los composites MONW/C alcanzaron hasta 3,8 electrones transferidos en el caso de MONW/CNT, y 3,4 en los otros dos composites. En la OER, CNF también muestra la más alta actividad entre los materiales carbonosos. Entre los composites, es MONW/rGO (**Figura 14**b) el más activo. Los composites basados en CNT no mostraron actividades especialmente altas ni para OER ni ORR, lo que se atribuye a su baja área superficial y alta grafitización, con ausencia de defectos estructurales.

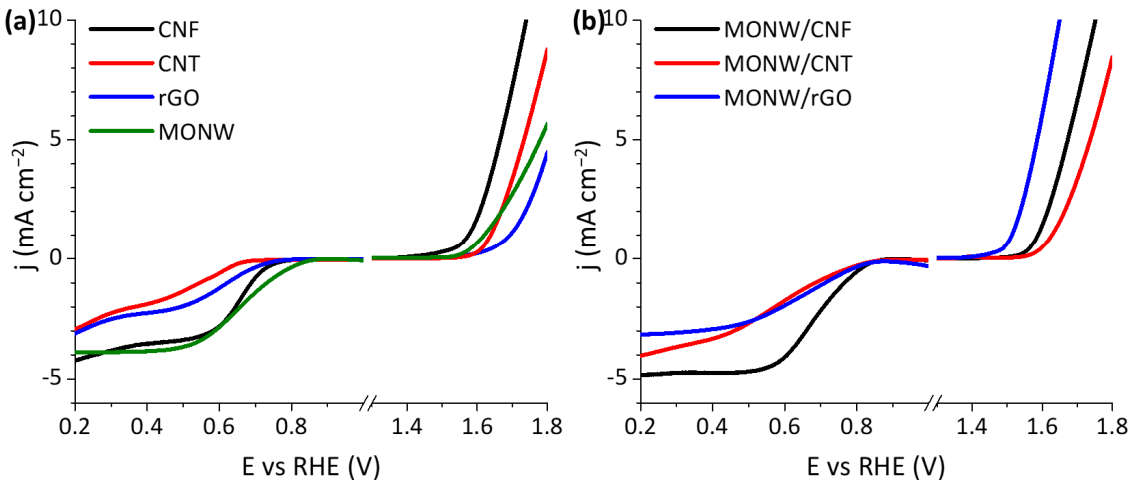

Figura 14. Actividad catalítica de los materiales carbonosos y sus composites con MONW

Tabla 8. Parámetros de ORR y OER de catalizadores MONW/C

Catalizador	ORR				OER		ΔE (V)
	E_{hwp} (V *vs.* RHE)	E_{onset} (mV)	j_L (mA cm^{-2})	n	E_{10} (V *vs.* RHE)	E_{onset} (mV)	
CNF	0,66	0,78	−4,23	2,9	1,74	1,58	1,08
CNT	0,48	0,68	−2,90	2,9	1,82	1,64	1,34
rGO	0,57	0,76	−3,06	3,0	1,92	1,69	1,35
MONW	0,66	0,84	−3,89	2,7	1,90	1,62	1,24
rGO-CNF	0,69	0,79	−3,80	2,9	1,76	1,58	1,07
MONW/CNF	0,69	0,85	−4,84	3,4	1,75	1,59	1,06
MONW/CNT	0,57	0,82	−4,02	3,8	1,83	1,63	1,25
MONW/rGO	0,64	0,83	−3,15	3,4	1,65	1,51	1,01
MONW/rGO-CNF	0,74	0,90	−5,26	3,7	1,73	1,54	0,99

Para investigar las causas de las diferencias en actividad entre los composites y los materiales que los conforman, se analizaron las pendientes de Tafel (**Figura 15**). De acuerdo a lo planteado en diversos artículos, las pendientes de Tafel de la OER y de la ORR se ven afectadas por el paso limitante de velocidad [9] (para más detalle, ver Sección 3 del Anexo I). En el caso de la ORR, CNF muestra una pendiente de Tafel de 76 mV dec^{-1}, mientras que MONW, de 136 mV dec^{-1}. Esto indica que los pasos limitantes de velocidad sobre estos dos materiales no son el mismo, lo que implica que, sobre cada uno de estos materiales, la energía de activación de cada paso es distinta. De esta forma, combinando los materiales, se pueden obtener catalizadores capaces de reducir la energía de activación de distintos pasos de la reacción de forma

simultánea, obteniéndose un efecto catalítico potenciado. De forma análoga, para la OER, MONW tiene una pendiente de Tafel de 73 mV dec^{-1}, mientras que rGO muestra una pendiente de 131 mV dec^{-1}. Así, el catalizador MONW/rGO es capaz de catalizar distintos pasos de la OER y presenta la actividad más elevada para esta reacción.

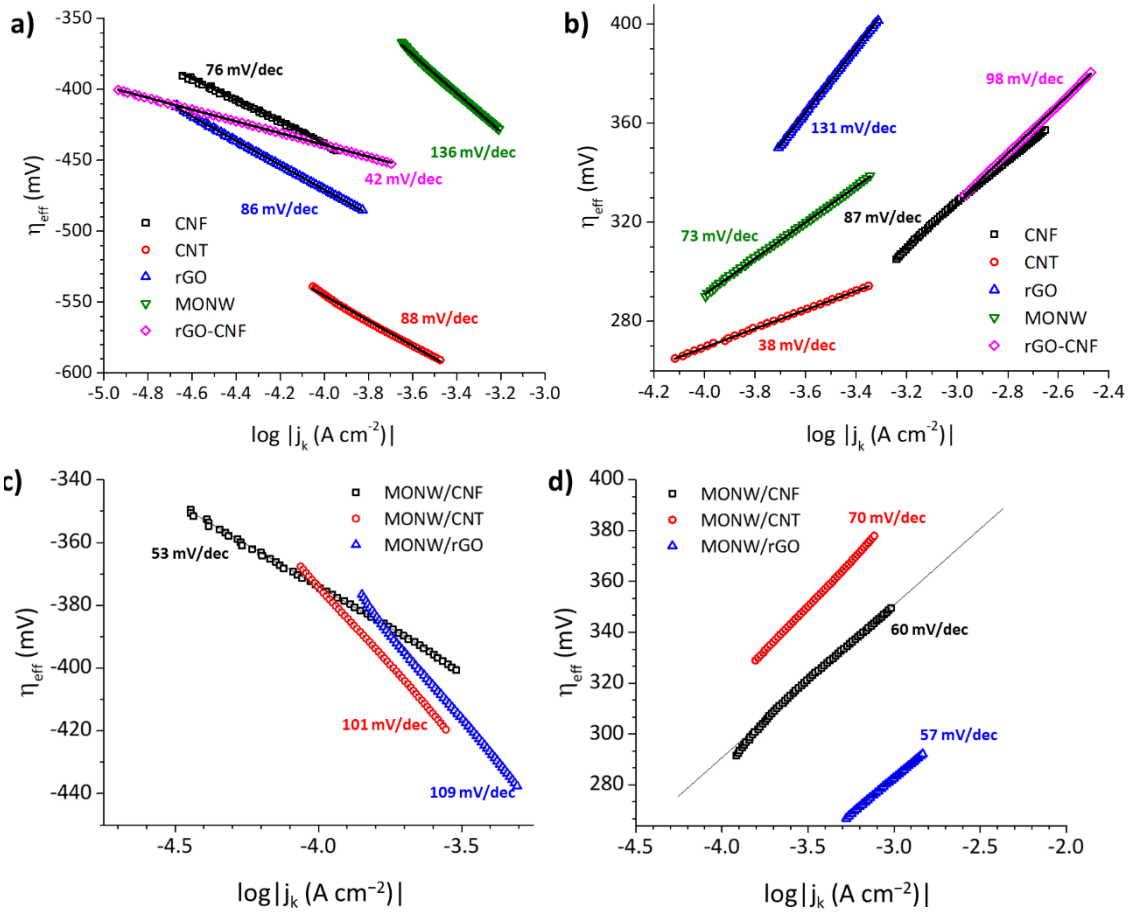

Figura 15. Pendientes de Tafel para la ORR (a, c) y OER (b,d) de materiales y compositess

Considerando estos resultados, se propuso sintetizar un material híbrido rGO-CNF y preparar con él un composite que combinase las propiedades de los composites MONW/CNF y MONW/rGO, buscando una elevada bifuncionalidad. Para este efecto, se depositaron nanopartículas de níquel sobre óxido de grafeno reducido. Las nanopartículas de níquel se usaron para hacer crecer nanofibras utilizando descomposición catalítica de metano. Este material híbrido rGO-CNF, al igual que el resto de materiales de carbono, se mezcló en molino de bolas con MONW, para obtener un composite.

La caracterización electroquímica de este composite indicó una actividad catalítica para la ORR que superó incluso a la del composite MONW/CNF, un potencial de *onset* 50 mV menos negativo, (100 mV más positivo que el catalizador de referencia). La corriente límite de este material y número de electrones transferidos también se vio mejorada con respecto al resto de

los composites, alcanzando 3,7 electrones, sugiriendo que usar distintos tipos de carbones grafíticos puede potenciar aún más el efecto sinérgico entre estos y el óxido de manganeso. Para la OER, el composite MONW/CNF-rGO mostró una actividad ligeramente inferior a MONW/rGO, sin embargo, aún superior al catalizador de referencia. De esta forma, el composite logró un ΔE de 0,99 V, logrando bajar de 1 V, al igual que los composites dopados con hierro sintetizados en el artículo 3.

En la **Figura 16** se comparan las actividades catalíticas de los mejores catalizadores de cada estudio: 5Fe-MONW-120/CNF en el artículo 2 y MONW/rGO-CNF en el artículo 4. Se incluyen también el composite MONW-120/CNF y los catalizadores de referencia para ORR y OER, a modo de comparación. Se puede ver que ambos tienen más actividad catalítica y bifuncionalidad que el composite MONW-120/CNF, y que ambos tienen entre sí una actividad muy similar. EL composite MONW/rGO-CNF destaca por su mayor corriente límite en la ORR, casi un 10 % mayor que los otros dos catalizadores. Asimismo, muestra un menor potencial de *onset* para la OER, sin embargo, a densidades de corriente elevadas, el catalizador 5Fe-MONW-120/CNF es el que presenta menor sobrepotencial, como muestra su E_{10} menos positivo.

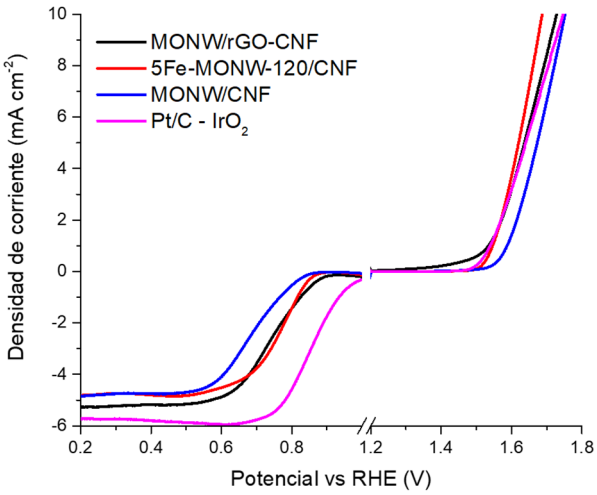

Figura 16. Comparación entre la actividad catalítica de los mejores catalizadores de cada estudio, el catalizador MONW/CNF y los catalizadores de referencia

3.3.4. Durabilidad de los catalizadores en ciclos carga-descarga

Pruebas de larga duración, mostradas en la **Figura 17**, a densidades de corriente más altas se realizaron en un electrodo de difusión de gas (GDE) para probar los catalizadores bajo condiciones más exigentes y realistas, específicamente, ±10 mA cm^{-2} para OER y ORR, y 2,5 h para cada reacción. Durante los primeros cuatro ciclos (20 horas de operación), 5Fe-MONW-120/CNF muestra un comportamiento razonablemente estable y buenas actividades tanto para

OER como para ORR, con ambos sobrepotenciales, aumentando muy lentamente, salvo en el cuarto ciclo de ORR, en que se observa una bajada hacia un potencial más negativo.

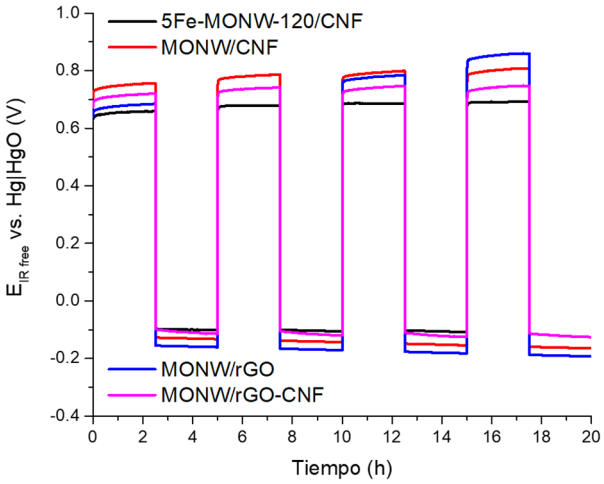

Figura 17. Ensayos de durabilidad de distintos catalizadores a ±10 mA cm^{-2} sobre GDE en KOH 6 M.

El catalizador MONW/rGO muestra, en un principio un sobrepotencial para OER casi idéntico al de 5Fe-MONW-120/CNF, sin embargo, se desactiva rápidamente, incrementando sus sobrepotenciales de OER y ORR. Por otro lado, el catalizador basado en el material híbrido de carbono muestra un sobrepotencial ligeramente superior al del composite dopado con hierro para la OER y casi idéntico para la ORR. Sin embargo, debido a su buena estabilidad, en el cuarto ciclo presenta un sobrepotencial para OER casi idéntico al de 5Fe-MONW-120/CNF y, para la ORR, el menor sobrepotencial de todos los catalizadores probados.

4. Referencias

[1] R.D. McKerracher, C. Ponce de Leon, R.G.A. Wills, A.A. Shah, F.C. Walsh, A Review of the Iron-Air Secondary Battery for Energy Storage, Chempluschem. 80 (2015) 323–335. https://doi.org/10.1002/cplu.201402238.

[2] H. Weinrich, Y.E. Durmus, H. Tempel, H. Kungl, R.A. Eichel, Silicon and iron as resource-efficient anode materials for ambient-temperature metal-air batteries: A review, Materials (Basel). 12 (2019) 2134. https://doi.org/10.3390/ma121321341-55.

[3] R.D. McKerracher, H.A. Figueredo-Rodriguez, K. Dimogiannis, C. Alegre, N.I. Villanueva-Martinez, M.J. Lázaro, V. Baglio, A.S. Aricò, C. Ponce de León, Effect of 1-octanethiol as an electrolyte additive on the performance of the iron-air battery electrodes, J. Solid State Electrochem. 25 (2021) 225–230. https://doi.org/10.1007/s10008-020-04738-4.

[4] D. Mitra, A.S. Rajan, A. Irshad, S.R. Narayanan, High Performance Iron Electrodes with Metal Sulfide Additives, J. Electrochem. Soc. 168 (2021) 030518. https://doi.org/10.1149/1945-7111/abe9c7.

[5] B.T. Hang, S.H. Yoon, S. Okada, J. ichi Yamaki, Effect of metal-sulfide additives on electrochemical properties of nano-sized Fe2O3-loaded carbon for Fe/air battery anodes, J. Power Sources. 168 (2007) 522–532. https://doi.org/10.1016/j.jpowsour.2007.02.067.

[6] R.D. McKerracher, H.A. Figueredo-Rodriguez, C. Alegre, A.S. Aricò, V. Baglio, C. Ponce de León, Improving the stability and discharge capacity of nanostructured Fe2O3/C anodes for iron-air batteries and investigation of 1-octhanethiol as an electrolyte additive, Electrochim. Acta. 318 (2019) 625–634. https://doi.org/10.1016/j.electacta.2019.06.043.

[7] W.S. Hummers, R.E. Offeman, Preparation of Graphitic Oxide, J. Am. Chem. Soc. 80 (1958) 1339. https://doi.org/10.1021/ja01539a017.

[8] D.C. Marcano, D. V. Kosynkin, J.M. Berlin, A. Sinitskii, Z. Sun, A. Slesarev, L.B. Alemany, W. Lu, J.M. Tour, Improved synthesis of graphene oxide, ACS Nano. 4 (2010) 4806–4814. https://doi.org/10.1021/nn1006368.

[9] T. Shinagawa, A.T. Garcia-Esparza, K. Takanabe, Insight on Tafel slopes from a microkinetic analysis of aqueous electrocatalysis for energy conversion, Sci. Rep. 5 (2015) 1–21. https://doi.org/10.1038/srep13801.

CAPÍTULO IV: CONCLUSIONES GENERALES

En este capítulo se presentan las conclusiones generales que se obtuvieron de las investigaciones que conforman esta tesis doctoral.

Conclusiones

La investigación relativa al electrodo negativo de baterías hierro-aire llevada a cabo en esta tesis doctoral reveló la viabilidad de los óxidos de hierro modificados con azufre combinados con un negro de carbono comercial como electrodos negativos. Los óxidos de hierro se obtuvieron en base a métodos de precipitación-calcinación con tres agentes precipitantes diferentes: ácido oxálico, hidróxido de sodio y ácido tartárico. Fueron tratados en dos atmósferas distintas: en aire a 350 °C y en nitrógeno a 500 °C. A diferencia de la mayoría de los electrodos negativos de hierro reportados en la literatura, el azufre se añadió directamente durante la síntesis del óxido de hierro, en lugar de ser añadido mediante una mezcla física. La síntesis de los óxidos de hierro fue sencilla y podría prepararse de manera escalable y a bajo costo.

Las capacidades de descarga de los electrodos de hierro variaron entre 350 y 850 mAh g_{Fe}^{-1}, dependiendo las capacidades de descarga del método de síntesis del óxido de hierro. Aunque los electrodos de hierro con modificación de azufre tuvieron capacidades más bajas que aquellos sin ella, la estabilidad cíclica mejoró enormemente con la adición de azufre, debido a que el método de síntesis permitió una distribución uniforme del azufre en la superficie del óxido de hierro. El alto grado de contacto físico entre las fases de hierro y azufre mejora la estabilidad electroquímica del electrodo, al mejorar la supresión de la evolución de hidrógeno y la pasivación.

Las características fisicoquímicas de los óxidos de hierro, principalmente las propiedades texturales, se ajustaron al cambiar las condiciones de síntesis. Se determinó que las propiedades texturales, especialmente el área superficial y el tamaño de poro, afectan la capacidad de descarga de los óxidos de hierro. Más importante aún, estas propiedades tienen un impacto significativo en la estabilidad de los electrodos. Se encontró una correlación lineal entre un área superficial grande y un tamaño de poro pequeño con una mejor estabilidad, porque se descubrió que un buen contacto entre las fases de óxido de hierro y carbono es crucial para prevenir la pasivación. Para poder comparar de forma objetiva la estabilidad de cada electrodo, se introdujo un modelo de caída exponencial (primer orden), donde la capacidad es proporcional a un factor de estabilidad, que varía entre 0 y 1, elevado al número de ciclos.

Los estudios de espectroscopía de impedancia electroquímica evidenciaron que la pasivación del electrodo es causada por una capa de hidróxido de hierro (II) no conductora que inhibe la reducción de esta especie a hierro metálico. La resistencia a la transferencia de carga en la reducción de $Fe(OH)_2$ a Fe aumenta significativamente en los electrodos que se desactivan

rápidamente. Se descubrió que la modificación con azufre tiene un efecto similar al de usar un electrodo con un área superficial grande y un buen contacto con la fase de carbono, ya que el sulfato se reduce a sulfuro y forma sulfuro de hierro (II), que reemplaza al hidróxido de hierro (II) y tiene una mayor conductividad.

Los óxidos de hierro modificados con azufre obtenidos mediante precipitación con oxalato (S-Fe_2O_3-OXL-air) o tartrato (S-Fe2O3-TAR-air) y calcinados en aire demostraron ser materiales superiores para el ciclado a largo plazo. La caída exponencial en la capacidad de descarga fue mucho menor, de manera que S-Fe_2O_3-OXL-air pudo mantener el 95 % y S-Fe_2O_3-TAR-air el 98 % de su capacidad inicial después de 20 ciclos (aproximadamente 100 horas) a tasas de 0.4C (carga) – 0.2C (descarga). S-Fe_2O_3-OXL-air mantuvo el 65% de la capacidad de descarga después de 500 horas de operación. Incluso, el electrodo S-Fe_2O_3-TAR-air fue capaz de operar por más de 100 ciclos de carga y descarga, reteniendo casi el 75 % de su capacidad de descarga inicial.

Se demostró también que se pueden controlar las tasas de carga y descarga para optimizar diferentes parámetros de rendimiento. Tasas de carga y descarga más bajas resultaron en que la operación de los electrodos fuera más estable, con menos del 0.5 % de pérdida de capacidad por ciclo en el electrodo S-Fe_2O_3-OXL-air, y al aumentar las tasas, se logró aumentar la eficiencia coulómbica del proceso del 35 % al 65 %. Esto se produce porque, al aumentar la velocidad de carga, se produce una separación entre el segundo *plateau* de carga (reducción de hidróxido de hierro a hierro) y el potencial al que ocurre la HER.

Para el electrodo positivo, se obtuvieron catalizadores bifuncionales de fácil síntesis basados en nanofilamentos de óxido de manganeso dopados con un 2 - 7 % másico de hierro (Fe-MONW) y nanofibras de carbono (CNF) que se ensayaron en las reacciones de evolución (OER) y reducción (ORR) de oxígeno en medio alcalino. Los compuestos Fe-MONW/CNF muestran una actividad mejorada en comparación con sus fases individuales (CNF y MONW) y potenciales de *onset* similares a los catalizadores de referencia, especialmente para OER. El dopado con hierro redujo el sobrepotencial de onset tanto para la ORR como para la OER, lo que resultó en una disminución en el *gap* de reversibilidad de aproximadamente 140 mV, alcanzando valores de 922 mV. El sobrepotencial para OER disminuyó monótonamente con la cantidad de hierro en el rango estudiado, mientras que el sobrepotencial para ORR alcanzó un óptimo con un 5% de másico de hierro. La caracterización físico-química determinó que el hierro crea vacantes de oxígeno en la red de MnO_2, lo que aumenta su actividad catalítica al favorecer la adsorción de oxígeno. El análisis de las pendientes de Tafel revela que combinar CNF y MONW

cambia el paso determinante de la velocidad de la reacción. Sin embargo, esto no ocurre al dopar MONW con hierro (las pendientes de Tafel no cambian significativamente). La sinergia entre la nanoestructura de manganeso dopada con hierro y la nanofibra de carbono lleva a una reversibilidad notable y un rendimiento mejorado para las reacciones de reducción (ORR) y evolución (OER) del oxígeno, junto con una estabilidad destacada, un tema clave para la futura implementación de este tipo de dispositivos.

Debido al fuerte efecto sinérgico entre las CNF y MONW observado para la ORR, se sintetizaron tres diferentes nanoestructuras de carbono: nanofibras de carbono (CNF), nanotubos de carbono (CNT) y óxido de grafeno reducido (rGO) y se mezclaron con nanofilamentos de óxido de manganeso para obtener electrocatalizadores bifuncionales de oxígeno (MONW/C, C: CNF, CNT, rGO). El tipo de carbono empleado en el catalizador tuvo un efecto importante en la actividad, siendo el catalizador sintetizado con CNF el más activo hacia ORR, y el composite con rGO, el más activo hacia OER, incluso superando el rendimiento del catalizador de referencia, IrO_2. Los catalizadores con CNT mostraron una pobre actividad para ambas reacciones, lo cual se atribuyó a su baja área superficial y falta de defectos estructurales. Los gráficos de Koutecky-Levich muestran que los catalizadores MONW/C tienen un mayor número de electrones transferidos en comparación con las fases por sí mismas, indicando un efecto sinérgico que va más allá de simplemente aumentar la conductividad o mejorar el área superficial, sino que también cambia la ruta de la reacción. El análisis de las gráficas de Tafel y la espectroscopía de impedancia electroquímica nos permitió concluir que las fases de carbono y óxido de manganeso son capaces de catalizar diferentes pasos de las rutas de reacción y que, al mezclarlas, se podría obtener un catalizador con barreras energéticas más bajas para las reacciones. Con esta información en mente, sintetizamos un material híbrido rGO-CNF y lo mezclamos con MONW, que mostró una actividad aumentada hacia ORR en comparación con MONW/CNF y una actividad cercana hacia OER a la del catalizador MONW/rGO.

Las pruebas de degradación en condiciones desafiantes mostraron una estabilidad notable para los composites 5Fe-MONW/CNF y MONW/rGO-CNF, los cuales mantuvieron potenciales estables durante 20 horas de operación a densidades de corriente de ±10 mA cm^{-2} en medio alcalino fuerte (KOH 6 M). 5Fe-MONW/CNF mantuvo una diferencia entre potenciales para OER y ORR en torno a 750 mV, y MONW/rGO-CNF, 770 mV (potenciales corregidos por IR), lo que es un resultado sobresaliente, teniendo en cuenta las condiciones desafiantes empleadas.

Los resultados obtenidos de esta investigación presentan una herramienta útil para la fabricación y operación de electrodos tanto negativos como positivos de baterías hierro-aire.

Para el electrodo negativo, se propone el diseño y síntesis de materiales porosos y de alta área superficial (sugiriéndose los óxidos de hierro obtenidos a partir de precipitación con ácidos orgánicos, por su síntesis económica, eficiente y escalable), con la adición de azufre, que puede ser en forma de sulfato. Para lograr una eficiencia coulómbica más alta, se recomienda una tasa de carga de 0.8 C y un tiempo de carga de 50 minutos. Se recomienda una tasa de carga más baja, 0.4 C, para extender la vida útil de los electrodos, pudiendo estos ser ciclados en dichas condiciones durante más de 100 ciclos, reteniendo hasta el 75 % de su capacidad de descarga.

Para el electrodo positivo, se demostró que el uso de un catalizador basado en materiales económicos y de fácil síntesis, como son los nanofilamentos de MnO_2 dopados con hierro pueden lograr un gran rendimiento si se usan en combinación con una nanoestructura de carbono grafítica adecuada. Se probó que la estructura de los materiales de carbono utilizados como aditivo en los catalizadores bifuncionales de oxígeno juega un papel clave tanto en los mecanismos de las reacciones como en el rendimiento de los catalizadores, lo que puede ser explotado para diseñar racionalmente catalizadores con actividad mejorada y/o bifuncionalidad.

ANEXO I: FUNDAMENTOS Y MEDIDAS ELECTROQUÍMICAS

1. Las ecuaciones de Nernst y de Butler-Volmer

Una batería es un dispositivo en que la energía se almacena en forma de energía química y se libera en forma de electricidad. Las celdas electroquímicas están compuestas por un ánodo, donde ocurre la oxidación de un material, y un cátodo, donde otro material se reduce, entre los cuales hay un electrolito, que tiene que ser conductor de iones, pero impermeable a los electrones. Por un conductor fuera de la celda, circulan los electrones desde el cátodo hacia el ánodo (la corriente eléctrica del ánodo al cátodo). El potencial de circuito abierto de la batería (OCP, por sus siglas en inglés), es decir, la diferencia de potencial entre los electrodos sin contar pérdidas por resistencia u otros factores, viene dado por la ecuación 1.1:

$$E_{OCP} = E_{cat}^{eq} - E_{and}^{eq} \tag{1.1}$$

En que E_{cat}^{eq} y E_{and}^{eq} son los potenciales de equilibrio del cátodo y el ánodo, respectivamente, los cuales vienen dados por la ecuación de Nernst (ecuación 1.2)

$$E^{eq} = E^{0} - \frac{RT}{nF}\ln(Q) \tag{1.2}$$

En la ecuación de Nernst, E^0 es el potencial estándar de semireacción, que corresponde al potencial de reducción para una especie a 25 °C y con una concentración de reactantes y productos disueltos de 1 mol l^{-1} (o una presión parcial de 1 atm para sustancias gaseosas), medido contra un electrodo estándar de hidrógeno (SHE), al que se le asigna un potencial estándar de 0 V. R es la constante de los gases ideales, 8.314 J mol^{-1} K^{-1} y F es la constante de Faraday, 96485 C mol^{-1}, equivalente a la magnitud de la carga eléctrica de un mol de electrones. El número de electrones que se intercambian en la semireacción se simboliza mediante n y Q es la productoria de compuestos involucrados elevados a su respectivo coeficiente estequiométrico. T es la temperatura absoluta.

Otro concepto importante es el concepto de sobrepotencial (η). Sobre un electrodo, puede existir un sobrepotencial aplicado que desplace la reacción del equilibrio, el cual se define según la ecuación 1.3:

$$\eta = E^{real} - E^{eq} \tag{1.3}$$

El concepto de sobrepotencial define tanto la dirección de la reacción (oxidación o reducción) como la velocidad de esta, reflejada en la densidad de corriente por unidad de superficie (j), medida en A cm^{-2}. Esta relación se describe mediante la ecuación de Butler-Volmer (1.4), válida cuando no hay limitaciones de transferencia de materia. Esta ecuación considera

que, en todo electrodo, hay tanto una corriente anódica (j_a) como catódica (j_c), cuya suma es la corriente total.

$$j = j_0 \left[\exp\left(\frac{\alpha_a nF}{RT}\eta\right) - \exp\left(-\frac{\alpha_c nF}{RT}\eta\right)\right] \tag{1.4}$$

Donde j_0 es la densidad de corriente de intercambio (la densidad de corriente tanto negativa como positiva de un electrodo sumergido que se encuentra en equilibrio), y α_a, α_c son los coeficientes de transferencia de carga anódico y catódico y tienen valores adimensionales entre 0 y 1 (en un electrodo ideal, $\alpha_c = 1 - \alpha_a$). Si el sobrepotencial es positivo, es decir, si el potencial sobre el electrodo es mayor al potencial de equilibrio, el término de la izquierda dentro del paréntesis en la ecuación 1.4 será mayor que el de la derecha, y se observará una corriente neta anódica (de oxidación). Por el contrario, si el sobrepotencial es negativo, se observará una corriente neta catódica o de reducción.

En una celda real, el potencial de operación de una batería durante su descarga siempre será menor que el potencial de circuito abierto. El potencial de celda real está determinado por la ecuación 1.5:

$$E_{celda} = E_{cat}^{real} - E_{and}^{real} \tag{1.5}$$

Combinando las ecuaciones 1.5 y 1.3, se obtiene:

$$E_{celda} = \left(E_{cat}^{eq} + \eta_{cat}\right) - \left(E_{and}^{eq} + \eta_{and}\right) \tag{1.6}$$

Notar que en el cátodo el sobrepotencial debe ser negativo para obtener una corriente catódica y en el ánodo, éste debe ser positivo, por lo que la ecuación 1.6 para la descarga de la batería se puede escribir como:

$$E_{celda} = E_{OCP} - |\eta_{cat}| - |\eta_{and}| \tag{1.6a}$$

Finalmente, se deben considerar también otras pérdidas energéticas, como la pérdida por la resistencia del electrolito (η_{elc}) y las pérdidas por difusión (η_{dif}). Agregando estas pérdidas a la ecuación 1.6a (y siempre en el caso de la descarga de la batería), se obtiene:

$$E_{celda} = E_{OCP} - |\eta_{cat}| - |\eta_{and}| - \eta_{elc} - \eta_{dif} \tag{1.7}$$

El sobrepotencial del electrolito sigue la ley de Ohm y depende de la intensidad de corriente (I) y la resistencia eléctrica del electrolito (R_{elc}), la que a su vez es función del tipo de electrolito, su concentración y la temperatura. Así, la ecuación 1.7 se puede escribir de la siguiente forma:

$$E_{celda} = E_{OCP} - |\eta_{cat}| - |\eta_{and}| - IR_{elc} - \eta_{dif} \quad (1.7a)$$

De la ecuación de Butler-Volmer (1.4), se puede deducir que la intensidad de corriente aumenta con la magnitud del sobrepotencial, tanto del ánodo como del cátodo. De esta forma, el potencial de celda disminuye con la intensidad de corriente. Recordando que el potencial está definido como energía por unidad de carga ($1\ V = 1\ J/C$), la potencia eléctrica (P) otorgada por una celda electroquímica está descrita por:

$$P = E_{celda} * I \quad (1.8)$$

Como ya se ha mostrado, el potencial de celda depende negativamente de la intensidad de corriente a la que opere, por lo que la ecuación 1.8 mostrará un punto máximo de potencia en función de la intensidad de corriente a la que opere la celda. Para optimizar este máximo, se deben diseñar los electrodos de forma de que maximice el área útil de éste, los coeficientes de transferencia catódicos y anódicos sean los más cercanos a la unidad y la densidad de corriente de intercambio se alta. Asimismo, se debe asegurar una buena conductividad (baja resistencia) del electrolito. De esta forma, el potencial de celda caerá de forma menos pronunciada con la intensidad de corriente y la eficiencia energética de la batería será mayor.

En el caso de la carga de la batería, las pérdidas de energía por sobrepotencial tienen el efecto inverso sobre potencial de operación de la batería, aumentándolo con respecto al potencial de circuito abierto, lo que se puede expresar mediante la ecuación 1.9:

$$E_{celda} = E_{OCP} + |\eta_{cat}| + |\eta_{and}| + IR_{elc} + \eta_{dif} \quad (1.9)$$

Otro concepto que se debe tener en cuenta es el de eficiencia faradaica o coulómbica (ϕ_Q). Éste corresponde a la razón entre la carga liberada durante descarga (Q_{dis}) y la carga eléctrica aplicada durante la carga de la batería (Q_{ch}). Como la carga corresponde a la integral de la corriente eléctrica en el tiempo, se puede obtener la ecuación 1.10:

$$\phi_Q = \frac{Q_{dis}}{Q_{ch}} = \frac{\int_0^{t_{dis}} I dt}{\int_0^{t_{ch}} I dt} \quad (1.10)$$

Donde t_{ch} y t_{dis} son los tiempos de carga y descarga, respectivamente. Si la corriente de carga y descarga son constantes, la ecuación 1.10 se puede convertir en la ecuación 1.11:

$$\phi_Q = \frac{I_{dis} * t_{dis}}{I_{ch} * t_{ch}} \quad (1.11)$$

La eficiencia energética ϕ_W se define como la razón entre la energía liberada por la batería durante la descarga (W_{dis}) y la energía aplicada durante la carga (W_{ch}). Como la energía

corresponde a la integral de la potencia eléctrica en el tiempo, se puede calcular usando la ecuación 1.12:

$$\phi_W = \frac{W_{dis}}{W_{ch}} = \frac{\int_0^{t_{dis}} P dt}{\int_0^{t_{ch}} P dt} = \frac{\int_0^{t_{dis}} E_{celda} * I dt}{\int_0^{t_{ch}} E_{celda} * I dt} \quad (1.12)$$

Una transformación matemática importante para determinar la actividad de los electrodos es lo que se conoce como pendientes de Tafel. La ecuación de Butler-Volmer (1.4) se puede linealizar aplicando logaritmo natural. Si el sobrepotencial es muy positivo, el término de la derecha dentro del paréntesis tiende a 0, obteniéndose al aplicar logaritmo natural la ecuación 1.13. En el caso opuesto, la situación es la misma, pero al ser la corriente negativa se debe tomar su valor absoluto (ecuación 1.14).

$$\ln(j) = \ln(j_0) + \frac{\alpha_a nF}{RT}\eta \quad (1.13)$$

$$\ln|j| = \ln|j_0| - \frac{\alpha_c nF}{RT}\eta \quad (1.14)$$

O, en su forma de logaritmo en base 10:

$$\log(j) = \log(j_0) + \frac{2.303\alpha_a nF}{RT}\eta \quad (1.15)$$

$$\log|j| = \log|j_0| - \frac{2.303\alpha_c nF}{RT}\eta \quad (1.16)$$

Las pendientes de Tafel entregan información sobre la actividad del catalizador, siendo una menor pendiente de Tafel preferible, debido a que significará un menor sobrepotencial necesario para aumentar en un orden de magnitud la intensidad de corriente. El intercepto la recta de Tafel con el eje x indica el logaritmo de la densidad de corriente de intercambio, que también es un indicador de la actividad de los electrodos para determinadas reacciones (una mayor densidad de corriente de intercambio indica un electrodo más activo). Otro aspecto interesante de las pendientes de Tafel es que permiten, en reacciones de múltiples pasos, ayudar a identificar el paso determinante de velocidad. Esto será discutido en profundidad en la sección 3.2.1.

2. La celda de tres electrodos

Como se vio en la sección anterior, el potencial en una batería se mide entre dos electrodos (de acuerdo con las leyes de Kirchoff), como se ve en la ecuación 1.5. Sin embargo, la ecuación de Butler-Volmer considera el sobrepotencial que actúa sobre un electrodo en particular (ecuación 1.4). Debido a esto, una celda de dos electrodos no permite caracterizar

correctamente el comportamiento de un electrodo en particular. Para solventar esta situación, se usa una celda de tres electrodos (**Figura 8**).

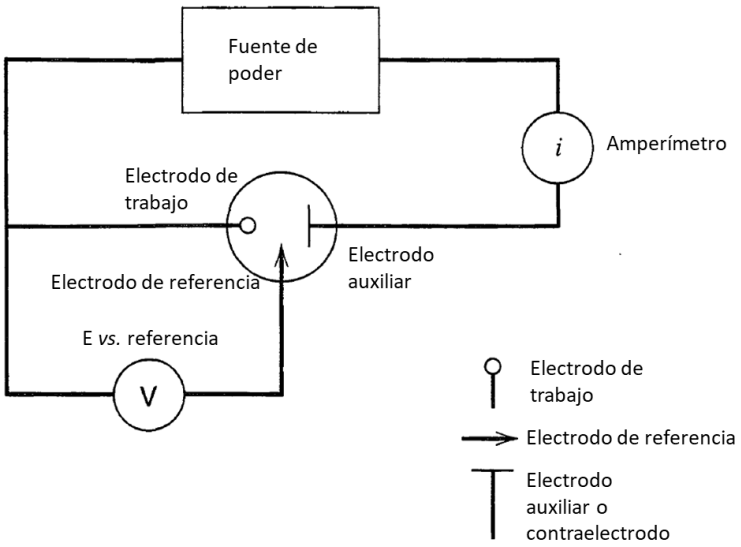

Figura 8. Esquema de una celda de 3 electrodos.

En este sistema, el electrodo de trabajo se conecta en serie con la fuente de poder o potenciostato y el contraelectrodo. El contraelectrodo debe ser un electrodo en que ocurre una reacción de baja resistencia a la transferencia de carga y, preferiblemente, de alta área superficial, para evitar que suponga una resistencia adicional a la corriente eléctrica. En este electrodo, ocurre el proceso inverso al que ocurre en el electrodo de trabajo: si en el electrodo de trabajo ocurre una oxidación, en el auxiliar ocurre una reducción, y viceversa. El electrodo de referencia se conecta en paralelo al electrodo de trabajo. Entre éste y el electrodo de trabajo debe existir resistencia eléctrica elevada, para evitar que fluya corriente que desplace el electrodo de referencia de su potencial de equilibrio, el cual debe ser conocido (en comparación con el electrodo estándar de hidrógeno, SHE). Otros aspectos que se deben considerar sobre un electrodo de referencia son su estabilidad y su rango de pH de operación. Algunos de los electrodos de referencia más utilizados son el electrodo reversible de hidrógeno, el electrodo de mercurio-óxido de mercurio (Hg|HgO), el electrodo de plata-cloruro de plata (Ag|AgCl) o el electrodo estándar de calomelanos (SCE).

3. Electrodo de disco rotario (RDE)

Para estudiar las reacciones de reducción y evolución de oxígeno (ORR y OER, respectivamente), se utiliza comúnmente un electrodo de disco rotatorio (RDE, por sus siglas en inglés). Como su nombre lo dice, este es un electrodo de trabajo que se sumerge en el electrolito y rota a una frecuencia controlada. En un experimento típico para estudiar la ORR, se realiza una

voltametría lineal desde el potencial de equilibrio hasta un potencial generalmente 1 V menor. Usando la aproximación de Koutecky-Levich, se puede expresar la densidad de corriente a partir de la ecuación 1.17:

$$\frac{1}{j} = \frac{1}{j_k} + \frac{1}{j_d} = -\frac{1}{j_0 \exp\left(-\frac{\alpha_c nF}{RT}\eta\right)} - \frac{1}{1.95nFC^*_{O_2}D^{1.5}_{O_2}\nu^{-\frac{1}{6}}f^{\frac{1}{2}}} \tag{1.17}$$

Donde j_k corresponde a la densidad de corriente cinética, que se calcula con la ecuación de Butler-Volmer (se puede obviar el término de corriente anódica), mientras que j_d es la densidad de corriente difusiva, o límite. Otros parámetros son $C^*_{O_2}$, que es la concentración de saturación de oxígeno en el electrolito, D_{O_2}, que es la difusividad de oxígeno en el electrolito, ν, la viscosidad cinemática del electrolito y f, la frecuencia de rotación del electrodo.

Al principio del barrido de potencial, la corriente aumenta en magnitud de forma exponencial siguiendo la ecuación de Butler-Volmer (1.4), siendo la corriente difusional órdenes de magnitud más alta que la cinética en este punto. Luego, al aumentar la magnitud del sobrepotencial, la corriente cinética se acerca a la difusional, que se mantiene constante, entrando en la zona de control mixto. Finalmente, alcanzado cierto sobrepotencial, se alcanza una corriente límite, la cual la densidad de corriente no supera, a pesar de aumentar la magnitud del sobrepotencial (**Figura 9**).

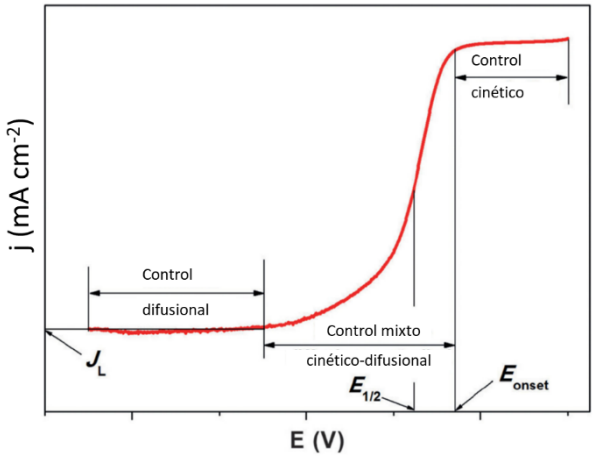

Figura 9. Curva de polarización típica para un experimento de ORR sobre un RDE. Adaptado de [1].

La curva obtenida en la **Figura 9** presenta algunos puntos interesantes. $E_{onset,ORR}$ corresponde al potencial de *onset* de la reacción, donde comienza el crecimiento exponencial de la magnitud de la corriente. Generalmente, este punto se considera como el potencial en que la densidad de corriente alcanza -0.1 mA cm^{-2}. Otro punto interesante es el potencial de semi-onda ($E_{1/2}$). Corresponde al potencial al cual la corriente alcanza la mitad de la corriente límite, representada en la gráfica como J_L.

Como se menciona en la sección 3.3.3, las pendientes de Tafel pueden entregar información valiosa sobre el mecanismo tanto de la ORR como de la OER. Shinagawa *et al.* estudiaron de forma teórica las pendientes de Tafel esperadas suponiendo distintas etapas como pasos determinantes de velocidad de las reacciones [2]. Suponiendo α=0.5 (que, coincidentemente, es ideal para un catalizador bifuncional), obtuvieron perfiles tanto para las pendientes de Tafel como para la cobertura de intermediarios (ecuaciones 1.26-1.29 y 1.32-1.35) en función del sobrepotencial sobre el electrodo. De esta forma, si en la ORR la adsorción no electroquímica de oxígeno es el paso determinante de velocidad (mecanismo de transferencia interna), se espera un pendiente de Tafel constante de 120 mV dec^{-1} en todo el rango de potenciales. Por contraste, si, por ejemplo, la segunda transferencia de un electrón es el paso determinante de velocidad (RDS), se debería observar una pendiente de 40 mV dec^{-1} a sobrepotenciales bajos en magnitud y a potenciales más alejados del de equilibrio, una pendiente de Tafel de 120 mV dec^{-1}. De la misma forma, si en la OER la primera transferencia de un electrón (ecuación 1.33) es el paso determinante de velocidad, se esperaría una pendiente de Tafel de 30 mV dec^{-1} a bajos sobrepotenciales y de 120 mV dec^{-1} a sobrepotenciales más altos, mientras que, si el RDS es la segunda transferencia electrónica, se estima una predicen 3 zonas con pendientes de 21, 40 y 120 mV dec^{-1}, respectivamente, ordenadas de sobrepotencial menor a mayor. De esta forma, obteniendo las pendientes de Tafel experimentales se puede estimar cuál es el paso determinante de velocidad de cada reacción.

4. Referencias

[1] W. Xia, A. Mahmood, Z. Liang, R. Zou, S. Guo, Earth-Abundant Nanomaterials for Oxygen Reduction, Angew. Chemie - Int. Ed. 55 (2016) 2650–2676. https://doi.org/10.1002/anie.201504830.

[2] T. Shinagawa, A.T. Garcia-Esparza, K. Takanabe, Insight on Tafel slopes from a microkinetic analysis of aqueous electrocatalysis for energy conversion, Sci. Rep. 5 (2015) 1–21. https://doi.org/10.1038/srep13801.